MINISTÉRIO DA CIÊNCIA, TECNOLOGIA, INOVAÇÕES E COMUNICAÇÕES
INSTITUTO NACIONAL DE PESQUISAS ESPACIAIS

sid.inpe.br/mtc-m21c/2018/10.31.20.40-TDI

STUDY OF MAGNETIC STRUCTURES OF AN ARCH FILAMENT SYSTEM IN THE SOLAR PHOTOSPHERE AND CHROMOSPHERE

Tardelli Ronan Coelho Stekel

Doctorate Thesis of the Graduate Course in Space Geophysics, guided by Drs. Luis Eduardo Antunes Vieira, and Alisson Dal Lago, and Andreas Lagg, approved in November 30, 2018.

URL of the original document:
<http://urlib.net/8JMKD3MGP3W34R/3S5N3AH>

INPE
São José dos Campos
2019

PUBLISHED BY:

Instituto Nacional de Pesquisas Espaciais - INPE
Gabinete do Diretor (GBDIR)
Serviço de Informação e Documentação (SESID)
CEP 12.227-010
São José dos Campos - SP - Brasil
Tel.:(012) 3208-6923/7348
E-mail: pubtc@inpe.br

COMMISSION OF BOARD OF PUBLISHING AND PRESERVATION OF INPE INTELLECTUAL PRODUCTION (DE/DIR-544):
Chairperson:
Dr. Marley Cavalcante de Lima Moscati - Centro de Previsão de Tempo e Estudos Climáticos (CGCPT)
Members:
Dra. Carina Barros Mello - Coordenação de Laboratórios Associados (COCTE)
Dr. Alisson Dal Lago - Coordenação-Geral de Ciências Espaciais e Atmosféricas (CGCEA)
Dr. Evandro Albiach Branco - Centro de Ciência do Sistema Terrestre (COCST)
Dr. Evandro Marconi Rocco - Coordenação-Geral de Engenharia e Tecnologia Espacial (CGETE)
Dr. Hermann Johann Heinrich Kux - Coordenação-Geral de Observação da Terra (CGOBT)
Dra. Ieda Del Arco Sanches - Conselho de Pós-Graduação - (CPG)
Silvia Castro Marcelino - Serviço de Informação e Documentação (SESID)

DIGITAL LIBRARY:
Dr. Gerald Jean Francis Banon
Clayton Martins Pereira - Serviço de Informação e Documentação (SESID)
DOCUMENT REVIEW:
Simone Angélica Del Ducca Barbedo - Serviço de Informação e Documentação (SESID)
André Luis Dias Fernandes - Serviço de Informação e Documentação (SESID)
ELECTRONIC EDITING:
Ivone Martins - Serviço de Informação e Documentação (SESID)
Murilo Luiz Silva Gino - Serviço de Informação e Documentação (SESID)

MINISTÉRIO DA CIÊNCIA, TECNOLOGIA, INOVAÇÕES E COMUNICAÇÕES
INSTITUTO NACIONAL DE PESQUISAS ESPACIAIS

sid.inpe.br/mtc-m21c/2018/10.31.20.40-TDI

STUDY OF MAGNETIC STRUCTURES OF AN ARCH FILAMENT SYSTEM IN THE SOLAR PHOTOSPHERE AND CHROMOSPHERE

Tardelli Ronan Coelho Stekel

Doctorate Thesis of the Graduate Course in Space Geophysics, guided by Drs. Luis Eduardo Antunes Vieira, and Alisson Dal Lago, and Andreas Lagg, approved in November 30, 2018.

URL of the original document:
<http://urlib.net/8JMKD3MGP3W34R/3S5N3AH>

INPE
São José dos Campos
2019

Cataloging in Publication Data

Stekel, Tardelli Ronan Coelho.

St38s Study of magnetic structures of an arch filament system in the solar photosphere and chromosphere / Tardelli Ronan Coelho Stekel. – São José dos Campos : INPE, 2019.

xxxii + 173 p. ; (sid.inpe.br/mtc-m21c/2018/10.31.20.40-TDI)

Thesis (Doctorate in Space Geophysics) – Instituto Nacional de Pesquisas Espaciais, São José dos Campos, 2018.

Guiding : Drs. Luis Eduardo Antunes Vieira, and Alisson Dal Lago, and Andreas Lagg.

1. Solar chromosphere. 2. GREGOR telescope. 3. Arch filament system. 4. Emerging flux region. 5. Spectropolarimetry. I.Title.

CDU 523.945:537.61

Esta obra foi licenciada sob uma Licença Creative Commons Atribuição-NãoComercial 3.0 Não Adaptada.

This work is licensed under a Creative Commons Attribution-NonCommercial 3.0 Unported License.

Aluno (a): *Tardelli Ronan Coelho Stekel*

Título: "STUDY OF MAGNETIC STRUCTURES OF AN ARCH FILAMENT SYSTEM IN THE SOLAR PHOTOSPHERE AND CHROMOSPHERE"

Aprovado (a) pela Banca Examinadora em cumprimento ao requisito exigido para obtenção do Título de *Doutor(a)* em

Geofísica Espacial/Ciências do Ambiente Solar-Terrestre

Dr. Marcelo Magalhães Fares Saba

Presidente / INPE / SJCampos - SP

( ) Participação por Video - Conferência

(X) Aprovado *( ) Reprovado*

Dr. Luis Eduardo Antunes Vieira

pp

Orientador(a) / INPE / São José dos Campos - SP

(X) Participação por Video - Conferência

(X) Aprovado *( ) Reprovado*

Dr. Alisson Dal Lago

Alisson Dal Lago

Orientador(a) / INPE / São José dos Campos - SP

( ) Participação por Video - Conferência

(X) Aprovado *( ) Reprovado*

Dr. Andreas Lagg

pp

Orientador(a) / MPS / Germany - GER

(X) Participação por Video - Conferência

(X) Aprovado *( ) Reprovado*

Dr. Joaquim Eduardo Rezende Costa

Membro da Banca / INPE / São José dos Campos - SP

( ) Participação por Video - Conferência

(X) Aprovado *( ) Reprovado*

Este trabalho foi aprovado por:

( ) maioria simples

(X) unanimidade

São José dos Campos, 30 de novembro de 2018

Aprovado (a) pela Banca Examinadora em cumprimento ao requisito exigido para obtenção do Título de ***Doutor(a)*** em

Geofísica Espacial/Ciências do Ambiente Solar-Terrestre

Dr. **Renato Sergio Dallaqua**

Membro da Banca / INPE / São José dos Campos - SP

( ) Participação por Vídeo - Conferência

(X) Aprovado ( ) Reprovado

Dra. **Adriana Benetti Marques Valio**

Convidado(a) / CRAAM/Mackenzie / São Paulo - SP

( ) Participação por Vídeo - Conferência

(X) Aprovado ( ) Reprovado

Dr. **Francisco Carlos Rocha Fernandes**

Convidado(a) / UNIVAP / São José dos Campos - SP

( ) Participação por Vídeo - Conferência

(X) Aprovado ( ) Reprovado

Este trabalho foi aprovado por:

( ) maioria simples

(X) unanimidade

São José dos Campos, 30 de novembro de 2018

ACKNOWLEDGEMENTS

First of all, I would like to thank my INPE advisors Dr. Alisson Dal Lago and Dr. Luis Eduardo Antunes Vieira. Not only for the great privilege to work with them, but further for all the complementary projects developed during this period. I'm also very grateful to Dr. Andreas Lagg, my advisor from MPS, for hosting me at MPS in Göttingen, and for sharing his knowledge about the GREGOR telescope data, the HeLix code and spectropolarimetry.

A great thanks goes to CAPES and CNPq for funding the development of this work. I am especially grateful to the PDSE/CAPES program for making possible the experience of developing part of this work abroad. I would like to acknowledge the Federal Institute of São Paulo (IFSP) for granting me with leave of absence to conclude this work.

I'd like to thank the National Institute for Space Research (INPE) for providing the necessary environment for the development of the research. Furthermore, I'm grateful to the INPE's Postgraduation Program in Space Geophysics for conferring all the classes, seminars and support for the Master and Ph.D. students.

I'm grateful to the Max-Planck-Institut für Sonnensystemforschung (MPS) for hosting and providing me the excellent infrastructure and computational support, fundamental for this work.

The 1.5-meter GREGOR solar telescope was built by a German consortium under the leadership of the Kiepenheuer Institut für Sonnenphysik in Freiburg (KIS) with the Leibniz-Institut für Astrophysik Potsdam (AIP), the Institut für Astrophysik Gottingen (IAG), the Max-Planck-Institut für Sonnensystemforschung in Gottingen (MPS), and the Instituto de Astrofísica de Canarias (IAC), and with contributions by the Astronomical Institute of the Academy of Sciences of the Czech Republic (ASCR).

The temporal analysis data applied in this work are Courtesy of NASA/SDO and the AIA, EVE, and HMI science teams.

ABSTRACT

In the last years, advances in solar observation provided by large improvements in the spatial, spectral and temporal resolution, have permitted the ground-based observatories to overcome the atmospheric seeing effect and obtain diffraction limited observations. Taking advantage of this new scenario of solar observations, we present an investigation of the magnetic structures of an arch filament system by using the Stokes profiles of the Si I 10827 Å line and He I 10830 Å triplet. The Stokes profiles are observed with GRIS spectrograph installed at the 1.5 m GREGOR telescope. We observed an emerging flux region over the NOAA AR 12252, with flux tubes emerging through the photosphere into the chromosphere. In the chromosphere it is identified as an arch filament system, with dark filaments, crossing the polarity inversion line, and connecting the footpoints of opposite polarity. The Doppler analysis of the He I 10830 Å triplet presents supersonic downflows of more than 40 $\mathrm{kms^{-1}}$ at the footpoints. The supersonic velocities are observed employing two different components for the He I, that presents subsonic and supersonic downflows in the same resolution element. The downflows result from the upward motions of new emerging flux tubes, that lead the photospheric material to higher layers close to the center of the filament. The upflows reach more than 1 $\mathrm{kms^{-1}}$ in the filament center. Then, the material flows down from the upper chromosphere to the photosphere, along with the field lines, reaching the chromospheric footpoint with supersonic velocities. The inversion of full-Stokes is performed with the HeLix+ code for both photosphere and upper chromosphere. We analyze the properties of the atmospheric parameters retrieved from the spectropolarimetric observation and provide a description of the magnetic structure of the emerging flux region and arch filament system. The magnetic structure are analyzed by using the azimuth ambiguity correction, polarity inversion line determination, magnetic loops reconstruction and linear force-free extrapolation.

Keywords: Solar chromosphere. GREGOR telescope. Arch filament system. Emerging flux region. Spectropolarimetry.

ESTUDO DE ESTRUTURAS MAGNÉTICAS DE UM SISTEMA DE FILAMENTO DE ARCO NA FOTOSFERA E CROMOSFERA

RESUMO

Nos últimos anos, os avanços nas observações solares promoveram grandes melhorias nas resoluções espacial, espectral e temporal, permitindo que os observatórios em terra superassem o efeito do seeing atmosférico e alcançassem observações no limite da difração. Utilizando deste novo cenário de observações solares, nós apresentamos uma investigação das estruturas magnéticas de um sistema de filamentos de arco, fazendo uso dos perfis de Stokes da linha do Si I 10827 Å e do tripleto He I 10830 Å. Os perfis de Stokes são observados com o espectrógrafo GRIS instalado no telescópio GREGOR de 1.5 m. Foi observado uma região de emergência de fluxo sobre a região ativa NOAA AR 12252, com tubos de fluxo emergindo através da fotosfera para a cromosfera. Na cromosfera essa região é identificada como um sistema de filamento em arco, com filamentos cruzando a linha de inversão de polaridade e conectando aos ponto base de polaridade oposta. A análise da velocidade Doppler para o tripleto He I 10830 Å apresenta fluxo supersônico descendente que alcançam mais de 40 kms^{-1} nos pontos base. As velocidades supersônicas são observadas empregando duas componentes atmosféricas para o He I, que apresenta fluxos descendentes subsônicos e supersônicos no mesmo elemento de resolução. Os fluxos descendentes resultam do movimentos ascendente dos novos tubos de fluxo emergentes, que conduzem o material da fotosfera para camadas mais altas, próximas ao centro do filamento. Os fluxos ascendentes alcançam mais de 1 kms^{-1} no centro de filamentos. Dessa forma, o material flui da cromosfera superior para a fotosfera, junto com as linhas de campo, alcançando o ponto base na cromosfera, com velocidades supersônicas. A inversão dos parâmetros de Stokes é realizada com o código HeLix^{+} para as linha Si I e tripleto He I. Analisamos as propriedades dos parâmetros atmosféricos recuperados da observação espectropolarimetricas e fornecemos uma descrição da estrutura magnética da região de emergência de fluxo e do sistema de filamentos de arco. As estruturas magnéticas são analizadas fazendo uso da correção de ambiguidade do azimute, determinação da linha de inversão de polaridade, reconstrução dos arcos magnéticos na cromosfera e extrapolação linear livre de força.

Palavras-chave: Cromosfera Solar. Telescópio GREGOR. Sistema de filamentos de arco. Regiões de emergência de fluxo. Espectropolarimetria.

LIST OF FIGURES

Page

1.1 Model for the Emerging flux region (EFR). The large arrows present the flux tube motion (expanding), the solid lines are the flux tubes and the dashed line the magnetic field orientation. The magnetic flux emerges as a set of flux tubes expanding through the convection zone. The pores and sunspots form as a consequence of the successive flux bundles emergence at the surface. 3

1.2 Solar chromosphere observed in the H-alpha by the Big Bear Solar Observatory (BBSO) on June 13, 1999. We can see in the solar disk the large QS filaments, the AR filament is inside the active region. In the border of the AR 08580 is the intermediate filament. On top we can note the polar crown (PC) filament. In the solar limb we can see the prominences, where the larger prominence, on top, seems to be related with the PC filament. Note the QS filaments follow the Polarity inversion line (PIL), presented as a green dashed line. 9

1.3 Flux rope formation model by Ballegooijen and Martens (1989). The rectangle represents the solar photosphere, and the dashed line the PIL, separating the two regions of opposite magnetic polarity. The initial configuration in panel (a) there are potential field lines (solid lines) that cross the PIL; (b) sheared magnetic field produced by flows along the neutral line; (c) magnetic shear is enhanced further because of the flows toward the neutral line; (d) the reconnection form the more extended loop AD and a shorter loop BC which tends to submerge. (e) Loops EF and GH are forced to the neutral line; (f) a new reconnection generates the helical loop EH and a shorter loop GF which again tends to submerges. Thus, dipped magnetic field lines are developed carrying the plasma higher to chromosphere and corona. 11

1.4 Schematic atomic model of the He I, with 46 energy levels and the transition between each pair of levels. The individual He I 10830 Å splitting and D_3 transitions are highlighted in the right lower inset panel. 15

1.5 Photoionization-recombination mechanism for the Helium atom. (1) In the absence of coronal irradiance, all the population of He is in the ground state of the singlet. (2) The coronal EUV radiation causes the ionization of the helium atoms in the chromosphere irradiance increasing the He II density. (3) The He II recombines with the free electrons, populating both singlet and triplet sets. 16

2.1 Representation of normal Zeeman effect. Transition between energy levels for the absence and presence of the magnetic field. Due to $J_l = 0$, the lower energy level does not split in the presence of a magnetic field. When $J_u = 1$, the upper energy level splits into three different sublevels with the magnetic quantum numbers $M = -1, 0, +1$. On the bottom, the spectral look for both cases. 23

2.2 Representation of anomalous Zeeman effect. Transition between energy levels for the absence and presence of the magnetic field. In both levels $J = 2$, so the upper and lower energy level split in the presence of a magnetic field. This case is called the anomalous Zeeman effect. 24

2.3 Transverse Zeeman effect that results when the magnetic field is perpendicular to the line-of-sight. The observer can view the π component (linearly polarized) and also the σ_b and σ_r components (circularly porlarized). 25

2.4 Longitudinal Zeeman effect that results when the magnetic field is parallel to the LOS. In this case, the observer can see only the circularly polarized components (σ_b and σ_r). 25

2.5 Synthetic Stokes profiles estimated by using a developed code for the Milne-Eddington atmosphere of the Fe I 6302.5 Å. The inclination angle was set to 80° and the azimuth is 70°. The colors represent the magnetic field strength from 0 (blue) to 3 kG (red), with step of 200 G. In the Stokes I we can see the Zeeman splitting of the Fe I when increasing the magnetic field strength. Note a lower amplitude of the V Stokes due to the high inclination angle. The spectral line is not well centered in the 6302.5 Å, it is shifted to the right due to the LOS-velocity that was set to 2 kms^{-1}. 35

2.6 Comparison between inversion maps, for the azimuth angle, computed with the genetic algorithm PIKAIA (top) and UOBYQA (bottom). Note the large gradient between neighboring pixels in the UOBYQA, indicating the optimization routine got stuck in some of the local minima of the parameter space. The PIKAIA shows robustness to find the global minimum. 39

3.1 (*a*) Panoramic view of the Observatorio del Teide where the two tallest buildings hosts the GREGOR (left) and VTT (right) telescopes. (*b*) Aerial view of the Observatorio del Teide, Tenerife on the Canary Islands, with the telescopes (from bottom right) THEMIS, VTT, GREGOR, OGS, and the Solar Pyramid. (*c*) The 1.5 m GREGOR telescope in operation. The dome is an open-foldable with diameter of 9 m. 42

3.2 Optical setup of the GREGOR telescope and the adaptive optic (AO) system. The configuration is a double Gregory-type telescope, with two intermediate focus F1 and F2. In the F1 a water-cooled field stop limits the field-of-view (FOV) to a diameter of 150". The dashed line outlines the adaptive optics. 45

3.3 Sketch of the optomechanical design and optical path from the focus F4 of the GREGOR telescope (see Figure 3.2) to the CMOS camera. *Top:* The light beam crosses the slit entrance and polarimeter package installed in the fifth floor of the building, then it is reflected down to the fourth floor (*bottom*) where it is collimated. The collimated bean reaches the grating ruling and is then scattered. The camera mirror drives and focuses the slit spectrum in the CMOS detector. 47

3.4 Czerny Turner configuration implemented in the GRIS spectrograph. The light coming from a solar region, determined by the field of view, enters the spectrograph through an entrance slit, then crossing the polarimeter package to produce the full Stokes parameter. The concave mirror collimates the light and reflects it onto the grating. The light diffracts and is reflected in the direction of the camera mirror that is responsible to focus the light on the CMOS detector, creating a spectra for each selected slit. 49

4.1 Position of the GRIS data in the solar disk. The background image is the continuum observation from the SDO/HMI. The initial slit position is centred in 570” × 250”. The arrow over the square border indicates the direction of the slit and the arrow outside the square represents the direction of the scan. The scanned image has as resolution of 64.26” × 47.25” (46.59 Mm × 34.26 Mm) with a spatial resolution of 0.135” (∼98 km). 52
4.2 GRIS observation of the active region NOAA 12552 in the continuum. The intensity is an average of selected wavelengths where there is no absorption or telluric line. The axis are in pixel to show the image resolution of 476” × 700”, where 476” × 350” for each frame. The $y-$axis is the distance measured along the slit and the $x-$axis the distance along the scan. The complex AR is characterized by having a sunspot with several pores, and a long penumbra scattered among them. 53
4.3 The spectrum of one slit observed by GREGOR/GRIS in the center of the active region NOAA 12552 for the unpolarized light (Stokes I). The spectral range comprises the wavelength from 10823.695 Å to 10841.880 Å. There are 1010 equally spaced wavelengths, with a spectral resolution of 18.03 mÅ pix^{-1}. The y−axis is the distance measured along the slit in arcsecond and the x−axis is the wavelength range. The vertical dark bands that seem to be oscillating are the absorption lines, where this movement is mainly due to the Doppler effect over the spectral line. On the other hand, the vertical dark lines, that look static, are the H_2O telluric lines. 55
4.4 Stokes I profile for an observed pixel of the GRIS scann. The spectrum comprises wavelengths from 10823.695 Å to 10841.880 Å and includes ten spectral lines and four telluric. The black line describes a pixel observed in a quiet region, with low polarization signal and the red dashed line is the profile for a pixel observed above a sunspot umbra. The splitting of the spectral lines is due to the Zeeman effect. There is a superposition between Ca I and the blue component of the He I. The red bands are the spectral lines and the blue ones the telluric lines. 57

4.5 Stokes maps observed in the photospheric line Si I 10827 Å. The Stokes I, Q, U and V are in relation to the continuum Stokes I (I_c) presented on Figure 4.2. The y-axis represents the distance (in arcsec) along the slit and the x-axis along the scan. The Stokes I, Q and U were obtained from the center of the Si I 10827 Å line and the Stokes V from the red wing. We can note by the Stokes Q, U and V, a high polarization signal in the photosphere in the region of the AR NOAA 12552, indicating the presence of magnetic field by the Zeeman effect. 58

4.6 Stokes maps observed in the Upper chromospheric line He I 10830 Å. The Stokes I, Q, U, and V are in relation to the continuum Stokes I (I_c) presented on Figure 4.2. The y-axis represents the Distance (in arcsec) along the slit and the x-axis along the scan. The Stokes I, Q and U were obtained from the central line of the He I 10830 Å and the Stokes V from the red wing. We can note by the Stokes Q, U and V, a high polarization signal in the chromosphere in the region of the AR NOAA 12552, indicating the presence of magnetic field by the Zeeman effect. The polarization signal seen in the Stokes maps are less intense than in the photospheric line due to the lower magnetic field strength in the chromosphere layer. We can note in the Stokes I/Ic, dark regions in 45° with the x-axis, they are the filaments studied in this work. The filaments can only be seen in the chromosphere strong line and not in the photosphere (Figure 4.5). . . 59

4.7 Map of the degree of polarization (P_{tot}) for the (Top) Photosphere with the Si I 10827 Å central line for the Q and U and red wing for the stokes V. ($Bottom$) (P_{tot}) for the chromosphere with the He I 10830 Å triplet. The lower polarized region, selected to perform the continuum calibration, is shown by the white square. 63

4.8 Wavelength scale calibration based on two telluric lines. In black the mean quite solar profile and in red the telluric lines 10832.108 Å and 10833.981 Å, described by “Telluric 10832” and “Telluric 10834”, respectively. The green regions denote the selected points to normalize the continuum. A relation between the two telluric lines and the atlas profile of the Fourier Transform Spectrometer resulted in a wavelength dispersion of 18.03 mÅ. The $y-$axis was drawn subsequent to the wavelength scale calibration. 65

4.9 Fourier power spectrum of the spatial frequencies for the Stokes I, Q, U and V for the Si I 10827 Å line. The displayed spectrum is the average of all the spectra along the slits. The red dashed line is the equivalent of white noise, where every spatial frequency has the same power. The blue dashed line determines the size of the minimum discernible structure, that was 0.40" for the Stokes I, 0.55" for Q and V, and 0.52" for the Stokes U. 68

4.10 Fourier power spectrum of the spatial frequencies for the Stokes I, Q, U and V for the He I 10830 Å line. The spectrum is the average of all the spectra along the slit. The red dashed line is the equivalent of white noise, where every spatial frequency has the same power. The blue dashed line determines the size of the minimum discernible structure, that was 0.47" for the Stokes I, 0.45" for Q and U, and 0.52" for the Stokes V. 69

4.11 Fried parameter r_0 observed along all the 700 slit scans. The first scan started at 07:53:41 UT and last 09:02:35 UT. We can note the r_0 reaches values larger than 15 cm in the beginning of the observation, indicating a better seeing condition in the first frame. The seeing can be consider good along all the observation. 71

4.12 Histogram of the relative frequency distribution of the Fried parameter. The $\langle r_0 \rangle = 10$ cm for our observation dataset. 71

5.1 Filaments over the upper chromosphere. (*Top*) The background is the Stokes I/Ic map, integrated 0.4 Å around the He I 10830 Å central line. (*Bottom*) Stokes V/Ic map integrated 0.4 Å in the red wing of the He I 10830 Å line. The yellow contours outline the selected filaments. The red lines represent the umbral regions and the dashed white line delimits the penumbral area obtained from the continuum map (Figure 4.2). 74

5.2 Geometry and distances of the filaments previous presented in Figure 5.1. The filaments are represented as the red contours with the number from 1 to 4 (in red). The width, length, and distances between filaments are displayed in Mm (1 Mm = 1.34"). 75

5.3 Overview of the AR 12552 at 07:52 UT on June 9th, 2018, observed with the SDO/HMI. In the (Top) The continuum image where we can see the complex AR including umbra, penumbra, pores, and light bridges. In the ($Botton$) The LOS-magnetic field, where the black and white are negative and positive polarities, respectively. The blue rectangle designated the region-of-interest (ROI) covering all the AR and used to compute the magnetic flux. The images were observed nearly the GRIS scan start time (07:53 UT). The red rectangle is the GRIS field-of-view (FOV) acquired from the full slit scan, starting from the left to right of the rectangle. . . 79

5.4 Evolution of the emerging magnetic flux in the AR 12552 in the HMI continuum, presented in six time frames, the first 24h before and the last almost 24 h after the GRIS observation (between the 3rd and 4th frame). We can note the evolution starting from two sunspots and few pores ($first frame$) to a very complex structure with extended penumbra and light bridges ($last frame$). 80

5.5 Evolution of the emerging magnetic flux in the AR 12552 in the HMI magnetograms, presented in six time frames, the first 48h before and the last 48h after the GRIS observation (between the 3rd and 4th frame). The black and white are negative and positive polarities, respectively. . . 81

5.6 Evolution of the magnetic flux computed for the HMI LOS-magnetic field comprising the ROI (blue rectangle in Figure 5.3). The red and blue lines describe the magnetic flux of the positive and negative polarity, respectively. The dashed vertical lines denote the GRIS observation time. We can note an increment of the magnetic flux due to the emerging magnetic flux in the AR 12552. 82

6.1 Spectral profiles of the Stokes I/I_C centered in the 10832.108 Å telluric line. The gray lines are the Lorentzian profiles for each pixel of the map and the red line is the mean intensity profile. We note the center of all fitted models is well defined in accordance to the telluric line center. However, the spectral line amplitude shows a considerable variation that needs to be improved. 86

6.2 Spectral profiles of the Stokes I/I_C centered in the 10832.108 Å telluric line. The colored curves are the Lorentzian profiles obtained for each pixel, with the corresponding color referring to the slit number. We note there is a fragmentation of profiles with the same colors and different amplitudes, indicating there is amplitude variation of the telluric line along the scan. 87

6.3 Doppler velocity map inferred by fitting a single Voigt profile for the He I red component. The red color corresponds to the downflows and blue to the upflows. The contours comprise the regions with supersonic flows and are candidates regions to present dual-flow profiles in the He I blended component. 92

6.4 (*Top*) The continuum map. (*Middle*) Stokes I/Ic for the He I 10830 Å. (*Bottom*) The Doppler velocity for the upper chromosphere. The black contours (white in the *Middle* panel) comprise the regions with supersonic flows, and the red ones, the filaments. We identify supersonic downflows in the footpoint of most filaments, as highlighted by the yellow arrow in the *Middle* panel. 93

6.5 Normalized Stokes I/I_c profiles for selected pixels where we can observe a dual-flow in the red component of the He I line. The black dots are the observed profile after the telluric line subtraction. The solid red line displays the best fit for the double-Voigt profile. It is composed of two single Voigt model, denoted by the dash and dash-dotted gray lines. The blue line is the Voigt fit for the single flow model. (a) Two subsonic flows. (b-c) Two clear spectral lines, one subsonic and one supersonic. (d) Dual-flow, with very large redshift. In all theses panels, we recorded a lower fitting error for the double Voigt (red line) than for the single Voigt (blue line) 95

6.6 Doppler velocity map for the fast component of the He I 10830 Å. The components were computed with double Voigt profiles. The prevalence of redshift is imposed by the range defined in the input parameters, in order to fit only the downflows. In the main panel, the black line contours the filaments and the white outlines the supersonic downflows. The dual flow is not present in the full map, but mainly in the regions with supersonic flow, as presented in Figure 6.3. The outer panels present the footpoints where we found the supersonic flows. The black line in the outer panels detaches where the dual flow are present ("I" refers to inside, and "O" to outside). 96

6.7 Doppler velocity map for the photosphere computed for the Si I line. The red color corresponds to the downflows and blue to the upflows. The black contours comprise the filaments, and the blue ones outline the supersonic downflow observed in the chromosphere. 98

6.8 Histogram distribution of the Doppler velocities for the filament 1 (*top*) and filament 2 (*botton*). The red filled histogram comprises the downflow, and the blue one involves the upflow, which can be seen only in the filament 1. The gray dashed line separates the sub and supersonic flows. The blue line is the Gaussian distribution with center = 1.85 kms^{-1} and FWHM = 4.56 for the filament 1, and center = 2.08 kms^{-1} and FWHM = 5.00 for the filament 2. 100

6.9 (a) Selected profiles crossing a filament, and the two footpoints. The ten profiles are one pixel shifted, side by side, to cover the full filament. The background panel is the Doppler velocity for a single Voigt profile. (b) The Doppler velocity profiles along the ten selected lines for a single component (blue) and the fast component of the double Voigt model (red). The gray lines are the extension of the fast component (red), and it needs to be rejected, due to the large fitting error. The bottom gray dashed line departs the downflow to the upflow, and the second gray line separates the sub and supersonic downflows. The dashed box “1” shows the region where we find upflows, and the box “2” highlight the region we find a small region similar to a footpoint. 102

7.1 Selected points to represent the full Stokes inversion for the Si I 10827 Å He I 10830 Å and Ca I 10839 Å. The background is the second frame of the Stokes I/Ic in the center of the He line. The Point 1 is placed in the center of the leading sunspot umbra. The point 2 is in the center of the first filament. The point 3 is placed in a border of the first filament. The point 4 in the surrounding region between the filament 1 an 2. 105

7.2 Stokes profiles for the full spectral range observed with GRIS over the umbra of the leading sunspot (point 1 of Figure 7.1). The black points represent the observed spectrum, and the red line is the best fit obtained with the HeLix^{+} inversion code. The vertical gray dashed lines are, from the left, the Si I 10827 Å the He I 10830 Åa,b,c triplet, and the Ca I 10839 Å. The blue dashed line outlines the telluric line recovered to be excluded from the He red component. The magnetic field retrieved for the photosphere using the Si line is $B \approx 1960$ G, $\gamma \approx 13°$, and $\chi \approx -87°$. For the upper chromosphere the magnetic field recovered is $B \approx 971$ G, $\gamma \approx 3°$, and $\chi \approx -79°$. The full parameters are described in Table 7.1 . . 107

7.3 Stokes profiles for the full spectral range observed with GRIS over the center of the first filament (point 2 of Figure 7.1). The black points represent the observed spectrum, and the red line is the best fit obtained with the HeLix^{+} inversion code. The vertical gray dashed lines oare, from the left, the Si I 10827 Å the He I 10830 Åa,b,c triplet, and the Ca I 10839 Å. The blue dashed line outlines the telluric line recovered to be excluded from the He red component. The magnetic field retrieved for the photosphere using the Si line is B = 734 G, γ = 32°, and χ = 75°. For the upper chromosphere the magnetic field recovered is B = 436 G, γ = 80°, and χ = 27°. The full parameters are described in Table 7.2 . . 108

7.4 Stokes profiles for the full spectral range observed with GRIS in a border of the first filament (point 3 of the Figure 7.1). The black points represent the observed spectrum, and the red line is the best fit obtained with the HeLix^{+} inversion code. The vertical gray dashed lines are, from the left, the Si I 10827 Å, the He I 10830 Åa,b,c triplet, and the Ca I 10839 Å. The blue dashed line outlines the telluric line recovered to be excluded from the He red component. The magnetic field retrieved for the photosphere using the Si line is B = 735 G, γ = 71°, and χ = 30°. For the upper chromosphere the magnetic field recovered is B = 509 G, γ = 74°, and χ = 17°. The full parameters are described in Table 7.3 109

7.5 Stokes profiles for the full spectral range observed with GRIS in the surrounding region between the first and second filament (point 4 of the Figure 7.1). The black points represent the observed spectrum, and the red line is the best fit obtained with the HeLix^{+} inversion code. The vertical gray dashed lines are, from the left, the Si I 10827 Å, the He I 10830 Åa,b,c triplet, and the Ca I 10839 Å). The blue dashed line outlines the telluric line recovered to be excluded from the He red component. The magnetic field retrieved for the photosphere using the Si line is B = 616 G, γ = 104°, and χ = 1°. For the upper chromosphere the magnetic field recovered is B = 33 G, γ = 101°, and χ = 0°. The full parameters are described in Table 7.4 111

7.6 Maps of all the parameters retrieved from full-Stokes for the photosphere, using the Si I 10827 Å line. (*a*) The magnetic field Strength (B), (*b*) the azimuth angle (χ), (*c*) the incination angle (γ), (*d*) the Doppler velocity (v_{LOS}), (*e*) the Doppler width ($\Delta\lambda_D$), (*f*) the gradient of source function ($S1$), (*g*) the opacity ratio between spectral line center and continuum (η_0) and (*h*) the damping factor (a). 114

7.7 Maps of all the parameters retrieved from the inversion of full-Stokes, observed in upper chromosphere using the He I 10830 Å line. (*a*) The magnetic field Strength (B), (*b*) the azimuth angle (χ), (*c*) the incination angle (γ), (*d*) the Doppler velocity ($v_{_{LOS}}$), (*e*) the Doppler width ($\Delta\lambda_D$), (*f*) the gradient of source function ($S1$), (*g*) the opacity ratio between spectral line center and continuum (η_0) and (*h*) the damping factor (a). . 116

7.8 LOS magnetic field component for the chromosphere (*top*) and photosphere (*bottom*). The black contours are the filaments, the white solid line contours the sunspot umbras and pores, and the white dashed line outlines are the penumbral region. In the background, the red color represents the outward magnetic field (positive, in the direction of the observer), and the blue denotes the inward magnetic field (negative). In the chromosphere, the region surrounding the AR present a week field. The same week field is found in the $B_{_{LOS}}$ component of the filament fields due to the high transverse field found in the filament. 118

7.9 Histogram of the magnetic field strength distribution inside each filament, in the upper chromosphere (*top*) and photosphere (*bottom*), highlighted in Figure 7.8. The blue curve outlines a Gaussian distribution with center and FWHM displayed in the upper right position of each panel. The y-axis is the histogram density that is fixed for all the plots, based on the distribution with the highest peak. The binsize is 50 G. 119

7.10 Histogram of the inclination angle distribution inside each filament, in the upper chromosphere (*top*) and photosphere (*bottom*), highlighted in Figure 7.8. The blue curve outlines a Gaussian distribution with center and FWHM displayed in the upper right position of each panel. The y-axis is the histogram density that is fixed for all the plots, based on the distribution with the highest peak. The binsize is 5°. 120

7.11 Histogram distribution of the azimuth angle in the upper chromosphere over each filament, in the upper chromosphere (*top*) and photosphere (*bottom*), highlighted in Figure 7.8. The blue curve outlines a Gaussian distribution with center and FWHM displayed in the upper right position of each panel. The y-axis is the histogram density that is fixed for all the plots, based on the distribution with the highest peak. 121

7.12 Scatter plot of the LOS magnetic field in the chromosphere vs the LOS magnetic field in the photosphere for the region inside of the filaments contoured in the in Figure 7.8. The red line is the interpolation of the B_{LOS} field distributions, considering always crossing the (0,0) coordinate, so $B_{Chrom} = sB_{Photo}$, where s is the slope, and $\langle s \rangle = 0.36$. The LOS field components has a high correlation between photosphere and chromosphere ($\langle R \rangle = 0.843$). 122

7.13 LOS-Magnetic field for the photosphere obtained with the full Stokes inversion. The black lines are the Polarity inversion lines (PIL) for the photosphere, and the wider black line is the main PIL that is associated with the filaments. 125

7.14 Inclination error for the PIL performed in Figure 7.13, on the photosphere. The angular error is less than 2°. 126

7.15 LOS-Magnetic field for the chromosphere obtained with the inversion of full Stokes. The black lines are the Polarity inversion lines (PIL) for the chromosphere, determined by using Butterwolf low-pass filter, histogram equalization, and edge detection. The broadest black line is the main PIL that is associated with the filaments. 127

7.16 Inclination angular error for the PIL performed in Figure 7.13 for the chromosphere. The angular error is less than 2° for most of the data. However, in the final PIL points, the error increases due to the faint Stokes V intensity for the He I 10830 Å when the magnetic field strength is low. 128

7.17 Projection of the vector magnetic field **B** onto the local frame. The γ is the inclination angle of **B** with respect to the line-of-sight (LOS). The χ is the azimuth angle of **B** projection in the $x - y$ plane with respect to the x-axis. Positive azimuth angle is counterclockwise. 129

7.18 Magnetic field azimuth for the photosphere obtained with inversion of the Si I 10827 Å line. The arrows indicate the direction of the magnetic field perpendicular to the LOS plane. The background color is the LOS magnetic field strength 132

7.19 Magnetic field azimuth for the photosphere obtained from the SDO/HMI data, using the MERLIN inversion code and AZAM utility for the 180° ambiguity solution. The HMI image is transposed and inclined in relation to Figure 7.18 due to the scan geometry presented in Figure 4.1. The background color is the LOS magnetic field strength. 133

7.20 Magnetic field azimuth for the chromosphere obtained with inversion of the He I 10830 Å triplet. The arrows indicate the direction of the magnetic field perpendicular to the LOS plane. The azimuth ambiguity was solved using the SFQ method we modified for the chromosphere. 134

7.21 (*a*) Scatter plot between the inclination angle of the magnetic field vector in the photosphere and chromosphere. The angles were taken along the profiles over the filament presented in the map (*b*). Representation of 20 profiles, side by side, 1 pixel shifted, covering the full filament. All the profiles are presented in panel (*c*), where the black lines delineate the chromospheric profiles and the red lines the profile over the photosphere. The Pearson correlation between the inclination of both layers, over the filament, was R = 0.956, and the inclination angle in chromosphere is shifted by 6.95° from the one in the photosphere. The large R and the shifted angle permit us to perform the analysis of the formation height difference between Si and He lines 136

7.22 Stokes V profiles along one of the 20 lines presented in Figure 7.21. The vertical dashed lines delimit the Si and He spectral lines. The amplitude of the He profile was multiplied by 3 to improve the visualization. The blue line represents the neutral line for the photosphere and the red line, the neutral line for chromosphere. The inner box displays the neutral lines over the Stokes V map. The letter "L" denotes the leading sunspot and "T" the trailing ones. The distance between both neutral lines is $\Delta d_{_{NL}} = 1.82''$, equivalent to about 1320 km. 138

7.23 Map of the coefficient ratio of the He I 10830 Å line core to continuum absorption (η_0) retrieved from the inversion process. The black line contours the filament regions. The η_0 becomes larger in some regions of the He filament structure, mainly in the first one, which confirm a larger opacity in these regions. 140

7.24 Reconstruction of the magnetic loops over AFS region, based on direct measurement of the magnetic vector of the upper chromosphere, observed with the He I 10830 Å. The loops connect the footpoints of inverse polarities with a width of five pixels, side by side, starting from the positive footpoint. The gray lines are the loop projection in the XZ and YZ plane and can indicate the estimated height (in Mm). The height reconstruction is based in the inclination angle and spatial dispersion along the pixel path connecting the footpoints. 142

7.25 Three dimension view of the of the linear force-free field. The background is the LOS magnetic field component. The linear force-free extrapolation is estimated by using the B_z component of the photospheric magnetic field computed with the Helix inversion code for the Si I 10827 Å line. The field lines are placed over the arch filament system, with the magnetic field associated with the large-scale main bipolar magnetic field of the active region, connecting the region between the leading sunspot and the trailing pores. 144

7.26 Sketch of the magnetic field structure and Doppler velocities in the observed filament system and the emerging flux region. The bottom panel represents a cutout of the photospheric level, based on the magnetic field observation of the Si I 10827 Å line, and the top panel the upper chromospheric level, based on the observation of the He I 10830 Å. The white and dark ellipses indicate the region of positive and negative polarity, respectively. The dashed line, in the top panel, represents the PIL that separates the region of positive and negative polarities. The helical arch connecting the opposite polarities in the upper chromosphere represents the flux rope that supports the filament. The red and blue shaded areas arrows above the flux rope indicate the Doppler velocity as downflows (redshift) and upflows (blueshift) observed in the upper chromosphere. The presence of upflows (blue arrows) indicates the arch filament is expanding in the direction of the observer. The triple arrows close to the filament footpoint designate the supersonic downflow observed in the Doppler maps of the helium line. In the photosphere, the footpoints with opposite polarity move apart from each other, as designated by the green arrows. 146

LIST OF TABLES

Page

1.1 Atomic data of the He I 10830 Å transitions. 14

2.1 Stokes vectors for completely polarized states. Intensities were normalized to unity. 20

3.1 Description of some main properties of the GREGOR telescope 44
3.2 Summary of some main properties of the GRIS spectrograph 50

4.1 Spectral lines in the wavelength range covered by GREGOR/GRIS . . . 56
4.2 Summary of the main aspects concerning the GRIS dataset used in this work. 60

5.1 Length, width, and distances between the filaments in the two frames observed with GRIS in the He I 10830 Å line 76

7.1 Retrieved parameters from the Stokes profiles presented in Figure 7.2. The parameters are obtained with the inversion of the Si I, He I and Ca I lines for a pixel in the leading sunspot umbra (highlighted with number 1 in Figure 7.1) 106
7.2 Retrieved parameters from the Stokes profiles presented in Figure 7.3. The parameters are obtained with the inversion of the Si I, He I and Ca I lines for a pixel in the center of the first filament (highlighted with number 2 in Figure 7.1) 106
7.3 Retrieved parameters from the Stokes profiles presented in Figure 7.4. The parameters are obtained with the inversion of the Si I, He I and Ca I lines for a pixel in the border of the filament 1 (highlighted with number 3 in Figure 7.1) 106
7.4 Retrieved parameters from the Stokes profiles presented in Figure 7.5. The parameters are obtained with the inversion of the Si I, He I and Ca I lines, for a pixel in a surrounding area between the filament 1 and 2. (highlighted with number 4 in Figure 7.1) 110

LIST OF ABBREVIATIONS

AFS – Arch Filament System
AO – Adaptive Optics
AR – Active Region
BBI – Broad Band Image
BLD – Bresenham Line Drawing algorithm
CME – Coronal Mass Ejection
CMOS – Complementary Metal Oxide Semiconductor
CZ – Czerny-Turner
DM – Deformable Mirror
EFR – Emerging Flux Region
EUV – Extreme ultraviolet
FLCR – Ferro-electric Liquid Crystal Retarders
FOV – Field-Of-View
FR – Flux Rope
FTS – Fourier Transform Spectrograph
FWHM – Full-Width at Half-Maximum
GFPI – GREGOR Fabry-Pérot Interferometer
GRIS – GREGOR Infrared Spectrograph
HELIX – Helium Line Information Extractor
HMI – Helioseismic and Magnetic Imager
HWHM – Half-Width at Half-Maximum
IAU – International Astronomical Union
JSOC – Joint Science Operations Center
KAOS – Kiepenheuer Adaptive Optics System
LCVR – Liquid Crystal Variable Retarder
LOS – Line-Of-Sight
LTE – Local Thermodynamical Equilibrium
MCAO – Multi-Conjugate Adaptive Optics
MHD – Magnetohydrodynamic
ME – Mildne-Eddington
MPS – Max-Planck-Institut für Sonnensystemforschun
NIST – National Institute of Standards and Technology
NLTE – Non-Local Thermodynamical Equilibrium
OT – Observatorio del Teide
PC – Polar Crown
PIL – Polarity Inversion Line
PR – Photoionization-Recombination
PSF – Point Spread Function
QS – Quiet Sun
RMS – Root Mean Square

ROI – Region-Of-Interest
RTE – Radiative Transfer Equation
SA – Sheared Arcade
SDO – Solar Dynamics Observatory
SFQ – Super Fast and Quality Azimuth Disambiguation
SIC – Seeing Induced Crosstalk
SNR – Signal to Noise Ratio
SOHO – Solar and Heliospheric Observatory
SSW – SolarSoftWare
STOPRO – STOkes PROfiles code
TIP – Tenerife Infrared Polarimeter
UOBYQA – Uncostrained Optimization BY Quadratic Approximation
VSO – Virtual Solar Observatory
VTT – Vacuum Tower Telescope
WFS – Wavefront Sensor

LIST OF SYMBOLS

χ^2 – merit function
χ – azimuth angle of the magnetic field
δ – goodness function
Δh_f – formation height difference
$\Delta d_{\scriptscriptstyle NL}$ – distances between neutral lines
η_0 – coefficient ratio
Γ_{col} – collisional damping factor
Γ_{rad} – radiative damping factor
Γ_G – FWHM for the Gaussian profile
Γ_L – FWHM for the Lorentz profile
Γ_V – FWHM for the Voigt profile
γ – inclination angle of the magnetic field
γ_{offset} – offset in the inclination angle
$\hat{\mathbf{k}}$ – propagation matrix
$\hat{\xi}_{x,y}$ – amplitudes of the electric field
$\hat{O}$ – evolution operator
$\hbar$ – reduced Planck constant
λ_σ – wavelength shift of the σ component
λ_0 – Central line wavelength
λ – wavelength
$\mathbf{1}$ – indentity matrix
$\mathbf{B}_v$ – Planck function
$\mathbf{I}$ – Stokes vector
$\mathbf{k_c}$ – continuum apsorption coefficient
$\mathcal{F}$ – Faraday function
$\mathcal{H}$ – Voigt function
$\mathcal{S}$ – fraction of spectral scattered light
ν_m – magnetic viscosity
$\omega_{x,y}$ – phase of the electric field
$\phi_{p,b,r}$ – absorption profile
$\psi_{p,b,r}$ – dispersion profile
ρ_i – external density
ρ_i – internal density
ρ – density
τ_c – continuum optical depth
τ – optical depth
$\mathbf{B}$ – magnetic field vector
θ_H – heliocentric angle
φ – angular frequency
$\xi_{x,y}$ – Components of the electric field vector

a – damping factor
B – magnetic field strength
C_n – turbulence profile
$E_{J,M}$ – energy of the of the atomic level
F_b – buoyant force
g_{eff} – effective Landé factor
$\mathcal{G}$ – Gaussian function
g – gravity constant
g_L – Landé factor
I^{obs} – observed Stokes
I^{syn} – synthetic Stokes
J – total angular momentum
k_{lin} – line absortpion coefficient
k – Boltzmann's constant
$\mathcal{L}$ – Lorentzian function
L – orbital angular momentum
m_e – mass of electron
M – magnetic quantum number
m – mass of indivudual gas molecule
P_{tot} – degree of polarization
p_e – external pressure
p_i – internal pressure
p_m – magnetic pressure
$R_\odot$ – solar radius
r_0 – Fried parameter
s_{i_j} – normalized strength of the Zeeman Components
S – spin angular momentum
T_e – external temperature
T_i – internal temperature
V_{pseudo} – pseudo-Voigt function
ζ – zenith angle

CONTENTS

Page

1 Introduction 1
1.1 Emergence flux region 2
1.1.1 Magnetic buoyancy 4
1.2 Arch filament system 6
1.3 Solar filaments 7
1.3.1 Flux rope model 10
1.3.2 Eruptive filament 12
1.4 Spectral lines 12
1.4.1 He I 10830 Å triplet 13
1.4.2 Si I 10827 Å line 17

2 Spectropolarimetry 19
2.1 Stokes parameters 19
2.2 Zeeman effect 21
2.3 Radiative Transfer Equation 26
2.3.1 RTE in local thermal equilibrium 30
2.3.2 RTE through isotropic media 30
2.3.3 Propagation along the optical axis 31
2.4 Solving the RTE 32
2.5 Milne-Eddington atmosphere approximation 33
2.6 Inversion of the Stokes profiles 36
2.7 HeLIx inversion 37

3 Telescope GREGOR and GRIS spectrograph 41
3.1 Telescope Design 43
3.2 GREGOR Infrared Spectrograph 46

4 GRIS observation and data reduction 51
4.1 Primary data reduction 60
4.2 Pre-processing 61
4.2.1 Wavelength Calibration 61
4.2.1.1 Selecting the Solar quiet region 62
4.2.1.2 Wavelength scale 62

4.3 Comparison to FTS atlas 64
4.4 Noise level 66
4.5 Power Spectrum 67
4.5.1 Seeing condition 67

5 Arch filament system and temporal evolution 73
5.1 Description of the filaments 73
5.2 Temporal evolution of emerging magnetic flux 77
5.2.1 General description of the ROI 78
5.2.2 Evolution of the magnetic flux in the GRIS dataset 83

6 Doppler velocity 85
6.1 Telluric line subtraction 85
6.2 Voigt profile 88
6.2.1 Pseudo-Voigt 90
6.3 Chromospheric Single-flow 91
6.4 Chromospheric Dual-flow 94
6.5 Doppler velocity for the Si line 97
6.6 Discussion 99

7 Magnetic structure of the filament system 103
7.1 Retrieval of physical parameters from the full Stokes 104
7.2 Inversion of the full Stokes maps 113
7.3 Analysis of the magnetic field in the filaments 117
7.4 Polarity inversion line 123
7.5 Determination of the magnetic field vector 129
7.5.1 Azimuth ambiguity 130
7.6 Formation height of He I line 135
7.7 Reconstruction of EFR loops 139
7.8 Linear force-free extrapolation 141
7.9 Overview of the magnetic structure of the filament 145

8 Summary and Conclusions 149

REFERENCES 153

1 Introduction

The magnetic field strength in the solar surface varies according to the solar feature. In the poles, the magnetic field is in the order of 1 G (HOWARD, 1972). In smaller magnetic structures like plages, the field intensity is about 200 G (PILLET; VAZQUEZ, 1993), and in large scale features, like in prominent sunspots, the field strength can reaches more than 3 kG (PILLET et al., 1997) at photospheric levels.

Since the studies and observations reported by Schwabe (1843), it is established that sunspot number observed in the solar surface follow a cycle of 11 years, called solar cycle. In 1896, the Dutch physicist Pieter Zeeman confirmed the investigations made by Hendrik Antoon Lorentz that spectral lines split into polarized components in the presence of a magnetic field (ZEEMAN, 1897). In 1908, George Ellery Hale (HALE, 1908) found that some solar spectral lines seems to be widened, splited, and polarized, and then concerned an explanation for the observed sunspot spectrum: the presence of strong magnetic fields in sunspots. Since that Nobel discovery, understanding the magnetic structures of the wide range of solar features has been one of the main challenges in the astrophysics.

The development of the solar magnetograph by Horace Babcock and Harold Babcock at the Hale Solar Laboratory (BABCOCK, 1953), permitted the observation of the longitudinal magnetic field by computing the circular polarization. The Babcock's magnetograph significantly increased the spatial resolution of the magnetic field observations, from one arcmin to few arcsec.

After many improvements in the observational techniques, the previously hidden magnetic features, have become measurable, but most of the magnetic structures are until now unsolved. The first observational report of small-scale magnetic features (in the order of 1") was performed by Sheeley Jr. (1967) using the 80 cm telescope at the Kitt Peak National Solar Observatory. Nowadays, the best spatial resolution for the full stokes observation reaches about 80 km.

In the last decades, a significant improvement in the spatial resolution was derived from the use of Adaptive Optics (AO), permitting the ground-based observatories to overcome the atmospheric seeing effect and obtain diffraction limited observations. The first solar observation using AO system was performed at the Dunn Solar Telescope by Hardy (1980). In the last decade, AO systems have been deployed at major ground-based solar telescopes.

Taking advantage of this new scenario of solar observations, the main objective of this work is to study the magnetic structures of the emerging flux region in the photosphere, and the arch filament system in the chromosphere, by using the Stokes profiles of the Si I 10827 Å line and He I 10830 Å triplet. The Stokes profiles are observed with GRIS spectrograph installed at the 1.5 m GREGOR telescope. We observed an emerging flux region over the NOAA AR 12252, with flux tubes emerging through the photosphere into chromosphere. In the chromosphere it is identified as an arch filament system, with dark filaments, crossing the polarity inversion line, and connecting the footpoints of opposite polarity. We aim to interpret the properties of the atmospheric parameters retrieved from the spectropolarimetric observation, to provide a description of the magnetic structure of the observed arch filament system.

The present Chapter provides a brief introduction of the emerging flux region, the arch filament system and the filaments in the chromosphere. Chapter 2 presents a review of the spectropolarimetry and the main methodology used in this work. Details of the GREGOR telescope and the GRIS spectrograph operation are introduced in Chapter 3. The observed dataset and all the data reduction and pre-processing are explained in Chapter 4. The main aspects of the observed arch filament system and its temporal evolution is described in Chapter 5. The determination of the Doppler velocity field in the photosphere and chromosphere is accomplished in Chapter 6. The retrieval of the magnetic field vector from the Stokes profiles is detailed in Chapter 7. By the end, the conclusion of the work is presented in Chapter 8.

1.1 Emergence flux region

In order to study the magnetic structure of the arch filament system, observing different solar layers, we need to understand how the magnetic field raises from the solar surface and evolve until develop the dark filaments seen in the chromosphere. To achieve this goal, the study of Emergence flux region is an essential point.

The study of the flux emergence starts assuming that bipolar magnetic flux emerges on the solar surface, resulting from the plasma rising from the tachocline into the overlying atmosphere. This mechanism was first described by Parker (1955) to explain the formation of sunspots (details of the Parker mechanism is described in the next subsection).

According to Priest and Krishan (1990), the solar magnetic dynamo is the physical process that continually generates the magnetic fluxtubes that emerge in the photosphere, adding new magnetic flux systems to the chromosphere and corona layers. By definition, the flux emergence consists of magnetic field reaching the atmospheric layers from the solar interior (CHEUNG; ISOBE, 2014).

The magnetic flux emergence in the photosphere appears with an ample range of scales. The smallest scale is the little granular magnetic loops (with a magnetic flux in the order of 10^{16} Mx). The ephemeral regions that appear in the interior of supergranules present a flux of 10^{19} Mx, and active regions that can reaches fluxes up to 10^{23} Mx (PRIEST, 2014).

Figure 1.1 - Model for the Emerging flux region (EFR). The large arrows present the flux tube motion (expanding), the solid lines are the flux tubes and the dashed line the magnetic field orientation. The magnetic flux emerges as a set of flux tubes expanding through the convection zone. The pores and sunspots form as a consequence of the successive flux bundles emergence at the surface.

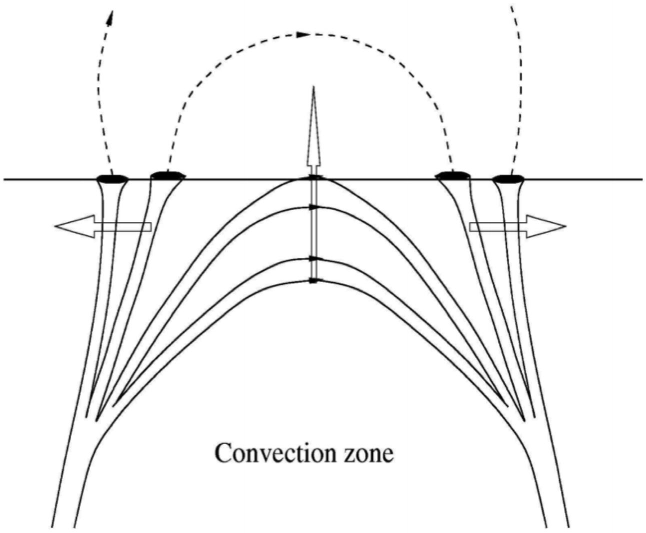

SOURCE: Zwaan (1985)

A representation model for the emerging flux region was created by Zwaan (1985), Zwaan (1978), as presented in Figure 1.1. The large arrows present the flux tube motion and the arrows over the dashed line indicate the field line orientation. The magnetic flux emerges as a set of arched flux tubes expanding through the convection zone. In the convection zone, the flux tubes connect to the same origin. As it rises, and reaches close to the surface, the flux tends to separate from each other.

The dark spots in the model correspond to positions where the flux tubes emerge at the solar surface. This region was represented as a dark color, once it is also dark in the observed map. This happens due to the horizontal magnetic fields that suppress the turbulent heat exchange. Once the top of each tube has emerged, the footpoints, in the surface, separate from each other, while the vertical magnetic field at these points starts to increase fast.

The coalescence of the footpoints increases the vertical magnetic flux in both polarities and can lead to a flux large enough to be accumulated, culminating in the formation of small pores, or even large sunspots.

1.1.1 Magnetic buoyancy

The solar magnetic dynamo continually makes conditions for the emergence of magnetic flux in the photosphere. According to Schrijver and Zwaan (2000) these emerging flux regions (EFRs) are mainly in the form of magnetic flux tube, which rises from the tachocline (base of the convective zone) to the solar surface, where they can generate more complex structures, such as sunspots.

The magnetic field emerges the solar surface by the phenomenon called *magnetic buoyancy*, and was first described by Parker (1955). A brief description of the magnetic buoyancy is presented along the present Section.

Considering a horizontal magnetic flux tube within the solar plasma medium. The magnetic pressure in the flux tube is

$$p_m = \frac{B^2}{2\mu}, \tag{1.1}$$

where B is the magnetic field strength, and μ is the magnetic permeability.

The diffusion equation is given by

$$\frac{\partial \mathbf{B}}{\partial t} = \nu_m \nabla^2 \mathbf{B}, \tag{1.2}$$

where ν_m is the magnetic viscosity. Supposing the medium is a good conductor, then ν_m becomes so small that

$$\frac{\partial \mathbf{B}}{\partial t} \approx 0. \tag{1.3}$$

Therefore, the magnetic field does not diffuse through the medium. Hydrostatic equilibrium requires that the magnetic pressure (p_m) stays balanced by the gas pressure outside the flux tube (p_e, external pressure). If p_i is the gas pressure inside the tube, then

$$p_e = p_i + p_m. \tag{1.4}$$

From the Equations (1.2) and (1.4), p_e becomes

$$p_e = p_i + \frac{B^2}{2\mu} \tag{1.5}$$

The magnetic pressure (p_m) is always positive, then by the Equation (1.4) we can conclude that $p_i < p_e$. Supposing the internal gas is under the same temperature as the one outside ($T_i = T_e$), then we can assume that the internal tube density is smaller than the external density ($\rho_i < \rho_e$). Hence, the flux tube will attempt to rise; this is the called *magnetic buoyancy*.

Assuming a flux tube of cross-sectional area A, the buoyant force will be given by $g\left(\rho_e - \rho_i\right)A$. The magnetic tension force is $AB^2/2\mu$. Consider a flux tube of length L clamped at both ends. If the flux tube can rise, we must require that the buoyant forces exceed the tension at the end of the length. Thus, it must satisfy the relation

$$Lg\left(\rho_e - \rho_i\right)A > \frac{2AB^2}{2\mu}. \tag{1.6}$$

The internal and external pressure are given, respectively, by

$$p_i = \frac{kT\rho_i}{m}, \tag{1.7}$$

$$p_e = \frac{kT\rho_e}{m}, \tag{1.8}$$

where m is the mass of an individual gas molecule and k is the Boltzmann's constant. The temperature T is equal for both inside and outside the flux tube.

Applying the Equation (1.7) and (1.8) to the Equation (1.5), the last can be written as

$$\frac{kT\rho_e}{m} = \frac{kT\rho_i}{m} + \frac{B^2}{2\mu}, \tag{1.9}$$

and,

$$\rho_e = \rho_i + \frac{m}{kT}\frac{B^2}{2\mu}. \tag{1.10}$$

Using the relation (1.6) and the Equation (1.10), then

$$Lg\left(\frac{m}{kT}\frac{B^2}{2\mu}\right)A > \frac{2AB^2}{2\mu}, \tag{1.11}$$

$$L > 2\frac{kT}{mg}. \tag{1.12}$$

The Equation (1.12) shows that the magnetic buoyancy is effective over any flux tube with the length exceeding twice the medium scale height.

The buoyant force per unit of volume is given by

$$F_b = \frac{mg}{kT}\frac{B^2}{2\mu} \tag{1.13}$$

In this way, a long horizontal flux tube will never be in static equilibrium. Once F_b is large enough not to be overwhelmed by other motions, such as turbulence, the flux tube will rise.

1.2 Arch filament system

The EFR emerges from the tachocline to the photosphere by the buoyancy mechanism, generating pores and sunspots by the coalescence of footpoints, as presented in Figure 1.1. The magnetic flux of EFRs can reach very high heights. When the magnetic flux emerges to the chromosphere, they look like filamentary systems, which connect two regions of opposite magnetic polarity, crossing the polarity inversion line (PIL). Bruzek (1967) reported these filamentary systems for the first time by observing the Sun with Hα and called them Arch Filament System (AFS).

Schmieder et al. (1991) proposed a formation mechanism for the AFS called *leaky bucket model*, based on the equation of motion for a fluid element falling freely along the field line (MEIN et al., 1996). When new flux emerges to the chromosphere, the material located in the top of the filament drains along the legs. With the material declining, the dark thread of AFS can get empty in few minutes. However, new loops with the condensed dark material can be formed again, so that the full chromospheric emergence can last for several hours or days. With the formation of new arch filaments, the old loops expand and can reach coronal heights (SPADARO et al., 2004). The model is still now the most accepted for the formation mechanism of AFS (SU et al., 2018).

The AFSs are observed in the strong chromospheric absorption lines, like the Hα line and in the line core of the Ca ii H K lines (BRUZEK, 1969). In the last years, with the significant advances in the spectropolarimetry, the AFS were also observed with the He i 10830 Å triplet (e.g., Solanki et al. (2003), Lagg et al. (2004), Lagg et al. (2007), Xu et al. (2010), Manrique et al. (2018)

Using Hα filtergrams, Bruzek (1969) determined that the length of the arch filaments can reach the size of supergranular network cells (20 – 30 Mm). The width of the filament comprehends few megameters, with a height between 5 and 15 Mm (MERENDA et al., 2011). Solanki et al. (2003) reported downflows in the footpoints, with velocities from 30 to 50 kms^{-1}, and upflows in the center of the arch.

1.3 Solar filaments

Prominences are amazing objects of great beauty whose formation, basic structure and eruption represent one of the basic unsolved problems in Solar Physics (PRIEST, 1989).

The term prominence refers to a large magnetic structure filled with plasma seen in corona, with lengths between 60 and 600 Mm (TANDBERG-HANSSEN, 1995). The prominences are usually bright features above the solar limb when observed in chromospheric spectral lines (SCHRIJVER; ZWAAN, 2008). The same magnetic structure, when seen in the solar disk, looks dark elongated features and are called *filaments*. Both terms, prominence or filament, are conventionally used to describe the same magnetic structure in the solar atmosphere.

The filaments can be classified into two main groups, the quiescent (QS) filaments, and the active region (AR) filaments. The QS filaments are one of the most studied structures in the Solar physics and are found in the quiet Sun or at the boundary of an active region (called *intermediate prominence*). In the quiet Sun, the QS filaments may present a much thicker and longer shape. They are typically more stable than the AR ones and have lifetimes that can reach several months.

On the other hand, the AR filaments are placed inside active regions and are much smaller than the QS filaments, with a length of about 10 Mm and height below 2.5 Mm. The temperature is similar to the QS one, but the density is slightly larger (usually larger than 10^{17} m^{-3}). The magnetic field is stronger, commonly from 20 to 70 G. However, it can be much stronger. Observations of Kuckein et al. (2009), Guo et al. (2010) in Tenerife result in longitudinal fields in filaments of 100 to 200 G and transverse fields of 500 to 600 G, implying a total field strength of 600 to 700 G.

There is a third group of filaments that is called polar crown (PC) filaments as observed by Cartledge et al. (1996). They are found at high latitudes and usually form a crown around the pole. The Figure 1.2 shows the Solar chromosphere observed in the H-alpha by the Big Bear Solar Observatory (BBSO) on June 13, 1999. We can see in the solar disk the dark QS and AR filaments (inside the active region) and also the polar crow (PC) filament. In the solar limb, we can see the prominences, where the largest one seems to be related with the PC filament.

The filament arrangement consists of three main structural components: the spine, barbs and two footpoints (MACKAY et al., 2010). The spine is the central part, as a long and horizontal body running along the top of the filament. It extends over the magnetic polarity inversion line. Barbs project from the sides of the spines and make an acute angle to the filament axis (MARTIN et al., 1992). When the prominence is close to the limb, barbs are seen to extend down from the spine in the direction of the photosphere (LIN et al., 2008). In some polar crown prominences, the spine are not clearly visible; only the barbs can be seen as vertical pillars (SCHMIEDER et al., 2010; DUDÍK et al., 2012). The beginning and end points of the filaments are known as two extreme ends (PANESAR, 2014).

According to Babcock and Babcock (1955), the filaments are always located above the neutral lines that separate regions of opposite magnetic polarity. This region is also called Polarity Inversion line (PIL). In the case of AR filaments, their shape follow the complicated magnetic field structure of the active region and they have the curved shape.

Observation by Manchester et al. (2008) shows that coronal mass ejections (CMEs) are often associated with AR filament eruptions. Therefore, it is highly important the study of the filament magnetic field and its evolution, from its emergence to the erupting phase.

Figure 1.2 - Solar chromosphere observed in the H-alpha by the Big Bear Solar Observatory (BBSO) on June 13, 1999. We can see in the solar disk the large QS filaments, the AR filament is inside the active region. In the border of the AR 08580 is the intermediate filament. On top we can note the polar crown (PC) filament. In the solar limb we can see the prominences, where the larger prominence, on top, seems to be related with the PC filament. Note the QS filaments follow the Polarity inversion line (PIL), presented as a green dashed line.

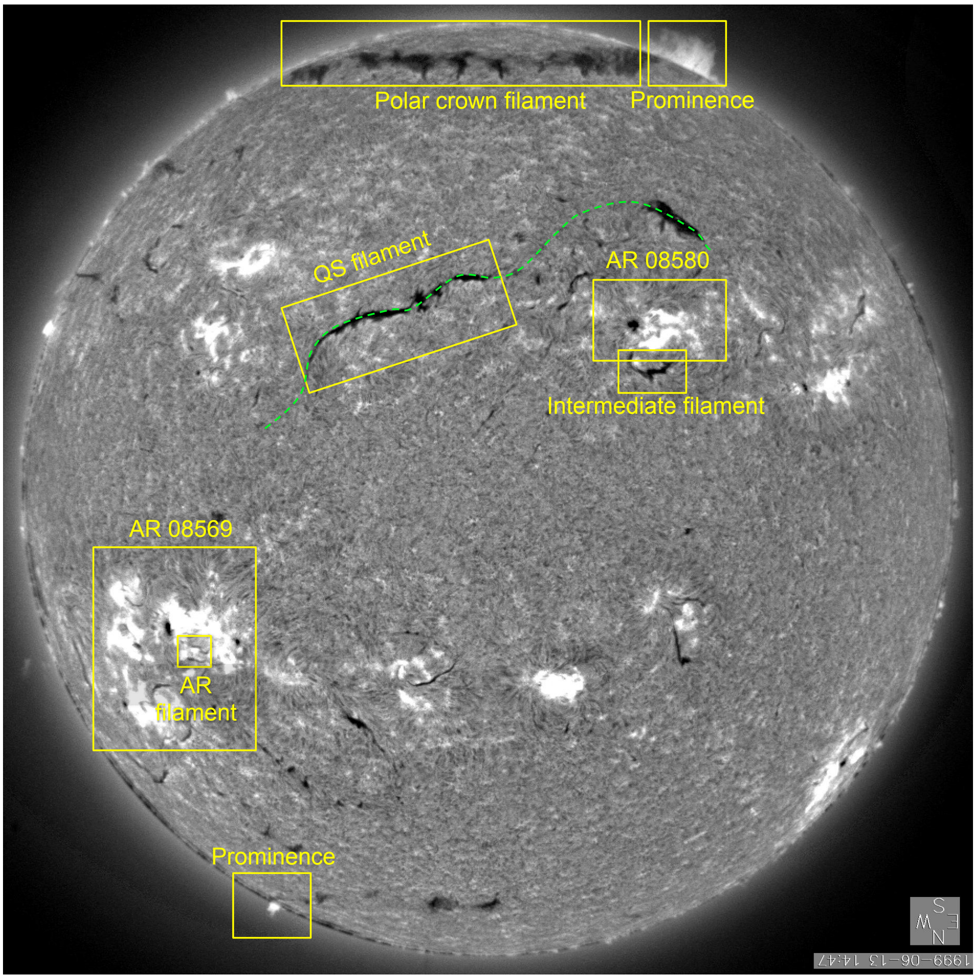
Polar crown filament
Prominence
QS filament
AR 08580
Intermediate filament
AR 08569
AR
filament
Prominence
S
W
E
N
1999-06-13 14:47

SOURCE: Author

In the last years, the solar community has presented several works concerning the formation and evolution of the quiescent filaments. However, studies of filament over active regions are still scarce in the solar physics literature, and it is not clear how related their formation process is to the quiescent (QS) ones.

1.3.1 Flux rope model

Two main models describe the development and configuration of filaments, the sheared arcade (SA) model and the flux rope (FR) model. The main divergence between both models is the formation height of the filament. In the SA model, the filament is formed in the solar corona by shearing motions in addition to converging flows at the (PIL) and reconnection processes. As a result, the magnetic structure can be a flux rope, as described in Ballegooijen and Martens (1989) or a dipped arcade (ANTIOCHOS et al., 1994). On the other hand, the FR model assumes that a flux rope emerges from below the photosphere ascending into the corona (OKAMOTO et al., 2008). Kuckein (2012) provides a great report of these two main models of filament configuration.

In the AR filaments, the flux ropes are the most accepted configuration to be responsible for supporting the filament's plasma. The most accepted flux rope model is the one introduced by Ballegooijen and Martens (1989). The model is based on the formation of filament through the flux cancellation by considering the shearing motions in a bipolar configuration.

A step-by-step explanation of the flux rope model is presented in Figure 1.3. The indices from (a) to (f) refers to each panel presented in the figure. The footpoints are represented by the capital letters, from A to H. The rectangle represents the solar photosphere, and the dashed line is the PIL separating the two regions of opposite magnetic polarity.

According to the flux rope model, the magnetic field lines are initially potential fields, which implies that they are perpendicular polarity inversion line (PIL) (a). Due to the shear flow, footpoints get displaced along the PIL (b). The shear presented on (b) is supplied mainly by the differential rotation on the Sun.

In the following panels, (c) and (d), the footpoints B and C starts to come closer, due to the flux convergence in the PIL direction. Once the footpoints come closer to each other, they can reconnect and create two new loops, the small loop BC and the long loop AD, as presented in the panels (d) and (e) of Figure 1.3.

Figure 1.3 - Flux rope formation model by Ballegooijen and Martens (1989). The rectangle represents the solar photosphere, and the dashed line the PIL, separating the two regions of opposite magnetic polarity. The initial configuration in panel (a) there are potential field lines (solid lines) that cross the PIL; (b) sheared magnetic field produced by flows along the neutral line; (c) magnetic shear is enhanced further because of the flows toward the neutral line; (d) the reconnection form the more extended loop AD and a shorter loop BC which tends to submerge. (e) Loops EF and GH are forced to the neutral line; (f) a new reconnection generates the helical loop EH and a shorter loop GF which again tends to submerges. Thus, dipped magnetic field lines are developed carrying the plasma higher to chromosphere and corona.

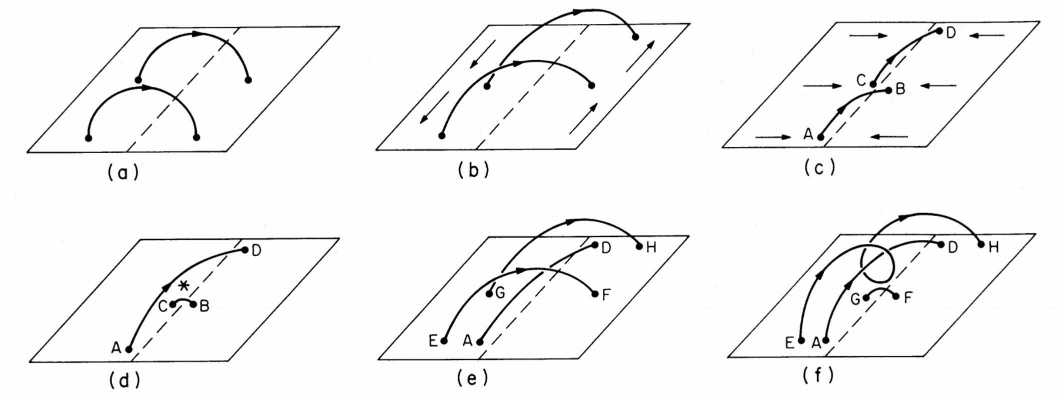

SOURCE: Ballegooijen and Martens (1989)

In a similar way to the last step, the footpoints of the overlying loops EF and GH come close and the footpoints F and G can reconnect, as seen in (e) and (f). It drives to the formation of a longer loop EH, that covers throughout the loop AD and forms a helical field structure (f). This helical field structure is supposed to carry the filament body. All this process can be replicated several times and develop a long helical structure. Hence, dipped magnetic field lines are developed carrying the plasma higher to the chromosphere and corona.

Flux ropes have also been modeled assuming to start in the convection zone and rise until reaching the upper chromosphere or corona, as presented by Archontis et al. (2004), Manchester W. et al. (2004), MacTaggart and Hood (2010). Nevertheless, many divergences were found in these models related to the emergence method. Since Parker, 1955, it is generally accepted that the flux rope rises through the convection zone led to the *magnetic buoyancy*.

The flux rope model permits also the presence of mass ejection. A reconnection below and above the flux rope is sufficient to drive an eruptive event, where the flux rope can eject, producing a Coronal Mass Ejection (CME).

1.3.2 Eruptive filament

Active-region and filaments may have some increase in turbulent (or helical) motion or flow along the filament. Such activation in most of the cases fade away after an hour or so, but in some cases, it leads to a *filament eruption*. In other cases, prominence material may have declining flow from the top, along curved arcs at speeds that can reach 100 kms^{-1} (DRIEL-GESZTELYI et al., 1997). In some cases, the filament activation can occur due to the shock wave that initiates in a distant flare event. This kind of activation is usually called *winking filament*.

At some stage, a filament over the AR may become absolutely unstable and erupt, it happens mainly when its height exceeds 50 Mm. Once it erupts, it tends to ascend as an erupting filament and often shows a substantial twist. It eventually entirely disappears, and some of the material escapes from the Sun, while some descend to the chromosphere along helical arches. Regularly, the filament reforms in the same place over the course of 1 to 7 days (PRIEST, 2014)

The eruption of a quiescent prominence is usually assigned a *sudden disappearance*. It starts with a slow rising motion at a few kms^{-1} and may take several hours. It is accompanied by an X-ray brightening and occasionally by the appearance of Hα flare ribbons. The eruption of an active region prominence is much faster and takes about 30 min or less. It is accompanied by a two-ribbon solar flare. The prominence generally reforms after only a few hours. It is usually called eruptive or impulsive flare (PALLAVICINI et al., 1977; PRIEST, 1981).

Most of the Coronal Mass Ejections (CMEs) are correlated with erupting filaments, and those which erupt from active regions are also associated with two-ribbon solar flares. Both are associated with energy release by magnetic reconnection (HARRISON, 1996; WEBB; HOWARD, 2012).

1.4 Spectral lines

According to Solanki et al. (2006), signatures of the magnetic field above the solar surface are usually faint and can sometimes be observed only indirectly. The emission lines of the coronal ions are usually very faint due to the lower plasma density. However, in the chromospheric heights, the atmospheric conditions to measure the

Zeeman effect are a more propitious, and even better for the filaments, where we find a cooler and denser plasma.

The Zeeman splitting of the spectral line increases with the square of the wavelength, so, the larger the wavelength of the spectral line, the more sensitive the line is to the Zeeman effect. Therefore, observations in the infrared provide great opportunities to observe the magnetic field. The combined Zeeman and Hanle effect measurements of the Ca I emissions at 8500 and 8540 Å have been used to observe the low chromosphere (SOCAS-NAVARRO et al., 2000), and more recent, the He I 10830 Å line have been used for observations of active regions and filaments. An important point of the He I is that it is populated in the upper chromosphere, close to the base of the corona. Details of the He I triplet formation is described in this Section.

Observations of the chromosphere have been made using the diagnostics of various spectral lines. The most common observed line is the Hα at 6563 Å where it is possible to see the long filament and prominences. Other important lines are D_3 line of He I at 5876 Å and Ca II lines at 8542 Å.

In this work we made use of two infrared spectral lines, the He I 10830 Å triplet for observation of the upper chromosphere and the Si I 10827 Å for observation of photosphere. As the lines are close to each other, a great advantage is that we performed spectropolarimetric observations of both lines at the same time.

1.4.1 He I 10830 Å triplet

The observation and analysis of the He I 10830 Å triplet can be great mechanism for investigating the magnetic properties of plasma structures in the solar chromosphere. According to Bueno and Ramos (2007), it results from the high sensitivity to the Hanle and Zeeman effects. The He I 10830 Å line has been analyzed in high-intensity fields observed in solar active regions (CENTENO et al., 2006), in weaker fields found in the arch filament system (BUENO et al., 2002), in regions of emerging magnetic flux (LAGG et al., 2004), in chromospheric spicules (SOCAS-NAVARRO et al., 2005) and also in prominences (MERENDA et al., 2006). Table 1.1 presents the Atomic data of the He I 10830 Å transitions.

According to Penn and Kuhn (1995), the He I 10830 Å triplet of the neutral helium is a set of transitions that take place between the levels $1s2s^3S_1 - 1s2p^3P_{0,1,2}$. Two spectral features arise from the He I triplet system, we call it as “blue” and “red” components. The blue component is placed at 10829.09 Å and comes from the

$2s^3S_1 - 2p_0^3$ transition. The red component is a blend of two spectral He I lines placed at 10830.25 Å and 10830.33 Å and is originated from the $^3P_1$ and $^3P_2$ levels. The central line of the red component is observed in laboratory is 10830.3 Å. Figure (1.4) shows a schematic atomic model (also know as Grotrian diagram) of the He I. The individual He I 10830 Å splitting and D_3 transitions are shown in the right lower inset panel.

According to Avrett et al. (1994), the He I 10830 Å is formed only in the upper chromosphere without any contribution from the photosphere. The strongest He lines in the solar atmosphere are in the extreme ultraviolet (EUV) below 584 Å. From the ground-based observatories, the only observable He line is in the infrared at 10830 Å.

The atom of helium reveals a complicated spectrum with two different spectral series: one of singlets (para-helium) involving singlet terms ($^1S,^1P,^1D$) and the other one of triplets (ortho-helium) involving triplet terms ($^3S,^3P,^3D$). At typical solar chromospheric conditions, the bulk of the helium population is mainly concentrated in the 1S atomic ground level, since the temperature is not high enough for populating significantly the rest of the levels.

Under normal chromospheric conditions of temperature and density, the majority of the helium population remains the He I singlet. In the electric dipole approximation, radiative transitions are not allowed between singlet and triplet terms, so the populations of the two sets of levels are not radiatively coupled. In order to produce the He I 10830 Å absorption, the triplet needs to be populated. The way that this spectral line turns excited is mainly due to a photoionization-recombination (PR) mechanism of the helium atom (Zirin (1975); Andretta and Jones (1997)). Figure 1.5 presents an overview of the PR mechanism.

Table 1.1 - Atomic data of the He I 10830 Å transitions.

Wavelength [Å]	*Lower Term*	*Upper Term*	g_{eff}	*Relative Strength*	*loggf*
10829.0911	3_1^S	3_0^P	2.00	0.111	-0.745
10830.2501	3_1^S	3_1^P	1.75	0.333	-0.268
10830.3398	3_1^S	3_2^P	1.25	0.556	-0.047

SOURCE: Kuckein (2012)

Figure 1.4 - Schematic atomic model of the He I, with 46 energy levels and the transition between each pair of levels. The individual He I 10830 Å splitting and D_3 transitions are highlighted in the right lower inset panel.

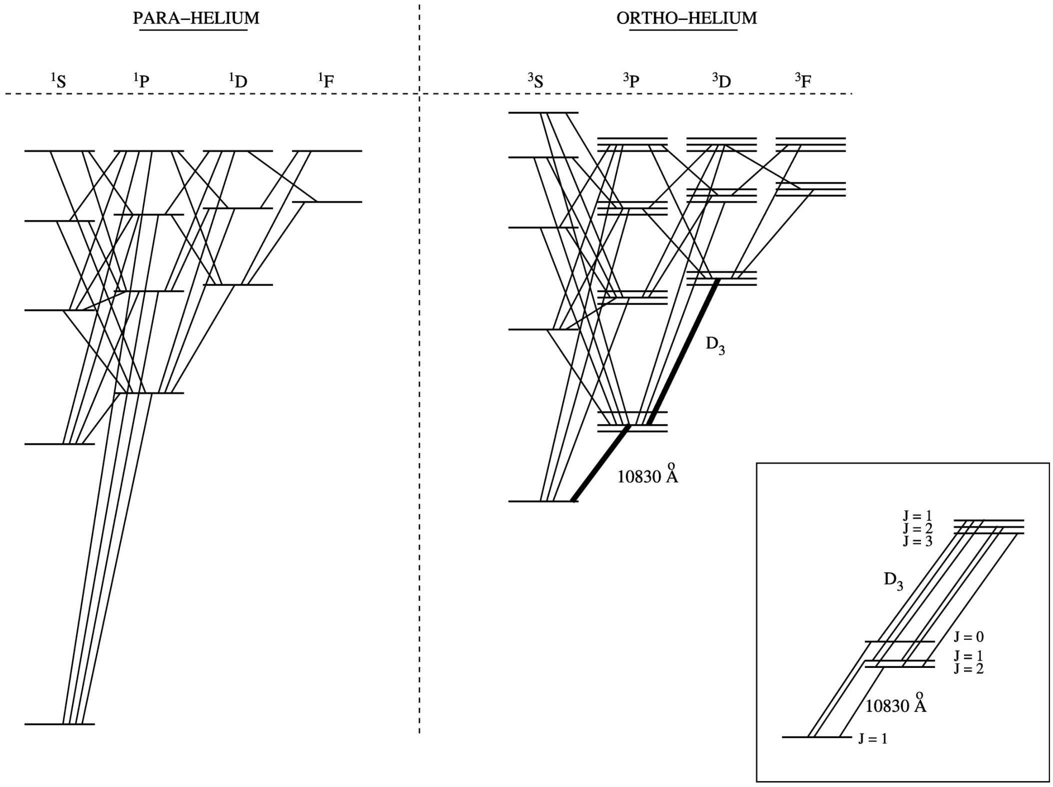

SOURCE: Centeno et al. (2008)

The extreme ultraviolet (EUV) radiation comming from the solar corona is the main cause of ionization of the helium atoms in the chromosphere (AVRETT et al., 1994). This EUV spectrum with $\lambda < 504$ Å ionizes the helium, increasing the He II density, which subsequently recombines with the free electrons, populating both singlet and triplet sets. The excess population in the triplet energy levels is responsible for enhancing the He I 10830 Å features in the upper chromosphere (CENTENO et al., 2008).

Figure 1.5 - Photoionization-recombination mechanism for the Helium atom. (1) In the absence of coronal irradiance, all the population of He is in the ground state of the singlet. (2) The coronal EUV radiation causes the ionization of the helium atoms in the chromosphere irradiance increasing the He II density. (3) The He II recombines with the free electrons, populating both singlet and triplet sets.

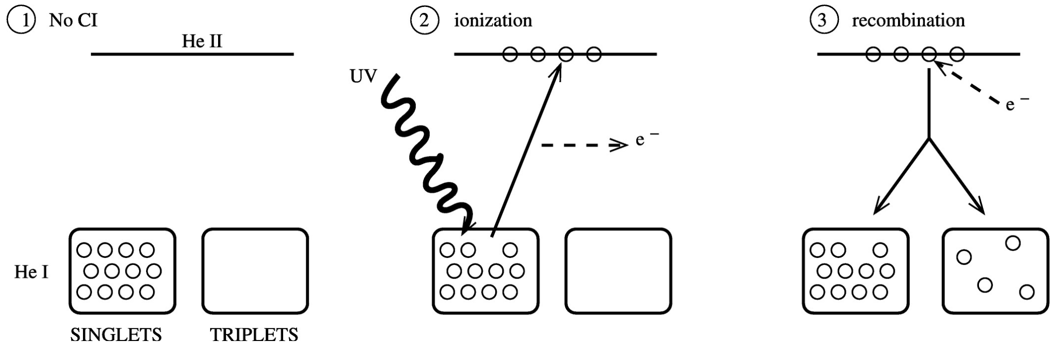

SOURCE: Centeno et al. (2008)

An alternative mechanism to populate the He I 10830 Å triplet levels in the chromosphere is the collisional excitation (ATHAY, 1960). The ionization of these He atoms is produced by combining them with higher temperature electrons (JORDAN, 1975). The combining procedure was introduced later by Shine et al. (1975) using numerical simulations. It was showed that difusion can enhance the He I and He II resonance lines. Moreover, in accordance with the observation, they conclude that the difusion effect happens more in active regions (with high pressure) and less in coronal holes (with low pressure).

Both the photoionization-recombination and collision mechanisms were proposed by Milkey et al. (1973) for producing the He I lines. In lower temperature regions of the chromosphere, the EUV radiation photoionizes the He I atoms which then recombine with free electrons. In higher temperature regions the collisions tend to dominate. This proposition makes sense since the formation height of He I 10830 Å is located between 1500 and 2000 km, but is also observed in high quiescent filaments (about tens of megameters), which indicates that He i is present at distinctive heights. (ANDRETTA; JONES, 1997) also supported the mixed phenomena, with the formation of two-layer of the helium lines.

1.4.2 Si I 10827 Å line

The GREGOR/GRIS covers not only the He I 10830 Å triplet but the wavelength range from 10823.695 Å to 10841.880 Å. On the left of the the He line, we can observe the the Si I 10827 Å line. The Si I line is a photospheric line, sensitive to the Zeeman effect. This line is an excellent complement to the study of the arch filament system in the chromosphere, as we can obtain the vector magnetic field and Doppler velocities in the photosphere under the filament region. Even better, the proximity of the He I 10830 Å triplet makes the observation simultaneously.

The effective Landé factor of the Si I 10827 Å line is $g_{eff} = 1.5$. The line originates from the transition between the $3p4s^3P_2$ and $3p4p^3P_2$ levels of the Si I atom. Bard and Carlsson (2008) observed the Si I 10827 Å line is developed in non-local thermodynamical equilibrium (NLTE). Fontenla et al. (1993) finds that for a quiet Sun model, the mean response height was about 540 km, while for a sunspot umbrae, it was about 300 km above the solar surface (MALTBY et al., 1986).

2 Spectropolarimetry

In this chapter, we present an overview of how to measure some solar physical parameters, like the magnetic field vector, by measuring characteristics of the light coming from the Sun. To make this possible, we made use of the *spectropolarimetry*, as its self-explanatory name says, it analyzes the light based on the two main characteristics: the wavelength and the polarization.

The chapter starts describing the theory of the polarized radiation, from the definition of the Stokes parameters (Section 2.1) and the introduction of the Zeeman effect (Section 2.2). Following, it presents the Radiative Transfer Equation (RTE) in the presence of a magnetic field (Section 2.3) and its formal solution (Section 2.4). The Mildne Eddington approximation is described in Section 2.5. To retrieve atmospheric parameters, we presente how inversions are computed (Section 2.6). At the end, we detail the state-of-the-art inversion technique we applied in this work (Section 2.7).

2.1 Stokes parameters

The observation and description of polarization signals in Fraunhofer lines were of exceptional importance concerning the investigation of solar and stellar magnetic fields (DEGL'INNOCENTI, 1992). The first report of the transfer equation for polarized light in a scattering atmosphere was reported by Chandrasekhar (1947). In this formulation, the polarization state of the radiation was represented by four so-called Stokes parameters (STOKES, 1852). Since that, the Stokes formalism has become the conventional representation of polarized radiation in astronomy (SOLANKI, 1987).

Let us suppose an electric field vector of a quasi-monochromatic beam of light propagating along the z-axis. The components of the electric field vector (ξ_x, ξ_y) in the plane perpendicular to the direction of propagation can be written as follow:

$$\xi_x(t) = \hat{\xi}_x \cos(\omega t - \varphi_x), \tag{2.1}$$

$$\xi_y(t) = \hat{\xi}_y \cos(\omega t - \varphi_y), \tag{2.2}$$

where $\hat{\xi}_{x,y}$ and $\varphi_{x,y}$ are the amplitude and phase of the electric field vector in x and y directions, and ω is the angular frequency.

The Stokes parameters are defined in terms of the amplitudes, $\hat{\xi}_{x,y}$, and the phases,

$\varphi_{x,y}$, as:

$$I = \left\langle \hat{\xi}_x^2 \right\rangle + \left\langle \hat{\xi}_y^2 \right\rangle, \tag{2.3}$$

$$Q = \left\langle \hat{\xi}_x^2 \right\rangle - \left\langle \hat{\xi}_y^2 \right\rangle, \tag{2.4}$$

$$U = 2 \left\langle \hat{\xi}_x \hat{\xi}_y \cos\left(\varphi_x - \varphi_y\right) \right\rangle, \tag{2.5}$$

$$V = 2 \left\langle \hat{\xi}_x \hat{\xi}_y \sin\left(\varphi_x - \varphi_y\right) \right\rangle, \tag{2.6}$$

where $\langle\ \rangle$ denotes the time average. The Stokes parameters completely characterize the polarization state of light and are often written in vector form, as $\mathbf{S} = (\mathrm{I, Q, U, V})^{\mathrm{T}}$. A condition for the Stokes I is that the intensity of the polarized light cannot be larger than the total intensity of light, i.e. $I^2 \geq Q^2 + U^2 + V^2$.

The Stokes I is the total intensity. The Stokes Q is the difference between the vertical and horizontal polarization. Stokes U represents the difference between the polarization in 45° and -45°, and the Stokes V is the difference between the clockwise and counterclockwise circularly polarized light. Examples of the Stokes vectors for particular cases of completely polarized states are shown on Table 2.1, where intensities have been normalized to unity.

Table 2.1 - Stokes vectors for completely polarized states. Intensities were normalized to unity.

Polarization state	*Stokes vector*
Natural	$(1, 0, 0, 0)^{\mathrm{T}}$
Linear at 0°	$(1, 1, 0, 0)^{\mathrm{T}}$
Linear at 90°	$(1, -1, 0, 0)^{\mathrm{T}}$
Linear at 45°	$(1, 0, 1, 0)^{\mathrm{T}}$
Linear at 135°	$(1, 0, -1, 0)^{\mathrm{T}}$
Right-handed circular	$(1, 0, 0, 1)^{\mathrm{T}}$
Left-handed circular	$(1, 0, 0, -1)^{\mathrm{T}}$

SOURCE: Iniesta (2003)

The degree of polarization (P_{tot}) can be given by

$$P_{tot} = \sqrt{\frac{Q^2 + U^2 + V^2}{I^2}}, \tag{2.7}$$

with $0 \leq P_{tot} \leq 1$. When $Q = U = V = 0$, the beam is totally unpolarized and when $I^2 = Q^2 + U^2 + V^2$ it is completely polarized.

The application of the Stokes vector becomes very simple for the treatment of polarization. Suppose a wave passes through optical components, the incident Stokes vector $(S)_{in}$ will be modified into the output Stokes vector $(S)_{out}$. This transformation can be described by multiplying $(S)_{in}$ matrix, which represents the full polarization properties of the optical component. The matrix that multiplies the incident Stokes vector was developed by Mueller (1943), and is called *Mueller Matrix*, it consists of a 4 × 4 matrix, which represents a particular or a group of optical elements.

2.2 Zeeman effect

In 1896, the Dutch physicist Pieter Zeeman confirmed the investigations made by Hendrik Antoon Lorentz that spectral lines were split into polarized components in the presence of a magnetic field (ZEEMAN, 1897). Zeeman and Lorentz shared the Nobel Prize for Physics in 1902. In 1908, George Ellery Hale (HALE, 1908) found that some solar spectral lines looked to be widened, splited, and polarized, and concerned an explanation for the observed sunspot spectrum: the presence of strong magnetic fields in sunspots.

A spectral line is produced by the transition of electrons between two energy levels. The quantum numbers L (orbital angular momentum), S (spin angular momentum), and J (total angular momentum) describe the quantum-mechanical state of the energy. The term symbols of the form ${}^{2S+1}L_J$ give information about the quantum numbers L, S and J. The letters S, P, D, F mean an orbital angular momentum corresponding to $L = 0, 1, 2, 3$.

In the presence of the of the magnetic field, the energy of the atomic level is given by:

$$E_{J,M} = E_J + \frac{\hbar e}{2m_e} g_L M B, \tag{2.8}$$

where e is the elementary charge, m_e the electron mass, $\hbar$ is the reduced Planck constant, g_L is the Landé factor of the energy level and M is the magnetic quantum number. The magnetic field splits the energy level (L,S,J) into $2J + 1$ sublevels of different energies, described by $M = -J, ..., 0, ..., +J$. The Landé factor (LANDÉ, 1923) is given by

$$g_L = \frac{3}{2} + \frac{S(S+1) - L(L+1)}{2J(J+1)}. \tag{2.9}$$

In Equations (2.8) and (2.9) was assumed the Russel-Saunders or LS coupling (RUSSELL; SAUNDERS, 1925). LS coupling is the interaction between the quantum numbers L and S and is presented in detail in Cowan (1981).

The transition between energy levels for both the absence and presence of the magnetic field is presented in Figure 2.1. The figure represents the Zeeman splitting where a Lorentz triplet is formed, which is called the normal Zeeman effect. Due to $J = 0$, the lower energy level does not split in the presence of a magnetic field. When $J = 1$, the upper energy level splits into three different sublevels with the magnetic quantum numbers $M = -1, 0, +1$. The transitions with $\Delta M = 0$ are called π component, and the $\Delta M = \pm 1$ transitions are the blue and red components. The formation of the three splitted lines is a singular case that occurs if one of the two energy levels has $J = 0$ or both levels have equal Landé factors.

The more general case, where $J \neq 0$, is known as the anomalous Zeeman effect. In this situation, the magnetic quantum number of the two energy levels is given by $\Delta M = M_u + M_l = -1, 0, +1$, where the l and u indices denote the lower and upper energy level, respectively.

The anomalous Zeeman effect is presented in Figure 2.2 that shows the transition between energy levels for both the absence and presence of the magnetic field. Note that both energy levels have $J = 2$, with different Landé factors.

The line splitting is determined as the wavelength shift of the σ (λ_σ) components to the reference wavelength of the non-magnetized case (λ_0), so:

$$|\Delta\lambda| = |\lambda_\sigma - \lambda_0| = \frac{eB\lambda_0^2}{4\pi c m_e} g_{eff} \tag{2.10}$$

where c is the speed of light and g_{eff} is the effective Landé factor, that designates the sensitivity of the spectral line to the Zeeman effect. According to Shenstone and Blair (1929), the effective Landé factor is given by

$$g_{eff} = \frac{1}{2}\left(g_u + g_l\right) + \frac{1}{4}\left(g_u - g_l\right)\left[J_u\left(J_u + 1\right) - J_l\left(J_l + 1\right)\right]. \tag{2.11}$$

Figure 2.1 - Representation of normal Zeeman effect. Transition between energy levels for the absence and presence of the magnetic field. Due to $J_l = 0$, the lower energy level does not split in the presence of a magnetic field. When $J_u = 1$, the upper energy level splits into three different sublevels with the magnetic quantum numbers $M = -1, 0, +1$. On the bottom, the spectral look for both cases.

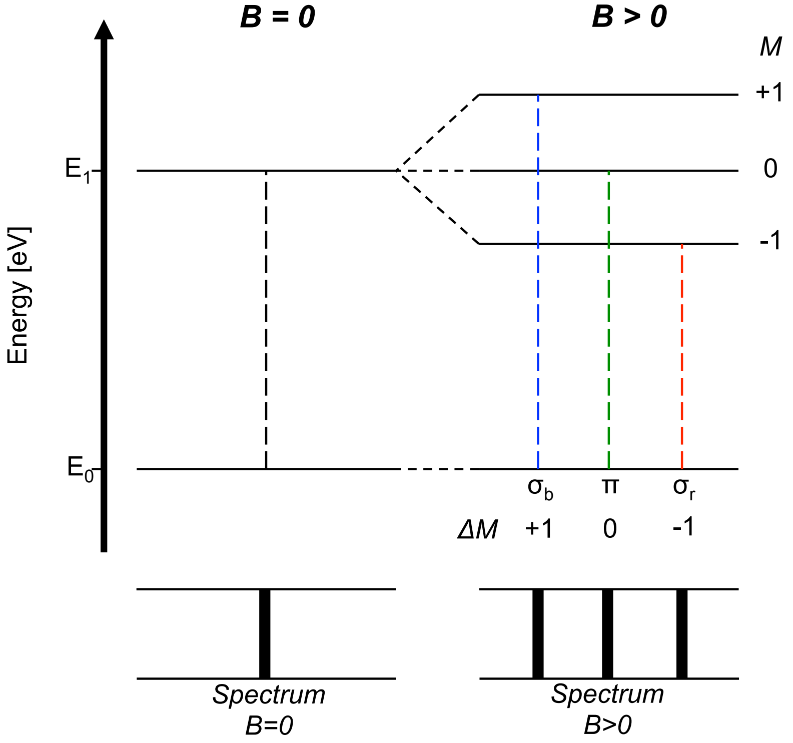
B = 0
B > 0
M
+1
0
-1
E1
E0
Energy [eV]
σb
π
σr
ΔM
+1
0
-1
Spectrum
B=0
Spectrum
B>0

SOURCE: Author

Figure 2.2 - Representation of anomalous Zeeman effect. Transition between energy levels for the absence and presence of the magnetic field. In both levels $J = 2$, so the upper and lower energy level split in the presence of a magnetic field. This case is called the anomalous Zeeman effect.

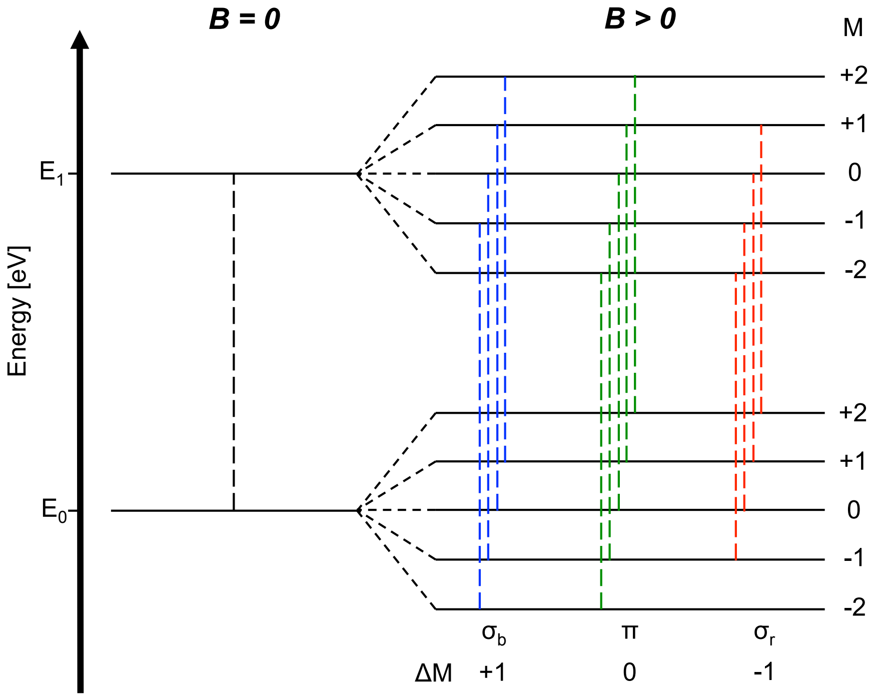

SOURCE: Author

From the Equation (2.10) we may note that the line splitting is directly proportional to the magnetic field strength and also to the square of the wavelength. In this work, we are analyzing GRIS data that have observations in the infrared, with large wavelengths, so by the Equation (2.10), we can presume it has a high sensitivity to the Zeeman effect.

The transverse Zeeman effect results when the magnetic field is perpendicular to the line-of-sight (LOS), as presented in Figure 2.3. In this particular case, the observer can view the π component (linearly polarized) and also the σ_b and σ_r components (circularly porlarized).

In the other way, when the magnetic field is parallel to the LOS, it is called the longitudinal Zeeman effect, as shown in Figure 2.4. In this case, the observer can see only the circularly polarized components (σ_b and σ_r).

Figure 2.3 - Transverse Zeeman effect that results when the magnetic field is perpendicular to the line-of-sight. The observer can view the π component (linearly polarized) and also the σ_b and σ_r components (circularly porlarized).

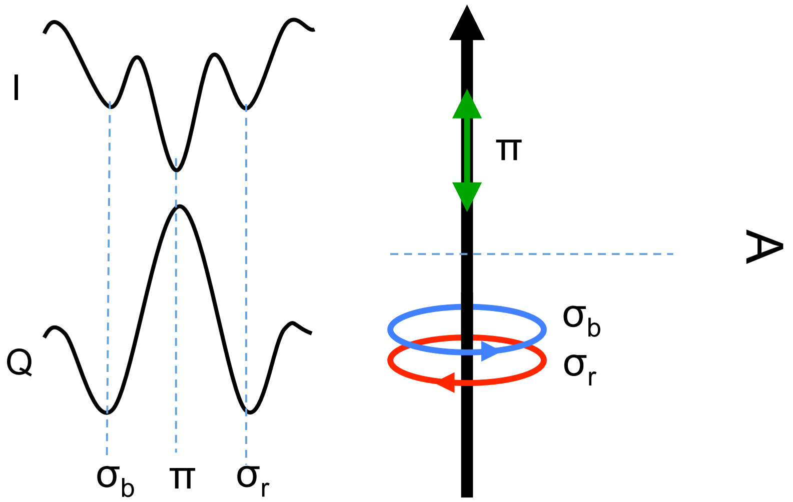

SOURCE: Author

Figure 2.4 - Longitudinal Zeeman effect that results when the magnetic field is parallel to the LOS. In this case, the observer can see only the circularly polarized components (σ_b and σ_r).

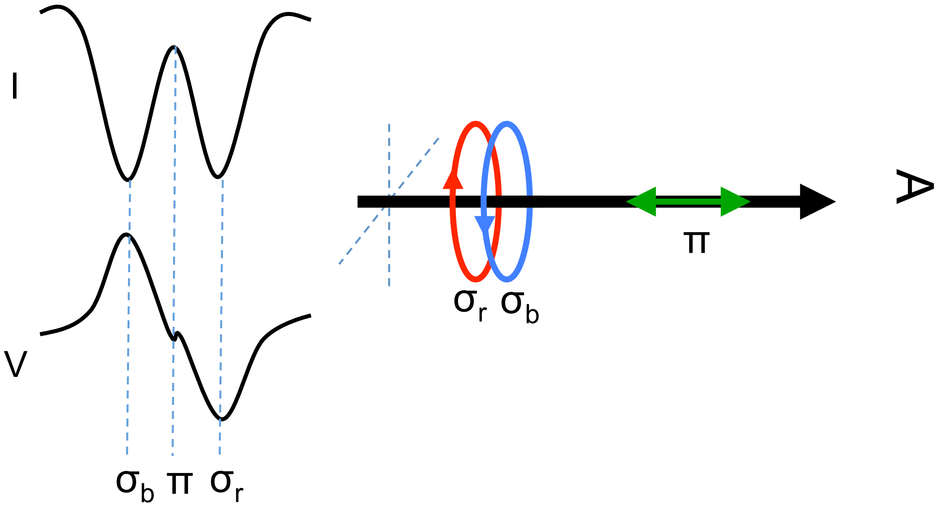

SOURCE: Author

2.3 Radiative Transfer Equation

In a magnetized medium like the solar atmosphere, the radiative transfer equation (RTE) describes how a polarized light beam is transferred considering the changes in its polarization state due to the magnetic field. The general RTE was first derived by Unno (1956) using classical electrodynamics, and six years later, Rachkovsky (1962) incorporated the magneto-optical effects.

To describe the RTE for our solar atmosphere, we first assume that the radiation is propagating normal to the solar surface (assumed as z-direction), in this way the RTE can be written in the form

$$\frac{\mathrm{d}\mathbf{I}(z)}{\mathrm{d}z} = -\hat{\mathbf{k}}\left[\mathbf{I}(z) - \mathbf{S}(z)\right], \tag{2.12}$$

where $\mathbf{I}(z)$ is the Stokes vector, given by $\mathbf{I} = (I, Q, U, V)$, that represents the full description of the polarized state light emerging from the magnetized medium. $\mathbf{S}(z)$ is the source function and $\hat{\mathbf{k}}$ is the propagation matrix and can be decomposed considering the contributions from both continuum and the spectral line forming process. Therefore, the propagation matrix can be written by

$$\hat{\mathbf{k}} = \mathbf{k_c}\mathbf{1} + \mathbf{k_{lin}}\hat{\phi}. \tag{2.13}$$

where $\mathbf{k_c}$ is the continuum absorption coefficient, $\mathbf{1}$ is the 4×4 identity matrix, $\mathbf{k_{lin}}$ is the line absorption coefficient and $\hat{\phi}$ includes the normalized absorption and dispersion profiles.

The line to continuum absorption coefficient ratio (η_0) can be defined by the ratio of both coefficients, as follows:

$$\eta_0 = \frac{k_{lin}}{k_c}, \tag{2.14}$$

so the Equation (2.13) can be rewritten as,

$$\hat{\mathbf{k}} = \mathbf{k_c}\mathbf{1} + \eta_0\hat{\phi}, \tag{2.15}$$

We may introduce now the *continuum optical depth*, that is given by:

$$\tau_c = \int_z^{z_0} \hat{\mathbf{k}}\mathrm{d}z. \tag{2.16}$$

Note that the presented definition implies that the optical depths are measured along the ray path, but in the opposite direction ($-z$) and the origin ($\tau_c = 0$) is located in the outermost boundary of the medium (z_0), where the observer is located. So τ_c represents the number of mean free paths of continuum photons between the outermost boundary and the point z.

Using the τ_c as a independent variable, in the derivative form, $\mathrm{d}\tau_c = -\hat{\mathbf{k}}\mathrm{d}z$, so the Equation (2.12) can be rewritten as:

$$\frac{\mathrm{d}\mathbf{I}(\tau_c)}{\mathrm{d}\tau_c} = -\hat{\mathbf{k}}\left[\mathbf{I}(\tau_c) - \mathbf{S}(\tau_c)\right], \tag{2.17}$$

where $\hat{\mathbf{k}}$ is the propagation matrix, given by

$$\hat{\mathbf{k}} = \begin{pmatrix} \eta_I & \eta_Q & \eta_U & \eta_V \\ \eta_Q & \eta_I & \rho_V & -\rho_U \\ \eta_U & -\rho_V & \eta_I & \rho_Q \\ \eta_V & \rho_U & -\rho_Q & \eta_I \end{pmatrix}, \tag{2.18}$$

and the element indices regard to the I, Q, U and V stokes parameters. In fact, the symmetries of matrix $\hat{\mathbf{k}}$ allow us to decompose it in three matrices:

$$\begin{aligned} \hat{\mathbf{k}} = & \begin{pmatrix} \eta_I & 0 & 0 & 0 \\ 0 & \eta_I & 0 & 0 \\ 0 & 0 & \eta_I & 0 \\ 0 & 0 & 0 & \eta_I \end{pmatrix} + \begin{pmatrix} 0 & \eta_Q & \eta_U & \eta_V \\ \eta_Q & 0 & 0 & 0 \\ \eta_U & 0 & 0 & 0 \\ \eta_V & 0 & 0 & 0 \end{pmatrix} \\ & + \begin{pmatrix} 0 & 0 & 0 & 0 \\ 0 & 0 & \rho_V & -\rho_U \\ 0 & -\rho_V & 0 & \rho_Q \\ 0 & \rho_U & -\rho_Q & 0 \end{pmatrix}. \end{aligned} \tag{2.19}$$

According to Iniesta (2003), the first matrix is a diagonal one that corresponds to absorption phenomena. The second, symmetric matrix matches to the dichroism, where some polarized components of the beam are extinguished more than others because the matrix elements are generally different. Finally, the third, antisymmetric matrix is derived from the dispersion.

According to Degl'Innocenti and Landolfi (2004), the elements of the propagation matrix can be written as

$$\eta_I = 1 + \frac{\eta_0}{2}\left(\phi_p sin^2\gamma + \frac{1}{2}\left[\phi_b + \phi_r\right]\left(1 + cos^2\gamma\right)\right), \tag{2.20}$$

$$\eta_Q = \frac{\eta_0}{2}\left(\phi_p - \frac{1}{2}\left[\phi_b + \phi_r\right]\right)\left(\sin^2\gamma\cos 2\chi\right), \tag{2.21}$$

$$\eta_U = \frac{\eta_0}{2}\left(\phi_p - \frac{1}{2}\left[\phi_b + \phi_r\right]\right)\left(\sin^2\gamma\sin 2\chi\right), \tag{2.22}$$

$$\eta_V = \frac{\eta_0}{2}\left[\phi_b + \phi_r\right]\cos\gamma, \tag{2.23}$$

$$\rho_Q = \eta_0\left(\psi_p - \frac{1}{2}\left[\psi_b + \psi_r\right]\right)\left(\sin^2\gamma\cos 2\chi\right), \tag{2.24}$$

$$\rho_U = \eta_0\left(\psi_p - \frac{1}{2}\left[\psi_b + \psi_r\right]\right)\left(\sin^2\gamma\sin 2\chi\right), \tag{2.25}$$

$$\eta_V = \frac{\eta_0}{2}\left[\psi_b + \psi_r\right]\cos\gamma, \tag{2.26}$$

where γ is the inclination of the magnetic field vector with respect to the observer line-of-sight (LOS) and χ is the azimuth angle. The p, b, r indices stands for the Zeeman components π, ω_b and ω_r, respectively.

The absorption ($\phi_{p,b,r}$) and anomalous dispersion ($\psi_{p,b,r}$) profiles, under the classical Lorentz electron theory, and considering thermal motions (as Doppler broadening and collisions) of the medium, can be written by:

$$\phi_j = \sum_{i_j=1}^{N_j} s_{i_j}\mathcal{H}\left(a, \nu + \nu_D + v_{i_j}\right), \tag{2.27}$$

$$\psi_j = 2\sum_{i_j=1}^{N_j} s_{i_j}\mathcal{H}\left(a, \nu + \nu_D + \nu_{i_j}\right), \tag{2.28}$$

where $j = b, p, r$ are the Zeeman multiplets and s_{i_j} are the normalized strength of the Zeeman components. The Voigt function, $\mathcal{H}$, and the Faraday function, $\mathcal{F}$, at a given damping, a, a given distance from the line center λ_0 are:

$$\mathcal{H}\left(a, \nu'\right) = \frac{a}{\pi} \int_{-\infty}^{+\infty} \frac{e^{-y^2}}{\left(\nu' - y\right)^2 + a^2} \mathrm{d}y, \tag{2.29}$$

$$\mathcal{F}\left(a, \nu'\right) = \frac{1}{2\pi} \int_{-\infty}^{+\infty} \frac{\left(\nu' - y\right) e^{-y^2}}{\left(\nu' - y\right)^2 + a^2} \mathrm{d}y. \tag{2.30}$$

There is a shift at the central position for each component of the Zeeman pattern, and this shift results from two main effects. The first is the Zeeman splitting that causes a shift in the absorption and dispersion profiles of each component of the Zeeman pattern, given by

$$\nu_{i_j} = \frac{\Delta\lambda_{i_j}}{\Delta\lambda_D}. \tag{2.31}$$

The second point is the Doppler effect that produces the same shifts in all of the components of the Zeeman pattern due to velocity along the vertical axis, ν_z, so we have that:

$$\nu_D = \frac{\nu_z \lambda_0}{c\Delta\lambda_D}. \tag{2.32}$$

The damping a and the Doppler width $\Delta\lambda_D$ are given as follow:

$$a = \frac{\lambda_0^2}{4\pi\Delta\lambda_D}\Gamma, \tag{2.33}$$

$$\Delta\lambda_D = \frac{\lambda_0}{c}\left(\frac{2kT}{M} + \nu_{misc}^2\right)^{1/2}, \tag{2.34}$$

where Γ is the damping factor that can be decomposed into spectral broadening due to the radiative (Γ_{rad}) and collisional (Γ_{col}) line broadening. In the Equation (2.34), T is the temperature, k is the Boltzmann constant, M is the mass of the atom. ν_{misc} is the *microturbulent velocity*, that is used to account it motions in smaller scales than the mean free path.

2.3.1 RTE in local thermal equilibrium

The local thermal equilibrium (LTE) hypothesis consists in considering that only radiation is allowed to deviate from a thermodynamic equilibrium situation because of the transport. All the thermodynamic properties of matter are assumed to be governed by the thermodynamic equilibrium equations, not global but at the local values of temperature, T , and density, ρ.

The formation of a large number of spectral lines in the solar photosphere can be well described by assuming that radiative transfer has taken place in conditions of local thermodynamic equilibrium.

In this way, we may conclude that assuming the LTE, the light streams through a plane–parallel or stratified medium according to the following RTE is

$$\frac{\mathrm{d}}{\mathrm{d}z}\begin{pmatrix} I \\ Q \\ U \\ V \end{pmatrix} = \begin{pmatrix} \eta_I & \eta_Q & \eta_U & \eta_V \\ \eta_Q & \eta_I & \rho_V & -\rho_U \\ \eta_U & -\rho_V & \eta_I & \rho_Q \\ \eta_V & \rho_U & -\rho_Q & \eta_I \end{pmatrix} \begin{pmatrix} I - B_\nu(T) \\ Q \\ U \\ V \end{pmatrix}, \tag{2.35}$$

where the source function $\mathbf{S}(z)$ is given by

$$\mathbf{S}(z) = (\mathbf{B}_\nu(T), 0, 0, 0)^{\mathrm{T}} \tag{2.36}$$

Therefore, in Local thermodynamic equilibrium (LTE) conditions, $\mathbf{S}(z)$ has the form of a Planck function, $\mathbf{B}_\nu(T)$, at the local temperature T.

2.3.2 RTE through isotropic media

The isotropic medium is characterized by a single refractive index, and the electromagnetic waves propagate throughout the medium with a single velocity in any direction.

Assuming that the medium is isotropic, then the Equations from (2.20) to (2.26) will be given by $\eta_Q = \eta_U = \eta_V = \rho_Q = \rho_U = \rho_V = 0$, once $\phi_j = \phi$ and $\psi_j = \psi$, $\forall\ j = r, b, p$. In this way, the propagation matrix, presented in the Equation (2.35) becomes a diagonal matrix. Therefore, the RTE will be given by the equations above, one for each Stokes parameter.

$$\frac{\mathrm{d}I}{\mathrm{d}\tau_c} = (1 + \eta_0 \phi)\,(I - B_\nu)\,, \tag{2.37}$$

$$\frac{\mathrm{d}Q}{\mathrm{d}\tau_c} = (1 + \eta_0 \phi)\,Q, \tag{2.38}$$

$$\frac{\mathrm{d}U}{\mathrm{d}\tau_c} = (1 + \eta_0 \phi)\,U, \tag{2.39}$$

$$\frac{\mathrm{d}V}{\mathrm{d}\tau_c} = (1 + \eta_0 \phi)\,V. \tag{2.40}$$

The Equation (2.37) is usually called the radiative transfer equation for unpolarized light. In the case when the boundary condition assumes that light is originally unpolarized ($Q_0 = U_0 = V_0 = 0$), the Equations (2.38), (2.39), and (2.40) shows that the light will remain unpolarized throughout the medium.

2.3.3 Propagation along the optical axis

Supposing that the optical axis, $\hat{e}_0$ coincides with the ray path and stays unaltered throughout all the medium, in this case the colatitude angle $\gamma = 0$. Then, the elements of the $\hat{\mathbf{k}}$, given by the Equations from (2.20) to (2.26) will turns out to:

$$\eta_I = 1 + \frac{\eta_0}{2}\left[\phi_b + \phi_r\right], \tag{2.41}$$

$$\eta_Q = \eta_U = \rho_Q = \rho_U = 0, \tag{2.42}$$

$$\eta_V = \frac{\eta_0}{2}\left[\phi_b - \phi_r\right], \tag{2.43}$$

$$\rho_V = \frac{\eta_0}{2}\left[\psi_b - \psi_r\right]. \tag{2.44}$$

Note that the ϕ_p and ψ_p are not present in the parameters equation anymore. It has disappeared, since the light polarized along $\hat{e}_0$ cannot propagate along $\hat{e}_0$, and the electromagnetic waves are transversal.

From the Equation (2.40), we can see that the source term is not present in the Stokes Q and U equations. Therefore, we can conclude that, if the light is initially unpolarized, the transfer will not produce any linear polarization. On the other hand, the source term appears in the Stokes Q and V. Hence, we can conclude that if the light is initially unpolarized before entering the medium, only circular polarization can be produced when the propagation is along the optical axis.

2.4 Solving the RTE

The radiative transfer equation can be solved if we know the propagation matrix and the source function vector. In order to solve the RTE, let us consider the transformation of the Stokes vector from one optical depth (τ_c), to another (τ_c'), in the absence of any emission process along the path. This transformation of the Stokes vector can be described with the evolution operator $\hat{O}(\tau_c, \tau_c')$, by assuming the relation

$$\mathbf{I}^*(\tau_c) = \hat{O}(\tau_c, \tau_c')\mathbf{I}^*(\tau_c'), \tag{2.45}$$

where $\mathbf{I}^*$ represents the solution of the homogeneous equation related to the non-homogeneous equation (2.17). The evolution operator fulfills the following conditions:

$$\hat{O}(\tau_c, \tau_c) = \mathbf{1}, \tag{2.46}$$

$$\hat{O}(\tau_c, \tau_c'') = \hat{O}(\tau_c, \tau_c')\hat{O}(\tau_c', \tau_c''). \tag{2.47}$$

Integrating the RTE (Equation (2.17)) with respect to the optical depth between the bottom and top of the atmosphere, τ_0 and τ_1, respectively, gives

$$\mathbf{I}(\tau_1) = \hat{O}(\tau_1, \tau_0)\mathbf{I}(\tau_0) - \int_{\tau_0}^{\tau_1} \hat{O}(\tau_1, \tau_c)\hat{\mathbf{k}}(\tau_c)\mathbf{S}(\tau_c)\mathrm{d}\tau_c. \tag{2.48}$$

The first term, on the right-side of the equation, gives us the Stokes parameters of the light, that has streamed through the medium (between τ_0 and τ_1) as if the medium were not emitting light (homogeneous solution). The second term of the equation provides the contribution from emission to the final Stokes parameters.

Supposing that the observer is located at $\tau_1 = 0$, then if the inner point is chosen to be deep enough ($\tau_0 \to \infty$), the atmosphere is so optically thick that no radiation emitted at τ_0 can reach the observer, then

$$\lim_{\tau_0 \to \infty} \hat{O}(0, \tau_0)\mathbf{I}(\tau_0) = 0. \tag{2.49}$$

We can then combine the Equations (2.48) and (2.49) to obtain a formal solution of the RTE, as follow

$$\mathbf{I}(0) = \int_0^\infty \hat{O}(0,\tau_c)\hat{\mathbf{k}}(\tau_c)\mathbf{S}(\tau_c)\mathrm{d}\tau_c. \tag{2.50}$$

The solution of the evolution operator cannot be obtained analytically for a general atmosphere, and has to be computed by numerical methods.

The evolution operator can be also represented by an exponencial, to obtain this we can derive it from the differential equation

$$\frac{\mathrm{d}\hat{O}(\tau_c,\tau_c')}{\mathrm{d}\tau_c} = \hat{\mathbf{k}}(\tau_c)\hat{O}(\tau_c,\tau_c'). \tag{2.51}$$

Hence, the evolution operator will be given by

$$\hat{O}(0,\tau_c) = e^{-\int_0^{\tau_c}\hat{\mathbf{k}}(\tau_c)\mathrm{d}\tau}. \tag{2.52}$$

Based on Equation (2.48), even if LTE can be assumed, there is no analytical expression for $\hat{O}$ in general. Thus, the equation has to be solved numerically, and some examples of the numerical RTE codes are the SIR code (COBO; INIESTA, 1992), the STOPRO code (Solanki (1987), Frutiger et al. (2000)) and the LILIA code (SOCAS-NAVARRO, 2001).

2.5 Milne-Eddington atmosphere approximation

Considering the simple case where the propagation matrix is constant with respect to the atmospheric height, as follow

$$\hat{\mathbf{k}}(\tau_c) = \hat{\mathbf{k}}_0, \tag{2.53}$$

and the source function varies linearly with the optical depth, given by

$$\mathbf{S} = \mathbf{S_0} + \mathbf{S1}\tau_c = (S_0 + S_1\tau_c)(1,0,0,0)^T, \tag{2.54}$$

So, the Equation (2.52) can be written as,

$$\hat{O}(0,\tau_c) = e^{-\hat{\mathbf{k}}_0\tau_c}. \tag{2.55}$$

A medium that satisfies the Equations (2.53) and (2.54) is called the *Milne-*

Eddington atmosphere. From the Equation (2.55) we can obtain that the propagation of polarized light, given by Equation (2.50), can now be written as:

$$\mathbf{I}(0) = \int_0^\infty e^{-\hat{\mathbf{k}}_0\tau_c}\hat{\mathbf{k}}_0(\mathbf{S}_0 + \mathbf{S}_1\tau_c)\mathrm{d}\tau_c, \tag{2.56}$$

which can be integrated analytically by parts to obtain:

$$\mathbf{I}(0) = \mathbf{S}_0 + \hat{\mathbf{k}}_0^{-1}\mathbf{S}_1. \tag{2.57}$$

Since the only non-zero element of both $\mathbf{S}_0$ and $\mathbf{S}_1$ is the first one, we only need to calculate the first column of the inverse $\hat{\mathbf{k}}_0^{-1}$ of the propagation matrix. The solution is also known as the Unno-Rachkowsky solution of the transfer equation, given by:

$$I(0) = S_0 + \frac{\eta_I S_1}{\Delta}\left[\eta_I^2 + \rho_Q^2 + \rho_U^2\rho_V^2\right], \tag{2.58}$$

$$Q(0) = \frac{S_1}{\Delta}\left[\eta_I^2\eta_Q + \eta_I\left(\eta_V\rho_U - \eta_U\rho_V\right) + \rho_Q\Pi\right], \tag{2.59}$$

$$U(0) = \frac{S_1}{\Delta}\left[\eta_I^2\eta_U + \eta_I\left(\eta_Q\rho_V - \eta_V\rho_Q\right) + \rho_U\Pi\right], \tag{2.60}$$

$$V(0) = \frac{S_1}{\Delta}\left[\eta_I^2\eta_V + \eta_I\left(\eta_U\rho_Q - \eta_Q\rho_U\right) + \rho_V\Pi\right], \tag{2.61}$$

where the determinant of the propagation matrix, Δ and Π, are given by:

$$\Delta = \eta_I^2\left(\eta_I^2 - \eta_Q^2 - \eta_U^2 - \eta_V^2 + \rho_Q^2 + \rho_U^2 + \rho_V^2\right) - \Pi^2, \tag{2.62}$$

$$\Pi = \eta_Q\rho_Q + \eta_U\rho_U + \eta_V\rho_V. \tag{2.63}$$

We developed a code to compute the synthetic Stokes profiles using the Milne-Eddington atmosphere for the Fe I 6302.5 Å, as showed in Figure 2.5. The inclination angle was set to 80° and the azimuth is 70°. The colors represent the magnetic field strength from 0 (blue) to 3 kG (red). In the Stokes I we can see the Zeeman splitting increasing due to the magnetic field. We can note a lower amplitude of the V Stokes due to the high inclination angle. The spectral line is not centered in the 6302.5 Å; it is shifted to the right due to the LOS-velocity that was set to 2 kms^{-1}.

Figure 2.5 - Synthetic Stokes profiles estimated by using a developed code for the Milne-Eddington atmosphere of the Fe I 6302.5 Å. The inclination angle was set to 80° and the azimuth is 70°. The colors represent the magnetic field strength from 0 (blue) to 3 kG (red), with step of 200 G. In the Stokes I we can see the Zeeman splitting of the Fe I when increasing the magnetic field strength. Note a lower amplitude of the V Stokes due to the high inclination angle. The spectral line is not well centered in the 6302.5 Å, it is shifted to the right due to the LOS-velocity that was set to 2 kms^{-1}.

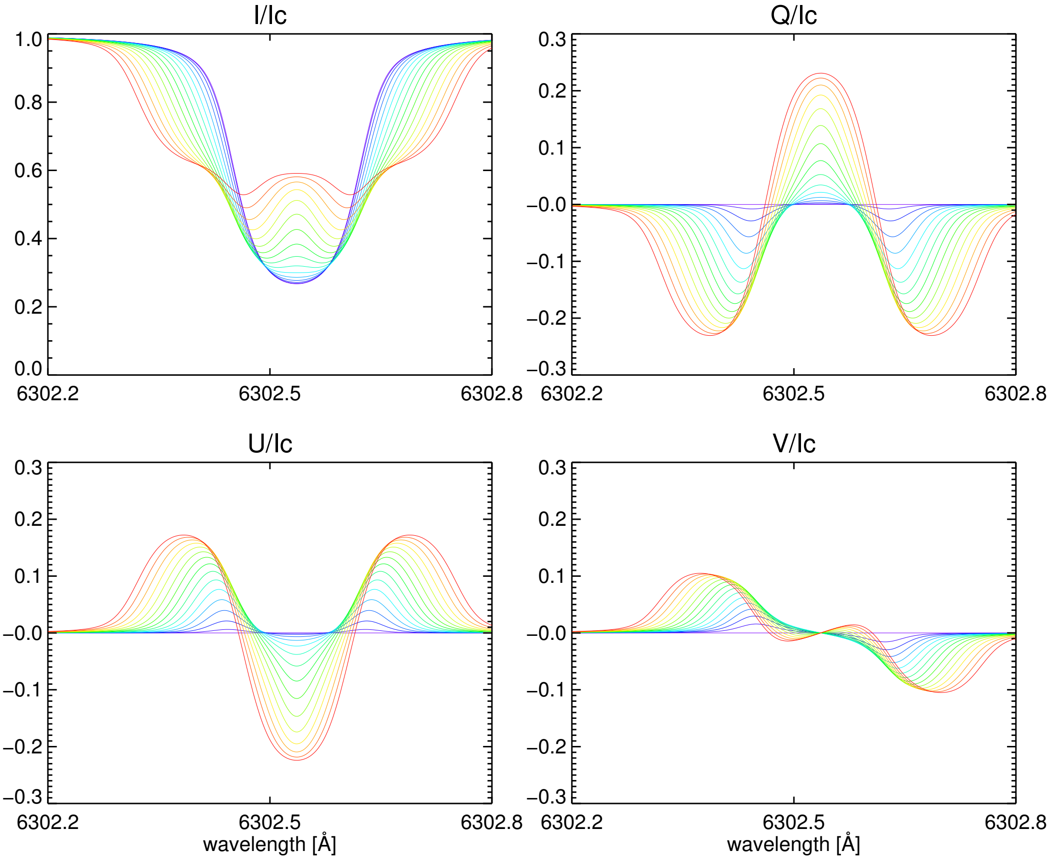

SOURCE: Author

2.6 Inversion of the Stokes profiles

The process to achieve the physical parameters of the solar atmosphere, based on the observations of the Stokes profiles, at some specific wavelengths, is called the *inversion of the Stokes profiles.*

Let us take our study as an example, we are focused on analyzing the data of the magnetic and velocity field in an arch filament system in the photosphere and upper chromosphere by inverting the Stokes profiles of the spectral lines Si I 10827.1 Å, He I triplet at 10830 Å and Ca I 10832.4 Å observed by the GRIS spectropolarimeter. To obtain these atmospheric parameters from the observed Stokes profiles, we made use of the inversion.

The Figure 2.5 presented the Stokes profiles obtained using Milde Eddington approximation for a given atmosphere, within input parameters like the magnetic field strength, inclination, azimuth, and LOS-velocities. This stokes profiles, as a solution of the RTE, provides what is called the synthetic Stokes parameters $\mathbf{I^{syn}}(\lambda)$, and is given by

$$\mathbf{I^{syn}}(\lambda) = \begin{pmatrix} I^{syn}(\lambda) \\ Q^{syn}(\lambda) \\ U^{syn}(\lambda) \\ V^{syn}(\lambda) \end{pmatrix}. \tag{2.64}$$

To obtain the appropriate inversion of the Stokes profiles we need to iteratively compare both observed ($\mathbf{I^{obs}}$) and synthetic $\mathbf{I^{syn}}$ stokes, it can be performed employing a merit function χ^2 such as

$$\chi^2 = \sum_{s=1}^{4} \sum_{i=1}^{N} \left[\frac{\mathbf{I}_s^{obs}\left(\lambda_i\right) - \mathbf{I}_S^{syn}\left(\lambda_i\right)}{\sigma_i} \right]^2 \omega_{s,i}^2, \tag{2.65}$$

where the s index applies to the scan of the four Stokes parameters and the i index to the wavelength positions. σ_i denotes the uncertainty in the measurement of each Stokes parameters s. The $\omega_{s,i}$ is the weight given for each wavelength and Stokes parameter. The minimization of the merit function χ^2 is an iterative process in which the atmospheric parameters are systematically modified, until a best fit between synthetic and observed Stokes profiles is reached.

The fit between $\mathbf{I^{obs}}(\lambda)$ and $\mathbf{I^{syn}}(\lambda)$ need to be performed with a method to solve the nonlinear least squares problem. The most common method used is the Levenberg-

Marquardt algorithm (MORE, 1978).

Once we obtained the observational Stokes profiles, the inversion technique needs to be applied for each pixel of the observed map of the solar atmosphere. The first estimative of the atmospheric parameters can be taken from an atmosphere model for the considered solar feature (quiet Sun, penumbra, umbra) or from the inversion resulting from an adjacent pixel.

2.7 HeLIx inversion

In the present study, we aim to analyze the data of the magnetic field vector and Doppler velocity in the photosphere and upper chromosphere, by using the GRIS spectrograph observations in the Si I 10827.1 Å line and He I 10830 Å triplet. To accomplish the described physical parameters regarding the solar surface and atmosphere we use the inversion code called HeLIx$^+$ (Helium Line Information Extractor), developed by Lagg et al. (2004).

HeLIx$^+$ solves the RTE under the Milne-Eddington approximation, for describing the radiative transfer in the He I 10830 Å multiplet lines. The He I triplet line forms only in the upper chromosphere and there is no contribution from the photosphere, once it is mostly optically thin. Due to these reasons, the Milne-Eddington approximation is an adequate approach as long as we are only focused in the magnetic and velocity parameters but not in the temperature profile of the atmosphere, or even in the exact height of formation.

The calculation of the Stokes profiles leads to the atmospheric model which consists of eight parameters, also called atmospheric components. The free parameters are the magnetic field strength B, the inclination angle γ, the azimuthal angle χ, the line-of-sight velocity v_{LOS}, the Doppler width $\Delta\lambda_D$, the damping a, the ratio between line center and continuum intensity η_0, and the slope of the source function $S1$.

The evaluation of the fitness of the synthetic Stokes profiles to the observed Stokes profiles is based on a minimization of the goodness function δ. The synthesized profiles are calculated assuming an arbitrary initial atmosphere, as described above. The parameters of this atmosphere are then adapted in such a way that the synthesized profiles match the observations. The goodness function δ is given by

$$
\begin{aligned}
\delta = & \sum_{\lambda_i=0}^{N} \omega_I \frac{(I_{obs} - I_{syn})}{I_c \sigma_I} \\
& + \sum_{\lambda_i=0}^{N} \omega_Q \frac{(Q_{obs} - Q_{syn})}{\sigma_Q} \\
& + \sum_{\lambda_i=0}^{N} \omega_U \frac{(U_{obs} - U_{syn})}{\sigma_U} \\
& + \sum_{\lambda_i=0}^{N} \omega_V \frac{(V_{obs} - V_{syn})}{\sigma_V},
\end{aligned}
\tag{2.66}
$$

where N is the number of wavelength positions along the profile and I_c is the continuum level. The $\omega_{I,Q,U,V}$ are the weighting functions for each Stokes along the wavelength. The subscripts *obs* and *syn* refer to observed and synthesized Stokes profiles respectively. $\sigma_{I,Q,U,V}$ are parameters defining the strength of the signal, as follow

$$
\sigma_I = \frac{1}{n} \sum_{\lambda_i=0}^{N} \left| \frac{I_{obs}}{I_c} - 1 \right|, \tag{2.67}
$$

$$
\sigma_{Q,U,V} = \frac{1}{n} \sum_{\lambda_i=0}^{N} \left| (Q, U, V)_{obs} \right|. \tag{2.68}
$$

The weighting configuration along the spectra can be chosen to reflect the peculiarities of each spectral region. Usually, the highest weight is given to the red component of the He I line (He Ib and He Ic blended line), since any other spectral line does not overlap them. For wavelengths less than 10829.6 Å, the weight function is reduced by a factor of 5. This region contains the He Ia line which is blended by the Ca I 10829.3 Å line. All wavelength points below 10828.5 Å and above 10832.5 Å were not used to fit the He I components ($\omega_{I,Q,U,V} = 0$).

In order to guarantee that the optimization method finds the global minimum of δ in parameter space, the HeLIx$^+$ code made use of the genetic algorithm PIKAIA (CHARBONNEAU, 1995). Lagg et al. (2004) contrasted this method with standard minimization routines and found superior robustness, however, with some computation time costs.

Figure 2.6 - Comparison between inversion maps, for the azimuth angle, computed with the genetic algorithm PIKAIA (top) and UOBYQA (bottom). Note the large gradient between neighboring pixels in the UOBYQA, indicating the optimization routine got stuck in some of the local minima of the parameter space. The PIKAIA shows robustness to find the global minimum.

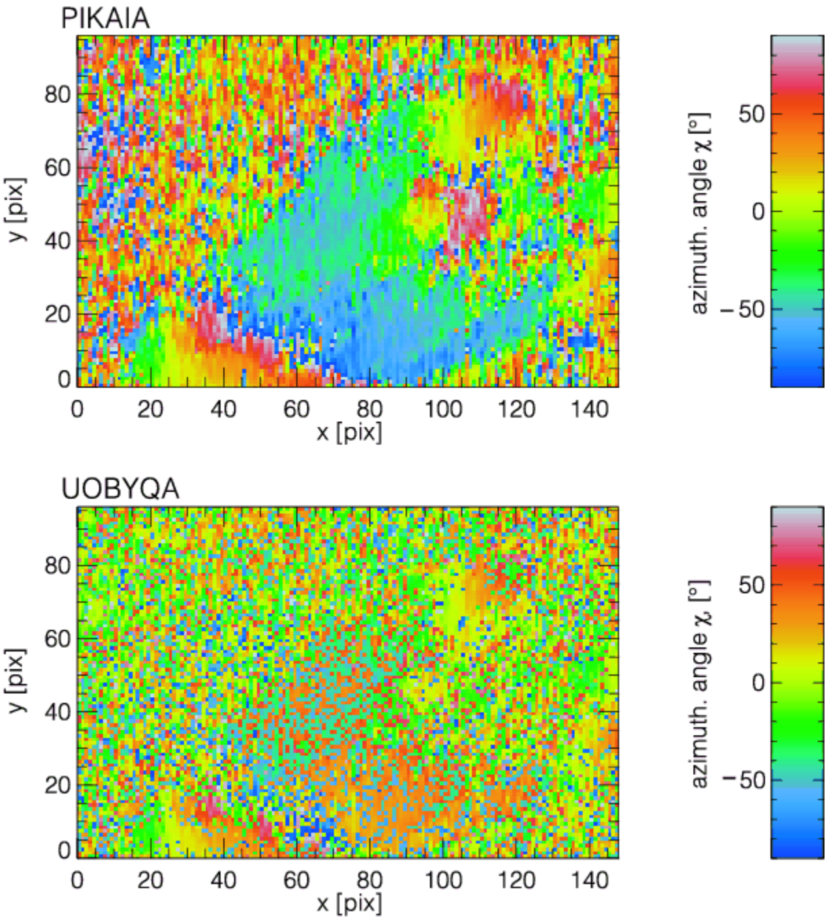

SOURCE: Lagg et al. (2004)

In order to demonstrate the superior robustness of the PIKAIA, Lagg et al. (2004) compared the results of an inversion map with the ones obtained with Unconstrained Optimization BY Quadratic Approximation (UOBYQA), as presented by Powell (2002), a code which estimates the derivatives using quadratic approximations, similar to the Milne-Eddington algorithm. The comparison between the inversion maps, for the azimuth angle, is presented in Figure 2.6. The large intensity variation between neighboring pixels in the UOBYQA, indicating the optimization routine got stuck in some of the local minima of the parameter space. It shows the superior robustness of the genetic algorithm.

The genetic algorithm PIKAIA is responsible for finding the global minimum in a multidimensional hypersurface independent of the initial input values. Therefore, the PIKAIA allows us to specify a fit range for each parameter aiming to guarantee that the output result of the inversion stays within the range of physically valuable solutions. The main issue in using the genetic algorithm is the computation time. However, as we are making use of the Milne-Eddington approximation to compute the synthesized profiles, the computation time limitation is minimized.

The HeLIx$^+$ code incorporates a processing method of the Hanle effect for a particular geometry case. The linear polarization signal of the He lines is altered due to the Hanle effect, producing a complex dependence of the linear polarization on magnetic field strength and direction. The atomic polarization and the Hanle effect incorporated in the code is presented in detail by Bueno et al. (2002) and more recent by Ramos et al. (2008) and Bueno et al. (2005).

3 Telescope GREGOR and GRIS spectrograph

The solar telescope GREGOR was built by a German consortium led by the Kiepenheuer-Institut für Sonnenphysik, with the Leibniz-Institut für Astrophysik Potsdam, the Max-Planck-Institut für Sonnensystemforschung (MPS) and the Institut für Astrophysik Göttingen as partners. The Instituto de Astrofísica de Canarias and the Astromomical Institute of the Academy of Sciences of the Czech Republic (ASU AV CR) contributed to the telescope or the instrumentation. The official proposal for the construction of the GREGOR telescope was prepared in March 2000 and after 10 years of planning and construction, the installation of GREGOR was officially inaugurated on May 21, 2011. In April 2012, MPS scientists joined the first scientific observing campaign with the GREGOR telescope.

GREGOR has an aperture of 1.5 m and replaces the former 45-cm Gregory-Coude Telescope (GCT,Kneer and Wiehr (1989)). It is installed at the Observatorio del Teide (OT) on Tenerife island (Canary Islands, Spain) located 2,400 m a.s.l. The OT is a major milestone for solar physics in Europe within the world's most powerful set of solar telescopes at a single site. The set of telescopes at the OT are the 90 cm THEMIS (MEIN; RAYROLE, 1985), 70 cm Vacuum Tower Telescope (VTT) (SOLTAU, 1991), and the 1.5 m GREGOR (SCHMIDT et al., 2012). Some non-solar telescopes were built at the OT, as the Optical Ground Station (OGS) (WEIGEL et al., 2001), the two 1.2 m STELLar Activity (STELLA) (STRASSMEIER, 2001) and others.

A panoramic view of the Observatorio del Teide is shown in Figure 3.1*a*, where the tallest buildings are the GREGOR and VTT. Figure 3.1*b* shows the aerial view of the Observatorio del Teide, with the telescopes (from the bottom right) THEMIS, VTT, GREGOR, OGS, and the Solar Pyramid. Figure 3.1*c* presents the GREGOR telescope in operation. The dome has a open-foldable design with a diameter of 9 m, it is shown close on panel (*a*) and opened on panel (*c*).

The GREGOR telescope is the largest solar telescope in Europe and third largest in the world, after the 1.6 m clear aperture Goode Solar Telescope (GST, Goode (2012)) at the Big Bear Observatory (BBSO, Zirin (1970)) and the 1.6 m $f/54$ McMath-Pierce solar telescope (PIERCE, 1964) at Kitt Peak National Observatory. A new large solar telescope with 4 m diameter named Daniel K. Inouye Solar Telescope (DKIST, Elmore et al. (2014)) is planned to have the first light in 2019.

Figure 3.1 - (*a*) Panoramic view of the Observatorio del Teide where the two tallest buildings hosts the GREGOR (left) and VTT (right) telescopes. (*b*) Aerial view of the Observatorio del Teide, Tenerife on the Canary Islands, with the telescopes (from bottom right) THEMIS, VTT, GREGOR, OGS, and the Solar Pyramid. (*c*) The 1.5 m GREGOR telescope in operation. The dome is an open-foldable with diameter of 9 m.

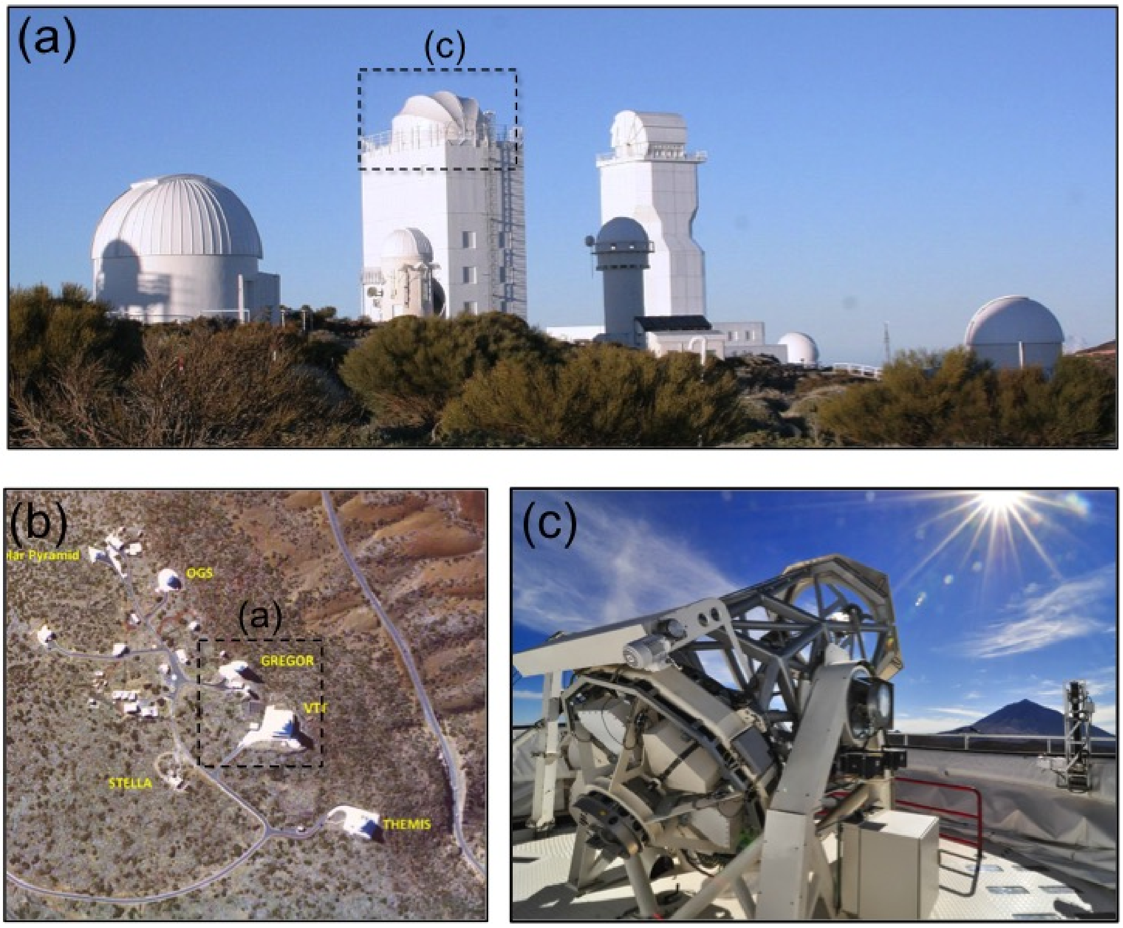

SOURCE: (*a*) Ribeiro (2009), (*b*) Schmidt et al. (2012) and (*c*) Schlichenmaier (2015)

The GREGOR adaptive optics (AO) has been developed significantly over the years (BERKEFELD et al., 2004; BERKEFELD et al., 2005; BERKEFELD et al., 2006; BERKEFELD et al., 2012) using many features of the Kiepenheuer Adaptive Optics System (KAOS, Luhe et al. (2003)) common to all AO projects at the Kiepenheuer Institute and which has been operated at the Vacuum Tower Telescope (VTT).

The wavefront sensor (WFS) is a correlating Shack-Hartmann (SH) WFS with 156 subapertures. The GREGOR AO uses a 256-actuator mirror; type stacked piezo and model CILAS SAM256 (BERKEFELD et al., 2012). A high-cadence camera and high-performance computer provide a 2.5-kHz control loop frequency to achieve a 0-dB bandwidth of correction at about 130 Hz. The optical design also includes an option for multi-conjugate adaptive optics (MCAO, Berkefeld et al. (2010), Schmidt et al. (2009), Schmidt et al. (2010). The MCAO system has been tested along many years at KIS and the VTT. The controlled FOV of the MCAO system has a diameter of about 60", which is about ten times larger than what can be accomplished with a conventional AO (DENKER et al., 2012).

The GREGOR telescope splits the solar light observation to three main instruments, the Broad Band Imager (BBI, Luhe et al. (2012)), the GREGOR Fabry Perot Interferometer (GFPI, Puschmann et al. (2012)) and the GREGOR Infrared Spectrograph (GRIS, Collados et al. (2012)).

In October 2017, a technical campaign installed a new hi-speed infrared camera at the GREGOR telescope. The new camera has a frame rate of up to 90 frames/s; the new infrared camera allows the image improvement from the distortion introduced by turbulence in the Earth atmosphere. A unique image reconstruction developed at MPS will be possible to reach the diffraction limit of the GREGOR telescope. The high quantum efficiency and the duty cycle of almost 100% enhance the photon efficiency by a factor of 2 compared to the old GRIS system. The data presented in this work was observed with the old infrared camera. However, the next steps in the study of filaments we hope to implemente using the new hi-speed infrared camera.

3.1 Telescope Design

The design of the GREGOR optical setup is presented on Figure 3.2. Initially, the Sun light comes from the top, in the direction of the 1.5 m primary mirror (M1). The primary mirror is an $f/1.67$ paraboloid.

The telescope employs a modified Gregory configuration, so the first focus (F1) is formed before the secondary mirror (M2). In the F1 a water-cooled field stop restricts the field-of-view (FOV) to a diameter of 150". The elliptical secondary mirror M2 images F1 on the secondary focus F2.

The elliptical mirror M3 picks up F2 and produces the $f/40$ science beam. The next mirrors are mainly disposed to transfer the light into the optical laboratory. The flat mirror M11 reflects the light to the adaptive optics bench. The collimator M12 images the entrance pupil on the deformable mirror (DM) M14. The tip−tilt mirror M13, situated before the pupil plane, eliminates the image jitter, leaving only the image blurring to be compensated by the DM (BERKEFELD et al., 2012).

The $f/40$ science beam is recreated by the reimager M15, imaging the pupil plane at infinity. The dashed line outlines the adaptive optics. More details of the GREGOR optical design of GREGOR is described by Soltau et al. (2012).

Table 3.1 - Description of some main properties of the GREGOR telescope

Description	*Value*
Observatory	Observatory de Teide (OT) - IAU code 954
Coordinate	28°18'00"N 16°30'35"W
Altitude	2390 m
Optical Design	Gregory
Primary mirror diam.	1500 mm
M1 Clear aperture	1440 mm
M1 material	Zerodur
M1 focal length	2.5 m
Secondary mirror diam.	430 mm
M2 material	Cesic Ceramic
Effective focal length	57.3 m
Field of View	150"
Spatial Resolution	0.08" (∼70 km)
Mount	Altazimuth
Dome size	9 m
Adaptive optics (AO):	
Type	KAOS.256
Size of subapertues	10 cm (sq.)
Iluminated subapertues	156
Actuators of deformable mirror	256
Closed-loop bandwidth	120 Hz
Instruments	GREGOR Infrared Spectrograph (GRIS) GREGOR Fabry-Pérot Interferometer (GFPI) Broad Band Imager (BBI)

SOURCE: Author

Figure 3.2 - Optical setup of the GREGOR telescope and the adaptive optic (AO) system. The configuration is a double Gregory-type telescope, with two intermediate focus F1 and F2. In the F1 a water-cooled field stop limits the field-of-view (FOV) to a diameter of 150”. The dashed line outlines the adaptive optics.

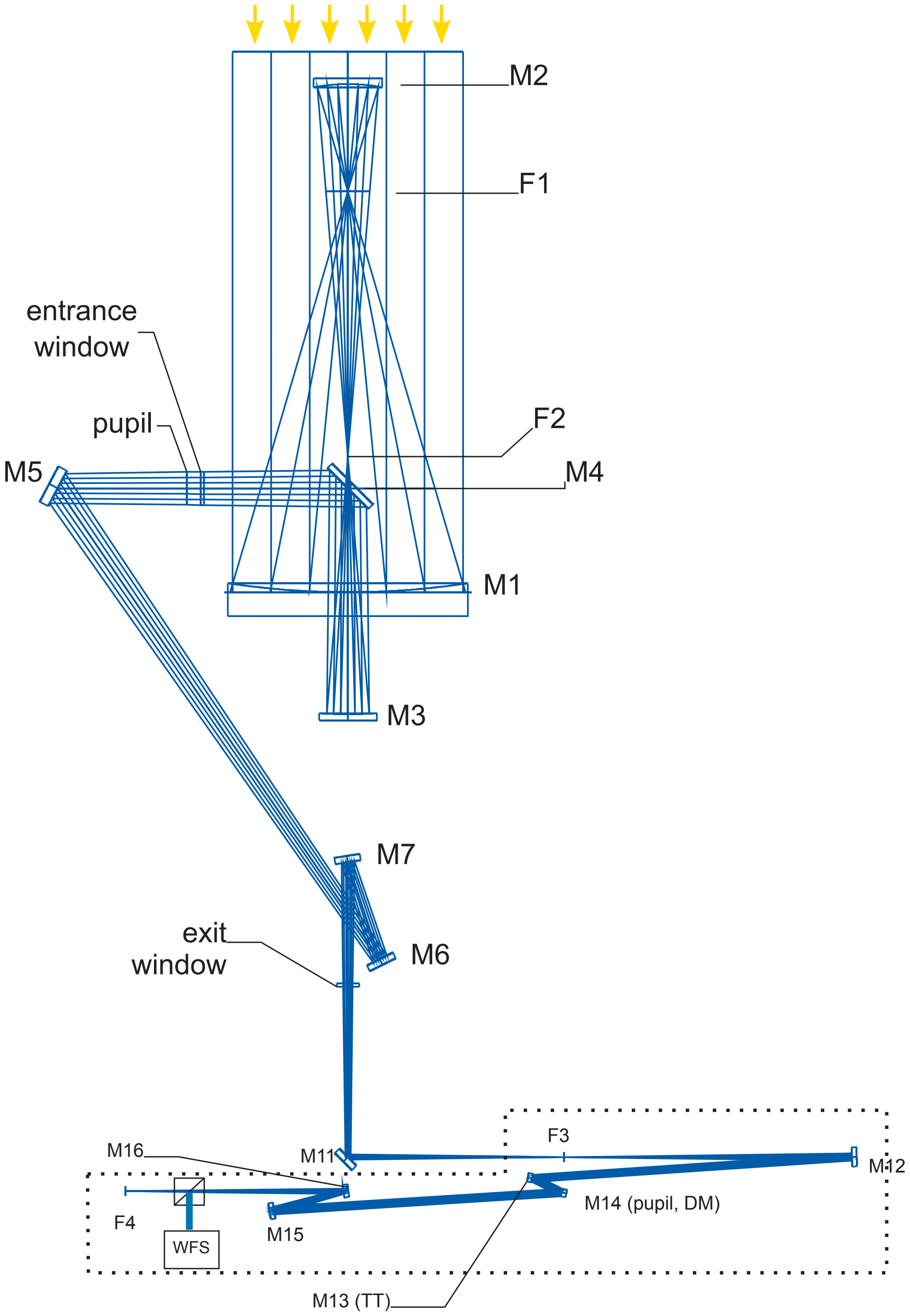
M2
F1
entrance window
pupil
F2
M5
M4
M1
M3
M7
exit window
M6
F3
M16
M11
M12
M14 (pupil, DM)
F4
M15
WFS
M13 (TT)

SOURCE: Soltau et al. (2012)

3.2 GREGOR Infrared Spectrograph

The GREGOR Infrared Spectrograph (GRIS) is the grating spectrograph installed at the GREGOR telescope. The GRIS derived many characteristics of the Tenerife Infrared Polarimeter II (TIP II, Collados et al. (2007)) instrument previous installed at the Vacuum Tower Telescope (VTT).

GRIS uses the same infrared detector of TIP II, a TCM 8600 CMOS camera (CAO et al., 2005), manufactured by the Rockwell Scientific Company (RSC, now Teledyne Imaging Sensors). The CMOS has a resolution of 1024 × 1024 pixel, a square pixel size of 18 μm and readout rate of 30Hz. The sensor has a pixel well depth of about 300,000 e^- and a quantum efficiency of more than 50% for the infrared.

The diffraction grating of GRIS has 316 grooves mm^{-1}, a blaze angle of 63.4°, and linear dimensions of 370 mm × 190 mm. The grating is inherited from Gregory-Coudé telescope (GCT, Schroeter et al. (1985)), an old 45 cm spectrograph which was installed in the same building.

In order to compute the Stokes parameters for each slit, the GRIS polarimeter package consists of two ferro-electric liquid crystal retarders (FLCR) and one polarizing beamsplitter.

The GREGOR telescope is installed in the top of the building, and the light is guided to the optical instruments with the focus F4, as presented in Figure 3.2. The first optical element of GRIS that is faced by the GREGOR light beam is the entrance slit, placed just following the beamsplitter pentaprisms, on the fifth floor of the building. The pentaprisms are arranged before the slit to transmit adequate light to the wavefront and the GFPI. The first beamsplitter is a 100 Å narrow band that rejects the spectrum centered at a wavelength of 5000 Å to the wavefront sensor, while the remainder wavelength is transmitted. The second beamsplitter denies the light bellow 6600 Å to the GFPI, and the wavelengths higher than this value are transmitted to the GRIS spectrograph.

The sketch of the optomechanical design and optical path from the focus F4 of the GREGOR telescope (see Figure 3.2) to the CMOS camera is presented in Figure 3.3 and detailed in the next paragraphs.

Figure 3.3 - Sketch of the optomechanical design and optical path from the focus F4 of the GREGOR telescope (see Figure 3.2) to the CMOS camera. *Top:* The light beam crosses the slit entrance and polarimeter package installed in the fifth floor of the building, then it is reflected down to the fourth floor (*bottom*) where it is collimated. The collimated bean reaches the grating ruling and is then scattered. The camera mirror drives and focuses the slit spectrum in the CMOS detector.

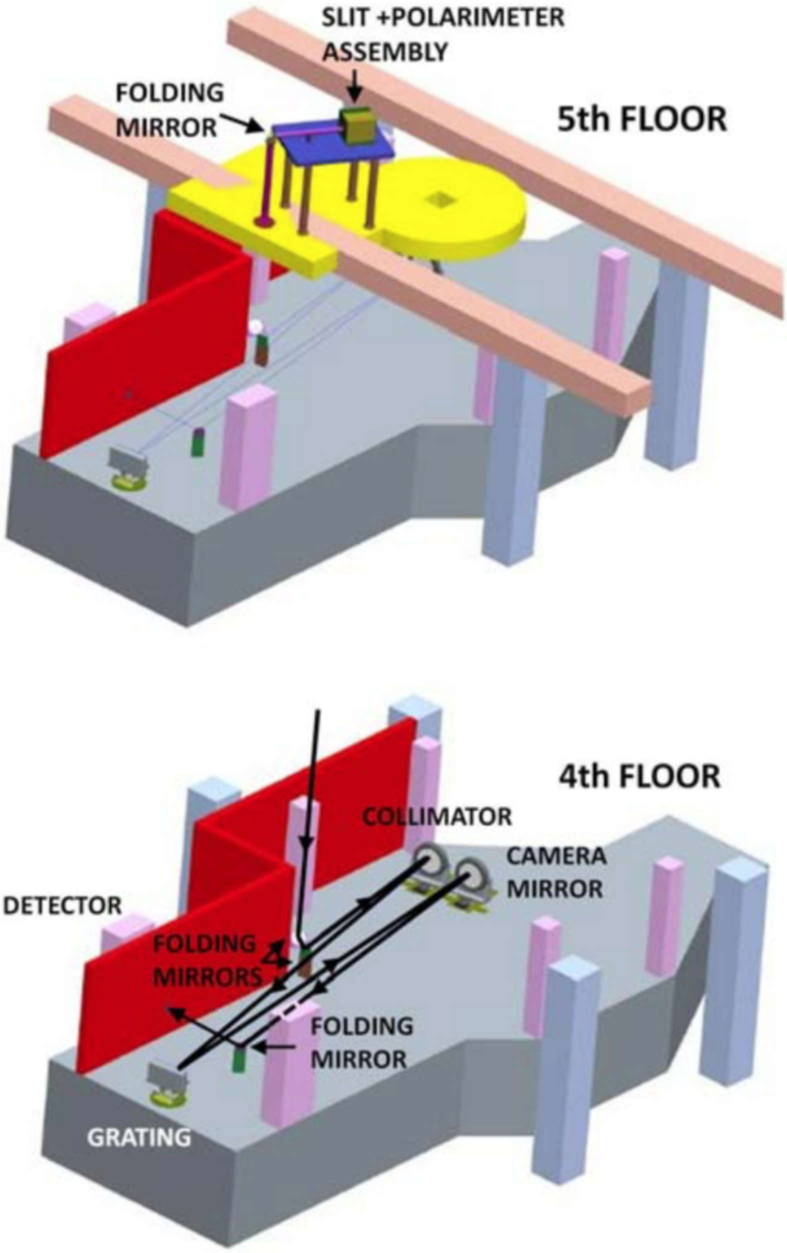
SLIT +POLARIMETER
ASSEMBLY
FOLDING
MIRROR
5th FLOOR
4th FLOOR
COLLIMATOR
CAMERA
MIRROR
DETECTOR
FOLDING
MIRRORS
FOLDING
MIRROR
GRATING

SOURCE: Collados et al. (2012)

The entrance slit has a length of 50 mm, corresponding to 180” and a width of 70 μm (0.25”). The slit is oriented horizontally, and the field-of-view (FOV) not used by the spectrograph is reflected back, with an inclination of 30°, to a slit-jaw imaging system. This unit has three channels; one channel is used to obtain images in a continuum window above 660 nm. A second channel is dedicated to chromospheric imaging, while the third channel is unused. Slit-jaw image acquisition can be synchronized with the other instruments.

After crossing the slit, the light beam is driven directly to the polarimeter package. The polarimeter is composed by a polarizing beamsplitter, consisting of five cubes, which generates two images of the slit that are linearly polarized at ±45° with respect to the slit direction (COLLADOS et al., 2007). The separation of these two images is 28.2 mm. However, this separation it is too large. To solve this issue, a system of prisms is used in the optical design to bring these two images closer together (with a separation 18 mm) to fit them onto the detector (COLLADOS et al., 2008). The scheme to correct the separation distance has previously been implemented at the VTT, without notable aberrations in the observations. In this mode, the slit length is reduced down to 18 mm (65”).

The light beam crossing the polarimeter package is conducted from the fifth floor (Figure 3.3*top*) to the fourth floor (Figure 3.3*botton*) of the building through a flat 45° folding mirror. This mirror has two working positions to keep the light beam on the optical axis with or without the polarimetric analyzer. In the fourth floor, two flat mirrors address the light to the collimator and align the image of the slit parallel to the diffraction grating ruling. Following the collimator, the light reaches the grating and it is then scattered (COLLADOS et al., 2012).

The camera mirror leads the light to a final 45° flat folding mirror that gives rise to the focal plane of the spectrograph. From the folding mirror, the light enters a reimaging optic system comprised of a collimating doublet lens and a camera doublet lens, which are responsible for the focal plane with the proper image scale on the CMOS detector. The final image scale is 7.2” mm^{-1}, so producing a spatial resolution of 0.13” pixel^{-1}. The high spatial resolution reached with the GRIS instrument can be considered in the frontier in terms of observation of full Stokes of a chromopheric line.

Figure 3.4 - Czerny Turner configuration implemented in the GRIS spectrograph. The light coming from a solar region, determined by the field of view, enters the spectrograph through an entrance slit, then crossing the polarimeter package to produce the full Stokes parameter. The concave mirror collimates the light and reflects it onto the grating. The light diffracts and is reflected in the direction of the camera mirror that is responsible to focus the light on the CMOS detector, creating a spectra for each selected slit.

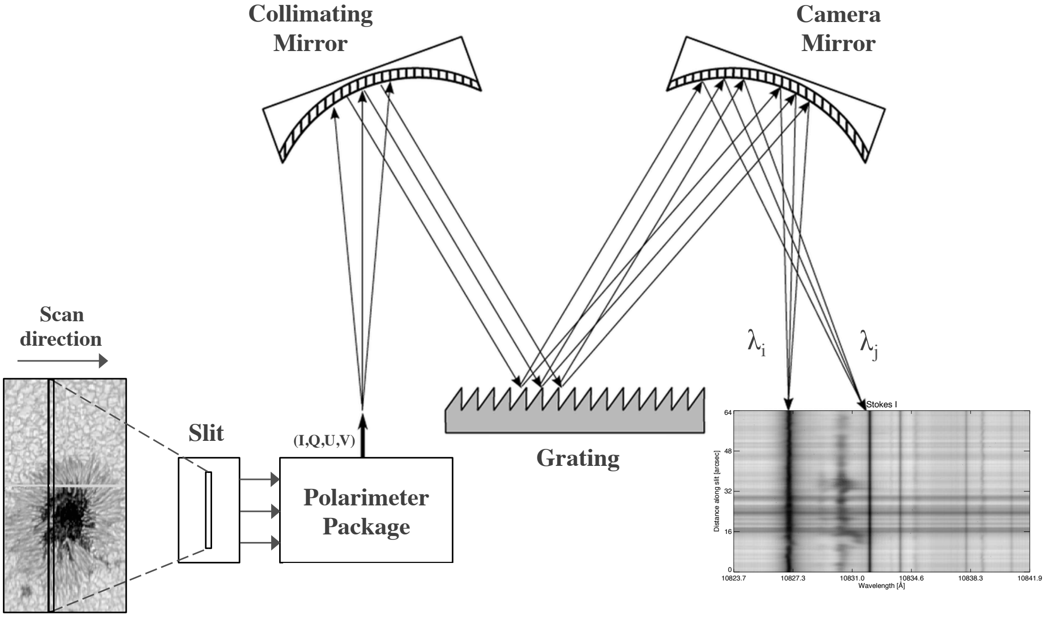
Collimating Mirror
Camera Mirror
Scan direction
Slit
(I,Q,U,V)
Polarimeter Package
Grating
λ_i
λ_j
Stokes I
Distance along slit [arcsec]
64
48
32
16
0
10823.7
10827.3
10831.0
10834.6
10838.3
10841.9
Wavelength [Å]

SOURCE: Author

The GRIS spectrograph has a standard Czerny-Turner configuration. The Czerny-Turner (CZERNY; TURNER, 1930) is the most widely used spectrograph configuration. The main advantages of this configuration are its relative simplicity and wavelength flexibility. Once the design is all-reflective, it is naturally achromatic. Vignetting at the edges of the spectrum is relatively large due to the considerable distance between the output collimator and the reflection grating. Thermal instability is also an issue in this configuration; it is a factor of 5 higher than one of an axial transmissive spectrograph (LONG, 2004).

The Czerny Turner configuration is presented on Figure 3.4. The slit selects a region of the solar field of view and then the light beam crosses the polarimeter package. The collimating mirror reflects the light onto the grating. The light diffracts and is reflected in the direction of the camera mirror that focuses the light on the CMOS detector, creating the spectral map for the selected slit.

The GRIS spectrograph can achieve one of the best spatial and spectral resolution for observation of both photosphere and upper chromosphere. The present study is only feasible due to the approach provided by the GREGOR/GRIS, as a significant advance in the spectropolarimetry. A summary of some main properties of GREGOR was presented in the Table 3.1, and for the GRIS spectrograph is displayed in Table 3.2.

Table 3.2 - Summary of some main properties of the GRIS spectrograph

Description	*Value*
Spectrograph Design	Czerny-Turner
Wavelength range	10000 - 22000 Å
Spatial resolution	0.13”
Spectral resolution	18.03 mÅ
Infrared camera:	
Detector	Rockwell TCM-8600
Resolution	1024 × 1024
Cooling system	Liquid nitrogen
Temperature operation	77 K
Pixel size	18 μm
Well depth	320,000 e^{-1}
Frame rate	36 fr/s
Quantum efficiency	$>$ 55% on infrared
Wavelength range	$0.9 - 2.5$ μm
Read noise	80 e^{-}
Dark current	220 e^{-}/s
Polarimeter:	
Retarder	2 ferro-electric liquid crystal retarders (FLCR)
Polarizer	1 beamsplitter polarizer
Grating:	
Grooves	316 grooves mm^{-1}
Blaze angle	63.4°
Grating size	370 mm × 190 mm

SOURCE: Author

4 GRIS observation and data reduction

We observed an emerging complex active region, NOAA 12552, with the GREGOR Infrared Spectrograph (GRIS) aboard the 1.5-meter GREGOR solar telescope on June 9, 2016. The center of the field-of-view (FOV) was located at 570" × 250". The seeing conditions were good during the full observation.

The time of observation started at 07:53:41 UT and extend to 09:02:35 UT. However, this observation presents only two image frames, the first one from 07:53:41 UT to 08:27:58 UT and the second one from 08:28:09 UT to 09:02:35 UT. So the total observation time interval was 68 minutes where the scanning took 34 min for each frame. The explanation for this long interval of only two frames is that GRIS scans slit by slit, with a total exposure time of 100 ms, with 10 accumulation, and performed it 700 times, that is the number of scans to compose the full scanned image used in this work.

The coordinates of the observed region in the solar disk are presented in Figure 4.1. The background image was obtained from the continuum observation of the Helioseismic and Magnetic Imager (HMI, Schou et al. (2012)) aboard the Solar Dynamics Observatory (SDO, Pesnell et al. (2012)) using the Virtual Solar Observatory (VSO) framework through the SolarSoft-Ware (SSW) tree. The arrow over the square border indicates the direction of the slit and the arrow outside the square represents the course of the scan. Details about the slit and scan size are presented below.

Before presenting all the Stokes observation for each spectral line, it is essential to compute the continuum image that is used as the reference for all the Stokes, as well as, gives us a good overview of the active region. The continuum was measured by doing the average of a spectral range in the Stokes I, where there are no absorption or telluric lines. The selected range is from 10835.8 Å to 10837.3 Å. The continuum is presented in Figure 4.2, where the axes are in pixel unit to show the image resolution of 476×700 pixels, where 476×350 pixels for each frame. The y$-$axis is the distance measured along the slit, and the x-axis is the distance along the scan. The involved AR is characterized by having a sunspot and several pores, with a large penumbra scattered among them. In this work, the Stokes I continuum is commonly used as a reference for all the Stokes, and it will be represented by I_c. The continuum spectra do not present a high spatial resolution due to the average of the spectrum.

Figure 4.1 - Position of the GRIS data in the solar disk. The background image is the continuum observation from the SDO/HMI. The initial slit position is centred in 570” × 250”. The arrow over the square border indicates the direction of the slit and the arrow outside the square represents the direction of the scan. The scanned image has as resolution of 64.26” × 47.25” (46.59 Mm × 34.26 Mm) with a spatial resolution of 0.135” (∼98 km).

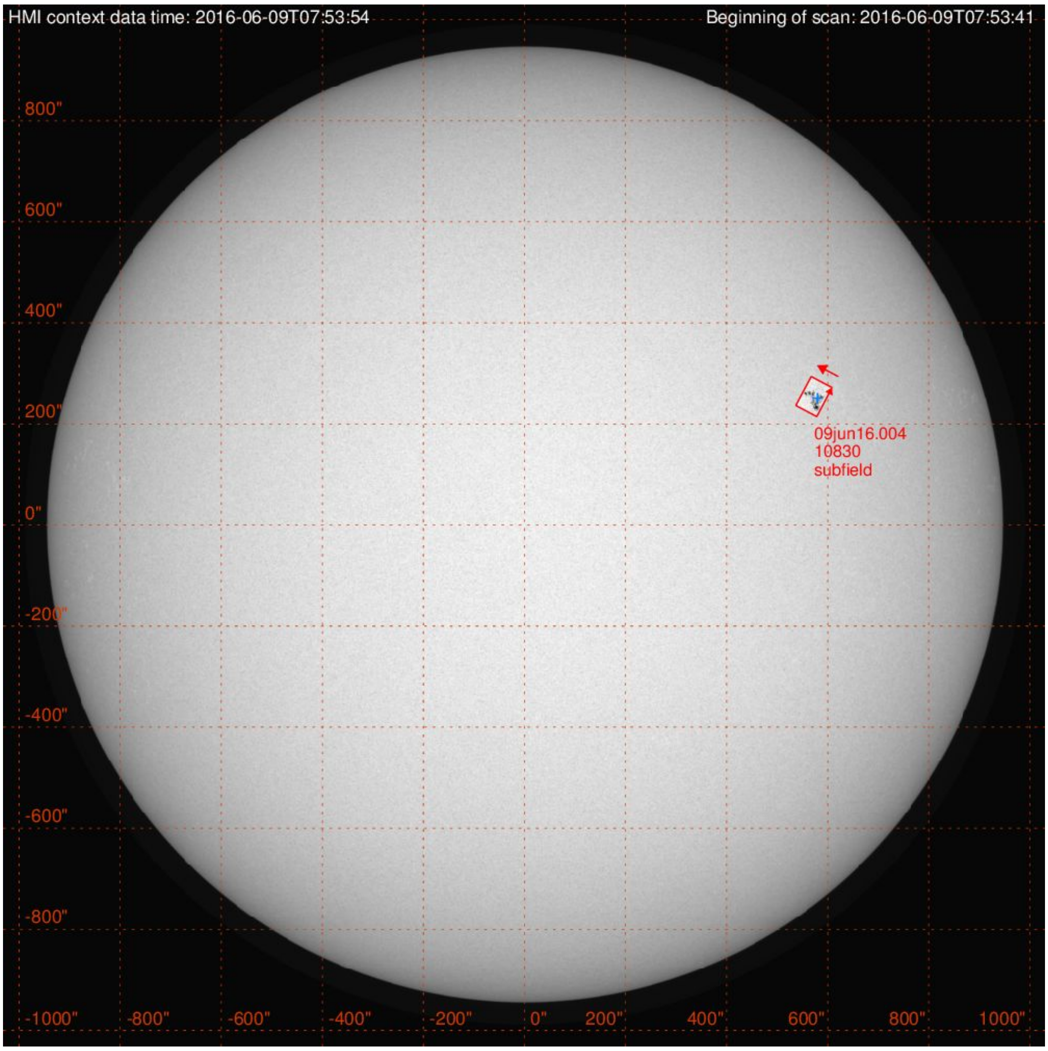
HMI context data time: 2016-06-09T07:53:54
Beginning of scan: 2016-06-09T07:53:41
800"
600"
400"
200"
0"
-200"
-400"
-600"
-800"
-1000"
-800"
-600"
-400"
-200"
0"
200"
400"
600"
800"
1000"
09jun16.004
10830
subfield

SOURCE: Author

Figure 4.2 - GRIS observation of the active region NOAA 12552 in the continuum. The intensity is an average of selected wavelengths where there is no absorption or telluric line. The axis are in pixel to show the image resolution of 476" × 700", where 476" × 350" for each frame. The $y-$axis is the distance measured along the slit and the $x-$axis the distance along the scan. The complex AR is characterized by having a sunspot with several pores, and a long penumbra scattered among them.

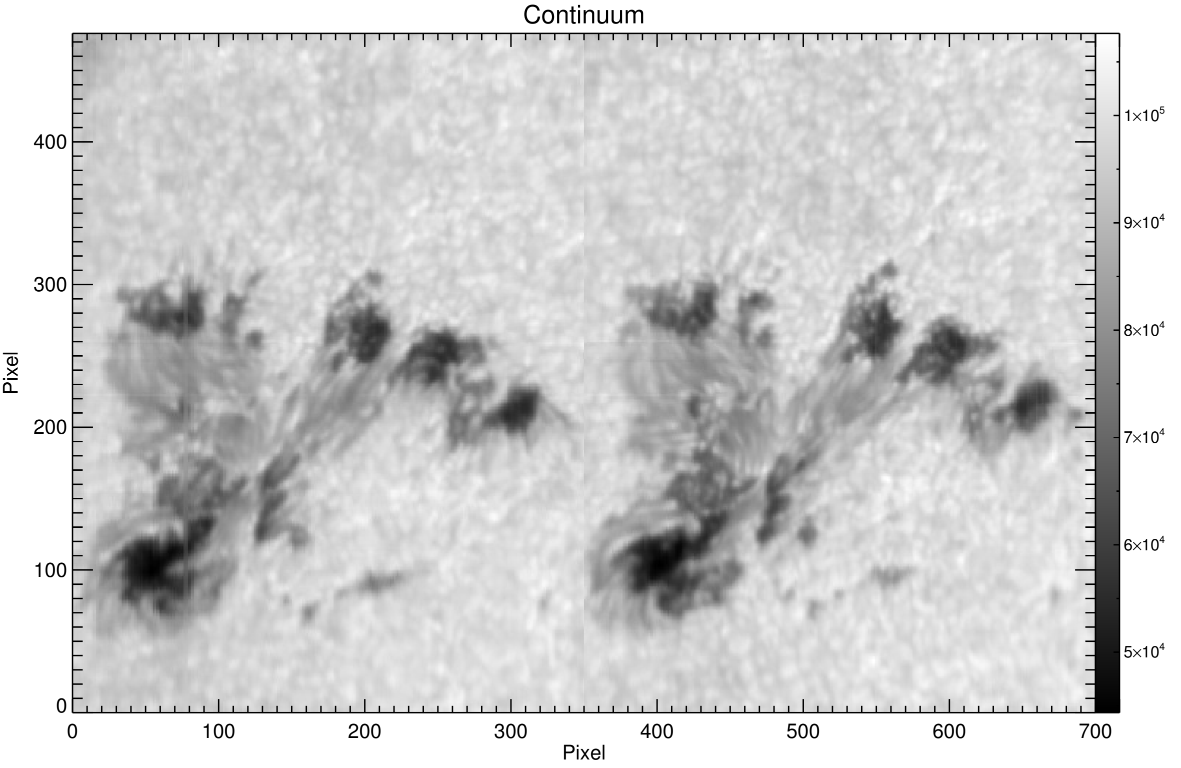

SOURCE: Author

In this work, we are focusing on analyzing the Si I 10827 Å for the photosphere and He I 10830 Å for the upper chromosphere. An advantage of GRIS is that the spectral profile for both lines is made at the same time, once the grating diffracts the incident light in the full spectrum and accumulate it in the CMOS sensor.

To observe the active region NOAA 10552, the first slit was centered at the position 570" × 250". Therefore, the distance between the slit center and disk center was

$r = \sqrt{x_{slit}^2 + y_{slit}^2} = 622.41$". The heliocentric angle (θ_H) can be determined as follow:

$$\theta_H = \arcsin\left(\frac{\sqrt{x_{slit}^2 + y_{slit}^2}}{R_\odot}\right), \tag{4.1}$$

where $R_\odot = 946.12$" is the solar radius in arcsec. Thus, the heliocentric angle for the slit center is 41.14° and $\mu = cos(\theta_H) = 0.75$.

The slit has a length equivalent to 476 pixels, and the scan was done along 700 positions. Thus, the image resolution is 476 × 700 pixels, where 476 × 350 for each frame. The distance between the center of two pixels in the $x-$ and $y-$ directions is 0.135" (∼98 km). Therefore, the field of view of each frame is given by 64.26"× 47.25" (46.59 Mm × 34.26 Mm). This spatial resolution is in the frontier of Stokes measurements for both photosphere and chromosphere.

The GRIS grating presents a spectral resolution of about 18.03 mÅ. The observed spectral range comprises the wavelength from 10823.695 Å to 10841.880 Å. Thus, there are 1010 equally spaced wavelengths along this range. Figure 4.3 shows the spectrum of one slit observation by GREGOR/GRIS in the center of the active region NOAA 12552. The y−axis is the distance measured along the slit in arcsecond and the x−axis is the wavelength observed with the grating. The vertical dark bands that seem to be oscillating are the absorption lines, where this movement is mainly due to the Doppler effect over the spectral line. In the other way, the vertical dark lines, that look static, are the H_2O telluric lines.

The spectrum presented in Figure 4.3 is the primary CMOS detection of the GREGOR/GRIS observation. After that, the polarimetric package needs to offset the retardance angle of the FLCR, in order to obtain a similar spectrum for the other Stokes. Since we have all Stokes spectrum for all the scanned slits, we can compute the Stokes maps.

Using the GRIS spectrograph, we observe a broad spectral range from 10823.695 Å to 10841.880 Å, that comprehends ten spectral lines and four telluric ones. The Table 4.1 presents the wavelength, $loggf$ and the effective Landé factor (g_{eff}) for each spectral line, as well as the wavelength of the four H_2O telluric lines.

Figure 4.3 - The spectrum of one slit observed by GREGOR/GRIS in the center of the active region NOAA 12552 for the unpolarized light (Stokes I). The spectral range comprises the wavelength from 10823.695 Å to 10841.880 Å. There are 1010 equally spaced wavelengths, with a spectral resolution of 18.03 mÅ pix^{-1}. The y−axis is the distance measured along the slit in arcsecond and the x−axis is the wavelength range. The vertical dark bands that seem to be oscillating are the absorption lines, where this movement is mainly due to the Doppler effect over the spectral line. On the other hand, the vertical dark lines, that look static, are the H_2O telluric lines.

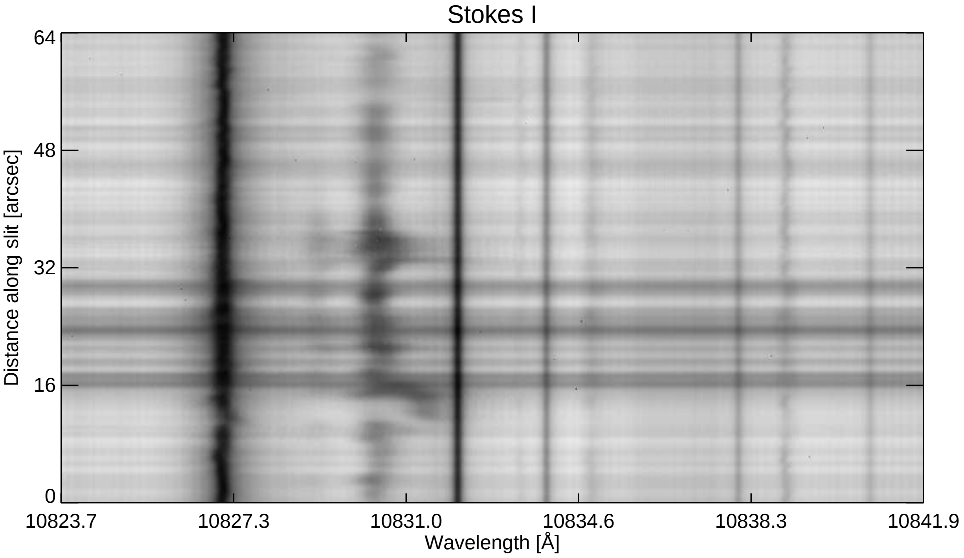

SOURCE: Author

Table 4.1 - Spectral lines in the wavelength range covered by GREGOR/GRIS

Line	*Wavelength [Å]*	*Log gf*	g_{eff}
Si I	10827.0877	0.185	1.5
He Ia	10829.0911	-0.745	2.0
Ca I	10829.3		1.0
He Ib	10830.2501	-0.268	1.75
He Ic	10830.3398	-0.047	0.875
H_2O Telluric	10831.626		
H_2O Telluric	10832.108		
Ca I	10833.382	-0.515	1.0
H_2O Telluric	10833.981		
Na I	10834.848	-1.800	1.03
Na I	10834.848	-0.500	1.07
Na I	10834.907	-0.650	0.9
H_2O Telluric	10838.034		
Ca I	10838.970	-0.033	1.5

SOURCE: Ramos et al. (2008)

In order to show the distribution and superposition of the spectral lines, we selected the Stokes I/Ic profile of two pixels and present it in Figure 4.4. The black line represents a pixel observed in a quiet region, with low polarization signal. Otherwise, the red dashed line is the profile for a pixel observed above the umbra of a sunspot. The splitting of the spectral lines is due to the Zeeman effect. There is a superposition between Ca I and the blue component of the He I and a blend between the transitions He Ib and He Ic, in the red component of the upper chromospheric line.

The Stokes map represent the polarization component of the measured light in the linear and circular polarizations. They have their singularities for each spectral line, e.g., for the photospheric line Si I 10827 Å line, the Stokes map observed is presented on Figure 4.5. The Stokes I/Ic, Q/Ic, U/Ic and V/Ic are the ratio between the Stokes maps and the continuum Stokes I (I_c) presented on Figure 4.2. The Stokes I, Q and U were obtained from the central line of the Si I 10827 Å, and the Stokes V from the red wing (shifted 0.2 mÅ from the central line). The high polarization signal in the photosphere can be seen in the Stokes Q, U and V, over the AR NOAA 12552, indicating the presence of magnetic field by the Zeeman effect.

Figure 4.4 - Stokes I profile for an observed pixel of the GRIS scann. The spectrum comprises wavelengths from 10823.695 Å to 10841.880 Å and includes ten spectral lines and four telluric. The black line describes a pixel observed in a quiet region, with low polarization signal and the red dashed line is the profile for a pixel observed above a sunspot umbra. The splitting of the spectral lines is due to the Zeeman effect. There is a superposition between Ca I and the blue component of the He I. The red bands are the spectral lines and the blue ones the telluric lines.

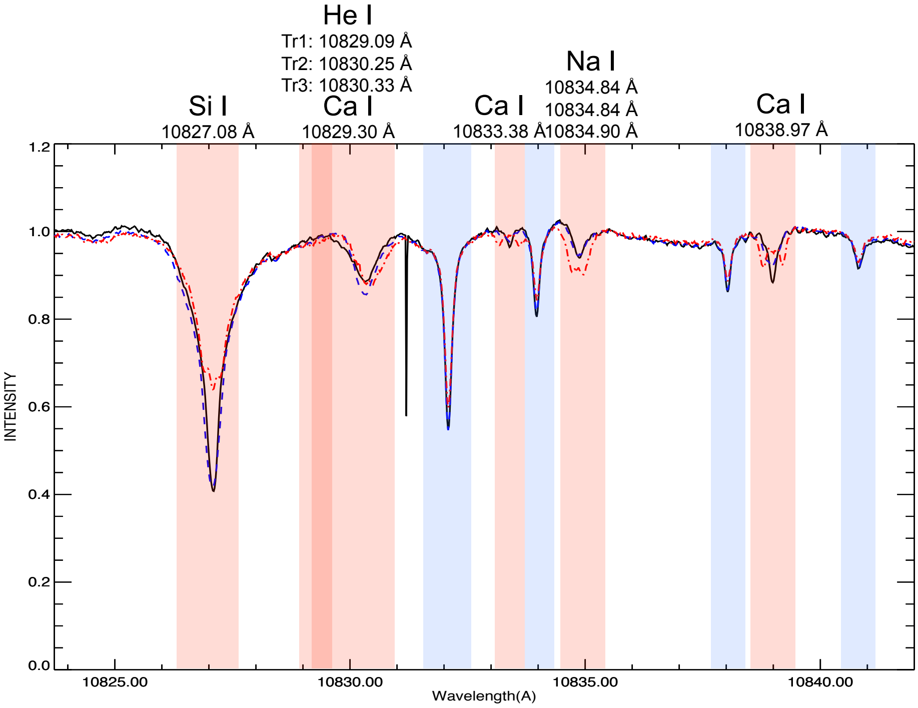

SOURCE: Author

Figure 4.5 - Stokes maps observed in the photospheric line Si I 10827 Å. The Stokes I, Q, U and V are in relation to the continuum Stokes I (I_c) presented on Figure 4.2. The y-axis represents the distance (in arcsec) along the slit and the x-axis along the scan. The Stokes I, Q and U were obtained from the center of the Si I 10827 Å line and the Stokes V from the red wing. We can note by the Stokes Q, U and V, a high polarization signal in the photosphere in the region of the AR NOAA 12552, indicating the presence of magnetic field by the Zeeman effect.

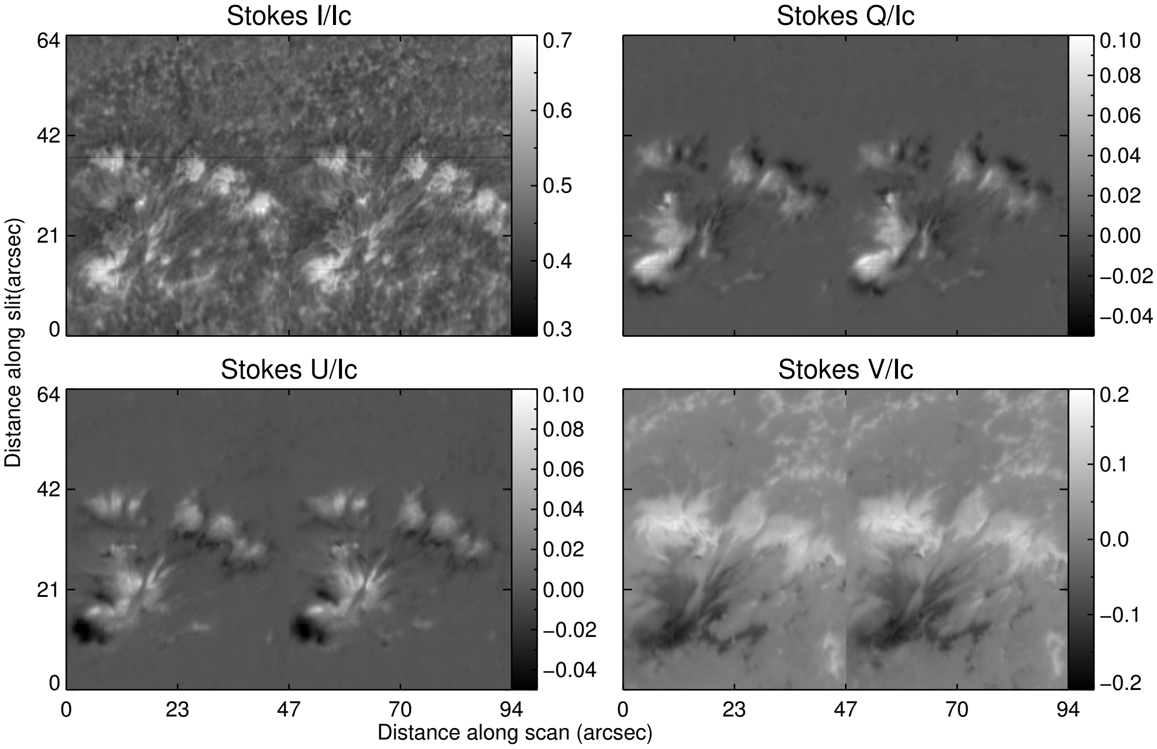

SOURCE: Author

The stokes maps were also computed for the chromosphere as presented by the Figure 4.6. The polarization signal seen in the chromospheric Stokes maps are less intense than in the photospheric line due to the lower magnetic field strength in the chromosphere. We can note in the Stokes I/Ic, dark regions in 45° with the x-axis, they are the filaments studied in this work. The filaments can be only seen in the chromospheric strong line (Figure 4.6) and not in the photosphere (Figure 4.5).

Figure 4.6 - Stokes maps observed in the Upper chromospheric line He I 10830 Å. The Stokes I, Q, U, and V are in relation to the continuum Stokes I (I_c) presented on Figure 4.2. The y-axis represents the Distance (in arcsec) along the slit and the x-axis along the scan. The Stokes I, Q and U were obtained from the central line of the He I 10830 Å and the Stokes V from the red wing. We can note by the Stokes Q, U and V, a high polarization signal in the chromosphere in the region of the AR NOAA 12552, indicating the presence of magnetic field by the Zeeman effect. The polarization signal seen in the Stokes maps are less intense than in the photospheric line due to the lower magnetic field strength in the chromosphere layer. We can note in the Stokes I/Ic, dark regions in 45° with the x-axis, they are the filaments studied in this work. The filaments can only be seen in the chromosphere strong line and not in the photosphere (Figure 4.5).

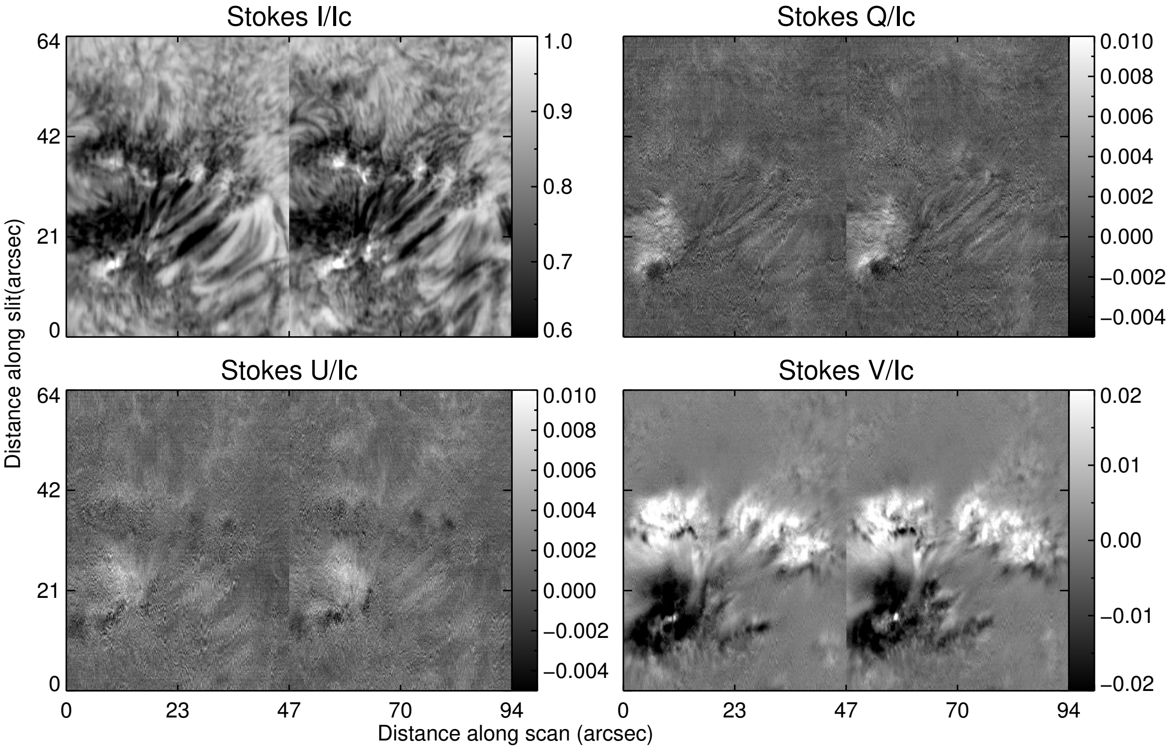

SOURCE: Author

A summary of all the main aspects of the GREGOR/GRIS observation used in this work is presented on Table 4.2.

Table 4.2 - Summary of the main aspects concerning the GRIS dataset used in this work.

Parameter	*Value*
Date	2016-06-09
Frames	2
Obs. Time (UT)	#1: 07:53:41 – 08:27:58
	#2: 08:28:09 – 09:02:35
Stokes	I, Q, U, V
Slit center X position	570”
Slit center Y position	250”
Heliocentric angle	41.14°
μ	0.75
Slit size (px)	476
Slit scans	700
Image Resolution (px)	476 × 350
Resolution	64.26” × 47.25” (46.59 × 34.26 Mm)
Spatial resolution	0.135” (97.88 km)
Spectral resolution	18.03 mÅ
Spectral range	10823.695 Å – 10841.880 Å
N spectral lines	10
N telluric lines	4
Exposure time	100 ms
Accumulation	10
B-angle	0.37°
P-angle	-12.01°
L-angle	319.21°

SOURCE: Author

4.1 Primary data reduction

The basic data reduction of the GREGOR/GRIS observational data is conducted on-site applying the GRIS data pipeline. The primary levels include the correction of the flat-field, subtraction of the dark current, crosstalk removal and calibration of the modulation matrix.

In order to perform the flat-field correction, a region of quiet-Sun and near to the solar center was scanned with 15 scan steps and 10 accumulations while the telescope was continuously changing the pointing.

The polarization observed by GRIS is computed through the modulation matrix obtained from the calibration of the polarization modulator. This calibration is performed by calculating the response of the polarimeter for each observed wavelength after producing light beams of known polarization states. It is achieved by including a calibration unit at one of the focus, which contains a linear polarizer and a FLCR. Thus, an observation similar to the usual is performed with the calibration unit in the beam path. The observed matrix is then used as the modulation matrix.

The determination of the Stokes parameter is affected by temporal variations coming from the seeing, that drives to false polarization signals. The effect of the seeing in the polarization signals is called seeing induced crosstalk (SIC). The SIC was analyzed in this work and corrected by using a statistical method explained in details in Schlichenmaier and Collados (2002).

4.2 Pre-processing

The data reduction was conducted on site by applying the GRIS data pipeline. The pre-processing is a step ahead of the data reduction. It includes many processes, and some of them are here described.

4.2.1 Wavelength Calibration

Performing the wavelength calibration of the GRIS dataset is a requirement to get the real spectral observation. To achieve an absolute wavelength calibration is however a challenging task that depends on the instrument or even the spectral window, it can be unreachable.

The GRIS observed spectrum holds numerous absorption lines and most of them can present wavelength shifts due to solar rotation, to the relative motion between Sun and Earth, waves, flows, convective blueshifts, as well as, many other effects generated by both the instrument and the terrestrial atmosphere. The first step consists in the selection of the solar quiet region.

4.2.1.1 Selecting the Solar quiet region

In order to achieve a proper wavelength calibration, some few steps need to be concluded. The first step is to select a region without induced wavelength shifts from active regions. The mean continuum solar profile is obtained by selecting a solar quiet region.

From the Figure 4.6 there are no clear regions which we would qualify precisely as quiet Sun. This feature is solved by characterizing the degree of polarization for each pixel (P_{tot}). Therefore, the (P_{tot}) was derived from the Stokes parameters as given by the Equation (2.7). The threshold for the magnetic activity classification was taken as the 3σ level of (P_{tot}).

$$P_{tot} = \frac{\sqrt{Q^2 + U^2 + V^2}}{I_c}, \tag{4.2}$$

where I_c is the continuum spectrum, Q and U are the maps for the Stokes Q and U observed in the center line and V in the red wing of the Stokes V. Figure 4.7 shows a map of the degree of polarization (P_{tot}) for the photospheric and chromospheric lines. Large regions with height polarization degree, followed by non-polarized regions can be identified in the map. To perform the calibration, we select a region with lower polarization for both photosphere and chromosphere, as presented in the white square. A concern with this method is that it consistently performs to select the internetwork regions, which indicate the mean profile may present a small offset due to convective blueshifts.

4.2.1.2 Wavelength scale

The wavelength profile observed by GRIS comprises the wavelength from 10823.695 Å to 10841.880 Å. In order to obtain the wavelength dispersion for the dataset, we made use of two H_2O telluric lines as the wavelength reference.

The first telluric line selected to perform the wavelength calibration, is the 10832.108 Å next to the red component of the He I 10830 Å triplet, and the other one is the 10833.981 Å placed between Ca I and Na I lines. The telluric wavelengths are described on Breckinridge and Hall (1973) with observation from the McMath Solar Telescope (PIERCE, 1964).

Figure 4.7 - Map of the degree of polarization (P_{tot}) for the (*Top*) Photosphere with the Si I 10827 Å central line for the Q and U and red wing for the stokes V. (*Bottom*) (P_{tot}) for the chromosphere with the He I 10830 Å triplet. The lower polarized region, selected to perform the continuum calibration, is shown by the white square.

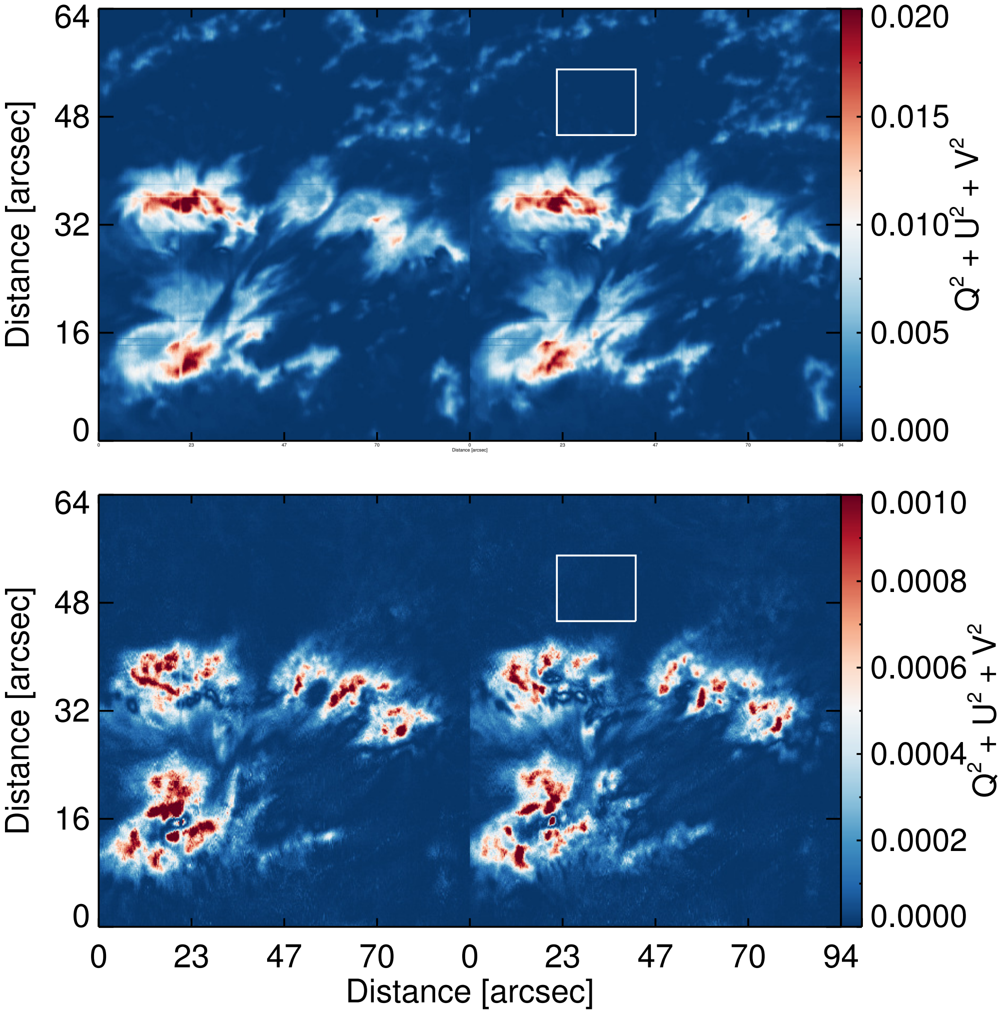

SOURCE: Author

Using the two telluric lines as a wavelength reference, we may perform the wavelength calibration. In Figure 4.8 we present the result of the calibration, with the x−axis presenting the real wavelength obtained from the presented procedure. The two red lines indicate the H_2O telluric lines used as the wavelength reference for the calibration.

A close comparison between the two telluric lines and the atlas profile of the Fourier Transform Spectrometer (FTS) (NECKEL; LABS, 1984) provided a wavelength dispersion of 18.03 mÅ.

According to Breckinridge and Hall (1973), the wavelength estimations for three water lines around 10830 Å and those at 10832.108 Å, 10833.981 Å have errors less than 1 mÅ and thus provide an excellent calibration of wavelength in the vicinity of the He triplet. The 1 mÅ error matches to a Doppler velocity of 30 ms^{-1} which means an excellent accuracy for both photospheric and chromospheric velocities.

4.3 Comparison to FTS atlas

To perform the pre-processing, an average profile was computed from all the spectra in the quiet Sun (QS). Then, we compare the QS spectrum to the FTS atlas developed by Livingston and Wallace (1991). The idea is to obtain the best fit between the QS profile and the FTS atlas. To eliminate the spectral lines, we selected all measurements from the QS spectrum having FTS atlas intensity between 0.99 and 1.01. We then fit the data with a polynomial curve. The polynomial order was allowed to vary, then we chose the best fit.

We approximated the point spread function (PSF) of GRIS by using the method of Prieto et al. (2004) and Solana et al. (2007). Aiming to perform it, we assumed that the PSF of the FTS is a delta function and then degraded its spectrum until it fits the QS profile recorded by GRIS. According to Franz et al. (2016), the QS spectra from GRIS (I^{GRIS}) is given by

$$I^{GRIS} = I^{FTS}_{convol} = \frac{I^{FTS} + \mathcal{S}}{1 + \mathcal{S}} \otimes \mathcal{G}(\omega), \tag{4.3}$$

where I^{FTS} is the QS spectra from FTS, $\mathcal{S}$ is the fraction of spectral scattered light and $\otimes$ is the convolution. The spectral PSF is assumed to be a Gaussian ($\mathcal{G}$) and ω the full width at half maximum (FWHM). We then obtained the best agreement between GRIS measurement and degraded FTS atlas.

Figure 4.8 - Wavelength scale calibration based on two telluric lines. In black the mean quite solar profile and in red the telluric lines 10832.108 Å and 10833.981 Å, described by “Telluric 10832” and “Telluric 10834”, respectively. The green regions denote the selected points to normalize the continuum. A relation between the two telluric lines and the atlas profile of the Fourier Transform Spectrometer resulted in a wavelength dispersion of 18.03 mÅ. The $y-$axis was drawn subsequent to the wavelength scale calibration.

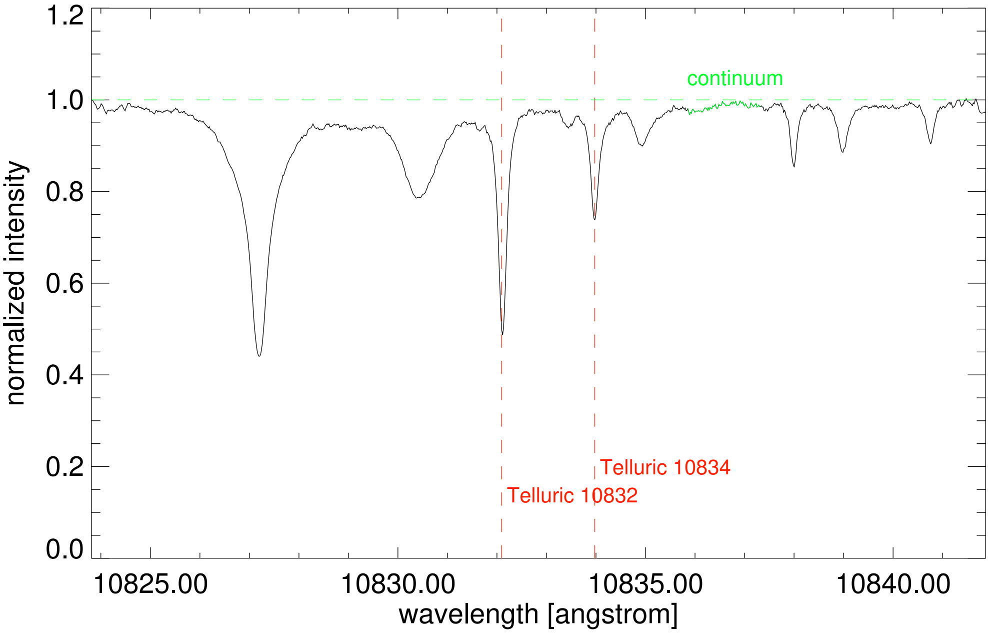

SOURCE: Author

4.4 Noise level

The determination of the noise level, by using the Root Mean Square (RMS) for each Stokes parameter, is crucial to determine which phenomena can be observed, as well as, to set the operational mode of the spectropolarimeter.

There is a tradeoff between the solar evolution speed and the RMS noise. The minimum and maximum integration time of each slit observation depend on the spatial sampling, the evolution speed ($\sim$7 kms^{-1} in the photosphere and up to $\sim$35 kms^{-1} in the chromosphere), the flux of photon (photon budget), and the RMS noise. In order to verify the quality of the Stokes data, the RMS noise measurement of the Q, U, and V is performed.

To compute the RMS noise, we first need to select a quiet solar region in the stokes maps. To perform the best selection we picked 100 pixels with the lowest degree of polarization given by the Equation (2.7). Then, we compute the RMS noise for the range from 10823.713 Å to 10824.055 Å of each Stokes spectral profile. This range means a series of 20 wavelengths, at the beginning of the spectrum observed by GRIS, and represent the main wavelength range without any spectral absorption or telluric line.

The computed RMS noise was $1.10 \times 10^{-3} I_c$ for the Stokes Q, $1.18 \times 10^{-3} I_c$ for the Stokes U, and $1.19 \times 10^{-3} I_c$ for the Stokes V.

Depending on the inclination of the magnetic field to the line-of-sight (LOS), the Stokes Q and U can present a weak signal level (in the order of 10^{-3}), that can interfuse with the noise signal. Based on that, we need to improve the signal to noise ratio (SNR) by reducing the RMS noise.

There are many ways to reduce the RMS noise by changing the spectropolarimeter mode, like increasing the integration time, exposure and accumulation. However, it is not feasible once the observation was already done. We can improve the RMS in a dataset, like performing an image binning or employing a low-pass filter. However, both binning and filter can directly affect the spatial resolution of the data. An estimation of the “minimum distinguishable spatial resolution”, by using the power spectrum, is presented in the next section.

4.5 Power Spectrum

According to the Table 4.2, the spatial resolution of the GRIS spectrograph is 0.135”. It means that the distance between the center of two pixels in the x− or y−direction is 0.135” ($\sim$98 km). However, due to the seeing, relative motions, and convective blueshifts, the size of the minimum discernible structure is not well represented by this value.

In order to compute the “real spatial resolution”, we need to observe the power spectrum of the observed data. The essential idea behind this is to calculate the Fourier power spectrum of the spatial frequencies and to discard the frequencies where there is no more clear information in the data (only white noise).

Given a specific wavelength and Stokes parameter, we calculate the Fourier power along each slit for all the 700 slits. Then, we did the average of all these power spectra and obtained the final Fourier power spectrum.

Once we have the Fourier power spectrum, we can discriminate where the power is equivalent to the white noise and then calculate the size of the minimum discernible structure.

Figure 4.9 shows the Fourier power spectrum vs. (spatial frequency)$^{-1}$ for all the Stokes of the photospheric line. For the Stokes I, Q and U, the power spectrum was performed with the center of the Si I 10827 Å line, and with the red wing for the Stokes V. From the power spectrum, we determine the size of the minimum discernible structure, that was 0.40” for the Stokes I, 0.55” for Q and V, and 0.52” for the Stokes U.

The Fourier power spectrum for the chromospheric line is presented on Figure 4.10. The size of spatial resolution observed was 0.47” for the Stokes I, 0.45” for Q and U, and 0.52” for the Stokes V.

4.5.1 Seeing condition

The Earth’s atmosphere produces irregular motion in the image observed by the telescope. Fluctuations in the refraction index along the Earth’s atmosphere produce image degradation. This effect is usually called *seeing* and restricts the telescope resolution (ÖZIŠIK; AK, 2004). The Fried parameter r_0 (FRIED, 1965) describes the seeing effect and can be measured from the image motion in a small telescope (TOKOVININ, 2002).

Figure 4.9 - Fourier power spectrum of the spatial frequencies for the Stokes I, Q, U and V for the Si I 10827 Å line. The displayed spectrum is the average of all the spectra along the slits. The red dashed line is the equivalent of white noise, where every spatial frequency has the same power. The blue dashed line determines the size of the minimum discernible structure, that was 0.40" for the Stokes I, 0.55" for Q and V, and 0.52" for the Stokes U.

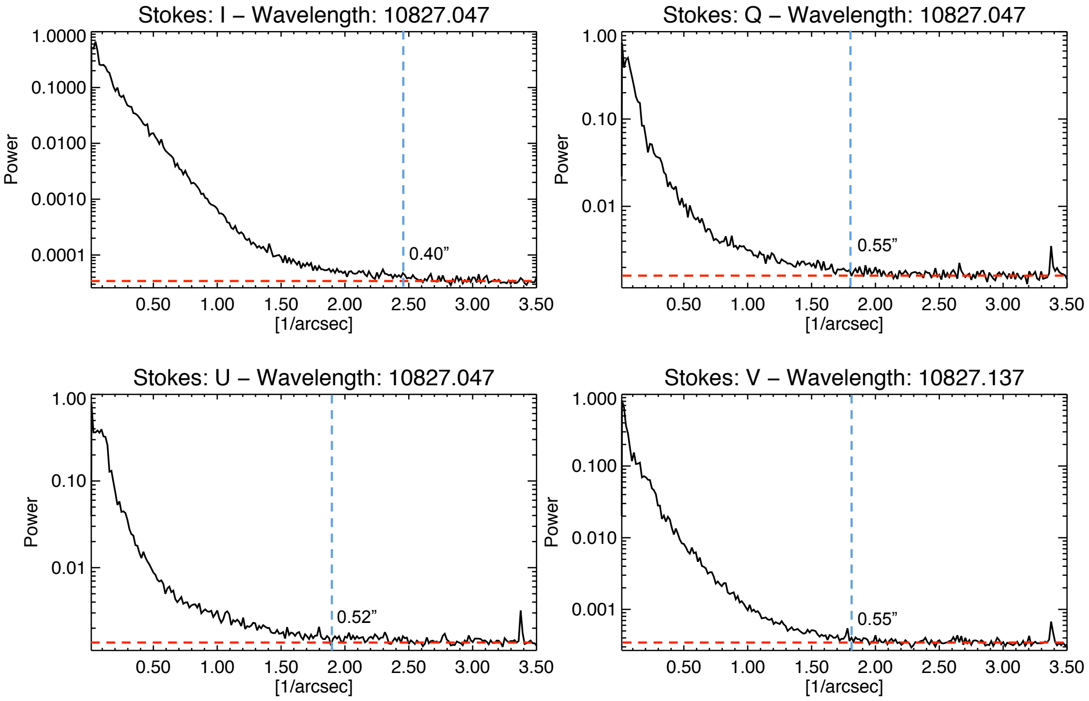

SOURCE: Author

Figure 4.10 - Fourier power spectrum of the spatial frequencies for the Stokes I, Q, U and V for the He I 10830 Å line. The spectrum is the average of all the spectra along the slit. The red dashed line is the equivalent of white noise, where every spatial frequency has the same power. The blue dashed line determines the size of the minimum discernible structure, that was 0.47" for the Stokes I, 0.45" for Q and U, and 0.52" for the Stokes V.

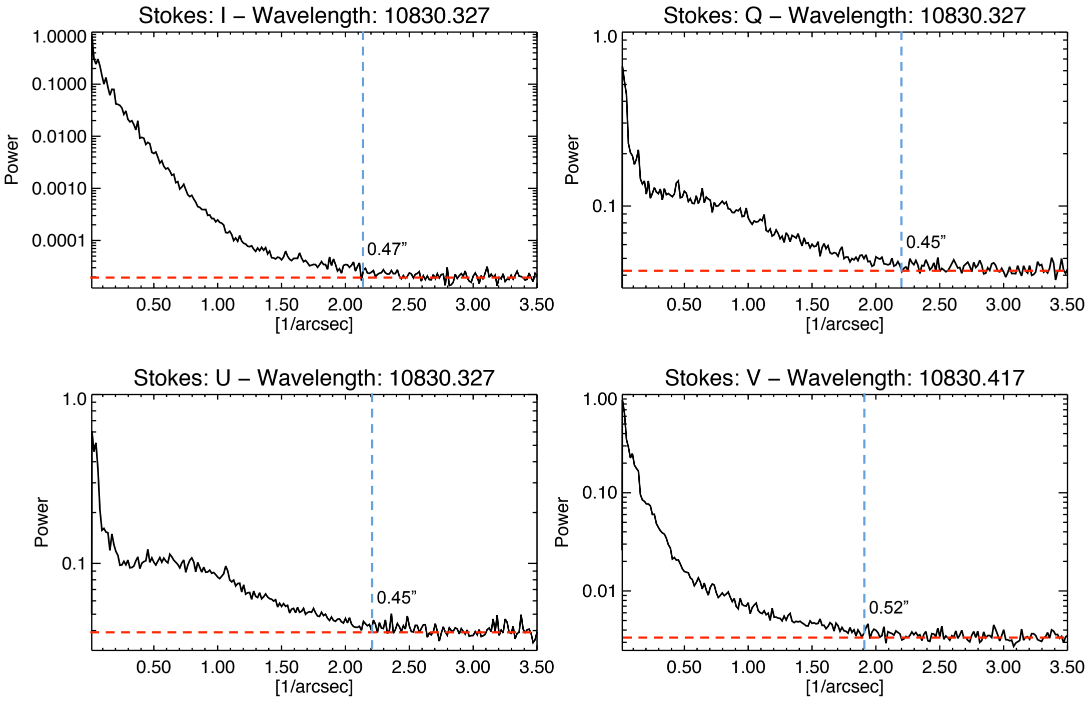

SOURCE: Author

The differential image motion produced by turbulence can be measured with a DIMM (Differential Image Motion Monitor) (SARAZIN; RODDIER, 1990). The Solar – Differential Image Motion Monitor (S-DIMM) is based on the DIMM, and it is used for solar observations by attaching a solar filter to it. Differential motions of the solar limb are observed with the S-DIMM in order to calculate the Fried parameter (BECKERS, 2001).

The Fried parameter, is a measure that manages the coherence diameter of the atmosphere (HUNT AMBER L. ILER, 2018). It can be given by

$$r_0 = \left(1.67\lambda^{-2}\sec\zeta\int_0^{\infty} C_n^2(z)dz\right)^{-3/5}, \tag{4.4}$$

where λ is the wavelength, ζ is the zenith angle and $C_n^2(z)$ is the turbulence profile along the altitude z. The r_0 is inversely proportional to the integral of the turbulence profile along the LOS through the atmosphere. Therefore, a larger Fried parameter corresponds to a smaller distortion being imposed on a focal plane image by the turbulent atmosphere. In other words, a larger Fried parameter means better seeing condition.

The Fried parameter r_0 over the scan number is presented on Figure 4.11. The x$-$axis presents the 700 scans of the full observation. We can note the seeing condition is better in the beginning of the observation. The $\langle r_0 \rangle = 12.04$ cm for the first frame and $\langle r_0 \rangle = 9.50$ cm for the second, so the first frame has a better seeing. Figure 4.12 presents the histogram of the relative frequency distribution of Fried parameter. The mean r_0 is 10 cm, it means the seeing condition can be considered good along the observation.

Figure 4.11 - Fried parameter r_0 observed along all the 700 slit scans. The first scan started at 07:53:41 UT and last 09:02:35 UT. We can note the r_0 reaches values larger than 15 cm in the beginning of the observation, indicating a better seeing condition in the first frame. The seeing can be consider good along all the observation.

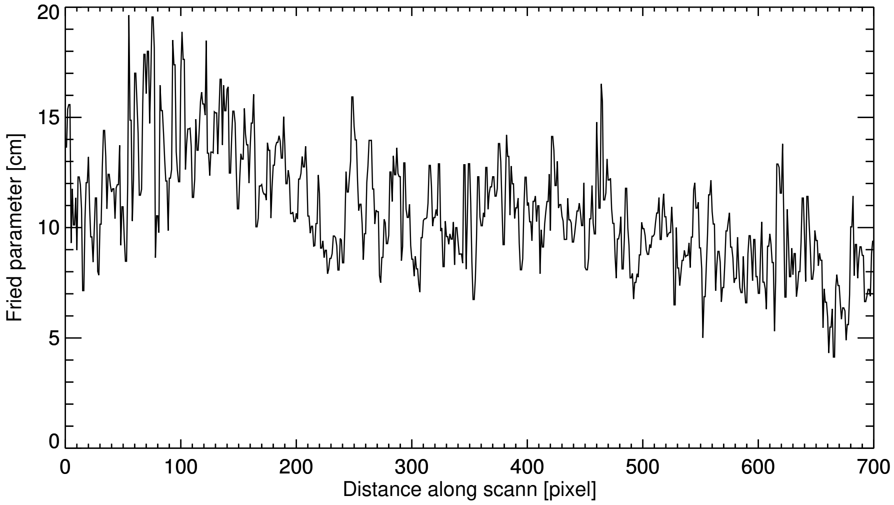

SOURCE: Author

Figure 4.12 - Histogram of the relative frequency distribution of the Fried parameter. The $\langle r_0 \rangle = 10$ cm for our observation dataset.

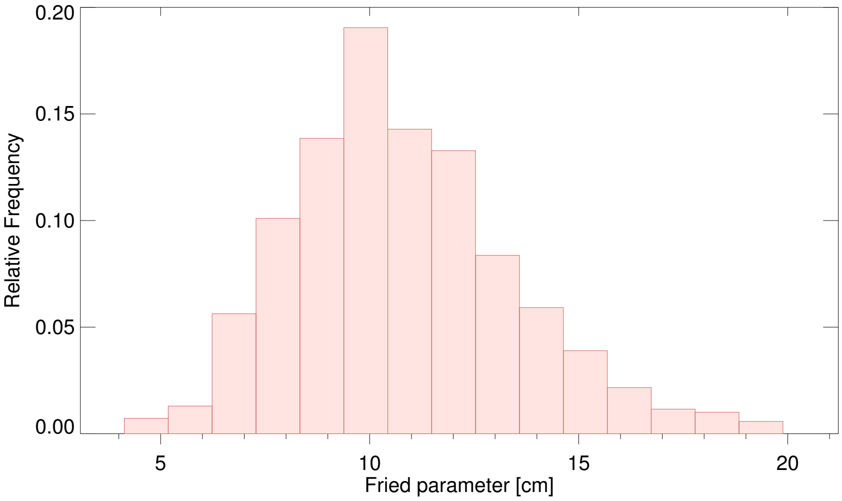

SOURCE: Author

5 Arch filament system and temporal evolution

5.1 Description of the filaments

The arch filament system studied in this work consists of filaments over the NOAA AR 12552 observed with full Stokes for the He I 10830 Å line. The filaments are visible in the Stokes I, that are taken in relation to the continuum (Ic, Figure 4.2) in order to enhance only the chromospheric structures.

Some of the filaments visible in the upper chromosphere are presented in Figure 5.1 and highlighted by the yellow contours. The red lines present the umbral region and the white dashed line the penumbral regions both selected from the continuum measurement (Figure 4.2), computed in the previous section.

The top panel background of Figure 5.1 shows the Stokes I/Ic map where the filaments are distinguishable from the surrounding area. The bottom panel background is the Stokes V/Ic where we can see the different polarities of the umbral regions.

From the Stokes V/Ic we can conclude that the filament follows the field line that connects inverse polarities, crossing the PIL line (described in the Section 7.4). We can note that most of the filaments also follow the field line that connect the leading sunspot (presented with the letter L in the first panel) to the trailing sunspot (letter T in the first panel). The leading is positioned in the dark region of the Stokes V (negative) and the trailing in the bright region (positive). However, it does not mean any magnetic polarity, once the same Stokes V map took from the blue wing would present an inverse color.

In Figure 5.1 the leading sunspot seems to be more to the west than the trailling, however it is due to the GREGOR/GRIS scanning, as presented in the Figure 4.1. The correct position would be like the one taken from the HMI in Figure 5.3 of the Section 5.2.

In order to investigate the physical properties of the filament over the active region, we determine the length, width, and distance between the filaments. The distances are computed using the relation between spatial resolution units, where 1 Mm $\approx$ 0.735" $\approx$ 0.098 pixels. The width is determined taken the average width along the filament length.

Figure 5.1 - Filaments over the upper chromosphere. (*Top*) The background is the Stokes I/Ic map, integrated 0.4 Å around the He I 10830 Å central line. (*Bottom*) Stokes V/Ic map integrated 0.4 Å in the red wing of the He I 10830 Å line. The yellow contours outline the selected filaments. The red lines represent the umbral regions and the dashed white line delimits the penumbral area obtained from the continuum map (Figure 4.2).

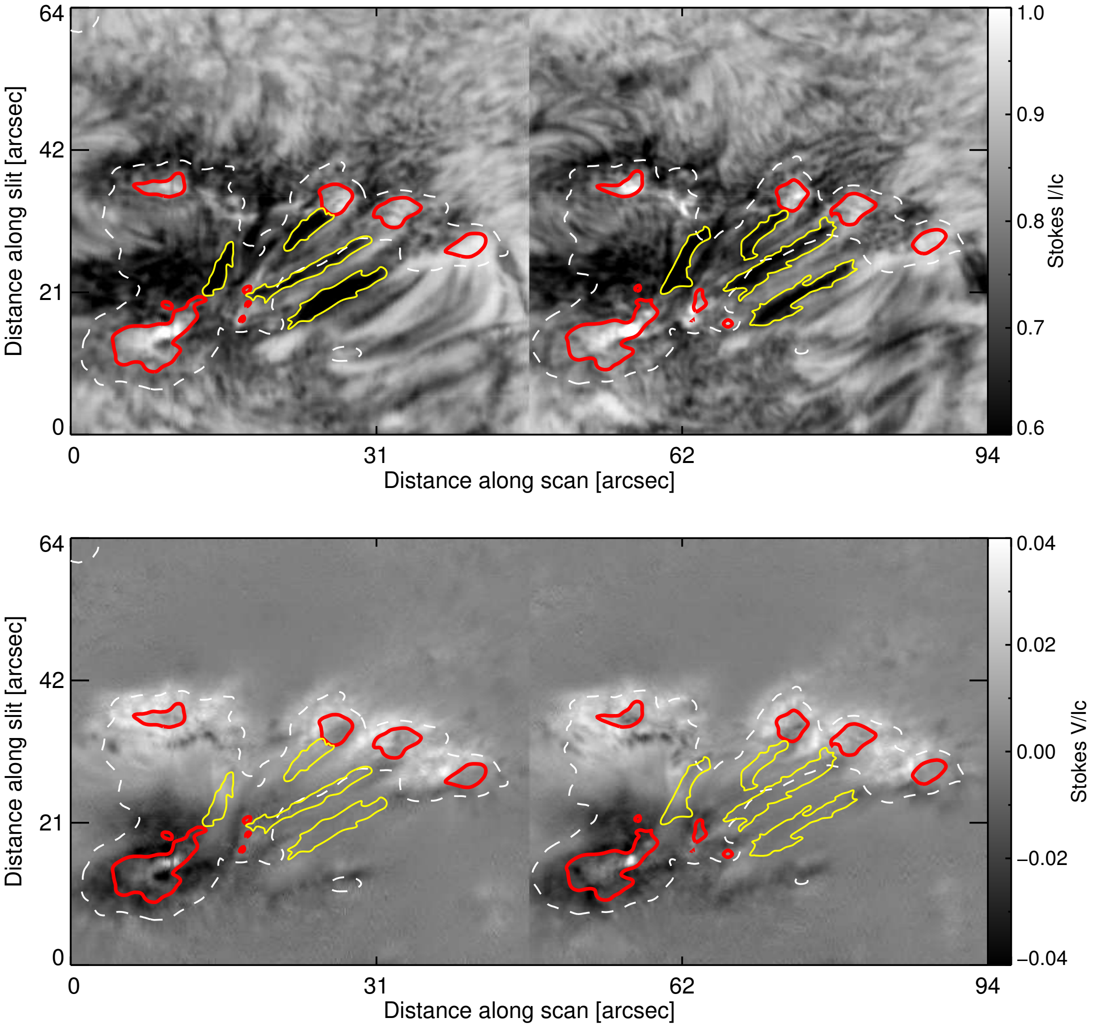

SOURCE: Author

Figure 5.2 - Geometry and distances of the filaments previous presented in Figure 5.1. The filaments are represented as the red contours with the number from 1 to 4 (in red). The width, length, and distances between filaments are displayed in Mm (1 Mm = 1.34”).

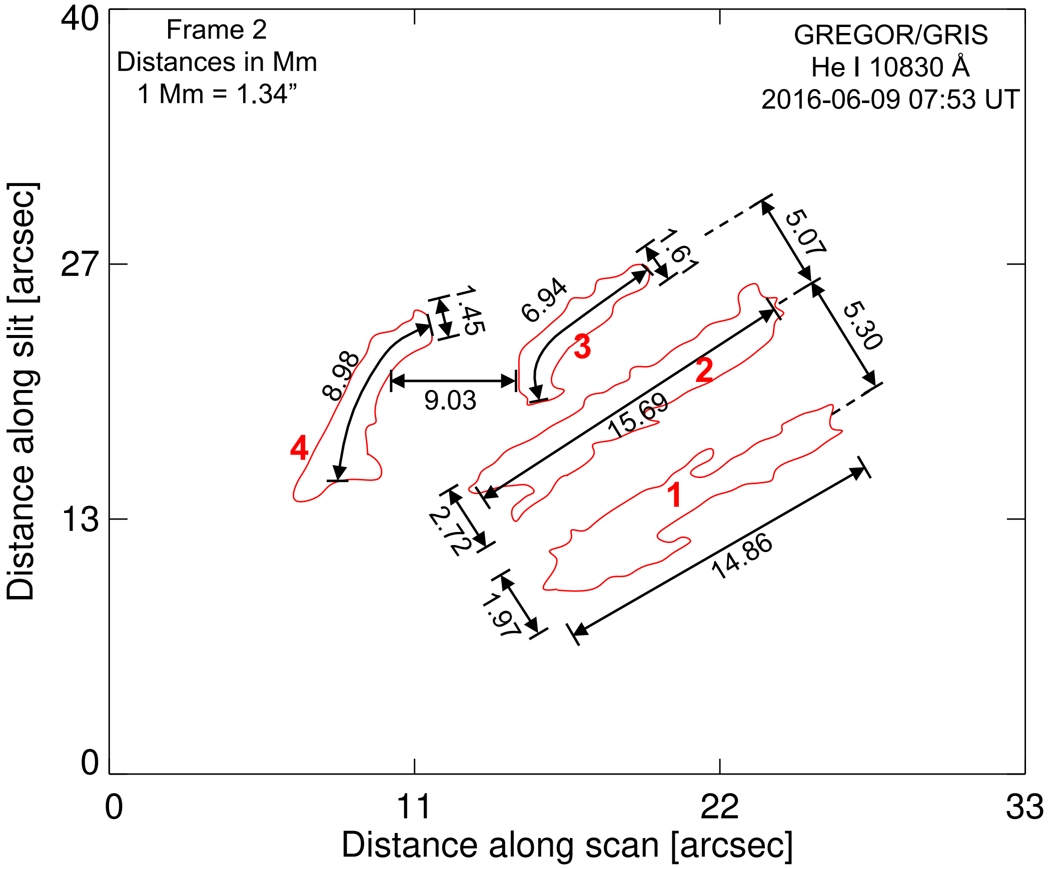

SOURCE: Author

Figure 5.2 presents the distances and distribution of the filaments previous presented in Figure 5.1. The filaments are represented as the red contours with the number from 1 to 4 (in red). The width, length, and distances between filaments are displayed in Mm. The filament length comes from 7 Mm to almost 16 Mm, the width from 1.45 Mm to 2.72 Mm and the distances between the filaments are from 5 to 9 Mm. The physical distances were computed for both frames, a description of the results is presented in Table 5.1.

Table 5.1 - Length, width, and distances between the filaments in the two frames observed with GRIS in the He I 10830 Å line

Filament	*Frame 1*	*Frame 2*
Filament 1:		
Length (Mm)	13.70	14.86
Width (Mm)	2.13	1.97
Filament 2:		
Length (Mm)	16.19	15.69
Width (Mm)	1.59	2.72
Filament 3:		
Length (Mm)	6.94	8.07
Width (Mm)	1.59	1.62
Filament 4:		
Length (Mm)	8.04	8.98
Width (Mm)	1.33	1.45
Distance fil. 1 and 2 (Mm)	6.10	5.30
Distance fil. 2 and 3 (Mm)	6.81	5.07
Distance fil. 3 and 4 (Mm)	9.69	9.03

SOURCE: Author

Many studies have been dedicated to investigating the physical properties of the filaments, like their length, height, width, and magnetic field strength. The typical length for the QS filaments is between 60 and 600 Mm (TANDBERG-HANSSEN, 1995), with an average of 200 Mm (ENGVOLD, 2015), however, can reach more than 600 Mm, as observed by Sankarasubramanian et al. (2005) and Kuckein et al. (2016). By contrast, the length of the AR filaments does typically not exceed 30 Mm (MURDIN, 2002). According to Priest (2014), the average length of the AR is 10 Mm. In the present study, the filament observed in the He line presents a length from 7 Mm to almost 16 Mm.

Yan et al. (2015) observed QS filaments, with width range from about 2.3 Mm to 3.3 Mm and average of 2.9 Mm. According to Priest (2014), the average thickness of the QS filament is from 3 to 10 Mm. In this work, we found that the filaments have a width values from 1.33 to 2.72 Mm, with an average of 1.8 Mm. Therefore, the average width, based on our filaments observation, is from 1.6 to 5.5 times narrower than the QS filaments.

5.2 Temporal evolution of emerging magnetic flux

The extensive time to conclude a cycle operation for the GRIS slit scan take it a disadvantage for the spectrographs in the temporal cadence. For the data presented in this work, there are only two frames, representing only two time instants.

To support the investigation of the transient evolution of the emerging magnetic flux, the dataset was based on time series of the HMI magnetograms aboard the Solar Dynamics Observatory (SDO, Pesnell et al. (2012)). The Helioseismic and Magnetic Imager (HMI, Schou et al. (2012)) is designed to measure the Doppler shift, intensity, and vector magnetic field at the solar photosphere using the Fe I 6173 Å absorption line (NORTON et al., 2006). The HMI instrument operates as a filtergraph, where it takes a sequence of images at distinct wavelengths and polarizations that are then combined to determine the solar physical parameters. It operates in contrast with spectrographs, (e.g., GRIS), that take spectra while scanning over the field of view.

The HMI time series was obtained from the Joint Science Operations Center (JSOC) based using the Virtual Solar Observatory (VSO) framework through the SolarSoftWare (SSW) tree. The time interval of the selected dataset comprehends 48 h, from June 6, 2016 at 07:53 UT to June 10, 2016 at 19:52 UT, within a cadence of 6 min.

The acquired data for the analysis were the continuum and the LOS-magnetic field. Both images have a 4096 × 4096 image resolution, 0.504" spatial resolution and the LOS-magnetic field has a precision of 10 G.

The data images were compensated by the solar differential rotation using the expansion

$$\omega = A + Bsin^2\varphi + Csin^4\varphi, \tag{5.1}$$

where φ is the latitude. We made use of the rotation coefficients obtained by Howard et al. (1990) (where $A = 2.894 \pm 0.011$, $B = -0.428 \pm 0.070$, and $C = -0.370 \pm 0.077\ \mu rad.s^{-1}$). The reference time for compensation of all the images is June 8, 2016 at 07:52 UT, beginning time of the first GRIS slit scan.

In order to compute the magnetic flux over the AR 12552, we did an image cut out to extract the region-of-interest (ROI) that cover the AR. The ROI is presented in Figure 5.3 (as a blue rectangle) over the HMI continuum map (*top*) and LOS-magnetic field map (*botton*). The ROI has a 59 by 63 arcsec. and encompasses the

AR as a whole for all the time interval cited above. The red rectangle in Figure 5.3 is the GRIS field-of-view (FOV) acquired with the full slit scan. Both images were observed at 07:52 UT on June 9th, 2018, at almost the same time as the GRIS scan (at 07:53 UT). The GRIS scan starts on the left and ends in the right of the red rectangle, producing a mirrored image of that shown by the HMI.

An analysis of the temporal evolution of the HMI continuum shows a progression of the emerging magnetic flux in the AR 12552, starting from two sunspots and few pores (first frame) to a very complex structure with extended penumbra and light bridges (last frame). The sunspot area (umbra + penumbra) grows about three times its size. Figure 5.4 shows the evolution of the of this AR in six time frames, the first 24 h before and the last almost 24 h after the GRIS observation.

The maps of magnetic field evolution give us a foresight of both negative and positive magnetic flux increases. The Figure 5.5 shows the evolution of the LOS-magnetic field in six time frames during 48h. The black and white are negative and positive polarities, respectively.

Once we have the magnetic field map over time as displayed in Figure 5.5, we can calculate the time evolution of the magnetic flux. Therefore, we integrate the magnetic field throughout the restricted area in the ROI (blue rectangle in Figure 5.5). The integration was computed by splitting the positive and negative magnetic fields in order to obtain both magnetic fluxes. Figure 5.6 shows the evolution of the positive and negative magnetic fluxes in the ROI area for a period of 48 h. The magnetic fluxes increase along time indicating the emerging magnetic flux in the photosphere, building a more complex AR.

5.2.1 General description of the ROI

The GRIS observation was made at the time that most of the magnetic flux had then emerged in the photosphere, as shown by the dashed line in Figure 5.6. Therefore, the results of our study lead us to observe and analyze the inquiries related to the flux emergence in our region of interest.

Based on the HMI LOS-magnetic field map, the AR12552 becomes visible at around 06:00 UT on June 7th, 2016 emerging from two pores with reverse polarities. The AR vanishes entirely in the solar limb at around 01:00 UT on June 13th, 2016.

Figure 5.3 - Overview of the AR 12552 at 07:52 UT on June 9th, 2018, observed with the SDO/HMI. In the (*Top*) The continuum image where we can see the complex AR including umbra, penumbra, pores, and light bridges. In the (*Botton*) The LOS-magnetic field, where the black and white are negative and positive polarities, respectively. The blue rectangle designated the region-of-interest (ROI) covering all the AR and used to compute the magnetic flux. The images were observed nearly the GRIS scan start time (07:53 UT). The red rectangle is the GRIS field-of-view (FOV) acquired from the full slit scan, starting from the left to right of the rectangle.

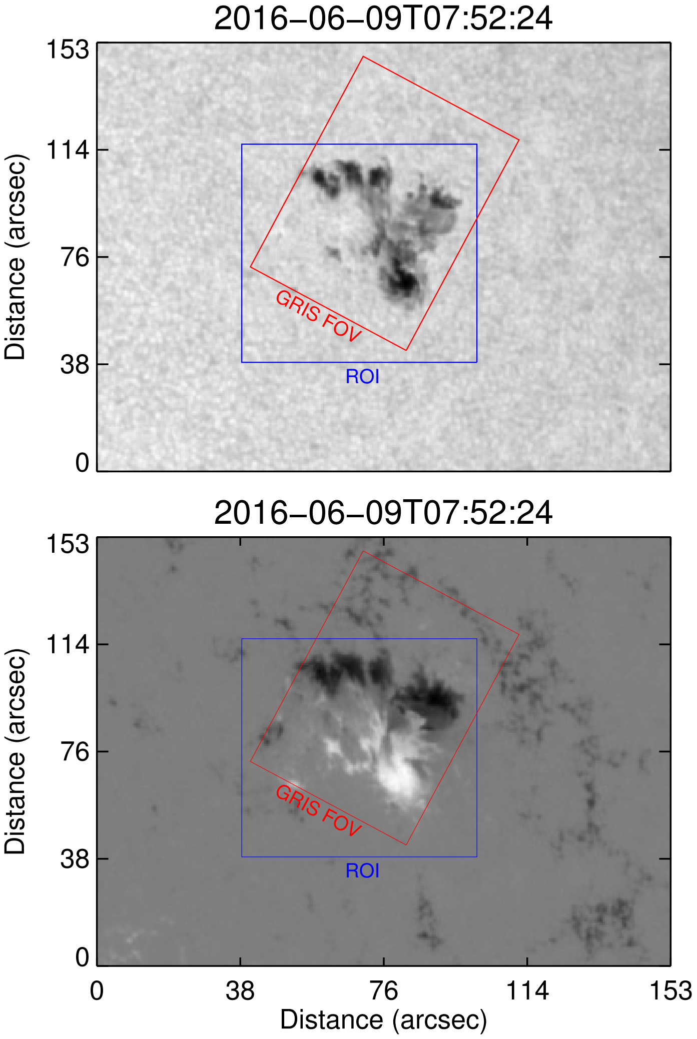
2016–06–09T07:52:24
153
114
76
38
0
Distance (arcsec)
GRIS FOV
ROI
2016–06–09T07:52:24
153
114
76
38
0
Distance (arcsec)
GRIS FOV
ROI
0
38
76
114
153
Distance (arcsec)

SOURCE: Author

Figure 5.4 - Evolution of the emerging magnetic flux in the AR 12552 in the HMI continuum, presented in six time frames, the first 24h before and the last almost 24 h after the GRIS observation (between the 3rd and 4th frame). We can note the evolution starting from two sunspots and few pores ($first frame$) to a very complex structure with extended penumbra and light bridges ($last frame$).

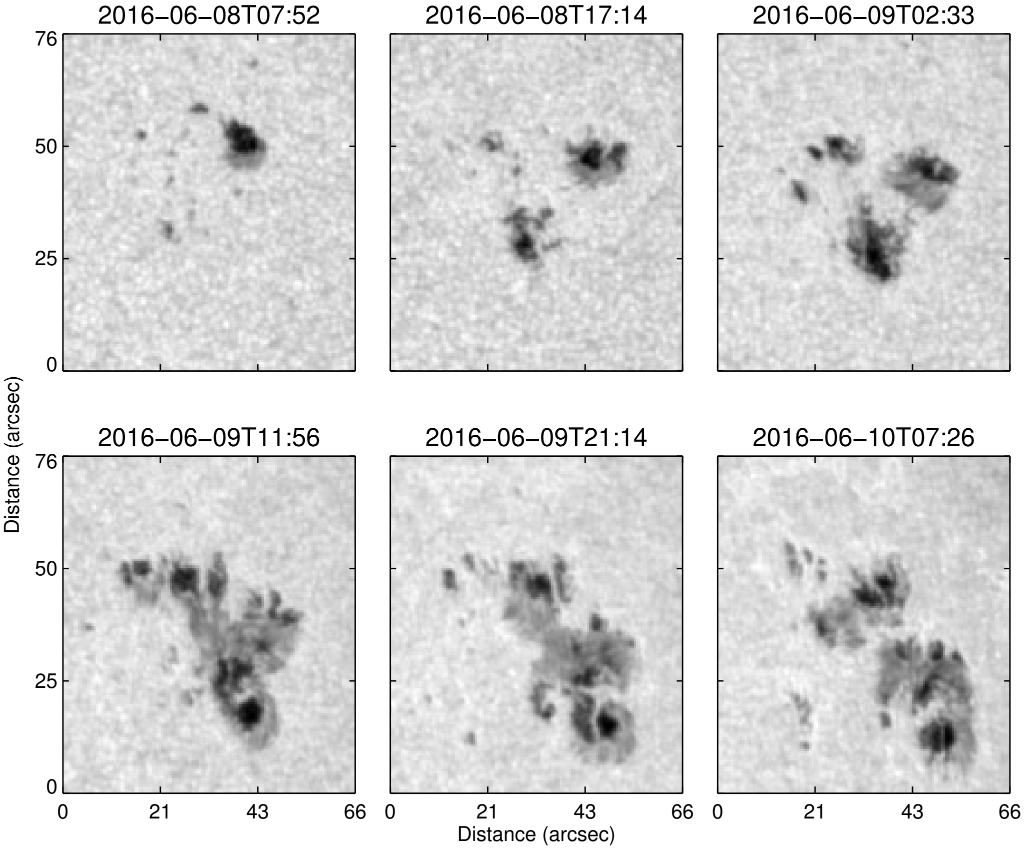
2016−06−08T07:52
2016−06−08T17:14
2016−06−09T02:33
2016−06−09T11:56
2016−06−09T21:14
2016−06−10T07:26
Distance (arcsec)
76
50
25
0
0
21
43
66
Distance (arcsec)

SOURCE: Author

Figure 5.5 - Evolution of the emerging magnetic flux in the AR 12552 in the HMI magnetograms, presented in six time frames, the first 48h before and the last 48h after the GRIS observation (between the 3rd and 4th frame). The black and white are negative and positive polarities, respectively.

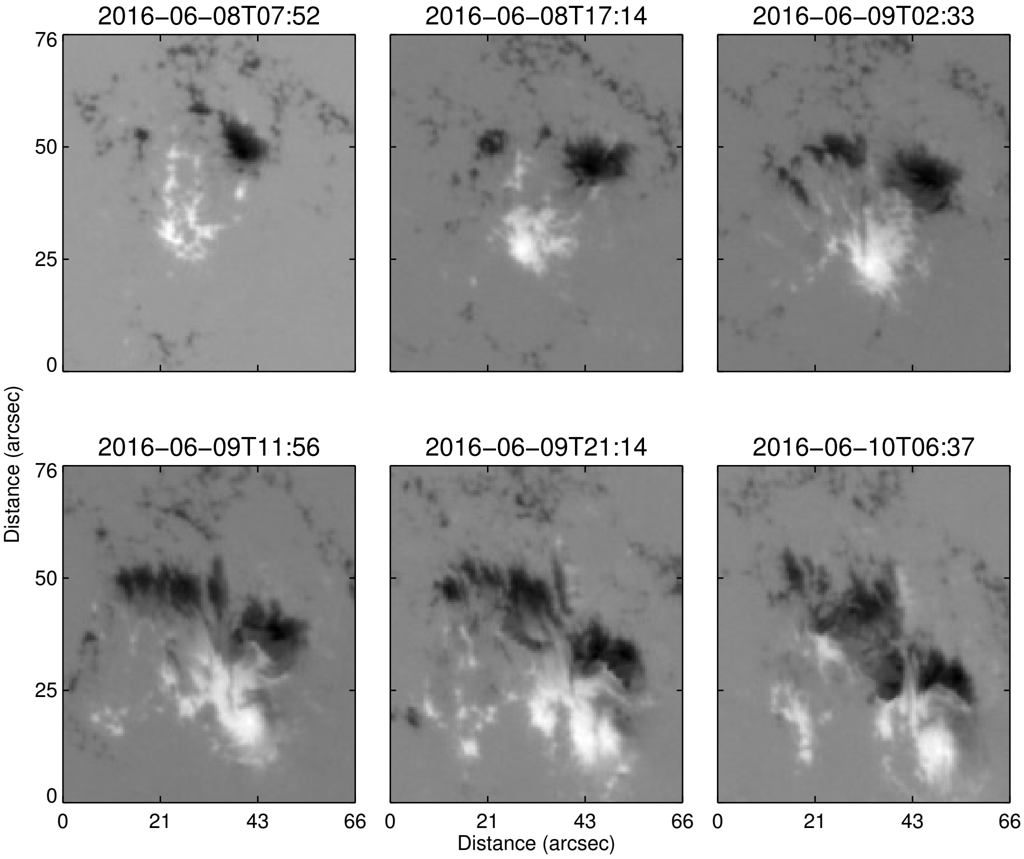

SOURCE: Author

Figure 5.6 - Evolution of the magnetic flux computed for the HMI LOS-magnetic field comprising the ROI (blue rectangle in Figure 5.3). The red and blue lines describe the magnetic flux of the positive and negative polarity, respectively. The dashed vertical lines denote the GRIS observation time. We can note an increment of the magnetic flux due to the emerging magnetic flux in the AR 12552.

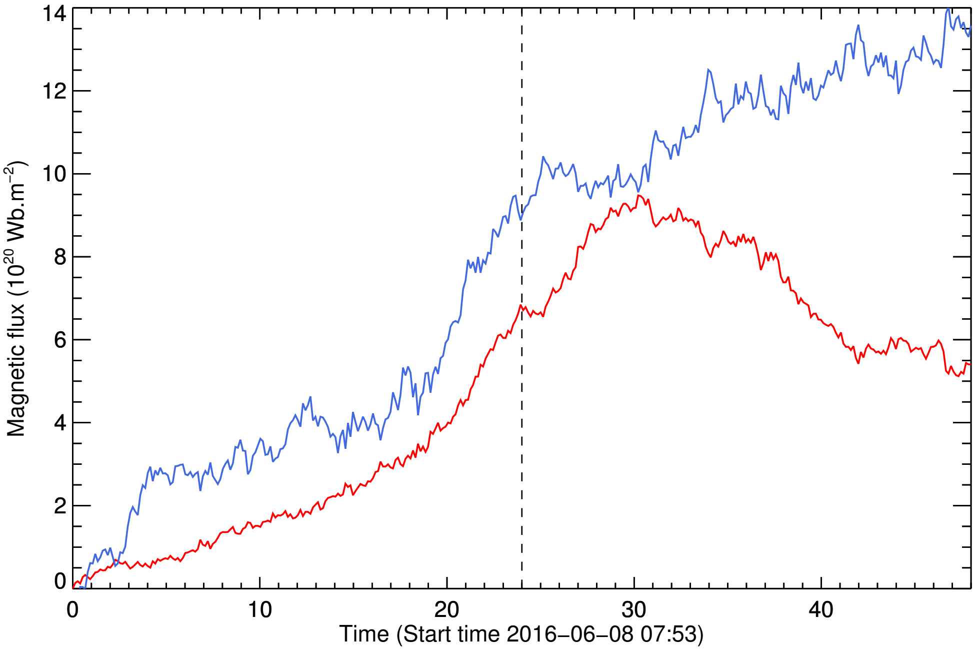

SOURCE: Author

The first penumbral regions start at 05:00 UT on June 8th, 2016 and many small magnetic features with positive and negative polarities emerge between the two initial pores. The region presents a clockwise rotation merging the penumbras of different polarities. During the GRIS scan, both magnetic fluxes were stable over about one hour.

The growth rate of the two polarities was different from each other, increasing much faster the positive polarity. There is a disproportion in the magnetic flux polarities that is not shown in the Figure 5.5. The negative polarity has a initial magnetic flux of $\phi_0^- = 2.03 \times 10^{21}\ Wb$ and the positive polarity a flux of $\phi_0^+ = 2.93 \times 10^{20}\ Wb$.

The difference in the magnetic flux of about $1.74 \times 10^{21}\ Wb$ may indicate that the determined ROI does not entirely comprise the whole bipolar region, with the flux moving over the ROI frontiers, or that there are many other magnetic structures surrounding that are not related to the AR.

The AR reaches the maximum positive magnetic flux ($1.24 \times 10^{21}\ Wb$) 2.5 days after the first visible magnetic flux emergence (6 hours after the GRIS observation). Meanwhile, the magnetic flux of negative polarity is still increasing.

At the end of our dataset, the AR starts to come pretty close to the solar limb. There, the AR presents many distortions, like vertical elongation and horizontal flattening, which make the analysis difficult due to the distortions. In a general way we can consider, the analyzed data are over an emerging flux region (EFR).

5.2.2 Evolution of the magnetic flux in the GRIS dataset

The GRIS dataset is composed of only two frames, where the column of each frame has a specific observation time. To compute the magnetic flux in the photosphere and chromosphere, observed with GRIS, we will assume that each frame is observed in a particular time interval. This assumption does not affect the result, once we are not using a large temporal cadence in the HMI observations.

In order to estimate the magnetic flux applied for the GRIS data, we obtained the magnetic field intensity in the line of sight (LOS). The B_{LOS} and the full magnetic vector is performed with the Helix inversion code, detailed in the Section 2.7, and all the inversion result is presented in the Chapter 7.

The $\phi^+_{He,f1} = 7.35 \times 10^{21}\ Wb$ is the positive magnetic flux for the first frame of the Helium line observation, and $\phi^+_{He,f2} = 7.76 \times 10^{21}\ Wb$ is the flux for the second frame. Then, the positive flux in the upper chromosphere is almost 6% larger for the second frame. The negative flux in the chromosphere is $\phi^{-}_{He,f1} = 2.32 \times 10^{22}\ Wb$ for the first frame, and $\phi^{-}_{He,f2} = 2.27 \times 10^{22}\ Wb$ for the second, decreasing more than 3% between the frames.

In the photosphere, the magnetic flux was computed observing the Si line. The positive flux in photosphere is $\phi^{+}_{Si,f1} = 1.53 \times 10^{22}\ Wb$ for the first frame, and $\phi^{+}_{Si,f2} = 1.58 \times 10^{22}\ Wb$ for the second one, increasing more than 3% between the frames. The $\phi^{-}_{Si,f1} = 3.51 \times 10^{22}\ Wb$ is the negative magnetic flux in the frame 1, and $\phi^{-}_{Si,f2} = 3.48 \times 10^{22}\ Wb$ in the flux for the frame 2, which decrease less than 1%.

From the two previous paragraphs, we can conclude that the positive flux increases for both photosphere and upper chromosphere. These results are in agreement with the temporal evolution of the magnetic flux presented in Figure 5.6 (red line). Furthermore, the negative flux increase for both He and Si lines in the analysis of the two frames, which are also in accordance with the blue line presented in Figure 5.6. For both frames, the positive magnetic flux in the photosphere is twice the flux in the upper chromosphere, and the negative magnetic flux is 1.5 larger in the photosphere.

6 Doppler velocity

The oscillations in the dark bands presented in Figure 4.3 are derived from the Doppler effect. These oscillations can be seen in the Si I 10827 Å and in He I 10830 Å line. The Doppler effect is caused by the upflows and dowflows in the region populated by both elements. In this chapter, we focus on the analysis of the Doppler velocities for both the photosphere and chromosphere layers.

We start by analyzing the Doppler velocity in the chromosphere, that presents many particular steps, with much more process to be performed before getting the Doppler velocity.

According to Penn and Kuhn (1995), the He I 10830 Å triplet of the neutral helium is a set of transitions that take place between the levels $1s2s^3S_1 - 1s2p^3P_{0,1,2}$. Two spectral features arise from the He I triplet system, we call it as "blue" and "red" components. The blue component is placed at 10829.09 Å and it comes from the $2s^3S_1 - 2p_0^3$ transition. The red component is a blend of two spectral He I lines placed at 10830.25 Å and 10830.33 Å and is originated from the $^3P_1$ and $^3P_2$ levels.

The first observation of multiple flows in the He I 10830 Å line was made by Schmidt et al. (2000), investigating a small plage region using the echelle spectrograph of the German Vacuum Tower Telescope (VTT).

In order to compare our Doppler measurements with the sound speed, we have to determine it for the chromosphere. An approximation for the sound speed (c_s) in chromosphere is given by using the ideal gas law, so the c_s for the ideal gas becomes

$$c_s = \sqrt{\frac{\gamma_i k T_c}{m_s}}, \tag{6.1}$$

where $\gamma_i \approx 5/3$ is the adiabatic index, $k \approx 1.38 \times 10^{-23} \mathrm{m^2 kg s^{-2} K^{-1}}$ is the Boltzmann constant and $m_s \approx 1.67 \times 10^{-27}$ kg is the mass for a single molecule. The typical formation temperature (T) of the He I line is from 8000 to 10000 K. Thus, the sound speed in the formation height of the He line is about 10 $\mathrm{kms^{-1}}$

6.1 Telluric line subtraction

The H_2O telluric line, placed at 10832.108 Å commonly superposes the fast component of the He line when the line presents a redshift due to the Doppler velocity. Therefore, we need to remove the telluric line from the spectrum so that we can clearly observe the pattern of the fast component.

Figure 6.1 - Spectral profiles of the Stokes I/I_C centered in the 10832.108 Å telluric line. The gray lines are the Lorentzian profiles for each pixel of the map and the red line is the mean intensity profile. We note the center of all fitted models is well defined in accordance to the telluric line center. However, the spectral line amplitude shows a considerable variation that needs to be improved.

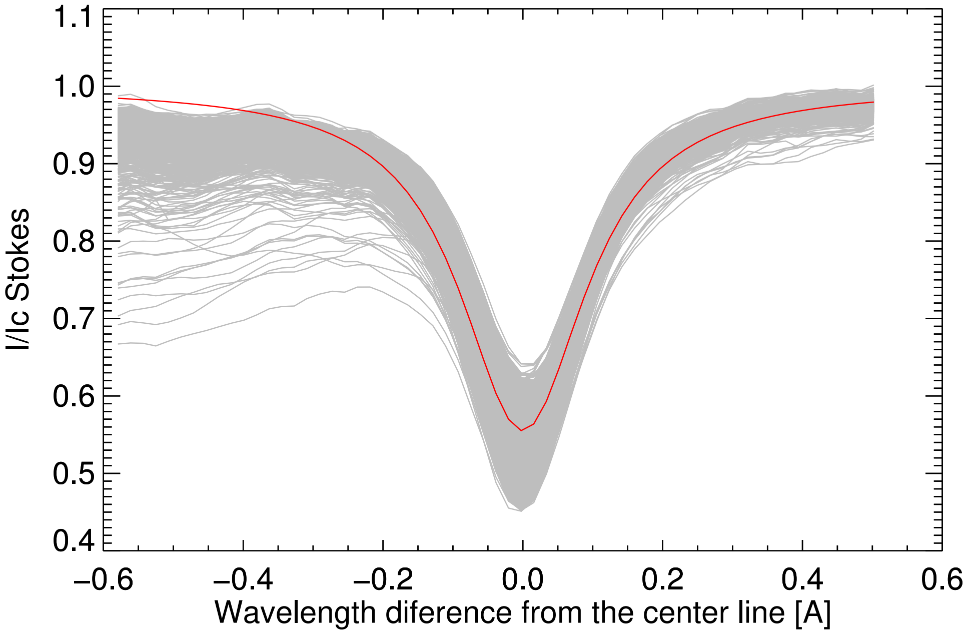

SOURCE: Author

In order to fit the telluric profile for each pixel of the map we use the Lorentzian profile ($\mathcal{L}$), as described above.

$$\mathcal{L}(x) = 1 - \frac{A_0}{\left(\dfrac{x - A_1}{A_2}\right)^2 + 1}, \tag{6.2}$$

where A_0 is the Lorentzian profile amplitude, A_1 the peak centroid and A_2, the half-width at half-maximum (HWHM). To perform the least squares curve fitting we used the Levenberg–Marquardt algorithm (MORE, 1978).

Figure 6.2 - Spectral profiles of the Stokes I/I_C centered in the 10832.108 Å telluric line. The colored curves are the Lorentzian profiles obtained for each pixel, with the corresponding color referring to the slit number. We note there is a fragmentation of profiles with the same colors and different amplitudes, indicating there is amplitude variation of the telluric line along the scan.

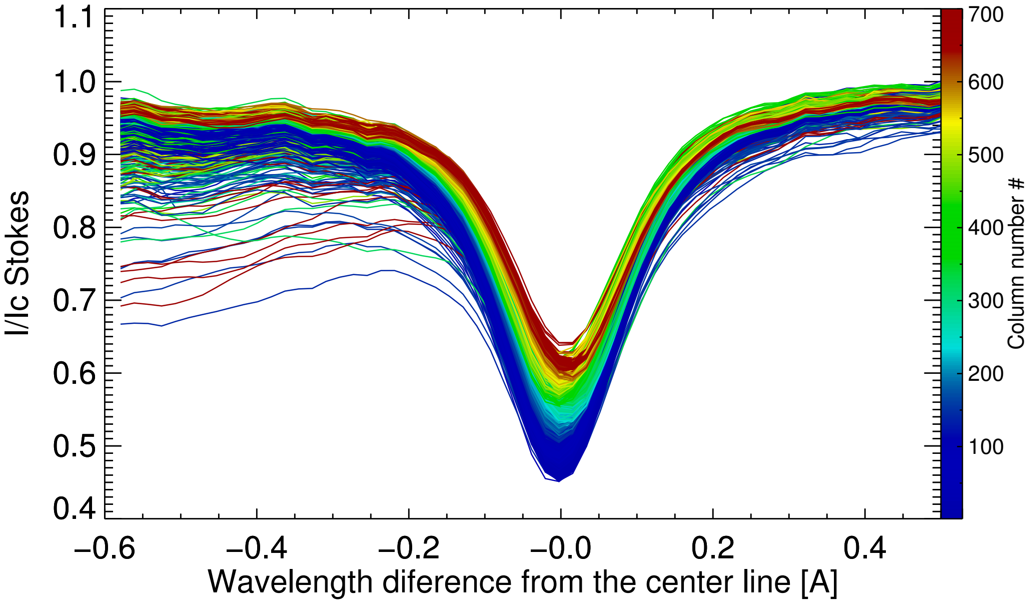

SOURCE: Author

We used the fit parameters retrieved from the Lorentzian fit to create the synthetic profiles of the telluric line. To perform the subtraction of the 10832.108 Å line, we averaged all synthetic spectral profiles from each pixel of the map and then, compute the mean intensity profile. To completely cover the telluric profile, a range between 10831.481 - 10832.562 Å was selected, within a total of 60 points in the spectrum.

Figure 6.1 presents the result of the mean intensity profile, where the gray lines are the Lorentzian models for each pixel of the map and red line is the averaged intensity profile.

The center of the telluric line is clearly defined along all the pixels. However, we can see a substantial variation in the amplitude of the telluric profile. When we subtract the computed telluric line from the original spectrum, we found large fitting errors.

In order to improve the telluric profile fitting, we investigate the variation of the telluric line amplitude over time. Each slit of the GRIS scanning represents one time interval. To analyze if the variation of the synthetic profile amplitude is related to each time interval (each slit) we developed the same plot of the Figure 6.1, however with different colors for each slit.

The result is presented in Figure 6.2, where the curves represent the telluric profiles for each pixel, and each color represents one slit. The fragmentation of the profiles is evident, confirming that there is an amplitude variation in the telluric line a long time, and then we can compute separated synthetic telluric profiles for each slit.

The synthetic telluric line is properly represented by the Lorentzian profile. However, for the spectral line, we made use of the Voigt profile to fit all the lines. Details of the Voigt profile are presented in the next section.

6.2 Voigt profile

In the solar atmosphere, there is a diversity of broadening mechanisms. Some mechanisms, like the thermal broadening, have a Gaussian profile and some others, like damping, have a Lorentzian profile (LIEBENBERG et al., 1975).

The approach to reach an accurate absorption profile must be made with the convolution of the thermal broadening and the damping profile. The damping profile is the reaction of oscillators (atoms) to the external radiation field, and the thermal broadening is due to random motion of atoms in the solar plasma (RAUTIAN; SOBEL'MAN, 1967).

To obtain the mutual effect of both broadening mechanisms, we need to convolve the Gaussian $\mathcal{G}(\nu)$ and Lorentz profile $\mathcal{L}(\nu)$. The $\mathcal{G}(\nu)$ and $\mathcal{L}(\nu)$ function are given by:

$$\mathcal{G}(\nu) = \frac{1}{\sqrt{\pi}\Delta\nu_D} e^{-(\nu-\nu_0)^2/\Delta\nu_D^2}, \tag{6.3}$$

$$\mathcal{L}(\nu) = \frac{\gamma/4\pi^2}{(\nu-\nu_0)^2 + (\gamma/4\pi)^2}, \tag{6.4}$$

where $\Delta\nu_D$ is the Doppler width and γ is the damping constant. We can define $V(\nu) = \mathcal{G}(\nu) * \mathcal{L}(\nu)$. Thus,

$$V(\nu) = \int_{-\infty}^{+\infty} \mathcal{G}(\nu')\mathcal{L}(\nu-\nu')\mathrm{d}\nu'. \tag{6.5}$$

In order to simplify, we can assume the follow transformations:

$$v = \frac{\nu - \nu_0}{\Delta\nu_D}, \tag{6.6}$$

$$a = \frac{\gamma}{4\pi\Delta\nu_D}, \tag{6.7}$$

$$y = \frac{\nu' - \nu_0}{\Delta\nu_D}. \tag{6.8}$$

Thus, the Equations (6.3),(6.4) and (6.5) can be rewritten as follow:

$$\mathcal{G}(\nu) = \frac{1}{\sqrt{\pi}\Delta\nu_D} e^{-y^2}, \tag{6.9}$$

$$\mathcal{L}(\nu) = \frac{a/\pi\Delta\nu_D}{y^2 + a^2}, \tag{6.10}$$

and

$$V(\nu) = \frac{1}{\sqrt{\pi}\Delta\nu_D} \frac{a}{\pi} \int_{-\infty}^{+\infty} \frac{e^{-y^2}}{(v-y)^2 + a^2} \mathrm{d}y. \tag{6.11}$$

The *Voigt function* is defined as $\mathcal{H}(a, v) = \sqrt{\pi}\Delta\nu_D V$, then

$$\mathcal{H}(a, v) = \frac{a}{\pi} \int_{-\infty}^{+\infty} \frac{e^{-y^2}}{(v-y)^2 + a^2} \mathrm{d}y. \tag{6.12}$$

The Voigt function was first time reported by Voigt (1913). $\mathcal{H}(a, v)$ has no analytical solution. More details related to the Voigt function is presented on Mihalas (1978).

The parameter v can be determined as a function of the distance from the center of the spectral line, as

$$v = \frac{\lambda - \lambda_0}{\Delta\lambda_D}, \tag{6.13}$$

where $\Delta\lambda_D$ is the Doppler width given by

$$\Delta\lambda_D = \frac{\lambda_0}{c}\sqrt{\zeta_{mic}^2 + \frac{2kT}{m_a}}. \tag{6.14}$$

On the Equation (6.14), c is the speed of light, ζ_{mic} is the microturbulence velocity, k is the Boltzmann constant, T is the temperature and m_a is the mass of the atom.

6.2.1 Pseudo-Voigt

The integral of the Equation (6.12) has no analytical solution, so can be estimated only numerically. The numerical integration is very time consuming and complex, as well as, inaccurate if the algorithm or the program is improperly designed (LIU et al., 2001). In order to perform a reliable solution for the Equation (6.12), we made use of the *pseudo-Voigt* function.

According to Wertheim et al. (1974), the pseudo-Voigt function is a linear combination of Gaussian and Lorentzian functions with the same full-width-at-half-maximum (FWHM) values, it means the pseudo-Voigt is a simple approximation for the Voigt profile function. The maximum deviation between the exact Voigt profile and the optimized pseudo-Voigt approximation is 0.77% relative to the peak height (IDA et al., 2000).

Thompson et al. (1987) have introduced a suitable representation of the pseudo-Voigt function by approximating the Voigt profile, in a way that the FWHM and Lorentzian weight of the pseudo-Voigt function is related to the FWHM of the deconvoluted Gaussian and Lorentzian profiles.

In the present work, we made use of the extended formula of the pseudo-Voigt function proposed by Thompson et al. (1987). The normalized pseudo-Voigt function is defined as

$$V_{pseudo} = (1-\eta)\mathcal{G}(x;\gamma_G) + \eta\mathcal{L}(x;\gamma_L), \tag{6.15}$$

where $\mathcal{G}(x;\gamma_G)$ is the normalized Gaussian and $\mathcal{L}(x;\gamma_L)$ the normalized Lorentzian function.

Thompson et al. (1987) have proposed expression for the pseudo-Voigt approximation, with FWHM values of Γ_G for the Gaussian and Γ_L for the Lorentzian function. In this expression η is a function of Γ_G, Γ_L and Γ_V

$$\eta = 1.36603\frac{\Gamma_L}{\Gamma_V} - 0.47719\left(\frac{\Gamma_L}{\Gamma_V}\right)^2 + 0.11116\left(\frac{\Gamma_L}{\Gamma_V}\right)^3, \tag{6.16}$$

and the total FWHM (Γ_V) is given by:

$$\begin{aligned}\Gamma_V = (&\Gamma_G^5 + 2.69269\Gamma_G^4\Gamma_L + 2.42843\Gamma_G^3\Gamma_L^2 \\ &+4.47163\Gamma_G^2\Gamma_L^3 + 0.07842\Gamma_G\Gamma_L^4 + \Gamma_L^5)^{1/5}.\end{aligned} \tag{6.17}$$

The FWHM for the Gaussian and Lorentzian profiles are given respectively by (LIU et al., 2001):

$$\Gamma_G = 2\sigma\sqrt{2\ln 2}, \tag{6.18}$$

and

$$\Gamma_L = 2\gamma. \tag{6.19}$$

Olivero and Longbothum (1977) proposed an approximation, but highly accurate formula relating the FWHM of the Voigt profile to both FWHM of the Gaussian and Lorentzian profile, as bellow

$$\Gamma_V \approx 0.5346\Gamma_L + \sqrt{0.2166\Gamma_L^2 + \Gamma_G^2}. \tag{6.20}$$

According to Oks (2017), the Equation (6.20) for the FWHM of the Voigt profile has the accuracy of 0.02%.

6.3 Chromospheric Single-flow

As a first approach to obtain the LOS velocity for the red component of the He I line, we assume a single flow, with a Voigt profile. This approach performs the best profile to recover the absorption line fit for the Si line and also for almost all the regions of the chromospheric lines.

According to the NIST database (KRAMIDA et al., 2018), the two spectral lines comprising the He red component are located on 10830.2501 Å and 10830.3398 Å. However, the wavelength reference used to compute the LOS velocities assuming a single flow is fixed to 10830.30 Å, corresponding to the average laboratory wavelength of the He i red component.

A map of the LOS velocity inferred by fitting a single Voigt profile is presented in Figure 6.3. The map was color-coded such that blue corresponds to motions toward (upflows) and red away from the observer (downflows). The black contour comprises the regions with the supersonic flow and are candidate regions to have a dual-flow in the He I blended component.

Figure 6.3 - Doppler velocity map inferred by fitting a single Voigt profile for the He I red component. The red color corresponds to the downflows and blue to the upflows. The contours comprise the regions with supersonic flows and are candidates regions to present dual-flow profiles in the He I blended component.

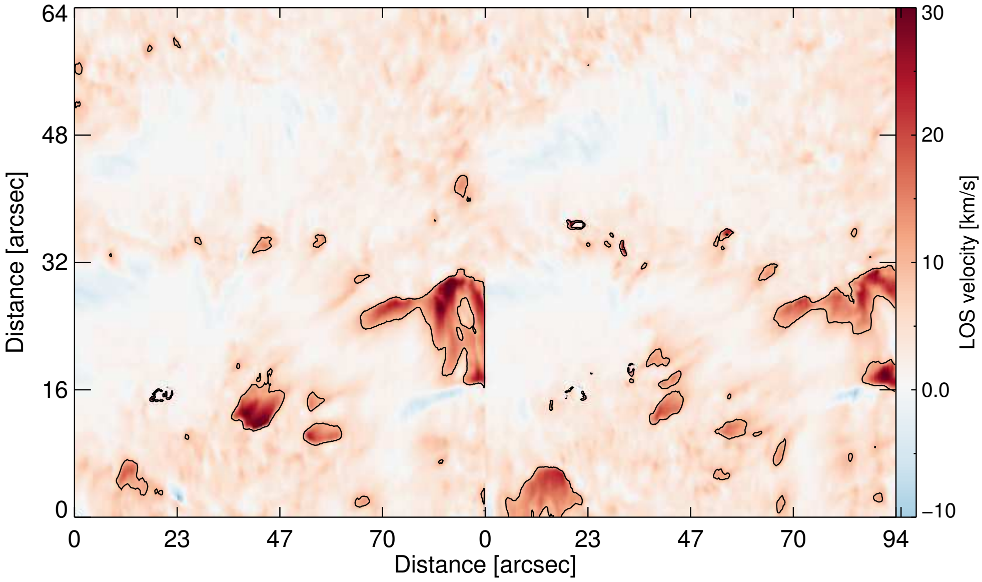

SOURCE: Author

In order to check where the supersonic downflows are present and its relation to the filaments position, we merge all these information in Figure 6.4. The *Top* panel present the continuum map, while the *Middle* panel displays the upper chromosphere observed with the He line. The *bottom* panel shows the Doppler velocity for a single flow. The red line contours the filaments and the black lines the region of supersonic velocity.

The velocities are larger close to the filament footpoints and lower near the filament center. Some filaments footpoins also present a supersonic downflow, as highlighted by the yellow arrows on the *Middle* panel of Figure 6.4. Most of the supersonic flows in the trailing sunspots are placed over the penumbra and umbra regions.

Figure 6.4 - (*Top*) The continuum map. (*Middle*) Stokes I/Ic for the He I 10830 Å. (*Bottom*) The Doppler velocity for the upper chromosphere. The black contours (white in the *Middle* panel) comprise the regions with supersonic flows, and the red ones, the filaments. We identify supersonic downflows in the footpoint of most filaments, as highlighted by the yellow arrow in the *Middle* panel.

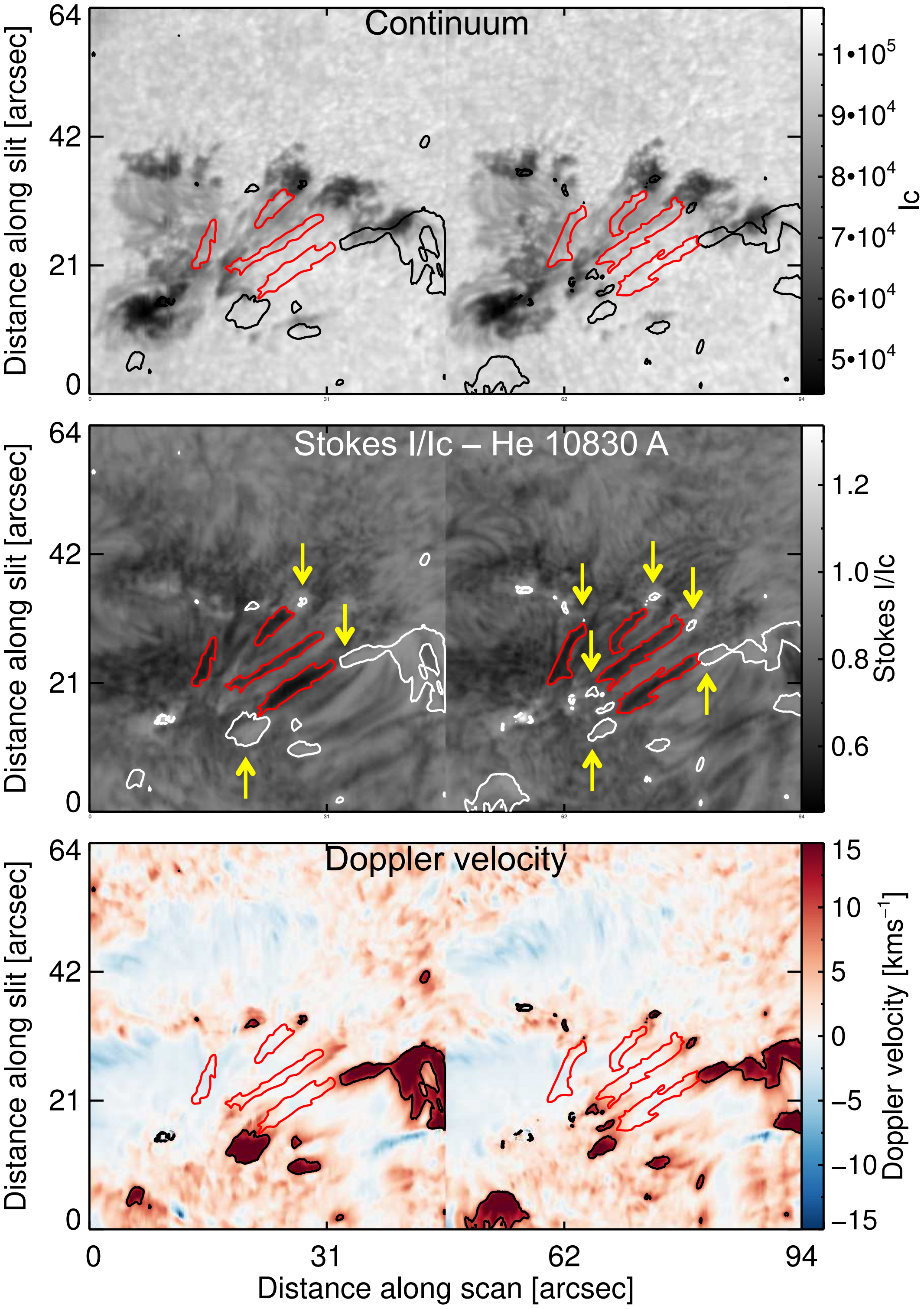

SOURCE: Author

6.4 Chromospheric Dual-flow

In previous section, we observed that the single flow model presents quite well the Doppler velocity for almost all regions in upper chromosphere. However, when the velocities are larger than the supersonic, the He absorption line seems to be splitting into two spectral lines. These double flows are expected, once the He I 10830 Å red component is composed of two spectral lines of the triplet, as detailed in Section 1.4. However, observations of dual flow in the same element are recent. The first record of dual flows in the He I 10830 Å, with subsonic and supersonic velocities, was performed by Schmidt et al. (2000).

A proper approach to compute the chromospheric Doppler velocity in the presence of a subsonic and supersonic flow is performing a dual-flow model, by using a double-Voigt profile. We developed a double-Voigt model using two pseudo-Voigt functions limited in velocity. For the slower component, we consider a velocity range from -10 to 15 $\mathrm{kms^{-1}}$, and from 7 to 60 $\mathrm{kms^{-1}}$ for the faster component. It will result in two maps, one for each component and then we need select it for each pixel by checking the spectrum profile and the fitting errors. We perform the fitting optimization for both models, by using the Levenberg–Marquardt algorithm (MORE, 1978).

The dual-flow model can present some issues, like finding a local minimum and assume it as the best fit. To reduce these issues, we need to select many pixels with dual-flows and investigate the main characteristics of these spectra.

As an example, we selected four pixels with the dual-flow presence, to compare the observed profiles with the fitted model. The four cases are presented in Figure 6.5. The Stokes I profiles are normalized in relation to the continuum. The black dots are the observed Stokes I/Ic without the telluric line. The solid red line displays the best fit by using the double-Voigt model. The double-Voigt comprises two single Voigt function, denoted by the dash and dash-dotted gray lines. The Voigt fit for the single flow model is presented with the blue line. (a) Two subsonic flows. (b-c) Two clear spectral lines, denoting both component flows. (d) Two flows, one subsonic and one supersonic. We recorded smaller fitting errors for the double Voigt (red line) than for the single Voigt (blue line) model, in all the four plots.

From Figure 6.5, it is clear the double Voigt profile reproduce much better the dual-flow than with the single Voigt. We recorded lower fitting errors for the double Voigt (red line) than the single Voigt (blue line) profiles, in all the four plots.

Figure 6.5 - Normalized Stokes I/I_c profiles for selected pixels where we can observe a dual-flow in the red component of the He I line. The black dots are the observed profile after the telluric line subtraction. The solid red line displays the best fit for the double-Voigt profile. It is composed of two single Voigt model, denoted by the dash and dash-dotted gray lines. The blue line is the Voigt fit for the single flow model. (a) Two subsonic flows. (b-c) Two clear spectral lines, one subsonic and one supersonic. (d) Dual-flow, with very large redshift. In all theses panels, we recorded a lower fitting error for the double Voigt (red line) than for the single Voigt (blue line)

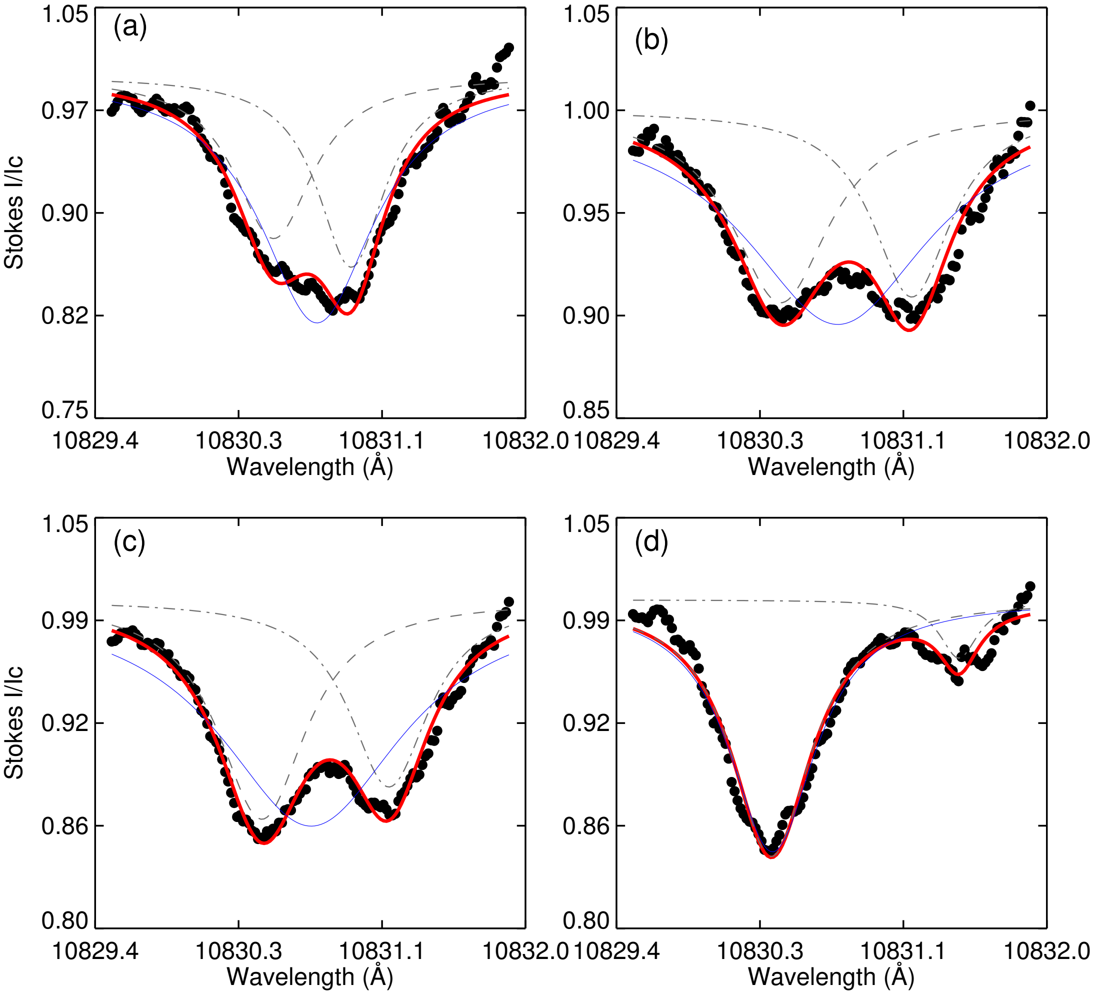

SOURCE: Author

Figure 6.6 - Doppler velocity map for the fast component of the He I 10830 Å. The components were computed with double Voigt profiles. The prevalence of redshift is imposed by the range defined in the input parameters, in order to fit only the downflows. In the main panel, the black line contours the filaments and the white outlines the supersonic downflows. The dual flow is not present in the full map, but mainly in the regions with supersonic flow, as presented in Figure 6.3. The outer panels present the footpoints where we found the supersonic flows. The black line in the outer panels detaches where the dual flow are present ("I" refers to inside, and "O" to outside).

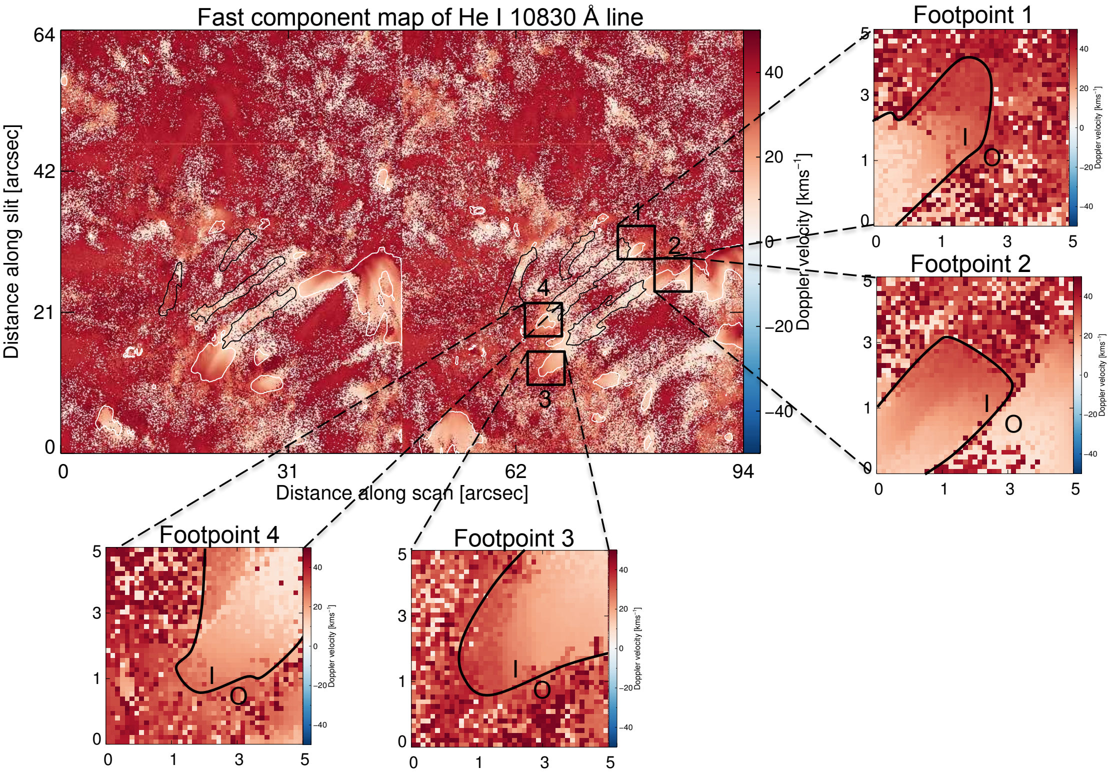

SOURCE: Author

To ensure we did not miss any pixel with a dual-flow profile, the double-Voigt model was applied for the full map. The map with the Doppler velocities determined for the fast component of the He line is presented in Figure 6.6, where the black lines are the filaments and the white ones delimits the supersonic velocities.

The map is displayed with a Doppler velocity range from -60 to +60 kms^{-1}, using the red color for the downflow and blue color for the upflows. However, the red color is predominant due to the imposed range defined in the input parameters, in order to fit only the downflows.

Most of the Doppler velocity map for the He line is better represented with the single flow model. However, there are few sectors that the dual-flow model are the best to be employed. The outer panels of Figure 6.6 are the zoom of the black squares presented in the main panel, over the filament footpoints. The solid black line in the outer panels delimits the region where double-Voigt model can be applied, In those panels, the letter "I" means inside, and "O" outside. The region of dual-flow is selected by using both the fitting error and the visual confirmation of dual-flow in the spectral line. The selected region seems more smoothed than the adjacent region, as displayed in the outer panels of Figure 6.6

6.5 Doppler velocity for the Si line

Similar to the first approach performed for the He I line, we employed a single Voigt profile to compute the Doppler velocity for the Si I line. This approach performs the best profile to recover the absorption spectrum of the photospheric line.

According to the NIST database (KRAMIDA et al., 2018), the 10827.0877 Å wavelength is the center line of the Si I, that is assumed as the reference to compute the Doppler velocity.

The Doppler velocity map recovered with the Si line by using a single Voigt is displayed in Figure 6.7. The black lines outline the filaments, and the blue ones detached the supersonic velocity observed in the upper chromosphere with the red component of the He I 10830 Å. The range of the Doppler velocity is from -3 to +3 kms^{-1}.

Figure 6.7 - Doppler velocity map for the photosphere computed for the Si I line. The red color corresponds to the downflows and blue to the upflows. The black contours comprise the filaments, and the blue ones outline the supersonic downflow observed in the chromosphere.

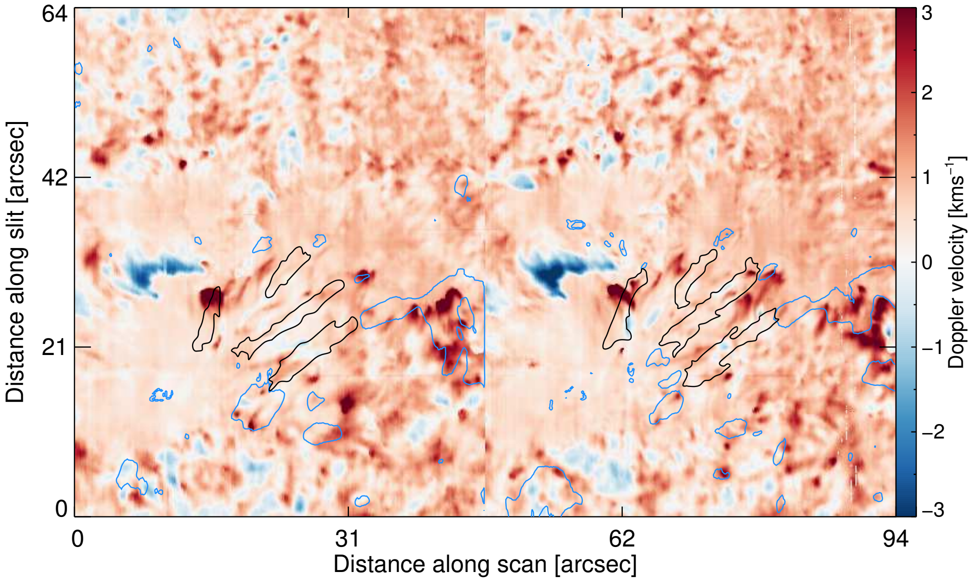

SOURCE: Author

It is evident the predominance of redshift in the Doppler map of the Si line. However, it presents a very low speed, far away from the supersonic velocity found in the upper chromosphere. Some filament footpoints presented a higher than the average velocity close to it. However, we did not notice a clear evidence of these higher velocity close to the footpoints in the photosphere, as we found in the upper chromosphere.

6.6 Discussion

We have analyzed the Doppler velocity field in both photosphere and chromosphere over the region of an arch filament system. The filaments in the chromospheric line presented supersonic downflows close to the footpoints, and some of them also presented upflows in the center of the filament. The distribution of the chromospheric Doppler velocity inside the filament is exhibited in Figure 6.8. The figure shows the histogram of the Doppler velocity distribution for the filament 1 (*top*) and filament 2 (*botton*). The red histogram represents the downflow, and the blue one comprises the upper flow, seen only in filament 1. The blue line denotes the Gaussian distribution with center = 1.85 kms^{-1} and FWHM = 4.56 for the filament 1, and center = 2.08 kms^{-1} and FWHM = 5.00 for the filament 2. Doppler velocities larger than the sound speed are separated by the gray dashed line.

When the velocity reaches close to the supersonic speed in the chromosphere, the red component of the He I triplet assumes a dual-flow model. The dual-flow is characterized by one subsonic and one supersonic flow, that is solved by employing a second Voigt profile. The upflow in the top of the filament can be explained as the filament are rising.

The presence of both subsonic and supersonic flow in the same spatial element is classified by analyzing the fitting error and the red component shape of the He line. We checked both single and dual-flow model along the filament, connecting both footpoints. The analysis is performed by tracing ten profiles, aligned, side by side, with 1 pixel shifted in both x- and y-direction, and connecting the footpoints of opposite polarities, as presented in Figure 6.9*a*. The background of the *top* panel is the chromospheric Doppler speed using a single flow model.

Figure 6.8 - Histogram distribution of the Doppler velocities for the filament 1 (*top*) and filament 2 (*botton*). The red filled histogram comprises the downflow, and the blue one involves the upflow, which can be seen only in the filament 1. The gray dashed line separates the sub and supersonic flows. The blue line is the Gaussian distribution with center = 1.85 kms^{-1} and FWHM = 4.56 for the filament 1, and center = 2.08 kms^{-1} and FWHM = 5.00 for the filament 2.

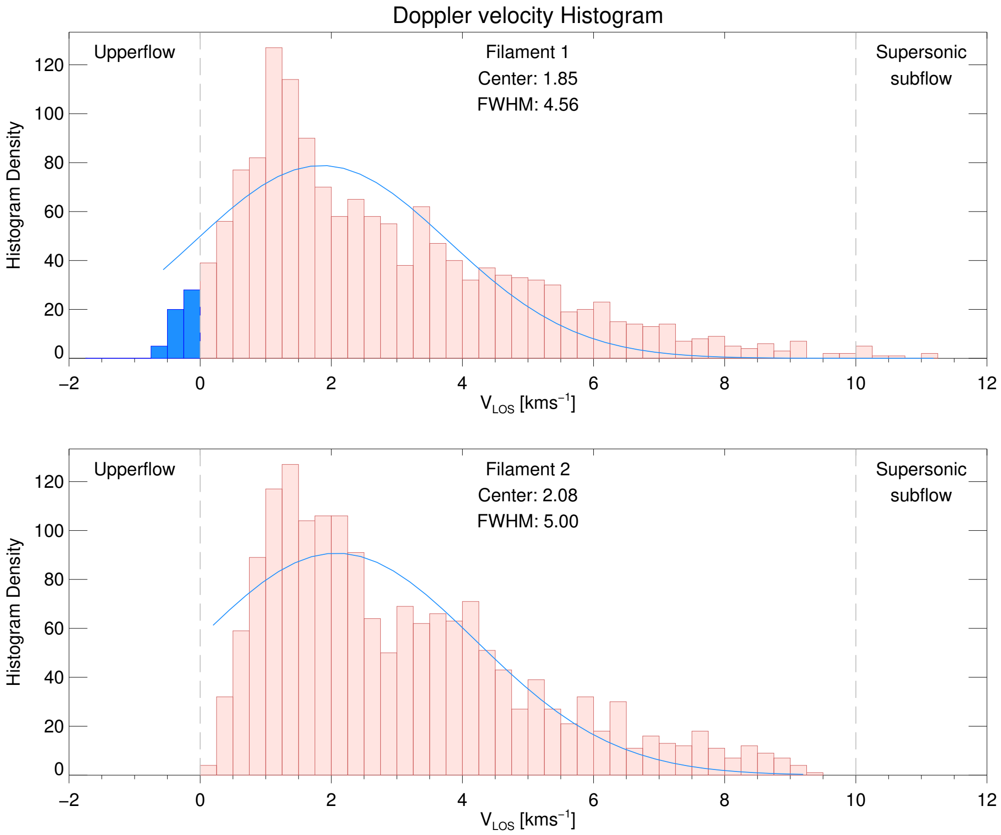

SOURCE: Author

The result of the selected profiles in the panel *a* is presented in the panel *b* of the same figure. The blue curves represent the ten profiles for the single flow model and the red ones for the dual-flow model. We observed that both present similar velocities at about 9 to 10 kms^{-1}, it means, close to the supersonic speed. When the speed reached around 15 kms^{-1}, the fitting discrepancy is large an the dual-flow dominates. We considered, in this work, that a velocity larger than supersonic is assumed as a dual-flow model, as soon as it presents a clear dual flow, like the ones exhibited in Figure 6.5.

The gray lines of Figure 6.9*b* are the extension of the red profiles, but for a region where the dual-flow model presents a large fitting error and the single flow has the best fit. Both gray dashed lines separate the upflow, downflow and supersonic downflow. The dashed box labeled with number "1" represents the region where the presence of upflow is evident, causing the filaments to rise. The box labeled with number "2" is a downflow region close to the upflow one. It is produced by a small region similar to a footpoint, that we also detected a magnetic field of opposite polarity.

As determined in Equation (6.1), the sound speed at the common formation height of the He I 10830 Å is in the order of 10 kms^{-1}. We measure, in the filament footpoints, Doppler velocities in the order of 40 kms^{-1}, with some regions reaching up to 44 kms^{-1}. Therefore, its clear that these velocities are much larger than the typical chromosphere sound speed. Let us suppose a free-fall speed, with a gravitational acceleration given by $g_\odot = GM_\odot/r_\odot^2$, where G is the gravitational constant, $M_\odot$ the solar mass, and $r_\odot$ the solar radius, so we have that $g_\odot \approx 274$ ms^{-2}. Then, the average velocity of 40 kms^{-1} give us a free-fall height of ~ 2.9 Mm.

Different from the chromospheric observation, the Doppler velocity in the photosphere presents an evident subsonic speed. The significant difference in the Doppler velocities between both, more than ten times, implying the presence of a shock in between the chromospheric and photospheric layers, similar to observed by Lagg et al. (2007) for the vicinity of a growing pore.

The supersonic downflow presented a very symmetric Doppler gradient from the center to the footpoints, for both single and dual-flow models, as presented in Figure 6.9*b*. We interpret these downflows as resulting from the upflows caused by the new emerging flux tubes, that carry the photospheric material to higher layers in the center of the filament, as presented in the square labeled as number "1" in Figure 6.9*b*. These upflows reach more than 1 kms^{-1} in the filament center.

Figure 6.9 - (*a*) Selected profiles crossing a filament, and the two footpoints. The ten profiles are one pixel shifted, side by side, to cover the full filament. The background panel is the Doppler velocity for a single Voigt profile. (*b*) The Doppler velocity profiles along the ten selected lines for a single component (blue) and the fast component of the double Voigt model (red). The gray lines are the extension of the fast component (red), and it needs to be rejected, due to the large fitting error. The bottom gray dashed line departs the downflow to the upflow, and the second gray line separates the sub and supersonic downflows. The dashed box “1” shows the region where we find upflows, and the box “2” highlight the region we find a small region similar to a footpoint.

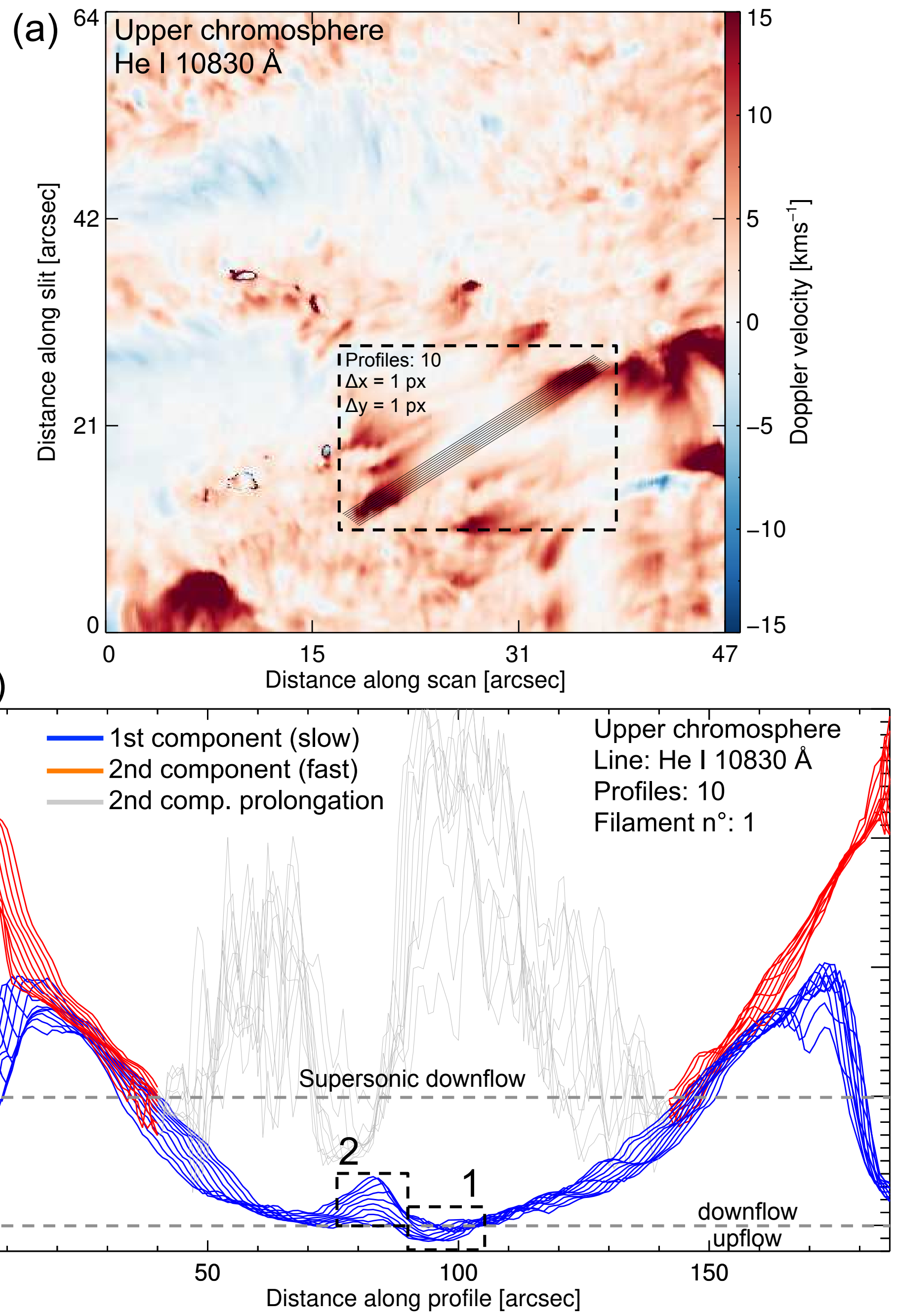

SOURCE: Author

7 Magnetic structure of the filament system

The magnetic field vector over the photosphere and chromosphere is determined by using the inversion of full Stokes for the Si I 10827 Å and He I 10830 Å lines, respectively. In the Section 7.1 we present the details of the inversion process by using the HeLix$^+$ code to obtain the physical parameters for both layers.

The inversion is employed for each pixel of the Stokes map. Therefore the inversion of a full map considering many atmospheres can take a considerable computational time. In Section 7.2 we detailed the process of inverting the full map, as well as presented the maps for all the parameters resulting from the inversion. An analysis of the retrieved parameters is presented in Section 7.3.

The characterization of the polarity inversion line has a great importance in the study of the filament. In Section 7.4 we present the result of the method developed to determine the PIL.

It is possible to infer the magnetic field vector from the full Stokes inversion obtained with the HeLIx$^+$ code, once the output data includes the magnetic field strength, azimuth, and inclination angle. However, the determination of the magnetic field from the Zeeman effect produces a non-unique solution for the azimuth component of the magnetic field vector. In Section 7.5 we present how to determine the magnetic vector.

When an AFS is observed away from the disk center, in both photospheric and chromospheric layers, the Stokes V profiles can be analyzed to perform an estimation of the formation height difference between the main population of the Si and He components, as presented in Section 7.6.

In Section 7.7, we present the result of the magnetic loops reconstruction, based in the chromospheric magnetic field vector, using the reconstruction method proposed by Solanki et al. (2003).

The magnetic field in the line of sight for the photosphere and chromosphere are used in the Linear force-free extrapolation in Section 7.8.

In Section 7.9, we combined the information obtained from the Doppler velocities maps and the full-Stokes inversions, then we present an overview of the magnetic structure of the filaments.

7.1 Retrieval of physical parameters from the full Stokes

In order to compute the physical parameters like the magnetic field vector, we made use of the full Stokes I, Q, U, and V profiles of both Si I 10827 Å line and He I 10830 Å triplet. To solve the physical parameter, we made use of the inversion method, using the HeLIx$^+$ code (LAGG et al., 2004).

The HeLIx$^+$ retrieve the physical parameters making use of the Unno-Rachkowsky analytic solution for the radiative transfer equation in a Milne-Eddington model atmosphere (detailed in Section 2.4).

The inversion code achieves the global minimum for the observed Stokes profiles, by employing the PIKAIA genetic algorithm and making use of eight free parameters. These parameters can represent the solar atmosphere for that component and are composed by: the magnetic field strength (B), the azimuth (χ), inclination angle (γ), Doppler velocity in LOS (v_{LOS}), Doppler width ($\Delta\lambda_{\mathrm{D}}$), damping constant ($a$), slope of the source function ($S1$), and the opacity ratio between spectral line center and continuum (η_0).

The HeLIx$^+$ code supports the inversion for all the atmospheric component simultaneously so that we can manage the presence of unsolved magnetic structures with a spatial resolution element, or even the scattered light from outside the resolution element. Another free parameter applied in the inversion code is the filling factor, f, it is applied in order to adjust each component weight.

The physical parameters in the photosphere are retrieved by using the inversion of the Stokes profiles observed with the Si I line. For this line, we made use of a two-component atmospheric model, that comprises one magnetic component and one field-free model. According to Xu et al. (2012), the field-free model represents the contribution of the field-free material to Stokes I, as well as, the straylight contamination of the Stokes I from the encompassing regions.

The formation level of the He I 10830 Å is described in the Section 1.4. From there, we know the He line formation is located in the upper chromosphere.

Figure 7.1 - Selected points to represent the full Stokes inversion for the Si I 10827 Å He I 10830 Å and Ca I 10839 Å. The background is the second frame of the Stokes I/Ic in the center of the He line. The Point 1 is placed in the center of the leading sunspot umbra. The point 2 is in the center of the first filament. The point 3 is placed in a border of the first filament. The point 4 in the surrounding region between the filament 1 an 2.

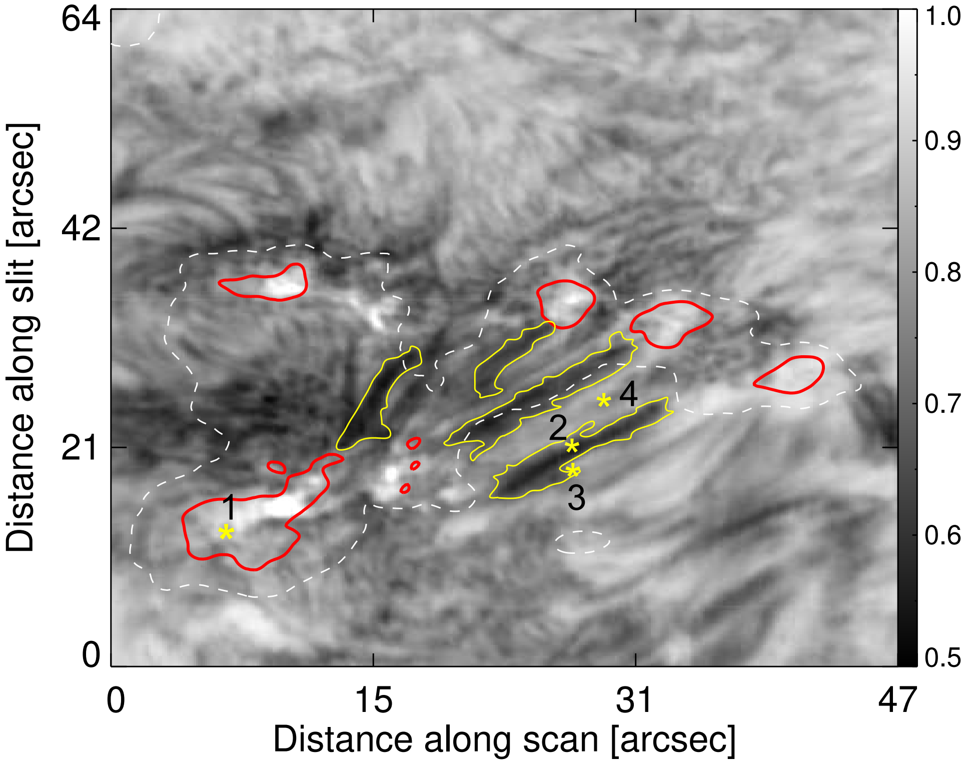

SOURCE: Author

According to Solanki and Steiner (1990), we can anticipate that the magnetic field satisfies the resolution element, based on the strong expansion in the chromosphere. Therefore, we can assume an only magnetic component atmospheric model for the He line. Nevertheless, the solution of the Doppler velocities performed with the Voigt function in Chapter 6 give us evidence of a second component for the He line. In this way, to better fit the profiles along the filaments and surrounding, two magnetic components are required, each one with separate Doppler velocities. The presence of the multiple line-profile components are discussed on Lagg et al. (2007) and Cuadrado et al. (2007).

Table 7.1 - Retrieved parameters from the Stokes profiles presented in Figure 7.2. The parameters are obtained with the inversion of the Si I, He I and Ca I lines for a pixel in the leading sunspot umbra (highlighted with number 1 in Figure 7.1)

Line	B [G]	χ [°]	γ [°]	v_{LOS} [ms^{-1}]	$\Delta\lambda_{\mathrm{D}}$ [Å]	$S1$	η_0	a
Si I 10827 Å	1960.46	-86.98	13.60	729.43	0.02	2.32	21.36	1.99
He I 10830 Å	971.33	-79.39	3.51	-89.19	0.18	0.81	1.81	3.21
Ca I 10839 Å	2263.65	-76.16	15.16	596.71	0.04	1.18	1.48	1.76

SOURCE: Author

Table 7.2 - Retrieved parameters from the Stokes profiles presented in Figure 7.3. The parameters are obtained with the inversion of the Si I, He I and Ca I lines for a pixel in the center of the first filament (highlighted with number 2 in Figure 7.1)

Line	B [G]	χ [°]	γ [°]	v_{LOS} [ms^{-1}]	$\Delta\lambda_{\mathrm{D}}$ [Å]	$S1$	η_0	a
Si I 10827 Å	734.06	32.06	75.30	532.04	0.04	7.23	18.93	0.92
He I 10830 Å	436.71	27.37	80.45	1662.68	0.23	1.96	1.65	1.30
Ca I 10839 Å	310.38	25.64	70.98	-284.94	0.05	1.53	0.88	2.39

SOURCE: Author

Table 7.3 - Retrieved parameters from the Stokes profiles presented in Figure 7.4. The parameters are obtained with the inversion of the Si I, He I and Ca I lines for a pixel in the border of the filament 1 (highlighted with number 3 in Figure 7.1)

Line	B [G]	χ [°]	γ [°]	v_{LOS} [ms^{-1}]	$\Delta\lambda_{\mathrm{D}}$ [Å]	$S1$	η_0	a
Si I 10827 Å	854.89	63.13	119.41	624.86	0.05	4.76	9.62	1.34
He I 10830 Å	580.41	-19.11	85.83	3807.19	0.20	1.63	1.56	5.01
Ca I 10839 Å	652.68	69.13	97.90	-48.51	0.02	1.01	2.09	3.25

SOURCE: Author

Figure 7.2 - Stokes profiles for the full spectral range observed with GRIS over the umbra of the leading sunspot (point 1 of Figure 7.1). The black points represent the observed spectrum, and the red line is the best fit obtained with the HeLix$^+$ inversion code. The vertical gray dashed lines are, from the left, the Si I 10827 Å the He I 10830 Åa,b,c triplet, and the Ca I 10839 Å. The blue dashed line outlines the telluric line recovered to be excluded from the He red component. The magnetic field retrieved for the photosphere using the Si line is $B \approx 1960$ G, $\gamma \approx 13°$, and $\chi \approx -87°$. For the upper chromosphere the magnetic field recovered is $B \approx 971$ G, $\gamma \approx 3°$, and $\chi \approx -79°$. The full parameters are described in Table 7.1

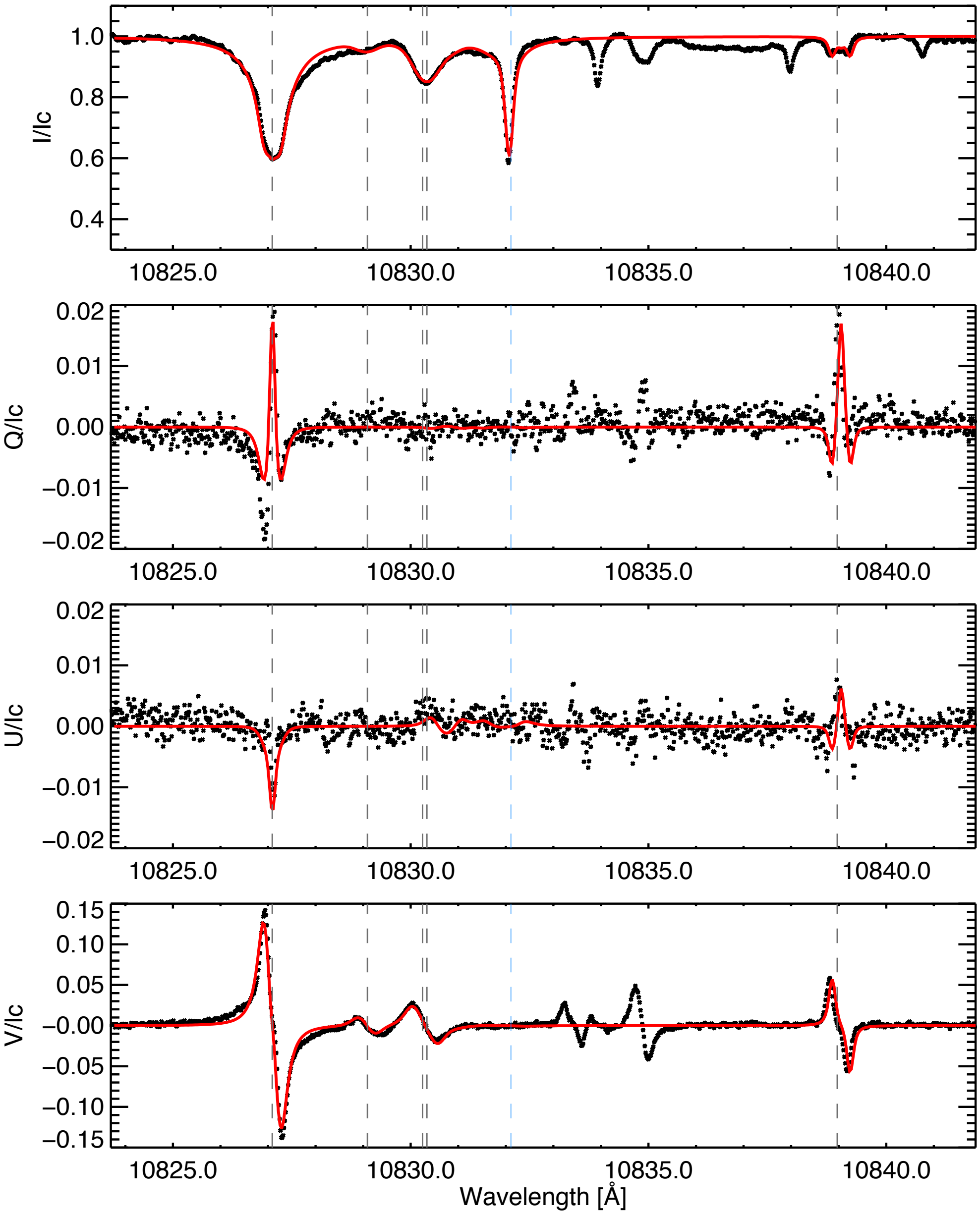

SOURCE: Author

Figure 7.3 - Stokes profiles for the full spectral range observed with GRIS over the center of the first filament (point 2 of Figure 7.1). The black points represent the observed spectrum, and the red line is the best fit obtained with the HeLix$^+$ inversion code. The vertical gray dashed lines oare, from the left, the Si I 10827 Å the He I 10830 Åa,b,c triplet, and the Ca I 10839 Å. The blue dashed line outlines the telluric line recovered to be excluded from the He red component. The magnetic field retrieved for the photosphere using the Si line is $B = 734$ G, $\gamma = 32°$, and $\chi = 75°$. For the upper chromosphere the magnetic field recovered is $B = 436$ G, $\gamma = 80°$, and $\chi = 27°$. The full parameters are described in Table 7.2

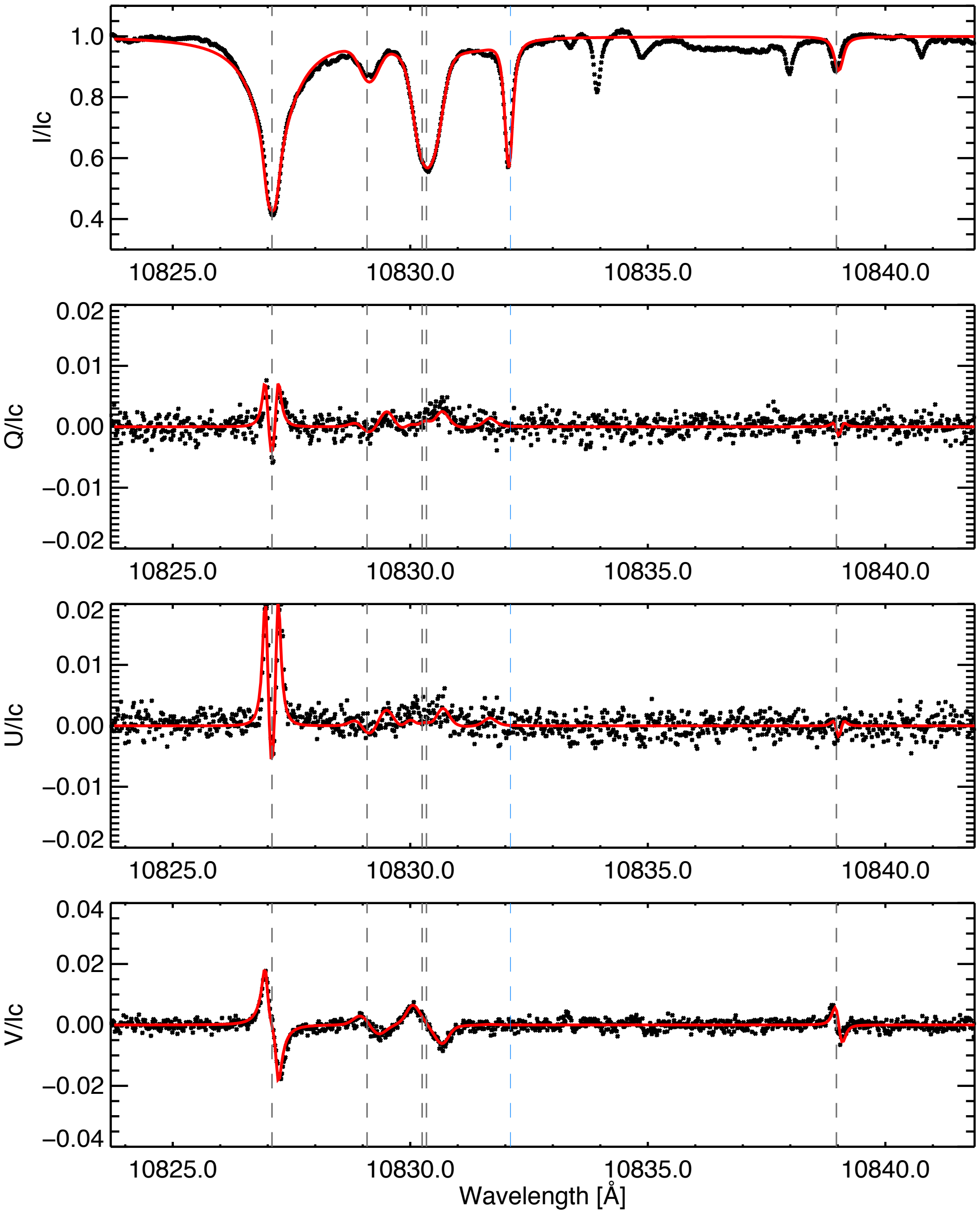

SOURCE: Author

Figure 7.4 - Stokes profiles for the full spectral range observed with GRIS in a border of the first filament (point 3 of the Figure 7.1). The black points represent the observed spectrum, and the red line is the best fit obtained with the HeLix$^+$ inversion code. The vertical gray dashed lines are, from the left, the Si I 10827 Å, the He I 10830 Åa,b,c triplet, and the Ca I 10839 Å. The blue dashed line outlines the telluric line recovered to be excluded from the He red component. The magnetic field retrieved for the photosphere using the Si line is $B = 735$ G, $\gamma = 71°$, and $\chi = 30°$. For the upper chromosphere the magnetic field recovered is $B = 509$ G, $\gamma = 74°$, and $\chi = 17°$. The full parameters are described in Table 7.3

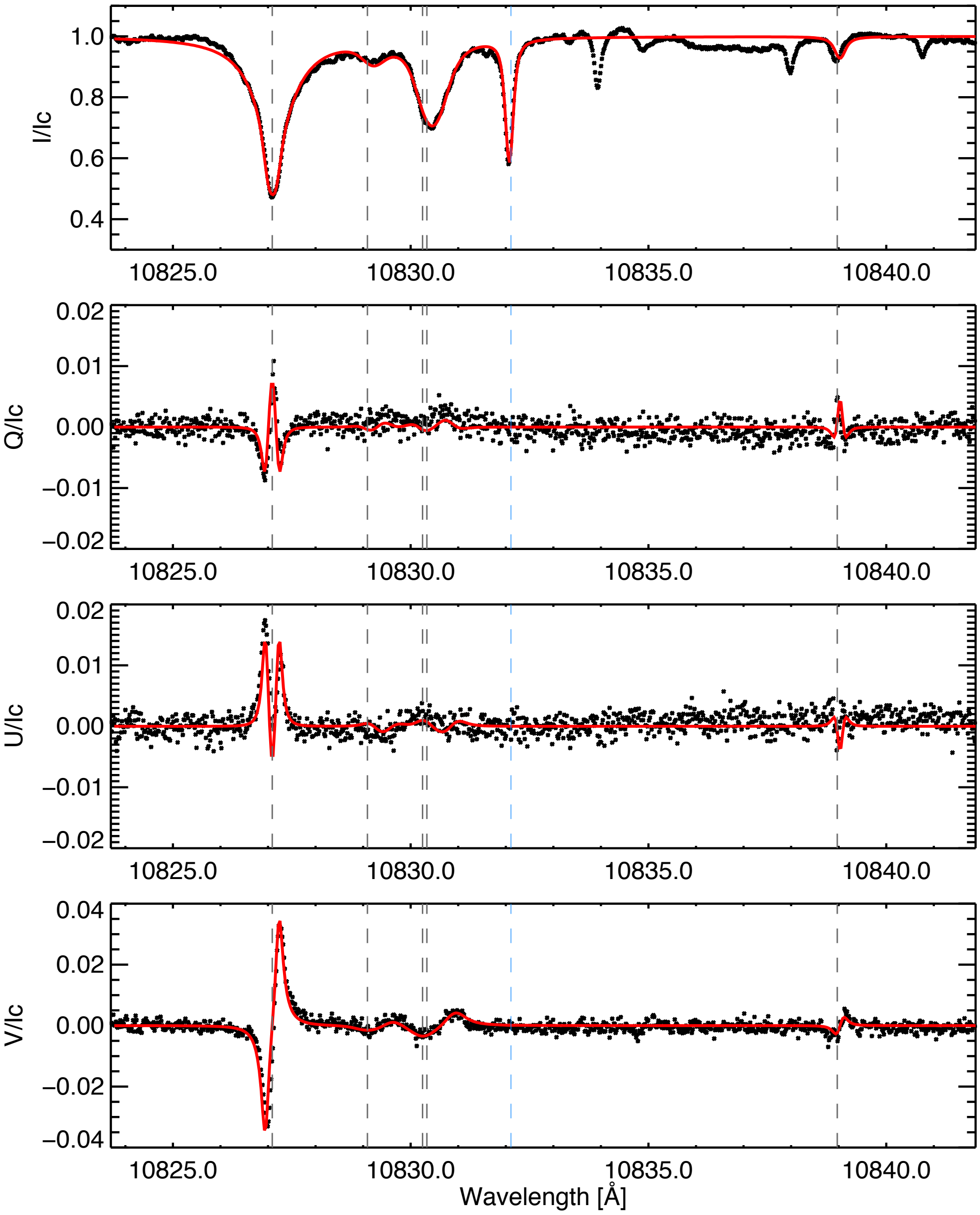

SOURCE: Author

Table 7.4 - Retrieved parameters from the Stokes profiles presented in Figure 7.5. The parameters are obtained with the inversion of the Si I, He I and Ca I lines, for a pixel in a surrounding area between the filament 1 and 2. (highlighted with number 4 in Figure 7.1)

Line	B [G]	χ [°]	γ [°]	v_{LOS} [ms^{-1}]	$\Delta\lambda_D$ [Å]	$S1$	η_0	a
Si I 10827 Å	616.54	1.75	104.01	1307.40	0.06	9.25	8.33	1.13
He I 10830 Å	33.89	0.73	101.51	1319.94	0.13	1.62	1.01	4.43
Ca I 10839 Å	261.81	22.22	89.29	176.47	0.01	3.17	1.86	2.82

SOURCE: Author

In order to examine the result of the inversion for the full Stokes profiles with the HeLix$^+$ code, we selected some points we are most interested to establish the magnetic field vector, as well as, the other physical parameters retrieved with the methodology described in this work.

The Figure 7.1 presents the four selected pixels we computed the physical parameters performed with the inversion code. The first point is placed inside the umbral region of the leading sunspot (1), the second point is located in the center of the first filament (2), the third point is positioned in one of the border of the same filament and the fourth point in the surrounding region between the first and second filament.

In this first moment, the inversion was applied for three spectral lines simultaneously, where the two photospheric lines are Si I 10827 Å and Ca I 10839 Å, and for the triplet of the upper chromospheric He I 10830 Å line. The best fit was also obtained for the telluric line at 10832.108 Å in order to extract it from the red component of the He line, similar to the one described in Section 6.1.

The first example of inversion is presented in Figure 7.2, where four panels represent the Stokes I, Q, U, and V profiles, respectively. The profiles are taken for the full spectrum scattered by the grating, from 10823.695 Å to 10841.880 Å (more details in Section 3.2). The black points denote the Stokes profile observed with GRIS in the pixels coordinate (410,88), this position is centered in the region of umbra, belonging to the leading sunspot. The red line is the result of the best fitting obtained with the inversion code for the spectral and telluric lines described before. Each of the gray dashed lines represent one of the spectral lines. The blue dashed line represents the H_2O telluric line that is removed from the red component of the He spectrum.

Figure 7.5 - Stokes profiles for the full spectral range observed with GRIS in the surrounding region between the first and second filament (point 4 of the Figure 7.1). The black points represent the observed spectrum, and the red line is the best fit obtained with the HeLix^{+} inversion code. The vertical gray dashed lines are, from the left, the Si I 10827 Å, the He I 10830 Åa,b,c triplet, and the Ca I 10839 Å). The blue dashed line outlines the telluric line recovered to be excluded from the He red component. The magnetic field retrieved for the photosphere using the Si line is $B = 616$ G, $\gamma = 104°$, and $\chi = 1°$. For the upper chromosphere the magnetic field recovered is $B = 33$ G, $\gamma = 101°$, and $\chi = 0°$. The full parameters are described in Table 7.4

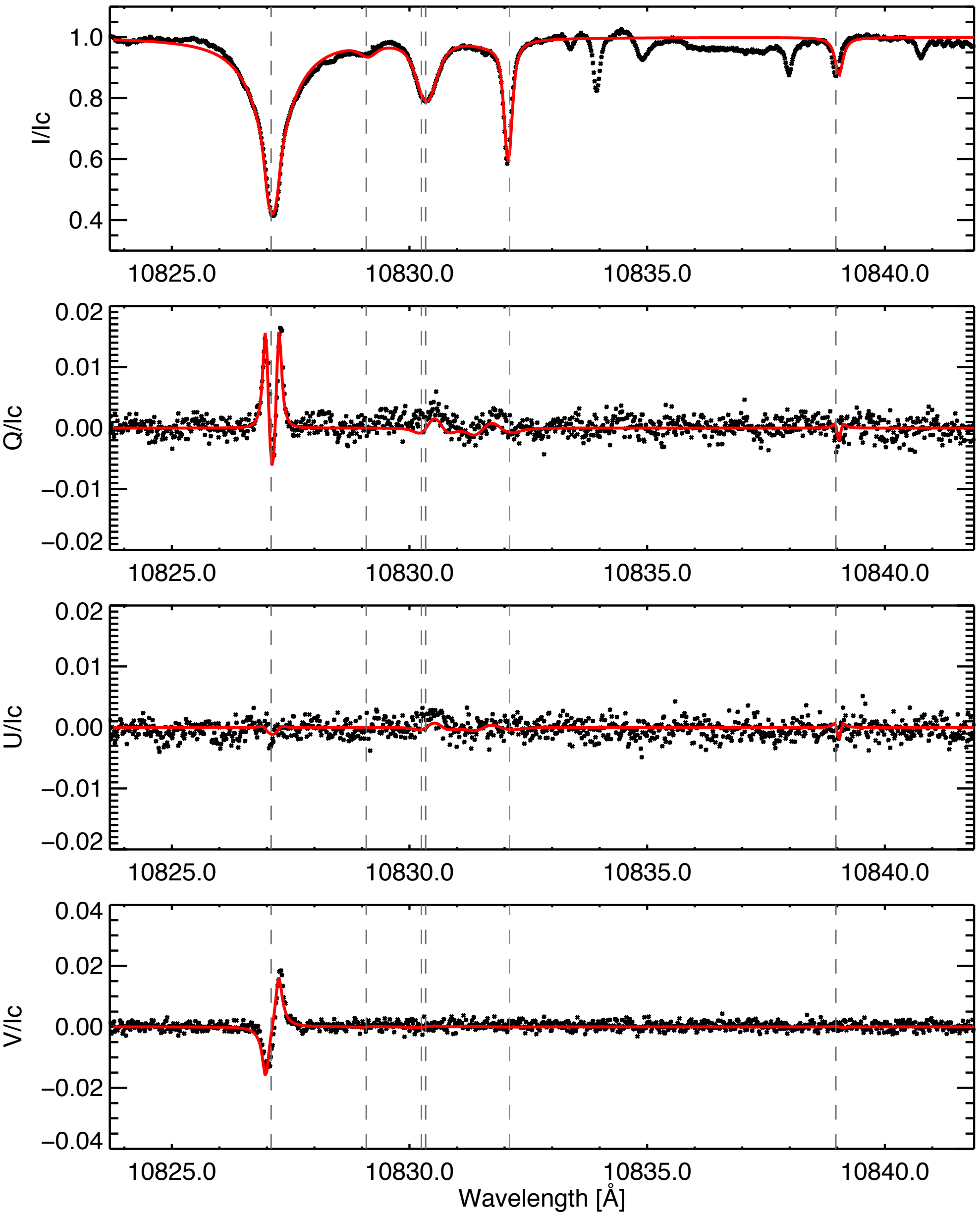

SOURCE: Author

The sunspot umbra has usually a high magnetic field strength, pointing close to perpendicular to its own plane (BRAY; LOUGHHEAD, 1965). The inversion of the Stokes profiles, presented in Figure 7.2, retrieve physical parameters that confirm these sunspot properties. The magnetic field strength in the photosphere, observed with the Si line is 1960 G, with an inclination of only 13°. The close to 0° angle indicate the magnetic field is pointing in the direction of the observer. Then, we can conclude that the leading sunspot has a positive polarity, with the field coming out of this sunspot and connecting in all the trailing pores. The full recovered parameters of the umbra region is presented in Table 7.1.

The Stokes parameters for the center of the filament 1, as well the fitting of the inversion response, is presented in Figure 7.3. The magnetic field strength obtained for the upper chromosphere is 436 G, which means a field much stronger than the observed in QS filaments. The inclination angle is 80°, indicating the magnetic field vector is almost parallel to the solar surface. The full computed parameters of the centered region, is presented in Table 7.2.

Most of the magnetic field strength measurements were conducted for quiescent prominences, all of them observing only a few Gauss in the spine. For AR filaments, the spectropolarimetric measurements using full Stokes with the He I 1083.0 nm line are rare (XU et al., 2012). Observations by Sasso et al. (2007) determined for the first time the magnetic field of an AR filament through its eruption phase and reported a magnetic field strengths in from 100 to 250 G. (KUCKEIN et al., 2009) found field strengths in the range of 600−700 G in the filament at the formation height of the He I. Xu et al. (2012) found strong magnetic fields, from 600 to 800 G in AR filaments.

The inversion solution and the Stokes parameters for the border of the filament 1, is given in Figure 7.4. The magnetic field strength of the border obtained for the upper chromosphere is 580 G, with an inclination angle of 86°. The full computed parameters of the region is presented in Table 7.3.

In the upper chromosphere, the region outside the filaments presented a very weak magnetic field, as presented in Figure 7.5 and the the full parameters are presented in Table 7.4. In the photosphere the magnetic field of the region between filament 1 and 2, is 616 G. On the other hand, the field strength in the upper chromosphere is only 33 G, indicating a very weak field outside the active region.

7.2 Inversion of the full Stokes maps

The section before showed the solution of the inversion method, retrieving the physical parameters of the atmosphere for only one element (98 km x 98 km) of the photosphere and upper chromosphere. However, to properly investigate the arch filament system and its surrounding we need to obtain the physical parameters for all the pixels of the Stokes maps.

The solution of the inversion problem for one pixel can take a few minutes to be performed. However, the inversion for 700 × 476 pixels, considering two Si and two He atmospheres would take a very large processing time. Therefore, when inverting several pixels we made use of parallel computing by using the MPICH (KARONIS et al., 2003). The MPICH divides the array of pixels to the multiple CPUs of several machines.

In this work, the applied the MPICH-3, that make use of the HYDRA as the default process management framework (DONNINGER; LORENZ, 2004). All the inversion processes were performed in the atlas high performance compute cluster from the compute resources of the MPS.

The maps for all the parameters from the inversion of the full-Stokes, observed in the photosphere with the Si I 10827 Å line, are presented in Figure 7.6. The magnetic field Strength (B) of the photospheric region reaches almost 2.5 kG in the leading sunspot umbra and presents few Gauss in the region outside the penumbra, as presented in Figure 7.6(a). The penumbra is overspread around and between the leading sunspot umbra and trailing pores.

The azimuth angle (χ) is displayed in Figure 7.6b with a range from -90° to +90°, so it does not cover all the possible azimuth angle, indicating only a direction of the field in the plane, without presenting the vector sense. This limitation is derived from the azimuth determination based on the ratio between Stokes Q and U, as presented in Equation (7.8). The equation creates a 180° ambiguity in the azimuth angle that needs to be solved in this work. The detailed solution of the ambiguity is described in Section 7.5.1. A positive value of the azimuth designates a counterclockwise angle.

Figure 7.6 - Maps of all the parameters retrieved from full-Stokes for the photosphere, using the Si I 10827 Å line. (*a*) The magnetic field Strength (B), (*b*) the azimuth angle (χ), (*c*) the incination angle (γ), (*d*) the Doppler velocity (v_{LOS}), (*e*) the Doppler width ($\Delta\lambda_D$), (*f*) the gradient of source function ($S1$), (*g*) the opacity ratio between spectral line center and continuum (η_0) and (*h*) the damping factor (a).

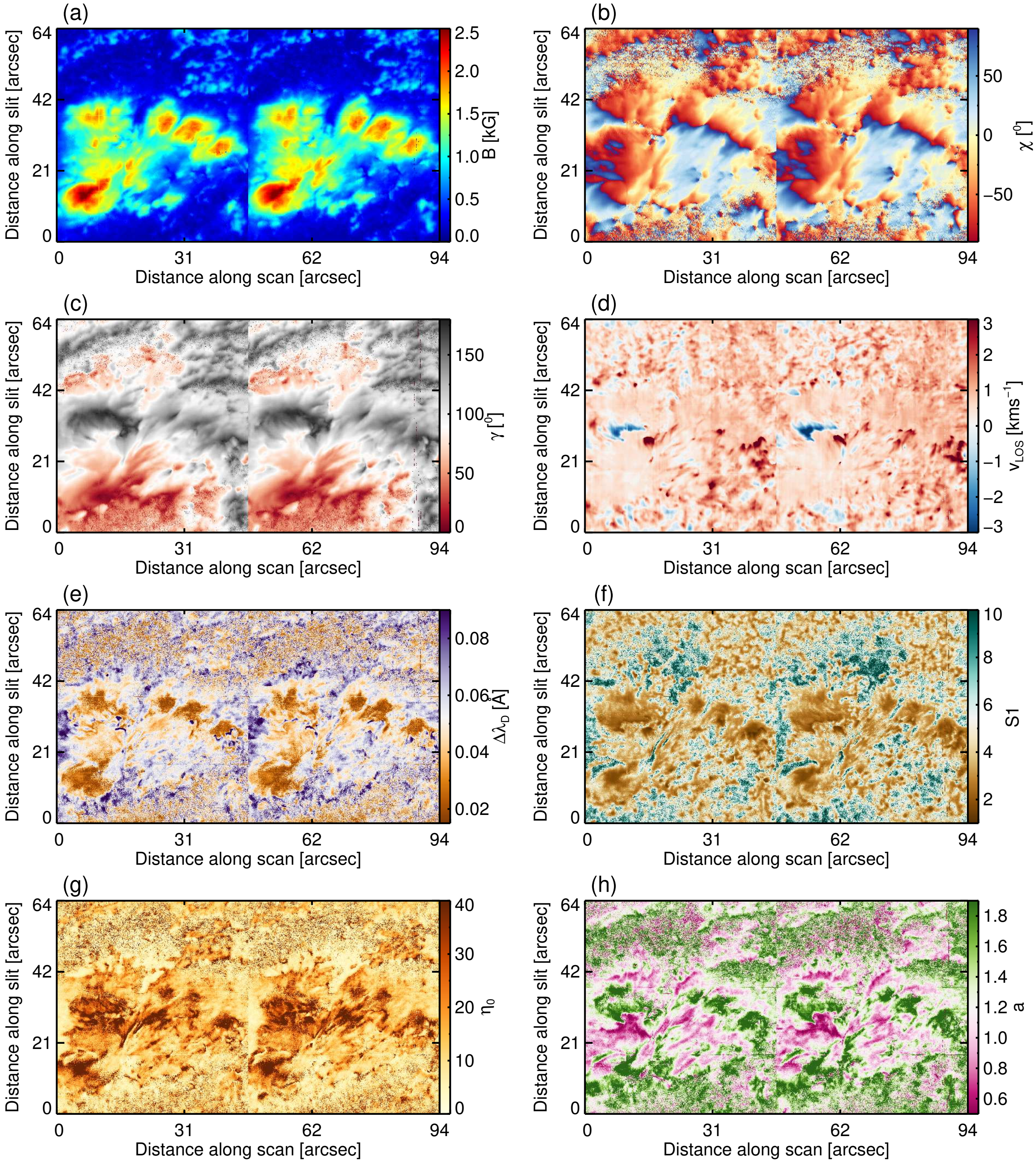
(a)
B [kG]
2.5
2.0
1.5
1.0
0.5
0.0
(b)
χ [⁰]
50
0
−50
(c)
γ [⁰]
150
100
50
0
(d)
v_LOS [kms⁻¹]
3
2
1
0
−1
−2
−3
(e)
Δλ_D [Å]
0.08
0.06
0.04
0.02
(f)
S1
10
8
6
4
2
(g)
η₀
40
30
20
10
0
(h)
a
1.8
1.6
1.4
1.2
1.0
0.8
0.6
Distance along slit [arcsec]
0
21
42
64
Distance along scan [arcsec]
0
31
62
94

SOURCE: Author

The magnetic field inclination angle has a 180° range, with 0 pointing perpendicular to the surface, in the direction of the observer. So, from 90° to 180°, the magnetic field have a negative signal, and from 0° to 90°, a positive signal. Inclination angle of 90° means the magnetic field is total transverse. The map of the inclination angle is displayed in Figure 7.6*c*.

In the photosphere, the Doppler speed is usually very low, in the order of less than 3 kms^{-1}, as presented in Figure 7.6*d*. More details about the Doppler velocity in the full map, as well in the filaments is described in Chapter 6. The Doppler width in the photosphere is usually much lower than in the chromosphere, as presented in Figure 7.6*e*.

The inversion is performed simultaneously for the photosphere and upper chromosphere. The maps for all the parameters retrieved from the chromosphere, with the He I 10830 Å line, is presented in Figure 7.7. From the panel (*a*) we can note that the magnetic field strength is lower than the one in the photosphere. We determined that the mean magnetic field strength is 675 G in the photosphere and 537 G in the chromosphere.

In photosphere, the inclination angle has higher rates in the regions of a strong magnetic field, than the one in the chromosphere. It is expected once the chromosphere has a higher altitude and the magnetic field tends to be close to perpendicular in the emerging flux region and more inclined as higher we measure the field. The inclination between both layers presented a high correlation ($R = 0.831$) for the full map, and the mean angle is about 97° for both.

For the photosphere, the Dopper width is 0.05 Å and for the upper chromosphere it is 0.19 Å as displayed in Figure 7.7.

Figure 7.7 - Maps of all the parameters retrieved from the inversion of full-Stokes, observed in upper chromosphere using the He I 10830 Å line. (*a*) The magnetic field Strength (B), (*b*) the azimuth angle (χ), (*c*) the incination angle (γ), (*d*) the Doppler velocity (v_{LOS}), (*e*) the Doppler width ($\Delta\lambda_D$), (*f*) the gradient of source function ($S1$), (*g*) the opacity ratio between spectral line center and continuum (η_0) and (*h*) the damping factor (a).

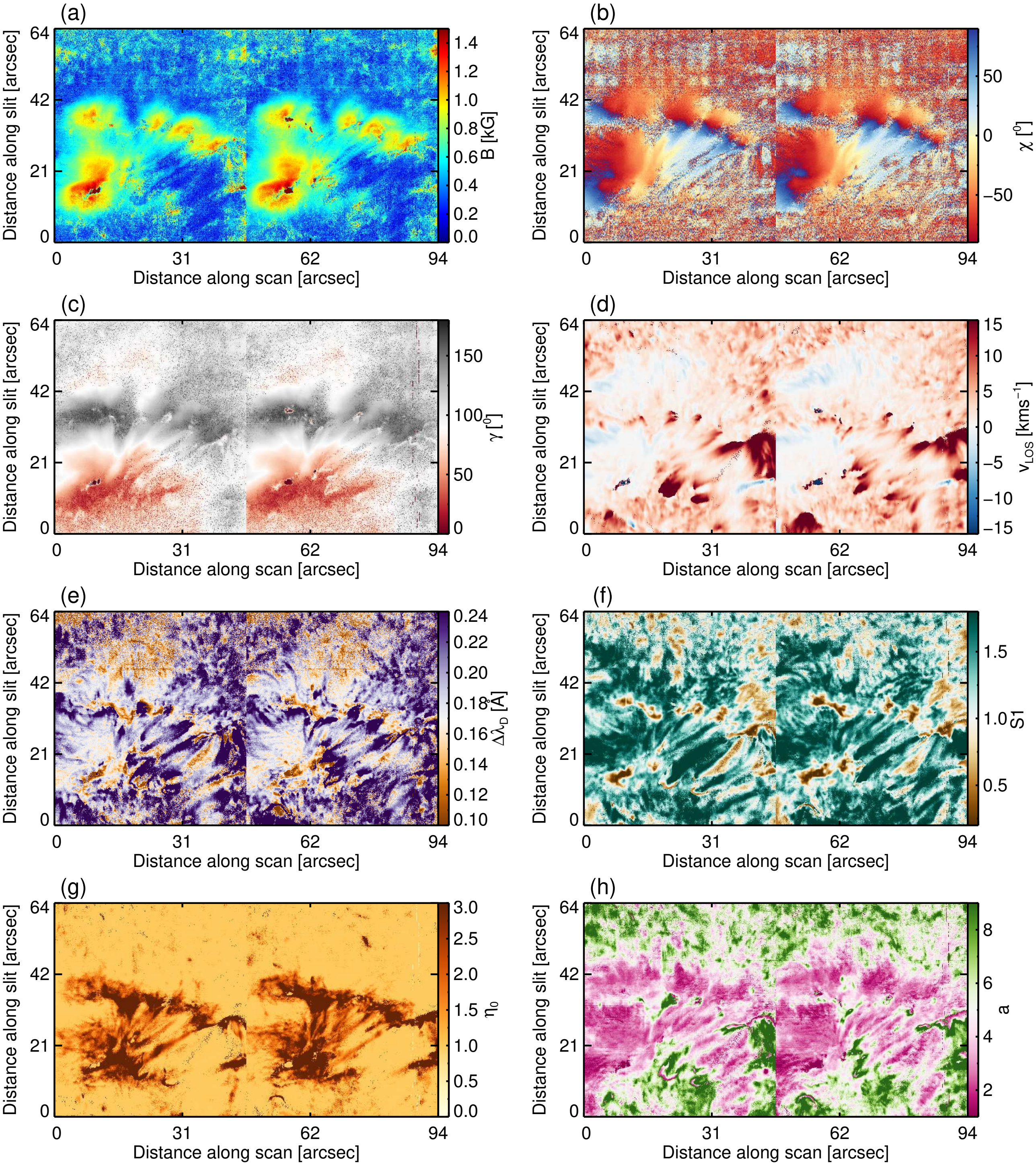
(a)
B [kG]
1.4
1.2
1.0
0.8
0.6
0.4
0.2
0.0
(b)
χ [°]
50
0
−50
(c)
γ [°]
150
100
50
0
(d)
v_LOS [kms⁻¹]
15
10
5
0
−5
−10
−15
(e)
Δλ_D [Å]
0.24
0.22
0.20
0.18
0.16
0.14
0.12
0.10
(f)
S1
1.5
1.0
0.5
(g)
η₀
3.0
2.5
2.0
1.5
1.0
0.5
0.0
(h)
a
8
6
4
2
Distance along slit [arcsec]
64
42
21
0
Distance along scan [arcsec]
0
31
62
94

SOURCE: Author

7.3 Analysis of the magnetic field in the filaments

We can determine the transverse (B_{TRA}) and longitudinal (B_{LOS}) components of the magnetic field vector, from the parameters retrieved of the Stokes profiles, presented in the Figures 7.6 and 7.7. The (B_{TRA}) and (B_{LOS}) for each element were calculated using the equations given by Degl'Innocenti (1992):

$$B_{TRA} = f|\mathbf{B}|\sin\gamma, \tag{7.1}$$

$$B_{LOS} = \sqrt{f}|\mathbf{B}|\cos\gamma, \tag{7.2}$$

where f is the filling factor. For the inversion of the He I 10830 Å line we can assume $f = 1$, as discussed in Section 7.1. The longitudinal index is represented by LOS, meaning the line-of-sight direction. The LOS component of the magnetic field vector is quite essential in this work, once both photospheric and chromospheric LOS fields are the main input for the LFF extrapolation, described in Section 7.8.

The LOS magnetic field component for the upper chromosphere and photosphere are presented in Figure 7.8. The black solid contours represent the filaments, the white solid line designates the sunspot umbras and pores compounding the NOAA AR 12552, and the white dashed line outlines the penumbral region observed in the continuum. In the background panel, the red color represents the outward magnetic field (positive, in the direction of the observer), and the blue denotes the inward magnetic field (negative).

In the chromosphere, the region surrounding the active region present a faint LOS field. Moreover, the same weak field is found in the filament. However, from Figure 7.7*a*,*b* we note that it results not from a weak magnetic strength, but from to the high transverse field, with almost no vertical field vector found in the center of the filament.

The distribution of the magnetic strength inside the filaments is presented in the histograms of Figure 7.9, where the top panels (a-d) are the histograms for each filament in the upper chromosphere, and the bottom panels (e-h) the distribution for the filaments in the photosphere. The binsize is 50 G for all the histograms and the filaments are highlighted in Figure 7.8.

Figure 7.8 - LOS magnetic field component for the chromosphere (*top*) and photosphere (*bottom*). The black contours are the filaments, the white solid line contours the sunspot umbras and pores, and the white dashed line outlines are the penumbral region. In the background, the red color represents the outward magnetic field (positive, in the direction of the observer), and the blue denotes the inward magnetic field (negative). In the chromosphere, the region surrounding the AR present a week field. The same week field is found in the B_{LOS} component of the filament fields due to the high transverse field found in the filament.

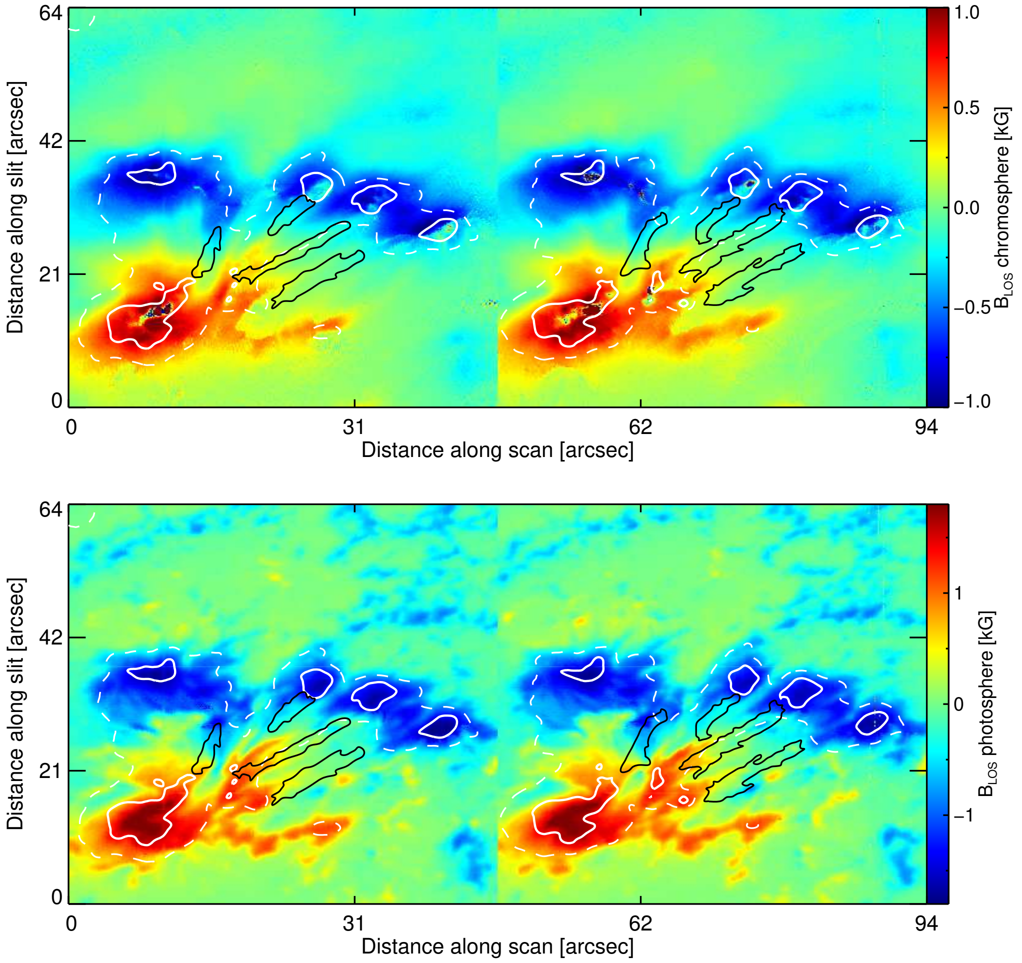

SOURCE: Author

Figure 7.9 - Histogram of the magnetic field strength distribution inside each filament, in the upper chromosphere (*top*) and photosphere (*bottom*), highlighted in Figure 7.8. The blue curve outlines a Gaussian distribution with center and FWHM displayed in the upper right position of each panel. The y-axis is the histogram density that is fixed for all the plots, based on the distribution with the highest peak. The binsize is 50 G.

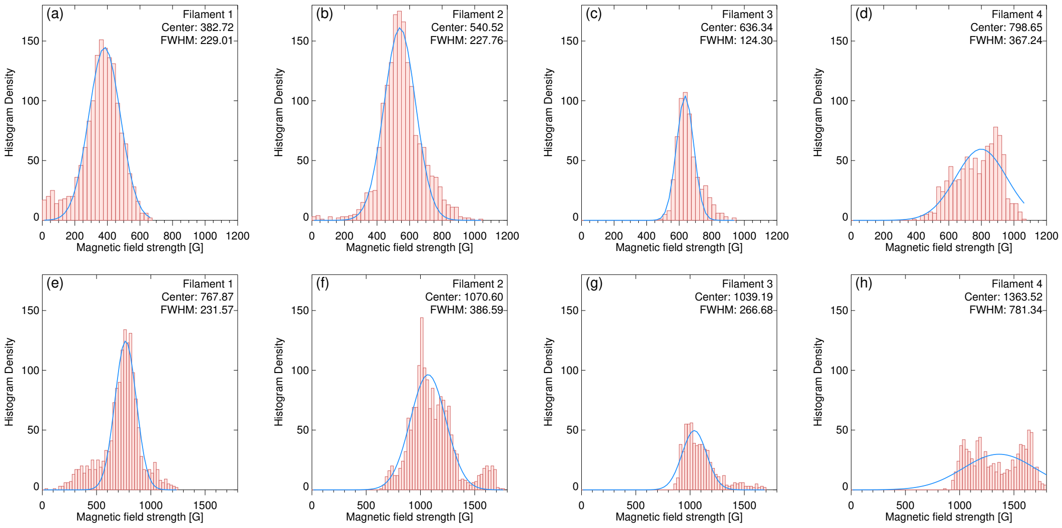

SOURCE: Author

Observations by Sasso et al. (2007) determined for the first time the magnetic field of an AR filament through its eruption phase and reported a magnetic field strengths from 100 to 250 G. (KUCKEIN et al., 2009) found field strengths in the range of 600−700 G in the filament at the formation height of the He I. Xu et al. (2012) found strong magnetic fields, from 600 to 800 G in filaments over active regions.

In the present work, we find an average magnetic field of about 382 G, 540 G, 636 G, and 798 G, for the filament 1-4, respectively. The magnetic field strength in the photosphere in the regions of the filaments are almost twice the value in the chromosphere, with a range from 767.87 G to 1363.52 G. The average magnetic field strength, based on the histogram centers is 589.80 G for the chromosphere and 1060.29 G for the photosphere.

Figure 7.10 - Histogram of the inclination angle distribution inside each filament, in the upper chromosphere (*top*) and photosphere (*bottom*), highlighted in Figure 7.8. The blue curve outlines a Gaussian distribution with center and FWHM displayed in the upper right position of each panel. The y-axis is the histogram density that is fixed for all the plots, based on the distribution with the highest peak. The binsize is 5°.

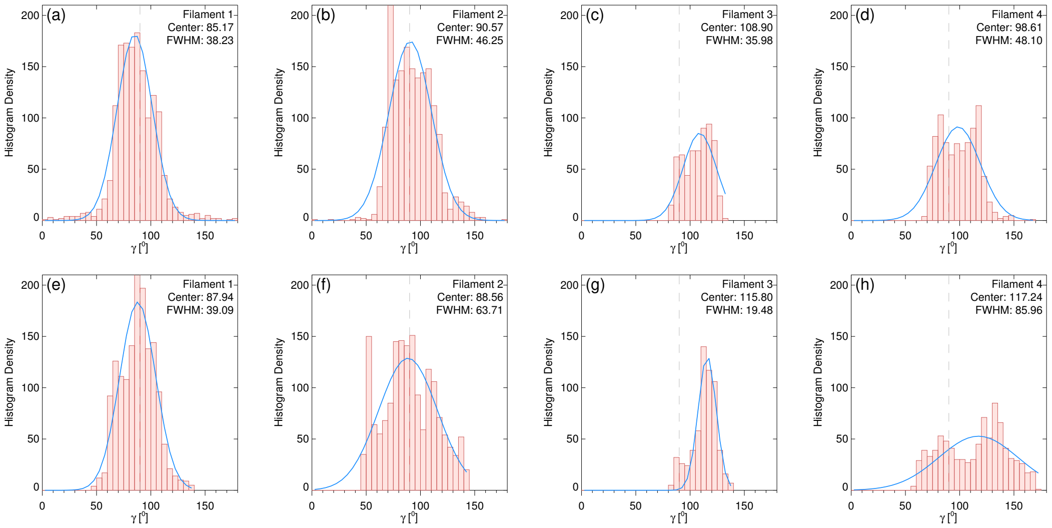

SOURCE: Author

The distribution of the inclination angle of the magnetic field inside the filaments is presented in the histograms of Figure 7.10, where the top panels (a-d) are the histograms for each filament in the upper chromosphere and the bottom panels (e-

h) the distribution for the filaments in the photosphere. The binsize is 5° for all the histograms and the filaments are highlighted in Figure 7.8.

In the present work, we find an average inclination angle of 85.17°, 90.57°, 108.9°, and 98.51°, for the filament 1-4, respectively. The inclination in the photosphere over the regions of the filaments presents a similar angle than in the upper chromosphere, however for most of the pixels it was a little more longitudinal than in the chromosphere, with a range of 87.94° − 117.24°. The average inclination angle over the filament is 95.94° for the chromosphere and 102.38° in the photosphere. The inclination angles in the filaments are more longitudinal as close as the filament is to the sunspots or pores.

From the histograms of Figure 7.10 and the previous paragraph, we can conclude the magnetic field vector over the filaments presents an almost transverse inclination. It results that almost all the magnetic flux is crossing the cross-sectional area of the filament.

Figure 7.11 - Histogram distribution of the azimuth angle in the upper chromosphere over each filament, in the upper chromosphere (*top*) and photosphere (*bottom*), highlighted in Figure 7.8. The blue curve outlines a Gaussian distribution with center and FWHM displayed in the upper right position of each panel. The y-axis is the histogram density that is fixed for all the plots, based on the distribution with the highest peak.

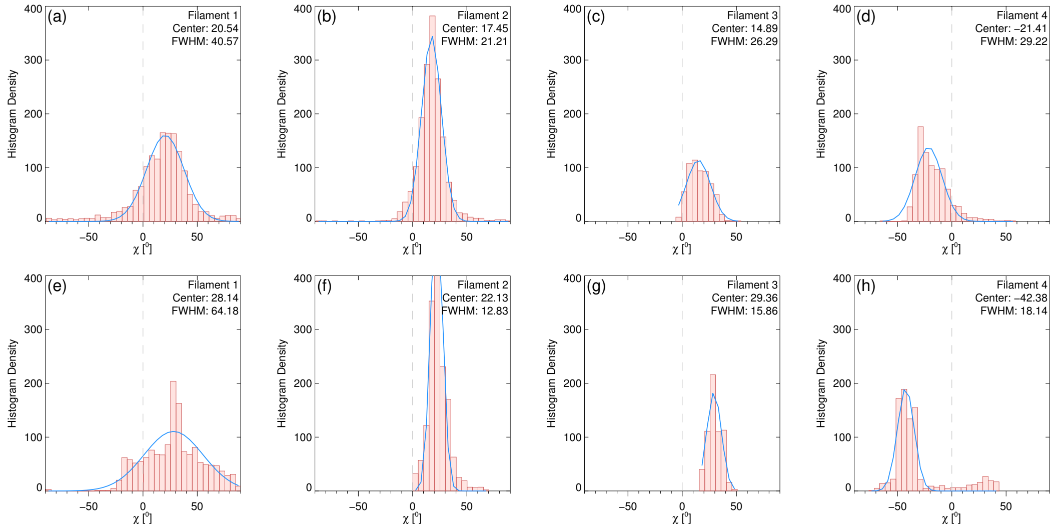

SOURCE: Author

The distribution of the magnetic field azimuth angle inside the filaments is presented in the histograms of Figure 7.11, where the top panels (a-d) are the histograms for each filament in the upper chromosphere and the bottom panels (e-h) the distribution for the filaments in the photosphere. The binsize is 5° for all the histograms.

In the present work, we find an average azimuth angle of 20.54°, 17.45°, 14.89°, and -21.41°, for the filaments 1-4, respectively. The azimuth angle in the photosphere over the regions of the filaments presents a larger angle than in the upper chromosphere, with 28.14°, 22.13°, 29.36°, and -42.38° for the filament 1-4, respectively.

Figure 7.12 - Scatter plot of the LOS magnetic field in the chromosphere vs the LOS magnetic field in the photosphere for the region inside of the filaments contoured in the in Figure 7.8. The red line is the interpolation of the B_{LOS} field distributions, considering always crossing the (0,0) coordinate, so $B_{Chrom} = sB_{Photo}$, where s is the slope, and $\langle s \rangle = 0.36$. The LOS field components has a high correlation between photosphere and chromosphere ($\langle R \rangle = 0.843$).

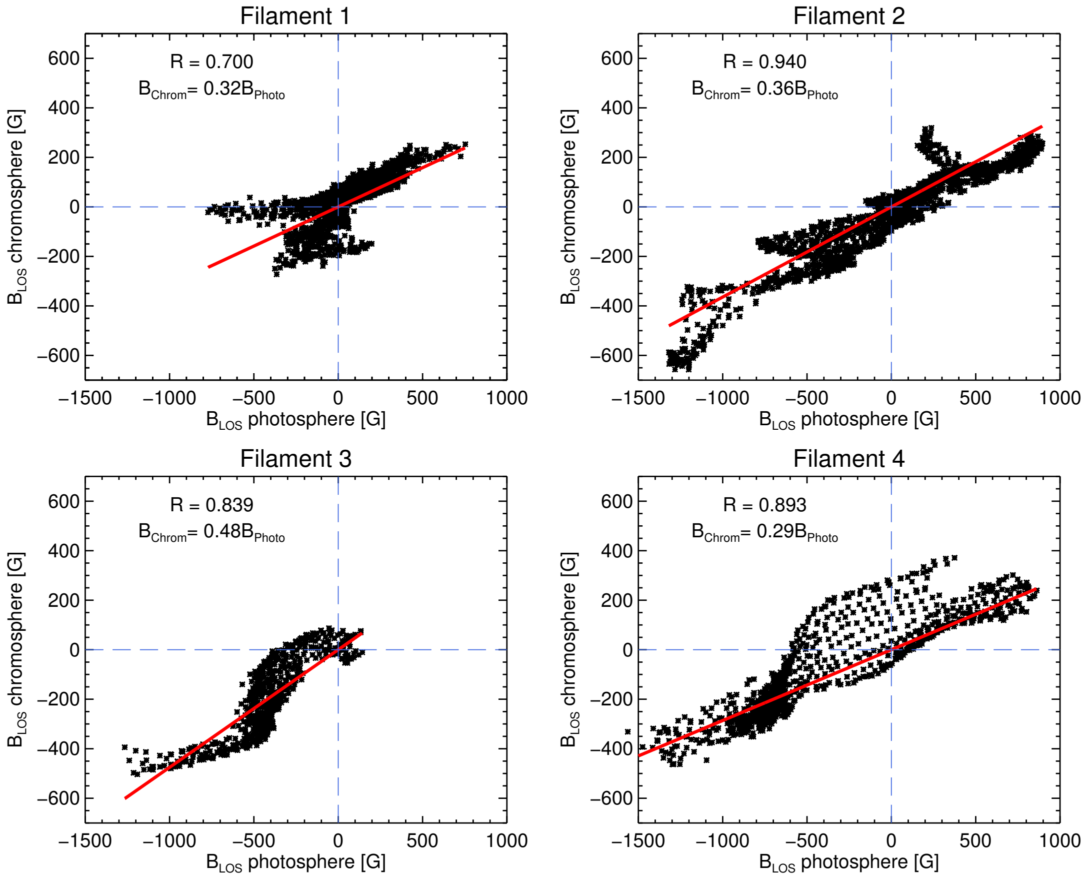

SOURCE: Author

The relation between the inclination angle of the filaments in the photosphere and upper chromosphere can be analyzed by correlating the magnetic field in the line of sight for both layers. We made use of a scatter plot for both LOS fields, chromosphere vs. photosphere, inside of the filaments displayed in Figure 7.8.

The result of the scatterplot is presented in Figure 7.12. The red line is the interpolation of the B_{LOS} field distribution, considering it cross the (0,0) coordinate, so $B_{Chrom} = sB_{Photo}$, where s is the slope between the fields.

It was determined the correlation coefficient (R) by computing the linear Pearson correlation. We find that the LOS field component holds a high R between photosphere and chromosphere, with $R = 0.7$, 0.94, 0.84, and 0.90, for the filaments 1-4, respectively. The average correlation coefficient is $\langle R \rangle = 0.843$, and the average slope is $\langle s \rangle = 0.36$.

We determine a relation between the LOS magnetic field in the photosphere and upper chromosphere, with a high correlation coefficient. It indicates that the LOS magnetic field in the photosphere presents a strength almost three times larger than in the chromosphere. A potential explanation for the high correlation coefficient is that the magnetic loops coming from the emerging flux region, that was introduced in Section 5.2, follow a close inclination angle along the filament. So, from the equation (7.2), the $\cos\gamma$ are quite similar for both layers. The ratio between the LOS magnetic field strength is explained by the difference in the formation height of the He I, in the upper chromosphere and Si, in high altitudes of the photosphere. Both spectral lines formation are better described in Section 1.4

7.4 Polarity inversion line

The filaments are found in upper chromosphere and lower corona, disposed above the magnetic *polarity inversion line* (PIL) of the photospheric magnetic field (BABCOCK; BABCOCK, 1955; ZIRKER, 1989). The PIL is the borderline which separates the two opposite magnetic polarities (MARTIN, 1973). According to Martin (1998), the occurrence of a PIL is a requirement, but not a sufficient condition for the development of a filament. For a filament to rise, a filament channel must exist at the chromosphere height (GAIZAUSKAS, 1998).

Identifying the location of PILS has exceptional importance for the study of solar eruptive phenomena. Historically, neutral lines in active regions have been widely used for predicting the positions of solar flares and CMEs (FALCONER et al., 2002).

They were also used to map and extrapolate coronal structures associated with filaments (MARTIN et al., 1994; CHAE et al., 2001).

Few works have been developed to perform a PIL determination. Therefore, we have developed a code that determinate the PILs, by using the magnetic field strength and inclination from the inversion data. The method is based on smoothing using a Butterwolf low pass-filter (BUTTERWORTH, 1930; ADELMANN, 1998). Histogram equalization is used to enhance the image contrast. The edge detection is determined by using a Canny edge detector (CANNY, 1986). The curve interpolation was performed using a cubic spline interpolation and the pixel discretization using the Bresenham's line algorithm (BRESENHAM, 1965).

The resulting PIL obtained for the photosphere is presented in Figure 7.13. The black lines are the PIL for the photosphere, and the wider black line is the main PIL that are involved with the filaments. The Figure 7.14 show the inclination error for the photosphere. The angular error was less than 2°, showing that the PIL determination was successfully achieved.

The chromospheric PIL is presented in Figure 7.15. The black lines are the Polarity inversion lines (PIL) for the chromosphere, and the broadest black line is the main PIL that are involved with the filaments. The Figure 7.16 shows the inclination error for the chromospheric PIL. The error is less than 2° for most of the data. However, in the final PIL points, the error increases due to faint Stokes V in He I 10830 Å due to low magnetic field strength.

In order to obtain all the pixel coordinates of the PIL, as well to have a better approximation of distance along it, we made use of a parametric cubic spline interpolation. To get the correct pixels coordinates representing the PIL curve, as well as, the accurate distance along the PIL, we need to discretize the PIL in pixels coordinates. To perform the discretization, we made use of the Bresenham's line drawing (BLD) algorithm (BRESENHAM, 1965). The method decides the position of the points that should be chosen in a raster (or bitmap) to produce the closest approximation to a line between each two pixels.

If the Bresenham discretization step were not performed, we should disregard any physical interpretation of the distances along the curve, since non-discretization in the pixel raster leads to huge errors of the spatial dimension in image processing.

Figure 7.13 - LOS-Magnetic field for the photosphere obtained with the full Stokes inversion. The black lines are the Polarity inversion lines (PIL) for the photosphere, and the wider black line is the main PIL that is associated with the filaments.

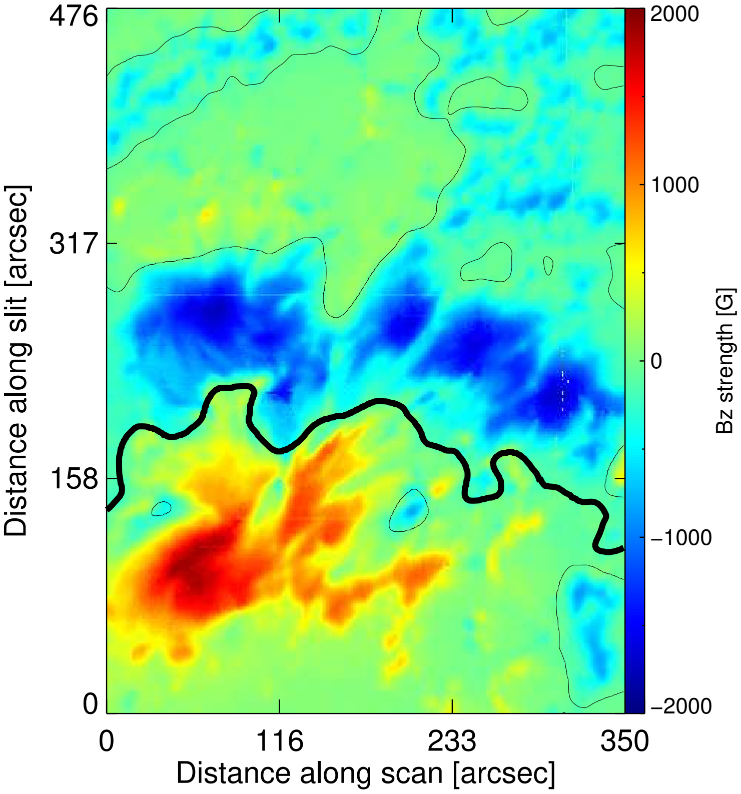

SOURCE: Author

Figure 7.14 - Inclination error for the PIL performed in Figure 7.13, on the photosphere. The angular error is less than 2°.

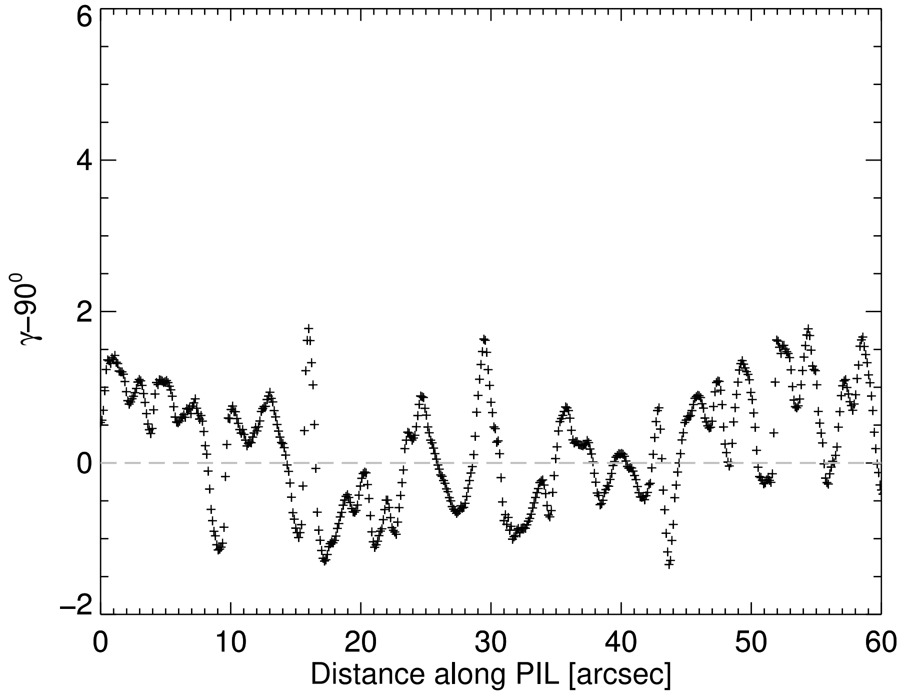

SOURCE: Author

Figure 7.15 - LOS-Magnetic field for the chromosphere obtained with the inversion of full Stokes. The black lines are the Polarity inversion lines (PIL) for the chromosphere, determined by using Butterwolf low-pass filter, histogram equalization, and edge detection. The broadest black line is the main PIL that is associated with the filaments.

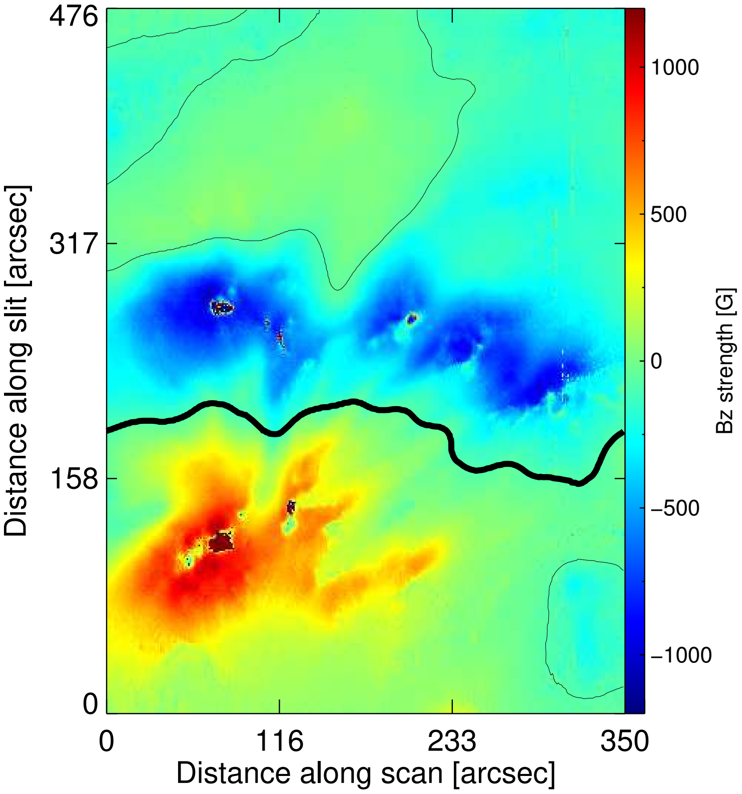

SOURCE: Author

Figure 7.16 - Inclination angular error for the PIL performed in Figure 7.13 for the chromosphere. The angular error is less than 2° for most of the data. However, in the final PIL points, the error increases due to the faint Stokes V intensity for the He I 10830 Å when the magnetic field strength is low.

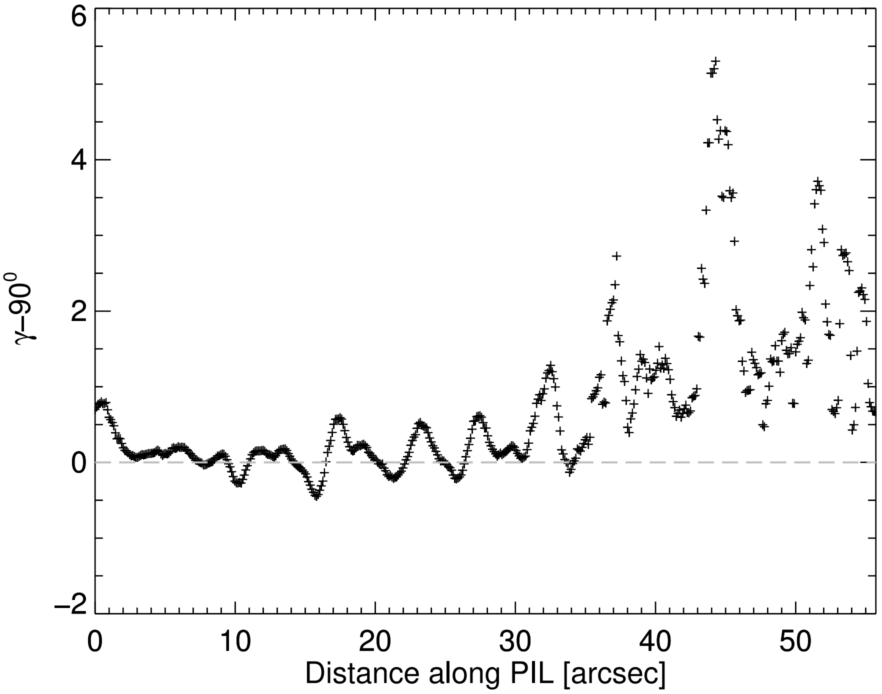

SOURCE: Author

7.5 Determination of the magnetic field vector

It is possible to infer the magnetic field vector from the full Stokes inversion obtained with the HeLIx^{+} code, once the output data includes the magnetic field strength, azimuth, and inclination angle. However, the determination of the magnetic field from the Zeeman effect produces a non-unique solution for the azimuth component of the magnetic field vector.

The projection of **B** over the $x-$, $y-$ (perpendicular to the LOS) and $z-$axis (parallel to the LOS) is given by:

$$B_x = |\mathbf{B}| \sin\gamma \cos\chi, \tag{7.3}$$

$$B_y = |\mathbf{B}| \sin\gamma \sin\chi, \tag{7.4}$$

$$B_z = |\mathbf{B}| \cos\gamma, \tag{7.5}$$

where γ is the inclination angle of **B** with respect to the LOS and χ is the azimuth angle in the $x - y$ plane. A better visualization of the magnetic field vector and its components is presented on Figure 7.17.

Figure 7.17 - Projection of the vector magnetic field **B** onto the local frame. The γ is the inclination angle of **B** with respect to the line-of-sight (LOS). The χ is the azimuth angle of **B** projection in the $x - y$ plane with respect to the x-axis. Positive azimuth angle is counterclockwise.

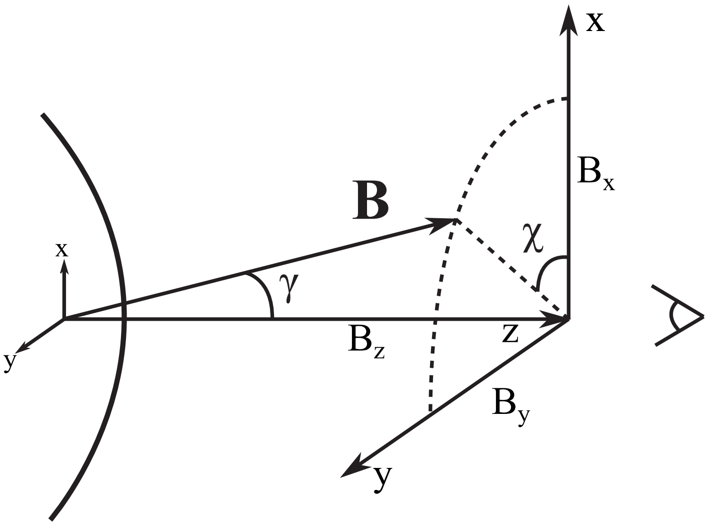

SOURCE: Author

Using the weak field approximation (see Degl'Innocenti (1992)), the relation between the Stokes Q and U can be given by Degl'Innocenti and Landolfi (2004):

$$Q(\lambda) \propto \sin^2\gamma \cos 2\chi, \tag{7.6}$$

$$U(\lambda) \propto \sin^2\gamma \sin 2\chi. \tag{7.7}$$

According to the proposed by Auer et al. (1977), the azimuth angle (χ) can be approximated by the ratio between $Q(\lambda)$ and $U(\lambda)$, as,

$$\chi = \frac{1}{2}\tan^{-1}\left(\frac{U(\lambda)}{Q(\lambda)}\right). \tag{7.8}$$

Before the correction of the azimuth ambiguity, we need to adjust the azimuthal angle from the observation data to the image map, due to the scan direction and slit orientation. The +Q direction for GRIS is always pointing to terrestrial North. The azimuthal angle starting with 0° at the +y direction of the map is given by:

$$\chi_{map_y} = \chi_Q + (\alpha_{slit} - 180^0), \tag{7.9}$$

where α_{slit} is the slit angle presented in Figure 7.18.

7.5.1 Azimuth ambiguity

Analyzing the Equations (7.6) and (7.7), we note that due to the arc 2χ, the function period changed from 2π to π, it means that a 180° rotation of the azimuth angle produces the same Stokes $Q(\lambda)$ and $U(\lambda)$. Therefore, the azimuth angle presents a 180° ambiguity that needs to be solved.

According to Kuckein (2012), the solution of the 180° ambiguity is not an easy task to be performed and many methods have been proposed to solve it (METCALF et al., 2006). Some of these methods are the *AZAM utility* (LITES et al., 1995), the *Minimum Energy solution* (METCALF, 1994), the *Uniform Shear* (MOON et al., 2003), the *Structure Minimization* method (GEORGOULIS et al., 2004), the *Chiral* method (MARTIN et al., 2008) and the SFQ method (RUDENKO; ANFINOGENTOV, 2011).

The disambiguation techniques are commonly developed for specific instruments dataset and inversion codes, e.g., the AZAM utility is performed with the Milne-Eddington gRid Linear Inversion Network (MERLIN) (LITES et al., 2007). However, there is no default code for the GRIS instrument. Hence, in the present work, we made several tests of algorithms to solve the 180° azimuth ambiguity, and the one we find a best and fast solution for our dataset was the *Super Fast and Quality Azimuth Disambiguation* (SFQ).

The SFQ is a two-step processing method. The first step comprises preliminary azimuth disambiguation, using grid difference metric relying on reference information of the potential field. The second step involves the use of smoothing masks in several scales (RUDENKO; ANFINOGENTOV, 2011).

Almost all the ambiguity correction methods were developed for the photospheric magnetic field. Therefore, for the upper chromosphere, we implemented many modifications in the code, in order to get the best correction.

The result of the magnetic field vector map, with the ambiguity correction, over the LOS-magnetic field is presented in Figure 7.18. The arrows indicate the direction of the magnetic field perpendicular to the LOS plane over the photospheric LOS-fied. The arrow size is given by $\sqrt{Bx^2 + By^2}$.

In order to check the quality of the ambiguity correction, we compare our solution with the one from SDO/HMI, as presented in Figure 7.19. Details of the HMI data is presented in Section 5.2.

The SDO/HMI magnetic vector data were obtained from the JSOC, with the parameters: ‘field’, ‘inclination’, ‘azimuth’ and ‘disambig’. The ‘disambig’ is a Boolean matrix which indicates the vector sence, once the azimuth only presents the vector direction (-90° to 90°). The azimuth correction was processed with the SSWIDL module *hmi_disambig.pro*. More detailed about the HMI data processing is presented in Hoeksema et al. (2014) and Sun et al. (2012).

We can compare the magnetogram reached for the Si I 10827 Å line (Figure 7.18) with the one obtained for the HMI (Figure 7.19). There is a quite similar result between both magnetograms. It confirms we can make use of the SFQ method. The HMI image is transposed and inclined in relation to the Figure 7.18 due to the geometry of the GRIS scan and slit angle presented in Figure 4.1.

The magnetic field vector for the chromosphere, over the LOS-magnetic field, is presented in Figure 7.20. The arrows indicate the direction of the magnetic field perpendicular to the LOS plane. The arrow length is given by $\sqrt{Bx^2 + By^2}$.

Figure 7.18 - Magnetic field azimuth for the photosphere obtained with inversion of the Si I 10827 Å line. The arrows indicate the direction of the magnetic field perpendicular to the LOS plane. The background color is the LOS magnetic field strength

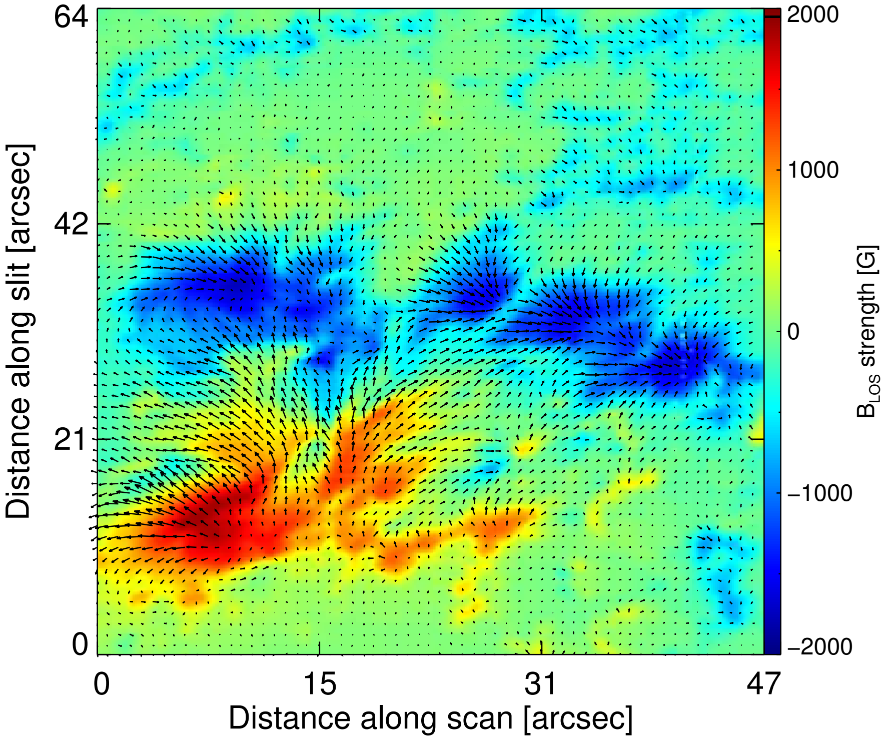

SOURCE: Author

Figure 7.19 - Magnetic field azimuth for the photosphere obtained from the SDO/HMI data, using the MERLIN inversion code and AZAM utility for the 180° ambiguity solution. The HMI image is transposed and inclined in relation to Figure 7.18 due to the scan geometry presented in Figure 4.1. The background color is the LOS magnetic field strength.

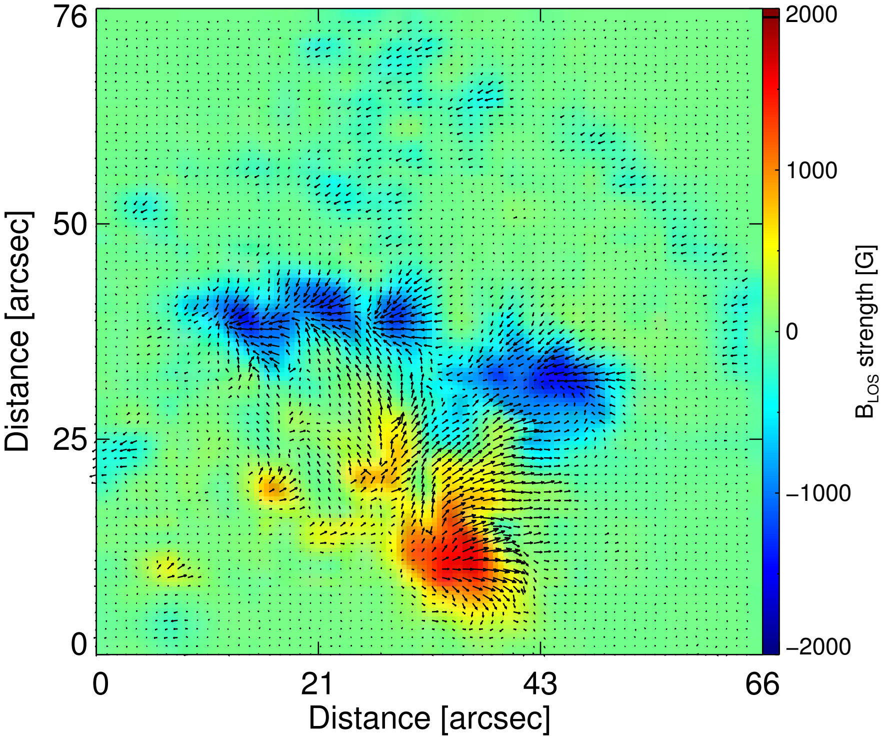

SOURCE: Author

Figure 7.20 - Magnetic field azimuth for the chromosphere obtained with inversion of the He I 10830 Å triplet. The arrows indicate the direction of the magnetic field perpendicular to the LOS plane. The azimuth ambiguity was solved using the SFQ method we modified for the chromosphere.

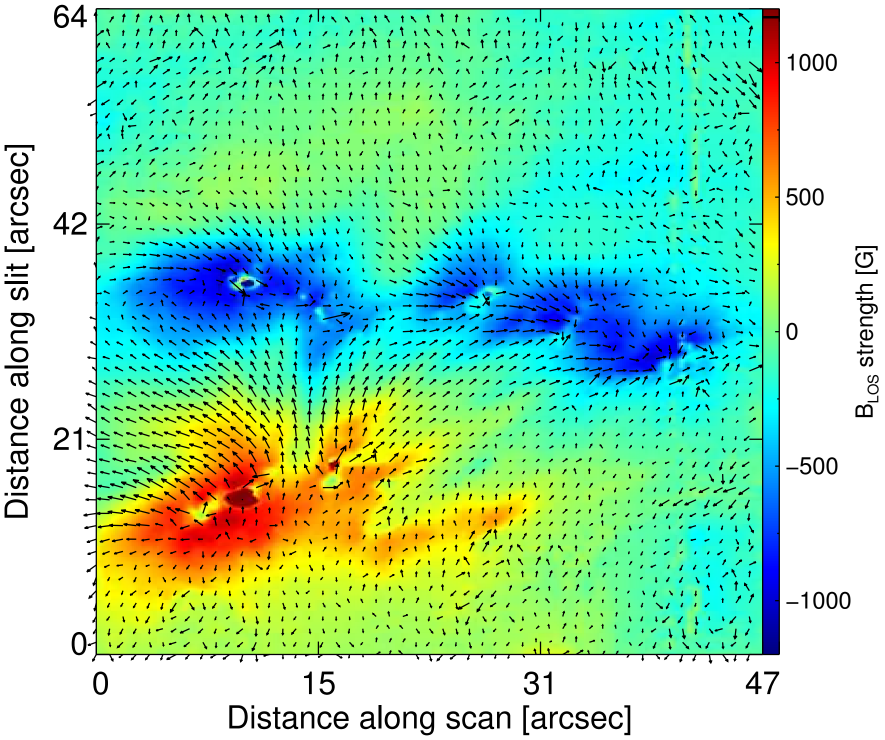

SOURCE: Author

Based on Figure 7.20, we note that the magnetic field line follows the same direction of the filaments. From that, we can obtain the path that cross the filaments and connect the footpoints of opposite polarities. Using the map of the magnetic field projection over the chromosphere (Figure 7.20), we can implement a reconstruction of the EFR loops, as described in Section 7.7.

7.6 Formation height of He I line

As discussed in Section 5.2, the arch filaments system (AFS) observed with GRIS is developed over an emerging flux region (EFR). A rising AFS is usually considered to confine photospheric material that is drained down to both ends, while the arch rises (BRUZEK, 1969; ZIRIN, 1987). With the formation of new arch filaments, the old loops expand and can reach coronal heights (SPADARO et al., 2004).

When the AFS is observed away from the disk center, in both photospheric and chromospheric layers, the Stokes V profiles can be analyzed to estimate the formation height difference between the main population of the Si and He lines.

Supposing the AFS are positioned in the solar center, the neutral lines from Si and He would be superposed and it would not be possible to determine the different height. However, when the heliocentric angle is larger, it means away from the disk center, the neutral lines projection is shifted from the original position.

A basic assumption to compute the height formation is that the inclination angle of the analyzed layers have a close behavior along the path we observe the filament. It can be confirmed by analyzing the correlation coefficient between the inclination profiles in the photosphere and in the chromosphere. In order to cover the full filament, we selected 20 profiles, side by side, 1 pixel shifted, along the filament.

The spatial distribution of the set of profiles is presented in Figure 7.21*b*. All the profiles are presented in panel (*c*), where the black lines delineate the chromospheric profiles and the red lines the profile over the photosphere. The scatter plot between both inclinations is displayed in panel (*a*). The Pearson correlation between the inclination angle, over the filament, was $R = 0.956$. This large correlation permits us to perform the analysis of height formation difference between Si and He population. Once the R is satisfied, we can consider we are comparing the neutral lines for both photosphere and chromosphere.

Figure 7.21 - (*a*) Scatter plot between the inclination angle of the magnetic field vector in the photosphere and chromosphere. The angles were taken along the profiles over the filament presented in the map (*b*). Representation of 20 profiles, side by side, 1 pixel shifted, covering the full filament. All the profiles are presented in panel (*c*), where the black lines delineate the chromospheric profiles and the red lines the profile over the photosphere. The Pearson correlation between the inclination of both layers, over the filament, was R = 0.956, and the inclination angle in chromosphere is shifted by 6.95° from the one in the photosphere. The large R and the shifted angle permit us to perform the analysis of the formation height difference between Si and He lines

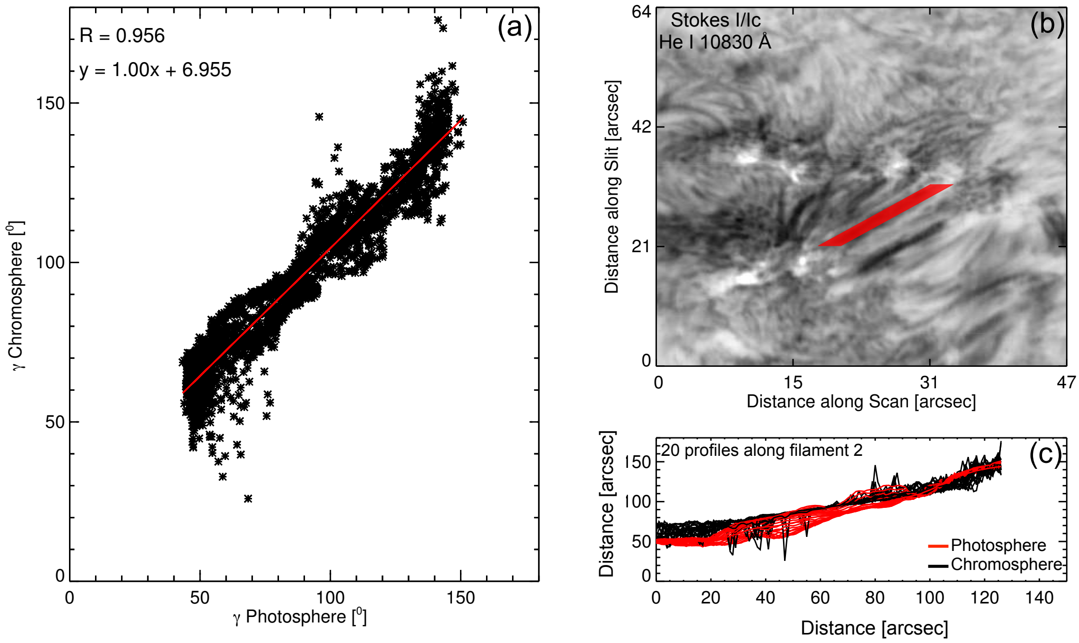

SOURCE: Author

The inclination presented an offset of $\gamma_{offset} = 6.95°$ between the photosphere an chromosphere. This offset is expected and needs to be considered in the determination of formation height.

The method is performed based on finding the neutral line in the Stokes V profiles of the slits presented in Figure 7.21. The neutral line is usually found close to the filament center. The Stokes V profiles for the central slit crossing the filament is presented in Figure 7.22. The vertical dashed lines delimit the Si and He spectral lines. The amplitude of the He profile was multiplied by 3 to improve the visualization. The blue line contour the neutral line for the photosphere and the red line, indicate the neutral line for chromosphere. The inner box displays the neutral lines over the Stokes V map. The letter "L" denotes the leading sunspot and "T" the trailing ones.

From Figure 7.22, we can determine the distance between the neutral line taken from the photosphere and chromosphere, given by $\Delta d_{_{NL}} = 1.82$”, which is equivalent to about 1320 km.

Before computing the difference in the formation height, we need to correct the distance $\Delta d_{_{NL}}$ for the foreshortening. According to Godoli and Fossi (1967), the projected distance $\Delta d_{_{NL}}$ need to be transformed in the corrected distance $\Delta d^c_{_{NL}}$, according to

$$\Delta d^c_{_{NL}} = \Delta d_{_{NL}} \sec \theta_H, \tag{7.10}$$

where θ_H is the heliocentric angle determined in Section 4, given by $\theta_H = 41.14°$ and $\mu = cos(\theta_H) = 0.75$. So the corrected distance between both neutral lines is $\Delta d^c_{_{NL}} = 1760$ km.

Once the difference between the neutral lines was determined, and we had already determined the heliocentric angle, θ_H, we can compute the variation in the formation heights, Δh_f, by

$$\Delta h_f = \frac{\Delta d^c_{_{NL}}}{\tan \theta_H}. \tag{7.11}$$

The Equation (7.12) can be used only when the magnetic field inclination angle is the same at both heights. However, as we determined in Figure 7.21a, there is an offset angle of $\gamma_{offset} = 6.95°$. So the Equation (7.12) need to be rewritten as,

$$\Delta h_f = \frac{\Delta d^c_{_{NL}}}{\tan(\theta_H + \gamma_{offset})}. \tag{7.12}$$

Figure 7.22 - Stokes V profiles along one of the 20 lines presented in Figure 7.21. The vertical dashed lines delimit the Si and He spectral lines. The amplitude of the He profile was multiplied by 3 to improve the visualization. The blue line represents the neutral line for the photosphere and the red line, the neutral line for chromosphere. The inner box displays the neutral lines over the Stokes V map. The letter "L" denotes the leading sunspot and "T" the trailing ones. The distance between both neutral lines is Δd_{NL} = 1.82", equivalent to about 1320 km.

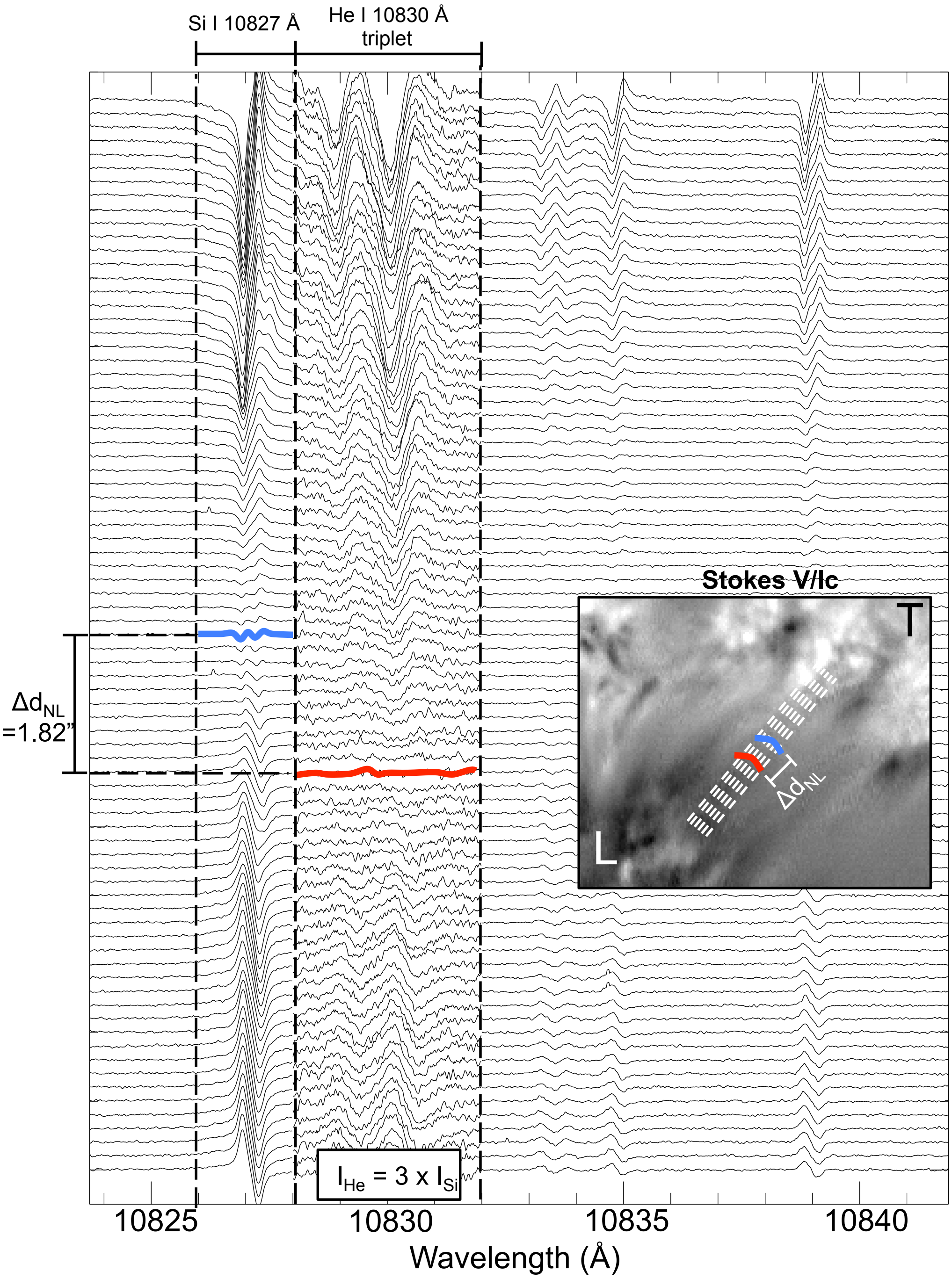

SOURCE: Author

Then, we can determine that the difference between the formation height of the He and Si in the AFS is given by $\Delta h_f = 1.72$ Mm. As a comparison, Joshi et al. (2016) analyzed the fine structures of the sunspot penumbra and found a formation height difference of 1.25 Mm using the same Si and He spectral lines. The discrepancy in the heights is explained once different solar features manages different formation height.

In Section 7.3, we verified that the magnetic field strength decreases with height, being almost twice stronger in the photosphere than in the upper chromosphere. The average magnetic field strength in the filaments is 589.80 G for the chromosphere and 1060.29 G for the photosphere. Adopting the difference between the formation height of the Si and He, $\Delta h_f = 1.72$ Mm , then the vertical gradient of the magnetic field strength is about 273 GMm^{-1}.

7.7 Reconstruction of EFR loops

In this section, we present the result of the magnetic loops reconstruction, based on the retrieved chromospheric vector field, assuming the He I 10830 Å line forms along magnetic field loops. The reconstruction method is based on the one proposed by Solanki et al. (2003).

According to Xu et al. (2010), the primary assumption is that the He absorption follows a set of magnetic field lines produced by the high density of chromospheric material emerging along the field. In our case, this field lines coincides with the filament and connect the footpoints of opposite polarities.

In Figure 7.23, we present the map of the ratio of the line core to continuum absorption coefficient (η_0). We find that η_0 becomes larger in some regions of the He filament structures, confirming a larger opacity in these regions, as well as, supporting us to estimate and trace the field from the magnetic field vector retrieved from the He observation line.

The field line reconstruction starts by selecting a pixel in the center of the filament, over the magnetic vector map (Figure 7.20), then identify the neighboring pixels to which the magnetic azimuth is pointing. The pixel that better matches the direction and strength field of the initial pixel is selected to be the one that follows the same field line.

Figure 7.23 - Map of the coefficient ratio of the He I 10830 Å line core to continuum absorption (η_0) retrieved from the inversion process. The black line contours the filament regions. The η_0 becomes larger in some regions of the He filament structure, mainly in the first one, which confirm a larger opacity in these regions.

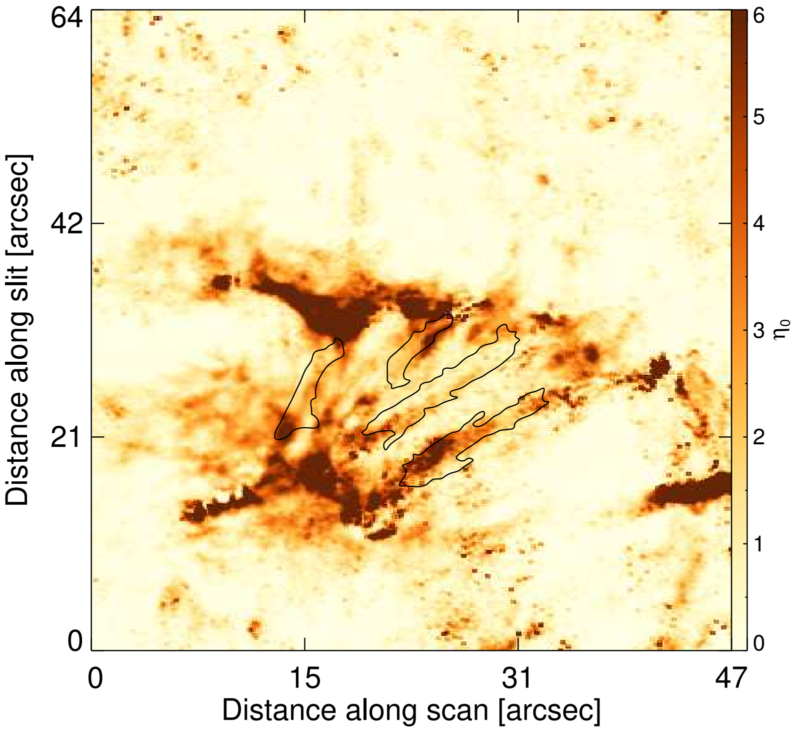

SOURCE: Author

The differential height between neighbors pixels is computed based on the inclination angle and spatial dispersion along the pixel path. Then, we follow the field line in both directions until reach the footpoints of opposite polarities. Once it touches the footpoints, we can trace the field lines with the accumulation of all the differential heights and pixel converted to the physical distance, in Mm. The profile of the three-dimension structure follow a loop-like field.

The magnetic field line reconstruction was performed for the four filaments previous selected, as presented in Figure 7.24. All the field lines loops connect the footpoints of inverse polarities with a width of five pixels that were disposable side by side starting from the positive footpoint. The reconstruction method was performed for each one of the five pixels.

Using the reconstructed loop geometry we estimate the height of the magnetic loops. The highest traced magnetic loops reach a height of 5.54 Mm (filament 1) from their footpoints at the level of He I 10 830 Å line formation. The field line over filaments 2 to 4 have a height of about 4.20 Mm, 3.38 Mm, 2.71 Mm, respectively. These heights are in accordance with the previous height observed by Solanki et al. (2003), Xu et al. (2010), Merenda et al. (2011).

The reconstruct method for the field loop, based in the He I 10830 Å, was contested by Judge (2009) in a research note. According to him, this reconstruction can not be completely performed because the field in these structures are supposed to be at nearly constant height, instead of along a magnetic loop. However, Xu et al. (2010) presented a list of arguments supporting the method, further the method was discussed and supported by Merenda et al. (2011).

7.8 Linear force-free extrapolation

There are various procedures to infer the magnetic field configuration in the photosphere and chromosphere. However, in order to get an overview of the field behavior in some particular solar region, as well as the determination of the magnetic field in the solar corona, a magnetic field extrapolation is required (PRIEST, 2000).

Figure 7.24 - Reconstruction of the magnetic loops over AFS region, based on direct measurement of the magnetic vector of the upper chromosphere, observed with the He I 10830 Å. The loops connect the footpoints of inverse polarities with a width of five pixels, side by side, starting from the positive footpoint. The gray lines are the loop projection in the XZ and YZ plane and can indicate the estimated height (in Mm). The height reconstruction is based in the inclination angle and spatial dispersion along the pixel path connecting the footpoints.

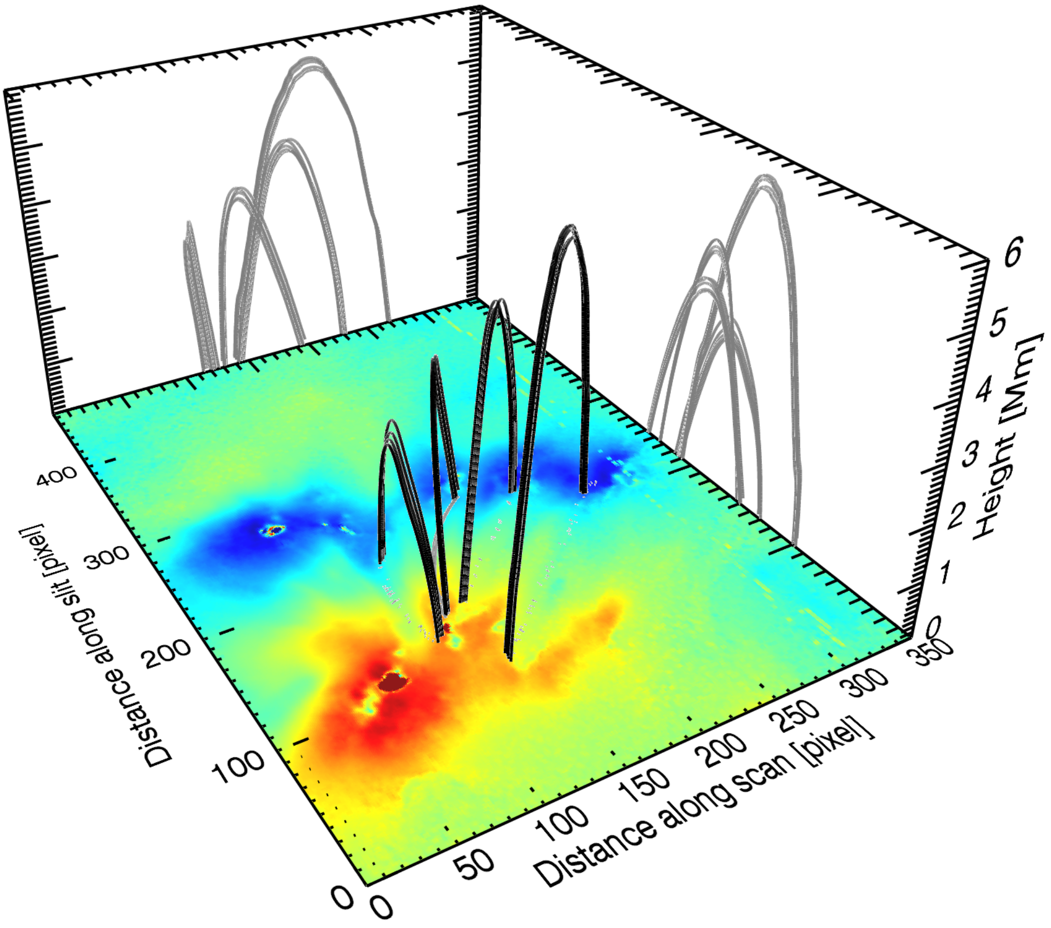

SOURCE: Author

In order to represent the magnetic field in the solar atmosphere, some plasma assumptions need to be done for simplifying the extrapolation method. The plasma β is given by

$$\beta = \frac{nk_BT}{B^2/(2\mu_0)}, \tag{7.13}$$

where μ_0 is the vacuum permeability. The primary assumption is that the plasma β is small, it means $\beta << 1$, so,

$$B^2/(2\mu_0) >> nk_BT. \tag{7.14}$$

From the above condition, the magnetic pressure is much higher than the plasma gas pressure, which is valid for the solar corona. This assumption results that the magnetic field is near to a force-free field.

Another assumption regarding the force-free extrapolation is that the coronal magnetic field is in equilibrium ($\mathrm{d}/\mathrm{d}t \approx 0$), so the plasma flows in this region can be neglected. Therefore, we can write the ideal magnetohydrodynamic (MHD) equations, relevant for the extrapolations, as,

$$\mathbf{j} \times \mathbf{B} = 0, \tag{7.15}$$

$$\nabla \times \mathbf{B} = \mu_0 \mathbf{j}, \tag{7.16}$$

$$\nabla \cdot \mathbf{B} = 0, \tag{7.17}$$

where **j** is the current density and **B** is the magnetic field.

From the Equation (7.15) we can conclude that **j** is paralell to **B**, and its proportionality is given by:

$$\mu_0 \mathbf{j} = \alpha_{ff} \mathbf{B}, \tag{7.18}$$

where α_{ff} is the called *force-free parameter*, that can be a constant or a function of the position, but it remains constant along each magnetic field line. Another important information about α_{ff} is that it also gives a measurement related to the level of twist of the magnetic field line, as presented above:

$$\nabla \times \mathbf{B} = \alpha_{ff} \mathbf{B}. \tag{7.19}$$

Based on the α_{ff}, we can differentiate three types of force-free extrapolation. When $\alpha_{ff} = 0$ the force-free is a *potential extrapolation*. In the case that $\alpha_{ff} = C$ and C is constant for all the field lines, the extrapolation is a linear force-free (LFF). For α_{ff} varying for different field lines, however with same value along each field line, it is called non-linear force-free (NLFF).

To perform the force-free field extrapolation, the observation of the photospheric magnetogram is taken as a boundary condition. While the NLFF field extrapolation require the three components of the magnetic field, the LFF method make use only of the magnetic field in the line-of-sight (B_{LOS}).

Figure 7.25 - Three dimension view of the of the linear force-free field. The background is the LOS magnetic field component. The linear force-free extrapolation is estimated by using the B_z component of the photospheric magnetic field computed with the Helix inversion code for the Si I 10827 Å line. The field lines are placed over the arch filament system, with the magnetic field associated with the large-scale main bipolar magnetic field of the active region, connecting the region between the leading sunspot and the trailing pores.

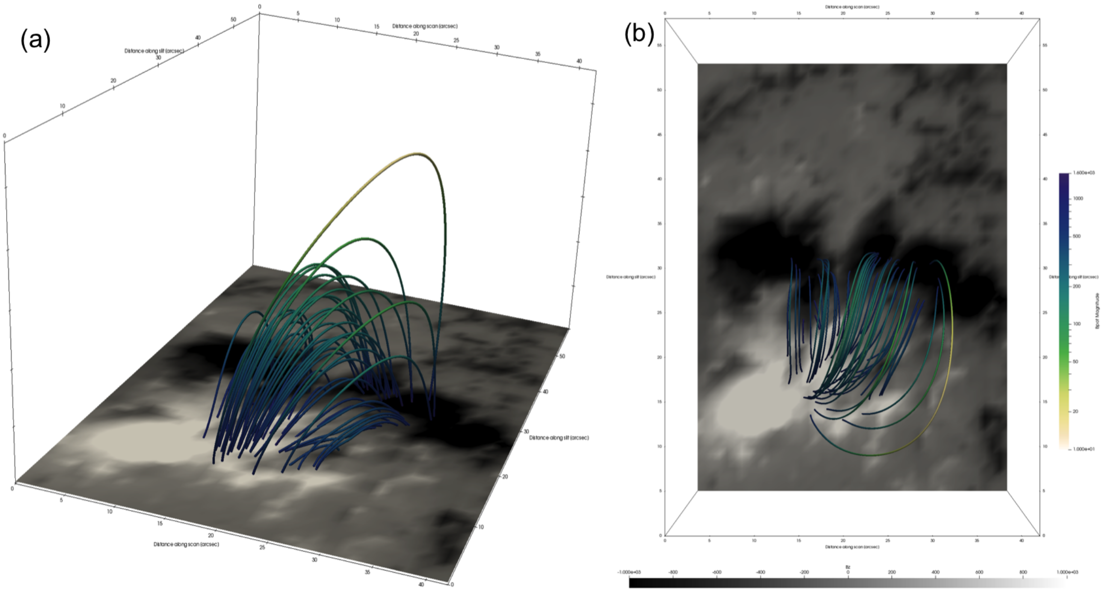

SOURCE: Author

Many methods have been developing to perform the magnetic field extrapolation using the linear force-free fields (LFF), some using spherical harmonics (NEWKIRK et al., 1968; ALTSCHULER; NEWKIRK, 1969), Fourier series (NAKAGAWA; RAADU, 1972; ALISSANDRAKIS, 1981), using Green's functions (CHIU; HILTON, 1977; SEEHAFER, 1978). Numerical codes to determine the linear force-free fields with MHD terms, such as the thermal pressure and gravity, have been done by using Fourier-Bessel series (LOW, 1992), Green's functions (PETRIE; NEUKIRCH, 2000), spherical solutions (NEUKIRCH; RASTÄTTER, 1999), and optimization methods (WIEGELMANN; NEUKIRCH, 2006)

To perform the extrapolation, we used the photospheric magnetic field computed with the Helix inversion code for the Si I 10827 Å line observed with GREGOR/GRIS. This observation is adopted as the bottom boundary condition for the vertical magnetic field B_z in the position $z = 0$. We considered the linear force-free field approximation ($\nabla \times \mathbf{B} = \alpha \mathbf{B}$). The force-free line extrapolation was done using the fast Fourier transform method proposed by Alissandrakis (1981). More details of the method used in this work are discussed in Gary (1989), Georgoulis and LaBonte (2007).

Figure 7.25 shows the result of the linear force-free field extrapolation and the topology of the AR NOAA 12552. The field lines belong to the outer connectivity domain and represent the magnetic field associated with the large-scale main bipolar magnetic field of the AR. The extrapolation FOV is equal to 34.26 Mm × 46.59 Mm.

We can also verify, from the linear force free extrapolation presented in Figure 7.25, the quality of our azimuth ambiguity correction, presented in Section 7.5. We can conclude that the azimuth correction follow a very similar pattern the one presented in X-Y view, presented in Figure 7.25b.

7.9 Overview of the magnetic structure of the filament

We combined the information obtained from the Doppler velocities maps and the full-Stokes inversions of the GRIS observed dataset. It was observed an arch filament system with filaments over the active region NOAA AR 12552. The filaments cross the polarity inversion lines connecting the footpoints of opposite polarities.

All the filaments presented downflows along almost all the filament, and most of the filaments present supersonic downflows in the footpoints. The most extended filament also presented upflow near the center of the of the filament, indicating the filament is expanding, while other filaments seem to be in equilibrium.

Figure 7.26 - Sketch of the magnetic field structure and Doppler velocities in the observed filament system and the emerging flux region. The bottom panel represents a cutout of the photospheric level, based on the magnetic field observation of the Si I 10827 Å line, and the top panel the upper chromospheric level, based on the observation of the He I 10830 Å. The white and dark ellipses indicate the region of positive and negative polarity, respectively. The dashed line, in the top panel, represents the PIL that separates the region of positive and negative polarities. The helical arch connecting the opposite polarities in the upper chromosphere represents the flux rope that supports the filament. The red and blue shaded areas arrows above the flux rope indicate the Doppler velocity as downflows (redshift) and upflows (blueshift) observed in the upper chromosphere. The presence of upflows (blue arrows) indicates the arch filament is expanding in the direction of the observer. The triple arrows close to the filament footpoint designate the supersonic downflow observed in the Doppler maps of the helium line. In the photosphere, the footpoints with opposite polarity move apart from each other, as designated by the green arrows.

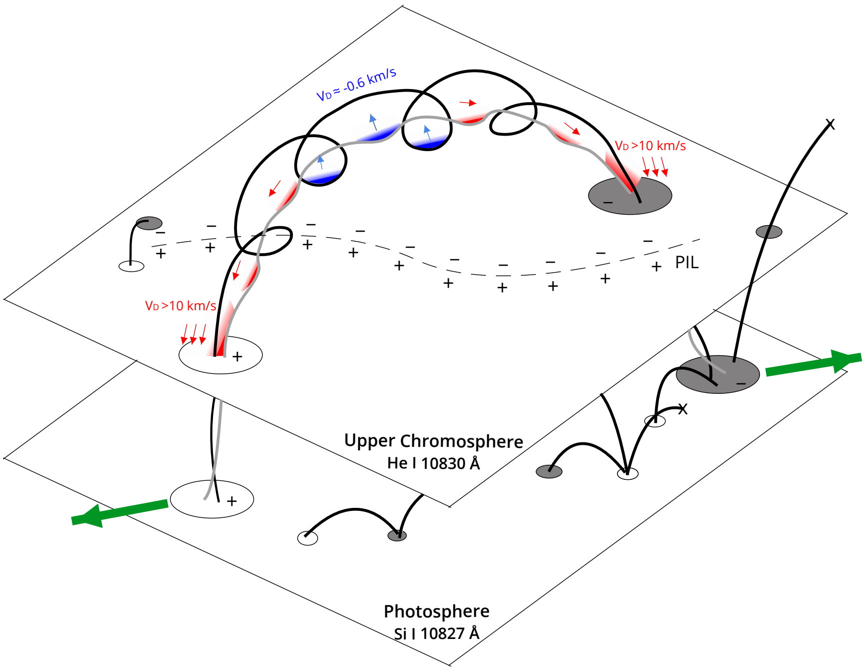

SOURCE: Author

In order to represent a overview of magnetic structure of the filaments studied in this work, we developed a sketch that better describes the most extended filament, that presented both supersonic downflows in the footpoints, as well as, upflows in the center of the filament. The other filaments follow a similar structure, but, they also manifests to be in equilibrium. The sketch model is displayed in Figure 7.26.

The sketch presents both the Doppler velocities and magnetic field structure in the arch filament system and the emerging flux region. The bottom panel represents the photospheric layer, based on the observation of the Si I 10827 Å line, and the top panel represent the upper chromospheric level, based on the observation of the He I 10830 Å.

The white and dark ellipses indicate the region where the field lines touch the chromosphere and photosphere layers, with positive and negative polarity, respectively. The dashed line, in the top panel, represents the PIL that separates the region of positive and negative polarities. The PIL was determined for both photosphere and chromosphere in Section 7.4.

The helical arch connecting the opposite polarities in the upper chromosphere represents the flux model that supports the filament mass. The red and blue shaded areas above the flux rope indicate the Doppler velocity as downflows (redshift) and upflows (blueshift), measured in the upper chromosphere. The presence of upflows (blue arrows) indicates the arch filament is rising. The triple arrows close to the filament footpoint designate the supersonic downflow observed in the Doppler maps of the helium line. In the photosphere, the footpoints with opposite polarity move apart from each other, as designated by the green arrows.

The supersonic downflow presented a very symmetric Doppler gradient from the center to the footpoints, for both single and dual-flow mode, as presented in Figure 6.9*b*. The plasma temperature in photosphere is lower than in the chromosphere. So, we interpret these downflows as resulting from the identified upflow caused by the new emerging flux tubes, that carry the photospheric cool mass to higher layers in the center of the filament. These upflows reach more than 1 kms^{-1} in the filament center. Thus, the cool material flows down from the upper chromosphere to the photosphere, along with the field lines, towards the region with strong magnetic field. The significant difference between the velocity in chromosphere and photosphere, suggest the presence of a shock in between the chromospheric and photospheric layers. A next step for this study, is to analyze where this shocks can happen, between the two layers.

8 Summary and Conclusions

We observed an emerging flux region over the NOAA AR 12252, with flux tubes emerging through the photosphere into chromosphere. In the chromosphere it is identified as an arch filament system, with dark filaments, crossing the polarity inversion line, and connecting the footpoints of opposite polarity. The active region, observed in the continuum, is composed by a sunspot and many pores with a large penumbral region among them. The observation was performed with the GRIS spectrograph installed in the 1.5 m GREGOR telescope. The GRIS scanned the active region, with a field of view of 34.2 × 46.6 Mm, achieving a spatial resolution of about 90 km.

The data reduction of the GREGOR/GRIS observation was conducted on-site applying the GRIS data pipeline. It includes the flat-field and dark current correction, crosstalk removal and calibration of the modulation matrix. The pre-processing was employed by calibrating the wavelength scale, obtaining the Stokes I continuum, and fitting it with the FTS atlas. We determined that the noise level of the Stokes dataset was about $1.10 \times 10^{-3} I_c$, with a minimum discernible structure of about 0.45”. The seeing condition was computed by using the Fried parameter, resulting on an average value of 10 cm, which is considered a good seeing along all the observation.

The filaments over the AR 12552 were observed in the Stokes I of the He I 10830 Å triplet. The most extended filament present a length of about 15.69 Mm and a width of about 2.7 Mm. We investigate the temporal evolution of the emerging flux region by using the SDO/HMI magnetograms, for a period of 48 h, centered in the GRIS observation time. It is evident the presence of an emerging flux region, with a positive flux of 7.35×10^{21} Wb in the chromosphere, and 1.53×10^{22} Wb in the photosphere.

The Doppler velocity was determined by both the photosphere and chromosphere, assuming the absorption line follow a Voigt profile. For the chromosphere, the LOS velocity was performed by using the red component of the He line; once the blue component is superposed by a Ca I line. The red component is a blend of two spectral He I lines placed at 10830.25 Å and 10830.33 Å. Thus, we implemented with success a double Voigt profile to fit the dual-flow.

The photospheric Doppler map presented a range of velocities from -3 to +3 kms^{-1}. While in the chromosphere the LOS velocity reaches more than 40 kms^{-1} in the faster component. However, the dual-flow is only necessary when the LOS velocity in chromosphere is very hight. We noted that when the speed is less than 7 kms^{-1}, the dual-flow model presents a large fitting error. However, when the velocity in the chromosphere is supersonic, the dual-flow has a better fitting than the single-flow. Therefore, we assumed that the dual-flow need to be employed for speeds faster than 10 kms^{-1}, while the single-flow for velocities lower than that.

The supersonic downflows were found in the footpoints of the arch filaments, and presented a very symmetric Doppler gradient from the center to the footpoints. We interpret these downflows as caused by the upward motions of new emerging flux tubes, that lead the photospheric material to higher layers close to the center of the filament. These upflows reach more than 1 kms^{-1} in the filament center. Thus, the material flows down from the upper chromosphere to the photosphere, along the field lines. The significant difference between the velocities in chromosphere and photosphere, suggest the presence of a shock in between the chromospheric and photospheric layers. A next step for this study, is to analyze where this shocks can happen, between the two layers.

We computed the magnetic field vector for each pixel that composes the GRIS scanning. To perform it, we made use of the full Stokes profiles of both Si I 10827 Å and He I 10830 Å lines. The magnetic field vector was computed by using the HeLIx$^+$ code. The best results were obtained by considering two atmospheres for both Si I and He I. For the Si, the atmospheres are composed of one magnetic component and one field-free component. For the He I line we also have better results with two atmospheres. However, the second atmosphere was considered only for the pixels that present a large redshift in the fast component of the He I triplet. The other parameters retrieved from the inversion are: the magnetic field strength (B), the azimuth (χ), inclination angle (γ), Doppler velocity (v_{LOS}), Doppler width ($\Delta\lambda_{\mathrm{D}}$), damping constant ($a$), slope of the source function ($S1$), and the opacity ratio between spectral line center and continuum (η_0). These parameters were computed for each atmosphere.

We computed the magnetic field over the arch filament region, which presented an average strength of about 590 G in the chromosphere and about 1060 G in the photosphere. In the chromosphere, the LOS magnetic field component, over the filament, presented a weak field. However, it is due to the strong transverse magnetic flux, concentrated in the direction of the flux tubes. The magnetic field vector in the center of the filament presented an inclination angle of about 90° with respect to the line of sight. The LOS magnetic field in the photosphere and chromosphere presented a significant correlation coefficient, $\langle R \rangle = 0.843$, over the filaments. An explanation is that the magnetic flux tubes emerging in the EFRs, follow a close inclination angle along the distance.

It was developed a code to determine the polarity inversion line by using the magnetic field vector retrieved from the inversion. We implemented it for both the photosphere and upper chromosphere. The computed PIL presented an error of less than 2° for the photosphere, and the most substantial error was about 6° for the chromosphere, the error increases because the faint Stokes V in He I 10830 Å due to low magnetic field strength.

The determination of the magnetic field from the Zeeman effect produces a non-unique solution for the azimuth component. To solve this azimuth ambiguity, we adapted the SFQ code to our dataset. We then analyzed the result of the azimuth correction, by comparing the map of the transverse magnetic field vector with the one obtained from the SDO/HMI. The method presented very accurate results for the photospheric magnetograms. Some necessary adjustments were implemented so that we have the azimuth correction for the He I triplet.

It was estimated the difference in the formation height of the Si I 10827 Å line and the He I 10830 Å triplet, over the region of the AFS. The formation height was determined by using the separation between the neutral lines of the Si and He, observed in the Stokes V profiles. This separation is derived from the neutral line projection in the solar disk, observed at $\mu = cos(\theta_H) = 0.75$, away from the disk center. We determine that the formation height of the He I triplet was 1.72 Mm above the Si I formation height. The mean magnetic field strength in the filaments is about 590 G in the chromosphere and 1060 G in the photosphere. Adopting the difference between the formation height of He I and Si I, we can conclude that the vertical gradient of the magnetic field strength is about 273 GMm^{-1}.

Solanki et al. (2003) have introduced a reconstruction technique to capture the three-dimensional magnetic field structure of an emerging flux region. The procedure assumes the He I is populated along the magnetic flux tube as it emerges through the chromosphere until reaching the corona. We verified the ratio of the line core to continuum absorption coefficient (η_0), and find that η_0 becomes larger in the region over the tallest arch filament, indicating the He line core is optically thick. Using the reconstructed loop geometry, we estimate that the tallest reconstructed loop reached its top at the height of 5.5 Mm from the footpoint, at the level of the He I line formation.

To better understand the retrieved magnetic connectivities within the active region, we constructed a linear force-free model by using both photospheric and chromospheric magnetic field in the line of sight, as the input for the extrapolation. We identified the flux tubes connecting the leading sunspot to the trailing pores over the region of the AFS. The direction of the magnetic field vector in the LFF extrapolation presented a good correlation with the vector projection previous computed, confirming that the azimuth ambiguity was properly performed. As a next step, we intend to implement a non-linear force-free field extrapolation (NLFFF) by using the magnetic field vector retrieved for the both Si I 10827 Å line and He I 10830 Å triplet, to identify the potential multiple flux ropes and provide a better representation of the filaments.

REFERENCES

ADELMANN, H. G. Butterworth equations for homomorphic filtering of images. **Computers in Biology and Medicine**, v. 28, n. 2, p. 169 – 181, 1998. ISSN 0010-4825. Available from: <`http://www.sciencedirect.com/science/article/pii/S0010482598000043`>. 124

ALISSANDRAKIS, C. E. On the computation of constant alpha force-free magnetic field. **Astronomy and Astrophysics**, v. 100, p. 197–200, jul. 1981. 145

ALTSCHULER, M. D.; NEWKIRK, G. Magnetic fields and the structure of the solar corona. **Solar Physics**, v. 9, n. 1, p. 131–149, Sep 1969. ISSN 1573-093X. Available from: <`https://doi.org/10.1007/BF00145734`>. 145

ANDRETTA, V.; JONES, H. P. On the role of the solar corona and transition region in the excitation of the spectrum of neutral helium. **The Astrophysical Journal**, v. 489, p. 375–394, nov. 1997. 14, 16

ANTIOCHOS, S. K.; DAHLBURG, R. B.; KLIMCHUK, J. A. The magnetic field of solar prominences. **The Astrophysical Journal**, v. 420, p. L41, jan. 1994. 10

ARCHONTIS, V.; MORENO-INSERTIS, F.; GALSGAARD, K.; HOOD, A.; O'SHEA, E. Emergence of magnetic flux from the convection zone into the corona. **Astronomy and Astrophysics**, v. 426, p. 1047–1063, nov. 2004. 11

ATHAY, R. G. Phenomena of the solar atmosphere. **Science**, v. 132, n. 3429, p. 707–11, Sep 1960. 16

AUER, L. H.; HEASLEY, J. N.; HOUSE, L. L. Non-LTE line formation in the presence of magnetic fields. **The Astrophysical Journal**, v. 216, p. 531–539, sep. 1977. 130

AVRETT, E. H.; FONTENLA, J. M.; LOESER, R. Formation of the solar 10830 Angstrom line. **Kluwer Academic Publishers**, v. 154, p. 35, 1994. 14, 15

BABCOCK, H. W. The solar magnetograph. **The Astrophysical Journal**, v. 118, p. 387, nov. 1953. 1

BABCOCK, H. W.; BABCOCK, H. D. The Sun's magnetic field and corpuscular emission. **Nature**, v. 175, p. 296, feb. 1955. 8, 123

BALLEGOOIJEN, A. A. van; MARTENS, P. C. H. Formation and eruption of solar prominences. **The Astrophysical Journal**, v. 343, p. 971, aug. 1989. xi, 10, 11

BARD, S.; CARLSSON, M. Constructing computationally tractable models of Si I for the 1082.7 nm transition. **The Astrophysical Journal**, v. 682, p. 1376–1385, aug. 2008. 17

BECKERS, J. M. A seeing monitor for solar and other extended object observations. **Experimental Astronomy**, v. 12, p. 1–20, jan. 2001. 70

BERKEFELD, T.; SCHMIDT, D.; SOLTAU, D.; LÜHE, O. von der; HEIDECKE, F. The GREGOR adaptive optics system. **Astronomische Nachrichten**, v. 333, p. 863, nov. 2012. 42, 43, 44

BERKEFELD, T.; SOLTAU, D.; LUHE, O. von der. Second-generation adaptive optics for the 1.5 m solar telescope GREGOR, Tenerife. **Advancements in Adaptive Optics**, v. 5490, p. 260–267, oct. 2004. 42

______. Results of the multi-conjugate adaptive optics system at the German solar telescope, Tenerife. **Astronomical adaptive optics systems and applications**, v. 5903, p. 219–226, aug. 2005. 42

______. Multi-conjugate solar adaptive optics with the VTT and GREGOR. In: SPIE ASTRONOMICAL TELESCOPES + INSTRUMENTATION. **Proceedings...** Orlando: Society of Photo-Optical Instrumentation Engineers (SPIE) Conference Series, 2006. v. 6272, p. 627205. 42

BERKEFELD, T.; SOLTAU, D.; SCHMIDT, D.; LÜHE, O. von der. Adaptive optics development at the German solar telescopes. **Applied Optics**, v. 49, p. G155, sep. 2010. 43

BRAY, R.; LOUGHHEAD, R. **Sunspots**. Wiley, 1965. (International Astrophysics series). Available from: <`https://books.google.com.br/books?id=9yw2AQAAIAAJ`>. 112

BRECKINRIDGE, J. B.; HALL, D. N. B. The absorption spectrum of atmospheric water vapor in the vicinity of the He 10830 Å triplet. **Solar Physics**, v. 28, p. 15–21, jan. 1973. 62, 64

BRESENHAM, J. E. Algorithm for computer control of a digital plotter. **IBM Systems Journal**, v. 4, n. 1, p. 25–30, 1965. ISSN 0018-8670. 124

BRUZEK, A. On arch-filament systems in spotgroups. **Solar Physics**, v. 2, p. 451–461, dec. 1967. 6

______. Motions in Arch Filament Systems. **Solar Physics**, v. 8, p. 29–36, jul. 1969. 7, 135

BUENO, J. T.; DEGL'INNOCENTI, E. L.; COLLADOS, M.; MERENDA, L.; SAINZ, R. M. Selective absorption processes as the origin of puzzling spectral line polarization from the Sun. **Nature**, v. 415, p. 403–406, jan. 2002. 13, 40

BUENO, J. T.; MERENDA, L.; CENTENO, R.; COLLADOS, M.; DEGL'INNOCENTI, E. L. The Hanle and Zeeman effects in solar spicules: a novel diagnostic window on chromospheric magnetism. **The Astrophysical Journal, Letters**, v. 619, p. L191–L194, feb. 2005. 40

BUENO, J. T.; RAMOS, A. A. Influence of atomic polarization and horizontal illumination on the Stokes profiles of the He I 10830 Å multiplet. **The Astrophysical Journal**, v. 655, p. 642–650, jan. 2007. 13

BUTTERWORTH, S. On the theory of filter amplifiers. **Wireless Engineer**, v. 7, p. 536–541, 1930. 124

CANNY, J. A computational approach to edge detection. **IEEE Transactions on Pattern Analysis and Machine Intelligence**, n. 6, p. 679–698, Nov 1986. ISSN 0162-8828. 124

CAO, W.; XU, Y.; DENKER, C.; WANG, H. 1024 × 1024 HgCdTe CMOS camera for infrared imaging magnetograph of Big Bear Solar Observatory. In: LONGSHORE, R. E. (Ed.). **Infrared and Photoelectronic Imagers and Detector Devices**. [S.l.: s.n.], 2005. v. 5881, p. 245–252. 46

CARTLEDGE, N. P.; TITOV, V. S.; PRIEST, E. R. A model for polar-crown prominences. **Astrophysical Letters and Communications**, v. 34, p. 89, jan. 1996. 8

CENTENO, R.; BUENO, J. T.; UITENBROEK, H.; COLLADOS, M. The influence of coronal EUV irradiance on the emission in the He I 10830 Å and D_3 multiplets. **The Astrophysical Journal**, v. 677, p. 742–750, apr. 2008. 15, 16

CENTENO, R.; COLLADOS, M.; BUENO, J. T. Spectropolarimetric investigation of the propagation of magnetoacoustic waves and shock formation in sunspot atmospheres. **The Astrophysical Journal**, v. 640, p. 1153–1162, apr. 2006. 13

CHAE, J.; MARTIN, S. F.; YUN, H. S.; KIM, J.; LEE, S.; GOODE, P. R.; SPIROCK, T.; WANG, H. Small magnetic bipoles emerging in a filament channel. **The Astrophysical Journal**, v. 548, n. 1, p. 497, 2001. Available from: <`http://stacks.iop.org/0004-637X/548/i=1/a=497`>. 124

CHANDRASEKHAR, S. On the radiative equilibrium of a stellar atmosphere. **The Astrophysical Journal**, v. 105, p. 424, may 1947. 19

CHARBONNEAU, P. Genetic algorithms in astronomy and astrophysics. **The Astrophysical Journal Supplement Series**, v. 101, p. 309, dec. 1995. 38

CHEUNG, M. C. M.; ISOBE, H. Flux emergence (theory). **Living Reviews in Solar Physics**, v. 11, n. 1, p. 3, Jul 2014. ISSN 1614-4961. Available from: <`https://doi.org/10.12942/lrsp-2014-3`>. 3

CHIU, Y. T.; HILTON, H. H. Exact Green's function method of solar force-free magnetic-field computations with constant alpha. I - theory and basic test cases. **The Astrophysical Journal**, v. 212, p. 873–885, mar. 1977. 145

COBO, B. R.; INIESTA, J. C. del T. Inversion of Stokes profiles. **The Astrophysical Journal**, v. 398, p. 375–385, oct. 1992. 33

COLLADOS, M.; CALCINES, A.; DÍAZ, J. J.; HERNNÁDEZ, E.; LÓPEZ, R.; PÁEZ, E. A high-resolution spectrograph for the solar telescope GREGOR. **Ground-based and Airborne Instrumentation for Astronomy**, v. 7014, p. 70145Z, jul. 2008. 48

COLLADOS, M.; LAGG, A.; GARCIA, J. J. D.; SUAREZ, E. H.; LOPEZ, R.; MANA, E. P.; SOLANKI, S. K. Tenerife infrared polarimeter II. **The physics of Chromospheric Plasmas**, v. 368, may 2007. 46, 48

COLLADOS, M.; LÓPEZ, R.; PÁEZ, E.; HERNÁNDEZ, E.; REYES, M.; CALCINES, A.; BALLESTEROS, E.; DÍAZ, J. J.; DENKER, C.; LAGG, A.; SCHLICHENMAIER, R.; SCHMIDT, W.; SOLANKI, S. K.; STRASSMEIER, K. G.; LÜHE, O. von der; VOLKMER, R. GRIS: the GREGOR infrared spectrograph. **Astronomische Nachrichten**, v. 333, p. 872, nov. 2012. 43, 47, 48

COWAN, R. D. **The theory of atomic structure and spectra**. Berkeley: University of California Press, 1981. 22

CUADRADO, R. A.; SOLANKI, S. K.; LAGG, A. Velocity distribution of chromospheric downflows. **Modern Solar Facilities - Advanced Solar Science**, p. 173, 2007. 105

CZERNY, M.; TURNER, A. F. Über den astigmatismus bei spiegelspektrometern. **Zeitschrift fur Physik**, v. 61, p. 792–797, nov. 1930. 49

DEGL'INNOCENTI, E. L. **Magnetic field measurements**: solar observations, techniques and interpretation. [S.l.: s.n.], 1992. 19, 117, 130

DEGL'INNOCENTI, E. L.; LANDOLFI, M. **Polarization in Spectral Lines**. Dordrecht: Springer Netherlands, 2004. (Astrophysics and Space Science Library, v. 307). 27, 130

DENKER, C.; LÜHE, O. von der; FELLER, A.; ARLT, K.; BALTHASAR, H.; BAUER, S. M.; GONZÁLEZ, N. B.; BERKEFELD, T.; CALIGARI, P.; COLLADOS, M.; FISCHER, A.; GRANZER, T.; HAHN, T.; HALBGEWACHS, C.; HEIDECKE, F.; HOFMANN, A.; KENTISCHER, T.; KLVANA, M.; KNEER, F.; LAGG, A.; NICKLAS, H.; POPOW, E.; PUSCHMANN, K. G.; RENDTEL, J.; SCHMIDT, D.; SCHMIDT, W.; SOBOTKA, M.; SOLANKI, S. K.; SOLTAU, D.; STAUDE, J.; STRASSMEIER, K. G.; VOLKMER, R.; WALDMANN, T.; WIEHR, E.; WITTMANN, A. D.; WOCHE, M. A retrospective of the GREGOR solar telescope in scientific literature. **Astronomische Nachrichten**, v. 333, p. 810, 2012. 43

DONNINGER, C.; LORENZ, U. **The chess monster hydra**. Berlin: Springer Berlin Heidelberg, 2004. 927–932 p. ISBN 978-3-540-30117-2. 113

DRIEL-GESZTELYI, L. V.; WIIK, J.; SCHMIEDER, B.; TARBELL, T.; KITAI, R.; FUNAKOSHI, Y.; ANWAR, B. Post-flare loops of 26 june 1992 – iv. formation and expansion of hot and cool loops. **Solar Physics**, v. 174, n. 1, p. 151–162, Aug 1997. ISSN 1573-093X. Available from: <`https://doi.org/10.1023/A:1004993809061`>. 12

DUDÍK, J.; AULANIER, G.; SCHMIEDER, B.; ZAPIÓR, M.; HEINZEL, P. Magnetic topology of bubbles in quiescent prominences. **The Astrophysical Journal**, v. 761, p. 9, dec. 2012. 8

ELMORE, D. F.; RIMMELE, T.; CASINI, R.; HEGWER, S.; KUHN, J.; LIN, H.; MCMULLIN, J. P.; REARDON, K.; SCHMIDT, W.; TRITSCHLER, A.; WÖGER, F. The Daniel K. Inouye solar telescope first light instruments and critical science plan. **Ground-Based and Airborne Instrumentation for Astronomy**, v. 9147, p. 914707, jul. 2014. 41

ENGVOLD, O. **Description and classification of prominences**. Cham: Springer International Publishing, 2015. 31–60 p. ISBN 978-3-319-10416-4. Available from: <`https://doi.org/10.1007/978-3-319-10416-4_2`>. 76

FALCONER, D. A.; MOORE, R. L.; GARY, G. A. Correlation of the coronal mass ejection productivity of solar active regions with measures of their global nonpotentiality from vector magnetograms: baseline results. **The Astrophysical Journal**, v. 569, n. 2, p. 1016, 2002. Available from: <`http://stacks.iop.org/0004-637X/569/i=2/a=1016`>. 123

FONTENLA, J. M.; AVRETT, E. H.; LOESER, R. Energy balance in the solar transition region. III. helium emission in hydrostatic, constant-abundance models with diffusion. **The Astrophysical Journal**, v. 406, p. 319, mar. 1993. 17

FRANZ, M.; COLLADOS, M.; BETHGE, C.; SCHLICHENMAIER, R.; BORRERO, J. M.; SCHMIDT, W.; LAGG, A.; SOLANKI, S. K.; BERKEFELD, T.; KIESS, C.; REZAEI, R.; SCHMIDT, D.; SIGWARTH, M.; SOLTAU, D.; VOLKMER, R.; LUHE, O. von der; WALDMANN, T.; OROZCO, D.; YABAR, A. P.; DENKER, C.; BALTHASAR, H.; STAUDE, J.; HOFMANN, A.; STRASSMEIER, K.; FELLER, A.; NICKLAS, H.; KNEER, F.; SOBOTKA, M. Magnetic fields of opposite polarity in sunspot penumbrae. **Astronomy and Astrophysics**, v. 596, p. A4, nov. 2016. 64

FRIED, D. L. Statistics of a geometric representation of wavefront distortion. **Journal of the Optical Society of America**, v. 55, p. 1427–1431, nov. 1965. 67

FRUTIGER, C.; SOLANKI, S. K.; FLIGGE, M.; BRULS, J. H. M. J. Properties of the solar granulation obtained from the inversion of low spatial resolution spectra. **Astronomy and Astrophysics**, v. 358, p. 1109–1121, jun. 2000. 33

GAIZAUSKAS, V. Filament channels: essential ingredients for filament formation. **Astronomical Society of the Pacific Conference Series**, v. 150, p. 257, 1998. 123

GARY, G. A. Linear force-free magnetic fields for solar extrapolation and interpretation. **The Astrophysical Journal Supplement Series**, v. 69, p. 323–348, feb. 1989. 145

GEORGOULIS, M. K.; LABONTE, B. J. Magnetic energy and helicity budgets in the active region solar corona. i. linear force-free approximation. **The Astrophysical Journal**, v. 671, n. 1, p. 1034, 2007. Available from: <`http://stacks.iop.org/0004-637X/671/i=1/a=1034`>. 145

GEORGOULIS, M. K.; LABONTE, B. J.; METCALF, T. R. On the resolution of the azimuthal ambiguity in vector magnetograms of solar active regions. **The Astrophysical Journal**, v. 602, n. 1, p. 446, 2004. Available from: <`http://stacks.iop.org/0004-637X/602/i=1/a=446`>. 130

GODOLI, G.; FOSSI, B. C. M. On the correction for foreshortening for Ca plages. **Solar Physics**, v. 1, p. 148–150, jan. 1967. 137

GOODE, W. C. P. R. The 1.6 m off-axis new solar telescope (nst) in big bear. **Proceedings of SPIE**, v. 8444, p. 1–8, 2012. Available from: <`https://doi.org/10.1117/12.925494`>. 41

GUO, Y.; SCHMIEDER, B.; DÉMOULIN, P.; WIEGELMANN, T.; AULANIER, G.; TÖRÖK, T.; BOMMIER, V. Coexisting flux rope and dipped arcade sections along one solar filament. **The Astrophysical Journal**, v. 714, p. 343–354, may 2010. 8

HALE, G. E. On the probable existence of a magnetic field in Sun-spots. **The Astrophysical Journal**, v. 28, p. 315, nov. 1908. 1, 21

HARDY, J. W. **Solar imaging experiment**: final report, feb. 1979 - jun. 1980. Lexington, sep. 1980. Available from: <`https://ui.adsabs.harvard.edu/#abs/1980itek.rept.....H`>. 1

HARRISON, R. A. Coronal magnetic storms: a new perspective on flares and the 'solar flare myth' debate. **Solar Physics**, v. 166, n. 2, p. 441–444, Jul 1996. ISSN 1573-093X. Available from: <`https://doi.org/10.1007/BF00149411`>. 12

HOEKSEMA, J. T.; LIU, Y.; HAYASHI, K.; SUN, X.; SCHOU, J.; COUVIDAT, S.; NORTON, A.; BOBRA, M.; CENTENO, R.; LEKA, K. D.; BARNES, G.; TURMON, M. The helioseismic and magnetic imager (HMI) vector magnetic field pipeline: overview and performance. **Solar Physics**, v. 289, p. 3483–3530, sep. 2014. 131

HOWARD, R. Polar magnetic fields of the sun: 1960–1971. **Solar Physics**, v. 25, n. 1, p. 5–13, Jul 1972. ISSN 1573-093X. Available from: <`https://doi.org/10.1007/BF00155740`>. 1

HOWARD, R. F.; HARVEY, J. W.; FORGACH, S. Solar surface velocity fields determined from small magnetic features. **Solar Physics**, v. 130, n. 1, p. 295–311, Dec 1990. ISSN 1573-093X. Available from: <`https://doi.org/10.1007/BF00156795`>. 77

HUNT AMBER L. ILER, M. A. R. B. R. Scalability conjecture for the fried parameter in synthesis of turbulent atmosphere point spread functions. **Journal of Applied Remote Sensing**, v. 12, p. 12 – 12 – 23, 2018. Available from: <`https://doi.org/10.1117/1.JRS.12.042402`>. 70

IDA, T.; ANDO, M.; TORAYA, H. Extended pseudo-Voigt function for approximating the Voigt profile. **Journal of Applied Crystallography**, v. 33, n. 6, p. 1311–1316, Dec 2000. Available from: <`https://doi.org/10.1107/S0021889800010219`>. 90

INIESTA, J. C. del T. **Introduction to spectropolarimetry**. Cambridge: Cambridge University Press, 2003. 20, 27

JORDAN, C. The intensities of helium lines in the solar EUV spectrum. **Memoirs of the Royal Astronomical Society**, v. 170, p. 429–440, feb. 1975. 16

JOSHI, J.; LAGG, A.; SOLANKI, S. K.; FELLER, A.; COLLADOS, M.; SUÁREZ, D. O.; SCHLICHENMAIER, R.; FRANZ, M.; BALTHASAR, H.; DENKER, C.; BERKEFELD, T.; HOFMANN, A.; KIESS, C.; NICKLAS, H.; YABAR, A. P.; REZAEI, R.; SCHMIDT, D.; SCHMIDT, W.; SOBOTKA, M.; SOLTAU, D.; STAUDE, J.; STRASSMEIER, K. G.; VOLKMER, R.; LÜHE, O. von der; WALDMANN, T. Upper chromospheric magnetic field of a sunspot penumbra: observations of fine structure. **Astronomy and Astrophysics**, v. 596, p. A8, 2016. Available from: <`https://doi.org/10.1051/0004-6361/201629214`>. 139

JUDGE, P. G. On magnetic field “reconstruction”. **Astronomy and Astrophysics**, v. 493, p. 1121–1123, jan. 2009. 141

KARONIS, N. T.; TOONEN, B.; FOSTER, I. Mpich-g2: A grid-enabled implementation of the message passing interface. **Journal of Parallel and Distributed Computing**, v. 63, n. 5, p. 551 – 563, 2003. ISSN 0743-7315. Special Issue on Computational Grids. Available from: <`http://www.sciencedirect.com/science/article/pii/S0743731503000029`>. 113

KNEER, F.; WIEHR, E. The Gregory-Coudé-telescope at the observatorio del Teide Tenerife. In: RUTTEN, R. J. (Ed.). **NATO Advanced Science Institutes (ASI) Series C**. [S.l.: s.n.], 1989. v. 263, p. 13. 41

KRAMIDA, A.; RALCHENKO, Y.; READER, J.; NIST ASD Team. **NIST atomic spectra database**. 2018. NIST Atomic Spectra Database. 91, 97

KUCKEIN, C.; CENTENO, R.; PILLET, V. M.; CASINI, R.; SAINZ, R. M.; SHIMIZU, T. Magnetic field strength of active region filaments. **Astronomy and Astrophysics**, v. 501, p. 1113–1121, jul. 2009. 8, 112, 120

KUCKEIN, C.; VERMA, M.; DENKER, C. Giant quiescent solar filament observed with high-resolution spectroscopy. **Astronomy and Astrophysics**, v. 589, p. A84, 2016. Available from: <`https://doi.org/10.1051/0004-6361/201526636`>. 76

KUCKEIN, D. C. **Study of the magnetic structure of active region filaments**. PhD Thesis (PhD in Astrophysics) — Universidad de La Laguna, Santa Cruz de Tenerife, 2012. 10, 14, 130

LAGG, A.; WOCH, J.; KRUPP, N.; SOLANKI, S. K. Retrieval of the full magnetic vector with the He I multiplet at 1083 nm. maps of an emerging flux region. **Astronomy and Astrophysics**, v. 414, p. 1109–1120, feb. 2004. 7, 13, 37, 38, 39, 104

LAGG, A.; WOCH, J.; SOLANKI, S. K.; KRUPP, N. Supersonic downflows in the vicinity of a growing pore. evidence of unresolved magnetic fine structure at chromospheric heights. **Astronomy and Astrophysics**, v. 462, p. 1147–1155, feb. 2007. 7, 101, 105

LANDÉ, A. Termstruktur und Zeemaneffekt der multipletts. **Zeitschrift fur Physik**, v. 15, p. 189–205, dec. 1923. 22

LIEBENBERG, D. H.; BESSEY, R. J.; WATSON, B. Coronal emission line profile observations at total solar eclipses. **Solar Physics**, v. 44, n. 2, p. 345–359, Oct 1975. ISSN 1573-093X. Available from: <`https://doi.org/10.1007/BF00153213`>. 88

LIN, Y.; MARTIN, S. F.; ENGVOLD, O. Filament substructures and their interrelation. **Subsurface and Atmospheric Influences on Solar Activity**, v. 383, p. 235, jan. 2008. 8

LITES, B.; CASINI, R.; GARCIA, J.; SOCAS-NAVARRO, H. A suite of community tools for spectro-polarimetric analysis. **Memoirs of the Royal Astronomical Society**, v. 78, p. 148, 2007. 130

LITES, B. W.; LOW, B. C.; PILLET, V. M.; SEAGRAVES, P.; SKUMANICH, A.; FRANK, Z. A.; SHINE, R. A.; TSUNETA, S. The possible ascent of a closed magnetic system through the photosphere. **The Astrophysical Journal**, v. 446, p. 877, jun. 1995. 130

LIU, Y.; LIN, J.; HUANG, G.; GUO, Y.; DUAN, C. Simple empirical analytical approximation to the voigt profile. **Journal of the Optical Society of America B**, v. 18, n. 5, p. 666–672, May 2001. Available from: <`http://josab.osa.org/abstract.cfm?URI=josab-18-5-666`>. 90, 91

LIVINGSTON, W.; WALLACE, L. **An atlas of the solar spectrum in the infrared from 1850 to 9000 cm-1 (1.1 to 5.4 micrometer)**: Nso technical report. Tucson, 1991. Available from: <`http://adsabs.harvard.edu/abs/1991aass.book.....L`>. 64

LONG, D. A. Handbook of raman spectroscopy. **Journal of Raman Spectroscopy**, v. 35, n. 1, p. 91–91, 2004. Available from: <`https://onlinelibrary.wiley.com/doi/abs/10.1002/jrs.1117`>. 49

LOW, B. C. Three-dimensional structures of magnetostatic atmospheres. IV - magnetic structures over a solar active region. **The Astrophysical Journal**, v. 399, p. 300–312, nov. 1992. 145

LUHE, O. van der; SOLTAU, D.; BERKEFELD, T.; SCHELENZ, T. KAOS: adaptive optics system for the vacuum tower telescope at Teide observatory. **Innovative Telescopes and Instrumentation for Solar Astrophysics**, v. 4853, p. 187–193, feb. 2003. 42

LUHE, O. von der; VOLKMER, R.; KENTISCHER, T. J.; GEISSLER, R. The GREGOR broad-band imager. **Astronomische Nachrichten**, v. 333, p. 894, nov. 2012. 43

MACKAY, D. H.; KARPEN, J. T.; BALLESTER, J. L.; SCHMIEDER, B.; AULANIER, G. Physics of solar prominences: magnetic structure and dynamics. **Space Science Review**, v. 151, p. 333–399, apr. 2010. 8

MACTAGGART, D.; HOOD, A. W. Simulating the "sliding doors" effect through magnetic flux emergence. **The Astrophysical Journal**, v. 716, p. L219–L222, jun. 2010. 11

MALTBY, P.; AVRETT, E. H.; CARLSSON, M.; KJELDSETH-MOE, O.; KURUCZ, R. L.; LOESER, R. A new sunspot umbral model and its variation with the solar cycle. **The Astrophysical Journal**, v. 306, p. 284, jul. 1986. 17

MANCHESTER, W. B.; VOURLIDAS, A.; JAI, Y.; LUGAZ, N.; ROUSSEV, I.; GOMBOSI, T.; OPHER, M. Comparison of MHD simulations of CME evolution and structure with coronagraph observations. In: AGU FALL MEETING, 2008. **Abstracts...** [S.l.], 2008. p. SH11A–07. 8

MANCHESTER W., I.; GOMBOSI, T.; DEZEEUW, D.; FAN, Y. Eruption of a buoyantly emerging magnetic flux rope. **The Astrophysical Journal**, v. 610, p. 588–596, jul. 2004. 11

MANRIQUE, S. J. G.; KUCKEIN, C.; COLLADOS, M.; DENKER, C.; SOLANKI, S. K.; GÖMÖRY, P.; VERMA, M.; BALTHASAR, H.; LAGG, A.; DIERCKE, A. Temporal evolution of arch filaments as seen in He I 10830 Å. **Astronomy and Astrophysics**, v. 617, p. A55, sep. 2018. 7

MARTIN, S. F. The evolution of prominences and their relationship to active centers. **Solar Physics**, v. 31, n. 1, p. 3–21, Jul 1973. ISSN 1573-093X. Available from: <`https://doi.org/10.1007/BF00156070`>. 123

_____. Conditions for the formation and maintenance of filaments – (invited review). **Solar Physics**, v. 182, n. 1, p. 107–137, Sep 1998. ISSN 1573-093X. Available from: <`https://doi.org/10.1023/A:1005026814076`>. 123

MARTIN, S. F.; BILIMORIA, R.; TRACADAS, P. W. **Magnetic Field Configurations Basic to Filament Channels and Filaments**. Dordrecht: Springer Netherlands, 1994. 303–338 p. ISBN 978-94-011-1188-1. Available from: <`https://doi.org/10.1007/978-94-011-1188-1_28`>. 124

MARTIN, S. F.; LIN, Y.; ENGVOLD, O. A method of resolving the 180-degree ambiguity by employing the chirality of solar features. **Solar Physics**, v. 250, p. 31–51, jul. 2008. 130

MARTIN, S. F.; MARQUETTE, W. H.; BILIMORIA, R. The solar cycle pattern in the direction of the magnetic field along the long axes of polar filaments. In: HARVEY, K. L. (Ed.). **The solar cycle**. [S.l.: s.n.], 1992. v. 27, p. 53. 8

MEIN, P.; DEMOULIN, P.; MEIN, N.; ENGVOLD, O.; MOLOWNY-HORAS, R.; HEINZEL, P.; GONTIKAKIS, C. Dynamics of solar magnetic arches in the photosphere and the chromosphere. **Astronomy and Astrophysics**, v. 305, p. 343, jan. 1996. 6

MEIN, P.; RAYROLE, J. Themis solar telescope. **Vistas in Astronomy**, v. 28, p. 567–569, 1985. 41

MERENDA, L.; BUENO, J. T.; DEGL'INNOCENTI, E. L.; COLLADOS, M. Determination of the magnetic field vector via the hanle and zeeman effects in the he i 10830 multiplet: evidence for nearly vertical magnetic fields in a polar crown prominence. **The Astrophysical Journal**, v. 642, n. 1, p. 554, 2006. Available from: <`http://stacks.iop.org/0004-637X/642/i=1/a=554`>. 13

MERENDA, L.; LAGG, A.; SOLANKI, S. K. The height of chromospheric loops in an emerging flux region. **Astronomy and Astrophysics**, v. 532, p. A63, 2011. Available from: <`https://doi.org/10.1051/0004-6361/201014988`>. 7, 141

METCALF, T. R. Resolving the 180-degree ambiguity in vector magnetic field measurements: the 'minimum' energy solution. **Solar Physics**, v. 155, n. 2, p. 235–242, Dec 1994. ISSN 1573-093X. Available from: <`https://doi.org/10.1007/BF00680593`>. 130

METCALF, T. R.; LEKA, K. D.; BARNES, G.; LITES, B. W.; GEORGOULIS, M. K.; PEVTSOV, A. A.; BALASUBRAMANIAM, K. S.; GARY, G. A.; JING, J.; LI, J.; LIU, Y.; WANG, H. N.; ABRAMENKO, V.; YURCHYSHYN, V.; MOON, Y.-J. An overview of existing algorithms for resolving the 180° ambiguity in vector magnetic fields: quantitative tests with synthetic data. **Solar Physics**, v. 237, n. 2, p. 267–296, Sep 2006. ISSN 1573-093X. Available from: <`https://doi.org/10.1007/s11207-006-0170-x`>. 130

MIHALAS, D. **Stellar atmospheres**. San Francisco: Freeman, 1978. 632 p. ISBN 78-0716703594. 89

MILKEY, R. W.; HEASLEY, J. N.; BEEBE, H. A. The excitation of chromospheric helium. **Bulletin of the American Astronomical Society**, v. 5, p. 277, mar. 1973. 16

MOON, Y.-J.; WANG, H.; SPIROCK, T. J.; GOODE, P.; PARK, Y. A new method for resolving the 180° ambiguity in solar vector magnetograms. **Solar Physics**, v. 217, n. 1, p. 79–94, Oct 2003. ISSN 1573-093X. Available from: <`https://doi.org/10.1023/A:1027365413021`>. 130

MORE, J. J. The levenberg-marquardt algorithm: implementation and theory. In: WATSON, G. A. (Ed.). **Numerical analysis**. Berlin, Heidelberg: Springer Berlin Heidelberg, 1978. p. 105–116. ISBN 978-3-540-35972-2. 37, 86, 94

MUELLER, H. **Memorandum on the polarization optics of the photo-elastic shutter**: Report no. 2 of osr. Washington, D.C, 1943. 21

MURDIN, P. **Encyclopedia of astronomy and astrophysics**. Bristol: Institute of physics publishing, 2002. 2500 p. 76

NAKAGAWA, Y.; RAADU, M. A. On practical representation of magnetic field. **Solar Physics**, v. 25, n. 1, p. 127–135, Jul 1972. ISSN 1573-093X. Available from: <`https://doi.org/10.1007/BF00155751`>. 145

NECKEL, H.; LABS, D. The solar radiation between 3300 and 12500 A. **Solar Physics**, v. 90, p. 205–258, feb. 1984. 64

NEUKIRCH, T.; RASTÄTTER, L. A new method for calculating a special class of self-consistent three-dimensional magnetohydrostatic equilibria. **Astronomy and Astrophysics**, v. 348, p. 1000–1004, aug. 1999. 145

NEWKIRK, G.; ALTSCHULER, M. D.; HARVEY, J. **Influence of magnetic fields on the structure of the solar corona**: structure and development of solar active regions. Dordrecht: Springer Netherlands, 1968. 379–384 p. ISBN 978-94-011-6815-1. Available from: <`https://doi.org/10.1007/978-94-011-6815-1_55`>. 145

NORTON, A. A.; GRAHAM, J. P.; ULRICH, R. K.; SCHOU, J.; TOMCZYK, S.; LIU, Y.; LITES, B. W.; ARISTE, A. L.; BUSH, R. I.; SOCAS-NAVARRO, H.; SCHERRER, P. H. Spectral Line Selection for HMI: a Comparison of Fe I 6173 Å and Ni I 6768 Å. **Solar Physics**, v. 239, n. 1, p. 69–91, Dec 2006. ISSN 1573-093X. Available from: <`https://doi.org/10.1007/s11207-006-0279-y`>. 77

OKAMOTO, T. J.; TSUNETA, S.; LITES, B. W.; KUBO, M.; YOKOYAMA, T.; BERGER, T. E.; ICHIMOTO, K.; KATSUKAWA, Y.; NAGATA, S.; SHIBATA, K.; SHIMIZU, T.; SHINE, R. A.; SUEMATSU, Y.; TARBELL, T. D.; TITLE, A. M. Emergence of a helical flux rope and prominence formation. In: AGU SPRING MEETING, 2008. **Proceedings...** [S.l.], 2008. p. SP43B–06. 10

OKS, E. **Diagnostics of laboratory and astrophysical plasmas using spectral lineshapes of one-, two-, and three-electron systems**. Oakland: World Scientific, 2017. 364 p. Available from: <`https://www.worldscientific.com/doi/abs/10.1142/9674`>. 91

OLIVERO, J.; LONGBOTHUM, R. Empirical fits to the voigt line width: a brief review. **Journal of quantitative spectroscopy and radiative transfer**, v. 17, n. 2, p. 233 – 236, 1977. ISSN 0022-4073. Available from: <`http://www.sciencedirect.com/science/article/pii/0022407377901613`>. 91

ÖZIŠIK, T.; AK, T. First day-time seeing observations at the TÜBİTAK National Observatory in Turkey. **Astronomy and Astrophysics**, v. 422, p. 1129–1133, aug. 2004. 67

PALLAVICINI, R.; SERIO, S.; VAIANA, G. S. A survey of soft X-ray limb flare images - the relation between their structure in the corona and other physical parameters. **The Astrophysical Journal**, v. 216, p. 108–122, aug. 1977. 12

PANESAR, N. K. **A Study of quiescent prominences using SDO and STEREO data**. PhD Thesis (PhD in Astrophysik) — Georg-August-Universität Göttingen, Institut für Astrophysik, Germany, may 2014. 8

PARKER, E. N. The formation of sunspots from the solar toroidal tield. **The Astrophysical Journal**, v. 121, p. 491, mar. 1955. 2, 4

PENN, M. J.; KUHN, J. R. Imaging spectropolarimetry of the He I 1083 nanometer line in a flaring solar active region. **The Astrophysical Journal, Letters**, v. 441, p. L51–L54, mar. 1995. 13, 85

PESNELL, W. D.; THOMPSON, B. J.; CHAMBERLIN, P. C. The solar dynamics observatory (SDO). **Solar Physics**, v. 275, n. 1, p. 3–15, Jan 2012. ISSN 1573-093X. Available from: <`https://doi.org/10.1007/s11207-011-9841-3`>. 51, 77

PETRIE, G. J. D.; NEUKIRCH, T. The Green's function method for a special class of linear three-dimensional magnetohydrostatic equilibria. **Astronomy and Astrophysics**, v. 356, p. 735–746, apr. 2000. 145

PIERCE, A. K. The McMath solar telescope of kitt peak national observatory. **Applied Optics**, v. 3, n. 12, p. 1337–1346, Dec 1964. Available from: <`http://ao.osa.org/abstract.cfm?URI=ao-3-12-1337`>. 41, 62

PILLET, V. M.; LITES, B. W.; SKUMANICH, A. Active region magnetic fields. I. plage fields. **The Astrophysical Journal**, v. 474, p. 810–842, jan. 1997. 1

PILLET, V. M.; VAZQUEZ, M. The continuum intensity magnetic field relation in sunspot umbrae. **International Astronomical Union Colloquium**, v. 141, p. 60–62, 1993. 1

POWELL, M. UOBYQA: unconstrained optimization by quadratic approximation. **Mathematical Programming**, v. 92, n. 3, p. 555–582, May 2002. ISSN 1436-4646. Available from: <`https://doi.org/10.1007/s101070100290`>. 39

PRIEST, E. Reconnection theory and the MHD of solar flares. In: IAU JOINT DISCUSSION, 2000. **Proceedings...** Manchester, 2000. v. 24, p. 5. 141

_____. **Magnetohydrodynamics of the Sun**. Cambridge: Cambridge University Press, 2014. 576 p. ISBN 978-0521854719. 3, 12, 76

PRIEST, E. R. **Solar magnetohydrodynamics**. New York: Springer, 1981. 500 p. ISBN 978-94-009-7958-1. 12

_____. **Dynamics and structure of quiescent solar prominences**. Boston: Kluwer Academic Publishers Dordrecht, 1989. 217 p. ISBN 978-94-009-3077-3. 7

PRIEST, E. R.; KRISHAN, V. Basic plasma processes on the Sun. In: IAU SYMPOSIUM, 1990. **Proceedings...** [S.l.], 1990. v. 142. 2

PRIETO, C. A.; ASPLUND, M.; BENDICHO, P. F. Center-to-limb variation of solar line profiles as a test of NLTE line formation calculations. **Astronomy and Astrophysics**, v. 423, p. 1109–1117, sep. 2004. 64

PUSCHMANN, K. G.; DENKER, C.; KNEER, F.; ERDOGAN, N. A.; BALTHASAR, H.; BAUER, S. M.; BECK, C.; GONZÁLEZ, N. B.; COLLADOS, M.; HAHN, T.; HIRZBERGER, J.; HOFMANN, A.; LOUIS, R. E.; NICKLAS, H.; OKUNEV, O.; PILLET, V. M.; POPOW, E.; SEELEMANN, T.; VOLKMER, R.; WITTMANN, A. D.; WOCHE, M. The GREGOR Fabry-Pérot interferometer. **Astronomische Nachrichten**, v. 333, p. 880, nov. 2012. 43

RACHKOVSKY, D. N. Magnetic rotation effects in spectral lines. **Izvestiya Ordena Trudovogo Krasnogo Znameni Krymskoj Astrofizicheskoj Observatorii**, v. 28, p. 259–270, 1962. 26

RAMOS, A. A.; BUENO, J. T.; DEGL'INNOCENTI, E. L. Advanced forward modeling and inversion of stokes profiles resulting from the joint action of the hanle and zeeman effects. **The Astrophysical Journal**, v. 683, n. 1, p. 542, 2008. Available from: <`http://stacks.iop.org/0004-637X/683/i=1/a=542`>. 40, 56

RAUTIAN, S. G.; SOBEL'MAN, I. I. The effect of collisions on the doppler broadening of spectral lines. **Soviet Physics Uspekhi**, v. 9, n. 5, p. 701, 1967. Available from: <`http://stacks.iop.org/0038-5670/9/i=5/a=R04`>. 88

RIBEIRO, J. **Observatorio Del Teide**. 2009. Available from: <`http://www.astrosurf.com/joseribeiro/poteide.htm`>. Access in: 08 Set. 2018. 42

RUDENKO, G. V.; ANFINOGENTOV, S. A. Super fast and quality azimuth disambiguation. **ArXiv e-prints**, p. arXiv:1104.1228, apr. 2011. 130, 131

RUSSELL, H. N.; SAUNDERS, F. A. New regularities in the spectra of the alkaline Earths. **The Astrophysical Journal**, v. 61, p. 38, jan. 1925. 22

SANKARASUBRAMANIAN, K.; PENN, M.; PEVTSOV, A. Large-scale structures and their role in solar activity. In: ASTRONOMICAL SOCIETY OF THE PACIFIC CONFERENCE SERIES. **Proceedings...** Sunspot, NM: ASP, 2005. v. 346. 76

SARAZIN, M.; RODDIER, F. The ESO differential image motion monitor. **Astronomy and Astrophysics**, v. 227, p. 294–300, jan. 1990. 70

SASSO, C.; LAGG, A.; SOLANKI, S. K.; CUADRADO, R. A.; COLLADOS, M. Full-Stokes observations and analysis of He I 10830 Å in a flaring region. **The Physics of Chromospheric Plasmas**, 2007. 112, 120

SCHLICHENMAIER, R. **Science with GREGOR: overview of solar science**. Tenerife, Spain, 2015. 42

SCHLICHENMAIER, R.; COLLADOS, M. Spectropolarimetry in a sunspot penumbra. spatial dependence of Stokes asymmetries in Fe I 1564.8 nm. **Astronomy and Astrophysics**, v. 381, p. 668–682, jan. 2002. 61

SCHMIDT, D.; BERKEFELD, T.; FEGER, B.; HEIDECKE, F. Latest achievements of the MCAO tested for the GREGOR solar telescope. **Adaptive Optics Systems**, v. 7736, p. 773607, jul. 2010. 43

SCHMIDT, D.; BERKEFELD, T.; HEIDECKE, F.; LÜHE, O. von der; SOLTAU, D. Test for the multi-conjugate adaptive optics system of the solar telescope GREGOR. **Astronomical and Space Optical Systems**, v. 7439, p. 74390X, aug. 2009. 43

SCHMIDT, W.; LÜHE, O. von der; VOLKMER, R.; DENKER, C.; SOLANKI, S. K.; BALTHASAR, H.; GONZALEZ, N. B.; BERKEFELD, T.; COLLADOS, M.; FISCHER, A.; HALBGEWACHS, C.; HEIDECKE, F.; HOFMANN, A.; KNEER, F.; LAGG, A.; NICKLAS, H.; POPOW, E.; PUSCHMANN, K. G.; SCHMIDT, D.; SIGWARTH, M.; SOBOTKA, M.; SOLTAU, D.; STAUDE, J.; STRASSMEIER, K. G.; WALDMANN, T. A. The 1.5 meter solar telescope GREGOR. **Astronomische Nachrichten**, v. 333, p. 796, nov. 2012. 41, 42

SCHMIDT, W.; MUGLACH, K.; KNÖLKER, M. Free-fall downflow observed in HE I 1083.0 nanometers and Hβ. **The Astrophysical Journal**, v. 544, p. 567–571, nov. 2000. 85, 94

SCHMIEDER, B.; CHANDRA, R.; BERLICKI, A.; MEIN, P. Velocity vectors of a quiescent prominence observed by Hinode/SOT and the MSDP (Meudon). **Astronomy and Astrophysics**, v. 514, p. A68, may 2010. 8

SCHMIEDER, B.; RAADU, M. A.; WIIK, J. E. Fine structure of solar filaments. II - dynamics of threads and footpoints. **Astronomy and Astrophysics**, v. 252, p. 353–365, dec. 1991. 6

SCHOU, J.; SCHERRER, P. H.; BUSH, R. I.; WACHTER, R.; COUVIDAT, S.; RABELLO-SOARES, M. C.; BOGART, R. S.; HOEKSEMA, J. T.; LIU, Y.; DUVALL, T. L.; AKIN, D. J.; ALLARD, B. A.; MILES, J. W.; RAIRDEN, R.; SHINE, R. A.; TARBELL, T. D.; TITLE, A. M.; WOLFSON, C. J.; ELMORE, D. F.; NORTON, A. A.; TOMCZYK, S. Design and ground calibration of the helioseismic and magneticiImager (HMI) instrument on the solar dynamics observatory (SDO). **Solar Physics**, v. 275, p. 229–259, jan. 2012. 51, 77

SCHRIJVER, C. J.; ZWAAN, C. Solar and stellar magnetic activity. **Cambridge Astrophysics Series**, 2000. 4

_____. Solar and stellar magnetic activity, reissue edition. **Cambridge Astrophysics Series**, 2008. 7

SCHROETER, E. H.; SOLTAU, D.; WIEHR, E. The German solar telescopes at the Observatorio del Teide. **Vistas in Astronomy**, v. 28, p. 519–525, 1985. 46

SCHWABE, S. H. Die sonne. **Astronomische Nachrichten**, v. 20, n. 17, p. 283–286, 1843. Available from: <`https://onlinelibrary.wiley.com/doi/abs/10.1002/asna.18430201706`>. 1

SEEHAFER, N. Determination of constant α force-free solar magnetic fields from magnetograph data. **Solar Physics**, v. 58, n. 2, p. 215–223, 1978. ISSN 1573-093X. Available from: <`https://doi.org/10.1007/BF00157267`>. 145

SHEELEY JR., N. R. Observations of small-scale solar magnetic fields. **Solar Physics**, v. 1, p. 171–179, mar. 1967. 1

SHENSTONE, A.; BLAIR, H. A method for the magnetic analysis of a spectrum by means of unresolved Zeeman patterns, and its application to Ag II. **Philosophical Magazine and Journal of Science**, v. 8, n. 52, p. 765–771, 1929. Available from: <`https://doi.org/10.1080/14786441108564938`>. 22

SHINE, R.; GEROLA, H.; LINSKY, J. L. Diffusion effects on the line intensities of He I and He II in the solar transition region. **The Astrophysical Journal**, v. 202, p. L101–L105, dec. 1975. 16

SOCAS-NAVARRO, H. Stokes inversion techniques: cecent achievements and future horizons. In: SIGWARTH, M. (Ed.). **Advanced solar polarimetry – theory, observation, and instrumentation**. [S.l.: s.n.], 2001. (Astronomical Society of the Pacific Conference Series, v. 236), p. 487. 33

SOCAS-NAVARRO, H.; BUENO, J. T.; COBO, B. R. Anomalous circular polarization profiles in sunspot chromospheres. **The Astrophysical Journal**, v. 544, p. 1141–1154, dec. 2000. 13

SOCAS-NAVARRO, H.; BUENO, J. T.; DEGL'INNOCENTI, E. L. Polynomial Approximants for the Calculation of Polarization Profiles in the He I 10830 ÅMultiplet. **The Astrophysical Journal Supplement Series**, v. 160, p. 312–317, sep. 2005. 13

SOLANA, D. C.; RUBIO, L. R. B.; BECK, C.; INIESTA, J. C. D. T. Temporal evolution of the Evershed flow in sunspots. I. observational characterization of Evershed clouds. **Astronomy and Astrophysics**, v. 475, p. 1067–1079, dec. 2007. 64

SOLANKI, S. K. **The photospheric layers of solar magnetic flux tubes**. PhD Thesis (PhD) — Max Planck Institute for Solar System Research, Germany, oct. 1987. 19, 33

SOLANKI, S. K.; INHESTER, B.; SCHÜSSLER, M. The solar magnetic field. **Reports on progress in physics**, v. 69, p. 563–668, mar. 2006. 12

SOLANKI, S. K.; LAGG, A.; WOCH, J.; KRUPP, N.; COLLADOS, M. Three-dimensional magnetic field topology in a region of solar coronal heating. **Nature**, v. 425, p. 692–695, oct. 2003. 7, 103, 139, 141

SOLANKI, S. K.; STEINER, O. How magnetic is the solar chromosphere? **Astronomy and Astrophysics**, v. 234, p. 519–529, aug. 1990. 105

SOLTAU, D. Windows of the German vacuum tower telescope. **Entrance Windows of Solar Telescopes**, p. 23–30, 1991. 41

SOLTAU, D.; VOLKMER, R.; LÜHE, O. von der; BERKEFELD, T. Optical design of the new solar telescope GREGOR. **Astronomische Nachrichten**, v. 333, p. 847–853, nov. 2012. 44, 45

SPADARO, D.; BILLOTTA, S.; CONTARINO, L.; ROMANO, P.; ZUCCARELLO, F. AFS dynamic evolution during the emergence of an active region. **Astronomy and Astrophysics**, v. 425, p. 309–319, oct. 2004. 7, 135

STOKES, G. G. Ueber die Veränderung der Brechbarkeit des Lichts. **Annalen der Physik**, v. 163, p. 480–490, 1852. 19

STRASSMEIER, K. G. STELLA: two new 1.2 m robotic telescopes for monitoring stellar activity. In: SCHIELICKE, E. R. (Ed.). **Astronomische Gesellschaft Meeting Abracts**. Munich: [s.n.], 2001. Available from: <`http://cdsads.u-strasbg.fr/abs/2001AGM....18JD102S`>. 41

SU, Y.; LIU, R.; LI, S.; CAO, W.; AHN, K.; JI, H. High-resolution observations of flares in an arch filament system. **The Astrophysical Journal**, v. 855, n. 2, p. 77, 2018. Available from: <`http://stacks.iop.org/0004-637X/855/i=2/a=77`>. 7

SUN, X.; HOEKSEMA, J. T.; LIU, Y.; WIEGELMANN, T.; HAYASHI, K.; CHEN, Q.; THALMANN, J. Evolution of magnetic field and energy in a major eruptive active region based on SDO/HMI observation. **The Astrophysical Journal**, v. 748, p. 77, apr. 2012. 131

TANDBERG-HANSSEN, E. **The nature of solar prominences**. Dordrecht: Springer, 1995. 308 p. 7, 76

THOMPSON, P.; COX, D. E.; HASTINGS, J. B. Rietveld refinement of Debye–Scherrer synchrotron X-ray data from Al_2O_3. **Journal of Applied Crystallography**, v. 20, n. 2, p. 79–83, Apr 1987. Available from: <`https://doi.org/10.1107/S0021889887087090`>. 90

TOKOVININ, A. From differential image motion to seeing. **Publications of the Astronomical Society of the Pacific**, v. 114, p. 1156–1166, oct. 2002. 67

UNNO, W. Line formation of a normal Zeeman triplet. **Publications of the Astronomical Society of Japan**, v. 8, p. 108, 1956. 26

VOIGT, W. Einige bemerkungen über das verhalten von spektrallinien mit trabanten im magnetfeld. **Annalen der Physik**, v. 347, p. 815–824, 1913. 89

WEBB, D. F.; HOWARD, T. A. Coronal mass ejections: observations. **Living Reviews in Solar Physics**, v. 9, n. 1, p. 3, Jun 2012. ISSN 1614-4961. Available from: <`https://doi.org/10.12942/lrsp-2012-3`>. 12

WEIGEL, T.; KUDIELKA, K.; THIEME, B.; MANNSTEIN, H.; MEYER, R.; WERNER, C.; BANAKH, V.; HOLOTA, W.; MANHART, S. **Optical ground station**: summary report. [S.l.], 2001. Available from: <`https://elib.dlr.de/9604/`>. 41

WERTHEIM, G. K.; BUTLER, M. A.; WEST, K. W.; BUCHANAN, D. N. E. Determination of the gaussian and lorentzian content of experimental line shapes. **Review of Scientific Instruments**, v. 45, n. 11, p. 1369–1371, 1974. Available from: <`https://doi.org/10.1063/1.1686503`>. 90

WIEGELMANN, T.; NEUKIRCH, T. An optimization principle for the computation of MHD equilibria in the solar corona. **Astronomy and Astrophysics**, v. 457, p. 1053–1058, oct. 2006. 145

XU, Z.; LAGG, A.; SOLANKI, S.; LIU, Y. Magnetic fields of an active region filament from full Stokes analysis of Si I 1082.7 nm and He I 1083.0 nm. **The Astrophysical Journal**, v. 749, n. 2, p. 138, 2012. Available from: <`http://stacks.iop.org/0004-637X/749/i=2/a=138`>. 104, 112, 120

XU, Z.; LAGG, A.; SOLANKI, S. K. Magnetic structures of an emerging flux region in the solar photosphere and chromosphere. **Astronomy and Astrophysics**, v. 520, p. A77, sep. 2010. 7, 139, 141

YAN, X.-L.; XUE, Z.-K.; XIANG, Y.-Y.; YANG, L.-H. Fine-scale structures and material flows of quiescent filaments observed by the new vacuum solar telescope. **Research in Astronomy and Astrophysics**, v. 15, n. 10, p. 1725, 2015. Available from: <`http://stacks.iop.org/1674-4527/15/i=10/a=1725`>. 76

ZEEMAN, P. On the influence of magnetism on the nature of the light emitted by a substance. **The Astrophysical Journal**, v. 5, p. 332, may 1897. 1, 21

ZIRIN, H. The big bear solar observatory. **Sky and Telescope**, v. 39, 1970. 41

______. The helium chromosphere, coronal holes, and stellar X-rays. **The Astrophysical Journal Letters**, v. 199, p. L63–L66, jul. 1975. 14

_____. Arch filaments associated with the formation of sunspots by umbral merging. **Solar Physics**, v. 114, p. 239–244, sep. 1987. 135

ZIRKER, J. B. Quiescent prominences. **Solar Physics**, v. 119, n. 2, p. 341–356, Sep 1989. ISSN 1573-093X. Available from: <`https://doi.org/10.1007/BF00146183`>. 123

ZWAAN, C. On the appearance of magnetic flux in the solar photosphere. **Solar Physics**, v. 60, p. 213–240, dec. 1978. 3

_____. The emergence of magnetic flux. **Solar Physics**, v. 100, n. 1, p. 397–414, Oct 1985. ISSN 1573-093X. Available from: <`https://doi.org/10.1007/BF00158438`>. 3